Microstructure Characterisation of Rapidly Solidified Al-Ni-Cr and Si-Ge Alloy Powders

Naveed Hussain

Submitted in accordance with the requirements for the degree of Doctor of Philosophy

The University of Leeds
School of Chemical and Process Engineering

November 2018

The candidate confirms that the work submitted is his/her own, except where work which has formed part of jointly-authored publications has been included. The contribution of the candidate and the other authors to this work has been explicitly indicated below. The candidate confirms that appropriate credit has been given within the thesis where reference has been made to the work of others.

The following publications have been made based on materials contained in chapter 5 and 6 of this thesis. The citations for these publications are as follows:

List of Article Publications and Presentations:

(From October 2015 to date)

- N. Hussain, A. M. Mullis and J. S. Forrester, "Effect of cooling rate and chromium doping on the microstructure of Al-25 at.% Ni Raney type alloy," *Journal of Alloys and Compounds,* vol. 744, pp. 801-808, 2018. https://doi.org/10.1016/j.jallcom.2018.02.123

- N. Hussain, A. M. Mullis and N. Haque, "Effect of Cooling Rate on the Microstructure of Rapidly Solidified SiGe," (*Manuscript submitted*).

Conference Presentations:

- N. Hussain and A. M. Mullis, "Microstructure Characterisation of Drop Tube Processed SiGe Semiconductor alloy," The 7th International Conference on Solidification and Gravity. Miskolc - Lillafüred, Hungary: SolGrav '18. 3rd-6th September 2018, p291.

- N. Hussain, A. M. Mullis and Jennifer S Forrester, "Microstructure Characterisation of Ni-75 at.% Al Raney Type Alloy as a Result of Cooling Rate and Chromium Doping," 2018 MRS Fall Meeting & Exhibit. Boston – Massachusetts, USA. 25th-30th November 2018. https://doi.org/10.1557/adv.2019.14

Acknowledgements

First and foremost I would like to thank God, without the favours that my lord has bestowed upon me I would not be where I am today.

I give a huge amount of gratitude and appreciation to my supervisors, Professor Andrew M. Mullis and Dr Robert F. Cochrane, who provided the best academic support and guidance I could ask for. Thank you for taking the time and effort to guide me through this incredible journey. It has been a pleasure working with you.

I must also thank the academic staff that were instrumental in helping me to gain the knowledge and skills to conduct my research: Mrs Diane Cochrane, Mr Robert J. Simpson, Dr Jennifer S. Forrester, Dr Faye Esat, Mr Stuart L. Micklethwaite, Mr John P. Harrington, Dr Zabeada Aslam, and Dr Duncan J. Hedges. I appreciate their patience while assisting me with lab inductions, sample preparation, XRD, GSAS, SEM, FIB, TEM and EBSD. I must also thank my friend and fellow PhD student, Nafis Ul Haque who helped me through my journey.

I would like to thank my mother, Tahira Hussain, who has supported me not only through my studies but in life, she has stuck by me no matter which path I chose to take, and has always encouraged me to be happy. My brother, Mohsin Adeeb Hussain, also deserves my appreciation as he has influenced the person that I am today, he has given me somebody to look up to and aspire to be like. Finally, I owe thanks to Yasmeen Begum, who has always motivated me to improve, especially in my quest for knowledge.

Abstract

Al-Ni and Si-Ge alloys were subject to microstructure and crystal characterisation techniques following rapid solidification processes.

Firstly, Al-25 at.% Ni was synthesised via close-coupled gas atomization and sieved into standard size fractions to investigate the microstructural effect of cooling rate. Cooling rate in the Al-Ni samples was found to affect not only the microstructure morphology but also the phase fractions. Al-23.5 at.% Ni-1.5 at.% Cr samples were also created using the same method to investigate the changes in the microstructure with the addition of Cr. When Cr was added to the alloy the same changes in microstructure and phase fraction was found with a change in cooling rate but the addition of a fourth phase: $Al_{13}Cr_2$ was revealed. While Cr doping has previously proven to enhance catalytic activity this study was conducted to understand the mechanism(s) that contribute to this increase in activity. The formation of better defined dendrites, and the addition Al-rich $Al_{13}Cr_2$ phase, means that after leaching a better nanoporous structure is achieved, which may explain the enhanced catalytic activity that has previously been observed in Cr-doped Al-Ni catalysts.

Si-30 wt.% Ge samples were created using a 6.5m drop tube and sieved into size fractions to understand the effect of cooling rate and solidification sequence. As the cooling rate increased finer grains are found as expected in rapid solidification. Partitioning however, does not follow the expected trend; a greater amount of partitioning was found in the faster cooled samples which is characteristic with the absence of solute trapping, instead it is hypothesised that the mechanism responsible is back-diffusion. Si-Ge is expected to solidify as a solid solution, but by using EDX analysis in the TEM small regions of preferred stoichiometry were observed. An interesting finding was that the Si-60 at.% Ge region, potentially Ge_3Si_2, was also chemically disordered like the rest of the alloy.

Table of Contents

List of Tables

List of Figures

List of Abbreviations

ESA – European Space Agency

EML – Electromagnetic Levitation

ISS – International Space Station

XRD – X-Ray Diffraction

SEM – Scanning Electron Microscopy

TEM – Transmission Electron Microscopy

SGR – Spontaneous Grain Refinement

SSPT – Solid-Solid Peritectic Transformation

ECN – Energy Research Centre of Netherlands

JAMIC – Japan Microgravity Centre

OM – Optical Microscopy

EDX – Energy Dispersive X-Ray

EDS – Energy Dispersive Spectroscopy

FIB – Focused Ion Beam

EBSD – Electron Backscatter Diffraction

ICDD – International Centre for Diffraction Data

SE – Secondary Electron

BSE – Back-Scattered Electron

PDBSE – Photodiode-Backscatter Electron

Ga+ – Gallium Ion

SAD – Selected Area Diffraction

BF – Bright Field

DF – Dark Field

GSAS – General Structure Analysis Software

EXPGUI – Graphical User Interface for GSAS Experiment Files

Chapter 1 Introduction

The work carried out in this research was influenced by the European Space Agency (ESA) NEQUISOL project. The objective of the NEQUISOL project is to study Al-based alloys ($Al_{68.5}Ni_{31.5}$ and $Al_{96}Fe_4$) and $Si_{95}Ge_5$. The research aims to study and improve properties of the materials through microstructure refinement, with the use several mechanisms, namely rapid solidification, undercooling and additional dopants. Al-alloys such as $Al_{96}Fe_4$ are advantageous in transport, particularly in the aerospace industry due to their small specific mass density, but their applications are not limited to just this; automotive systems and catalysis also utilise Al-alloys. $Al_{68.5}Ni_{31.5}$ is commonly used as a catalyst for hydrogenation reactions, research of which may lead to an increase in activity of $Al_{68.5}Ni_{31.5}$ sufficiently enough to replace Pt as a catalyst in hydrogen fuel cells, this would improve the cost efficiency in the manufacture of such fuel cells and therefore impacting on the viability of hydrogen powered vehicles. Strength and ductility are key properties that are sought after for Al-alloys. Si-Ge alloys are attractive in the production of solar cells. The use of Si-Ge in thermoelectrical materials has recently been of interest due to its ability to operate at high temperatures.

Undercooling has been investigated as an important route to achieving refined microstructures, since an enhanced undercooling allows the opportunity for a number of solidification pathways which would lead to metastable phases and altered properties. Containerless techniques are understood to be advantageous to achieve undercooling due to the absence of container wall, therefore eliminating possible heterogeneous nucleation. Additionally, levitation techniques allow for a suspended droplet to be accessed and investigated in the liquid state. Containerless processing techniques include electromagnetic levitation (EML) on earth and in space, melt fluxing, impulse atomization and gas atomization.

Undercooling in reduced gravity and terrestrial conditions would allow the investigation into the effects of convection as the forces that compensate disturbing accelerations are roughly three magnitudes smaller in space than those on earth (gravitational). Convection is thought to heavily influence the crystallisation process due to its dependence on heat and mass transfer. Dendrite growth velocity has been studied for $Al_{50}Ni_{50}$ under terrestrial conditions and reduced gravity conditions and the results show that the dendrite growth dynamics are affected by convection [1]. The NEQUISOL project aims to understand the crystal growth dynamics of the undercooled materials in order to achieve refined and more desirable microstructures for application. Both Al-alloys and $Si_{95}Ge_5$ are intended to be investigated in this way.

The objective of processing $Al_{68.5}Ni_{31.5}$ using EML on board the ISS is to understand the dendritic growth velocity as a function of undercooling, this is due to the anomalous behaviour of dendritic growth velocity in undercoolings of $\Delta T > 100$ K [2]. Dendritic growth velocity is found to decrease with increased undercooling, which is unexpected as a larger undercooling would allow a greater driving force for growth rate. The specific heat of $Al_{68.5}Ni_{31.5}$ is also to be measured in the undercooled melt as this would allow a greater understanding in the influence of inverse melting on the anomalous behaviour observed. Relative to Al-alloys, Si-Ge has not been investigated as much, and therefore the work carried out on $Si_{95}Ge_5$ using the EML on board the ISS would allow a greater understanding of development of the microstructure over a range of undercooling.

Intended work that influenced this research included the investigation of dendritic growth velocity as a function of undercooling. Melt fluxing is intended to be used, subject to appropriate flux material, with a high-speed video imaging camera to observe the recalescence front. Spontaneous and triggered nucleation is intended for data to be collected. Drop tube processing was chosen to supplement the melt fluxing process due to the high cooling rate achievable alongside undercooling. The high cooling rate of drop tube processing means that the relatively slow solid-state transformation experienced in melt fluxing can be identified during post-recalescence cooling. Characterisation techniques including optical microscopy, SEM, XRD, and potentially TEM are possible on post-processed samples.

Other projects that have proposed to share the same samples for $Al_{68.5}Ni_{31.5}$ include USTIP and THERMOLAB. $Si_{95}Ge_5$ have been proposed to be shared with SEMITHERM and USTIP projects.

Terrestrial experiments on board the ISS have experienced repeated delays to the effect that the first set of Al-Ni results were only presented in summer 2018. The Al-Ni samples have not yet returned to earth for further investigation, and Si-Ge samples have not yet flown to the ISS.

The objectives for the research conducted in this study are to characterise the microstructure morphology of Al-25 at.% Ni, Al-23.5 at.% Ni-1.5 at.% Cr, and Si-30 wt.% Ge. Characterisation of microstructure would lead to a greater insight into the solidification pathways and therefore the potential to achieve favoured refined microstructures. For Al-Ni and Al-Ni-Cr alloys the characterisation following gas atomisation would allow valuable information into the dendritic growth that is desired by the NEQUISOL project. The data that is obtained from gas atomised Al-Ni and Al-Ni-Cr would prove to be vital in the design and understanding of melt fluxing and/or levitation experiments on earth or on board the ISS. The findings from Al-Ni-Cr samples would provide conclusive evidence into the microstructural changes that are experienced with Cr doping and an understanding of the impact in hydrogenation reactions for industrial use. For Si-Ge samples the drop tube will be used to create particulate samples that are comparable to melt fluxing and/or levitated droplets. This would mean useful information into the solidification pathway and final microstructure can be obtained and employed in designing appropriate experiments on earth or on board the ISS. The characterisation of the microstructure following solidification would lead to a greater understanding of continuous/faceted growth that is affected by undercooling which can then be observed in the proposed experiments associated with the NEQUISOL project. The potential for benefit of the industry is also present: RGS Development is a company responsible for the research, development and manufacture of sustainable energy solutions for the steel, non-ferrous and glass industry as a spin off from the Energy Research Centre of the Netherlands (ECN). RGS Development develop a $Si_{85}Ge_{15}$ P1 n-type material in conjunction with a manganese silicide p-type material for use in thermoelectric generators that are suited to recover waste heat in processes of high temperature. The Si-Ge research conducted in this study would be valuable in the advancement of such developments. For both Al-Ni(-Cr) and Si-Ge samples the characterisation techniques described in **Sections 4.5.2** and **4.5.3** would provide greater understanding into the solidification pathway, phase fraction, microstructure morphology and crystal structure.

Chapter 2 Background Science

2.1 Unit Cells

A unit cell is the smallest number of periodically repeating atoms in three dimensions which make up a crystal structure. The lattice parameters represent the unit cell by the edges of the unit cell, and the angle, which the atoms create. The atoms inside the unit cell are denoted by their position from a defined lattice point on the x, y and z planes, though they can also be denoted by the fractional coordinates in proportion to the length of the edges of the unit cell. The length of edges are **a**, **b** and **c**, with **α**, **β** and **γ** denoting the angles between **b** and **c**, **c** and **a**, **a** and **b** respectively [3]. The six scalar lattice parameters can be seen in **Figure 2.1**.

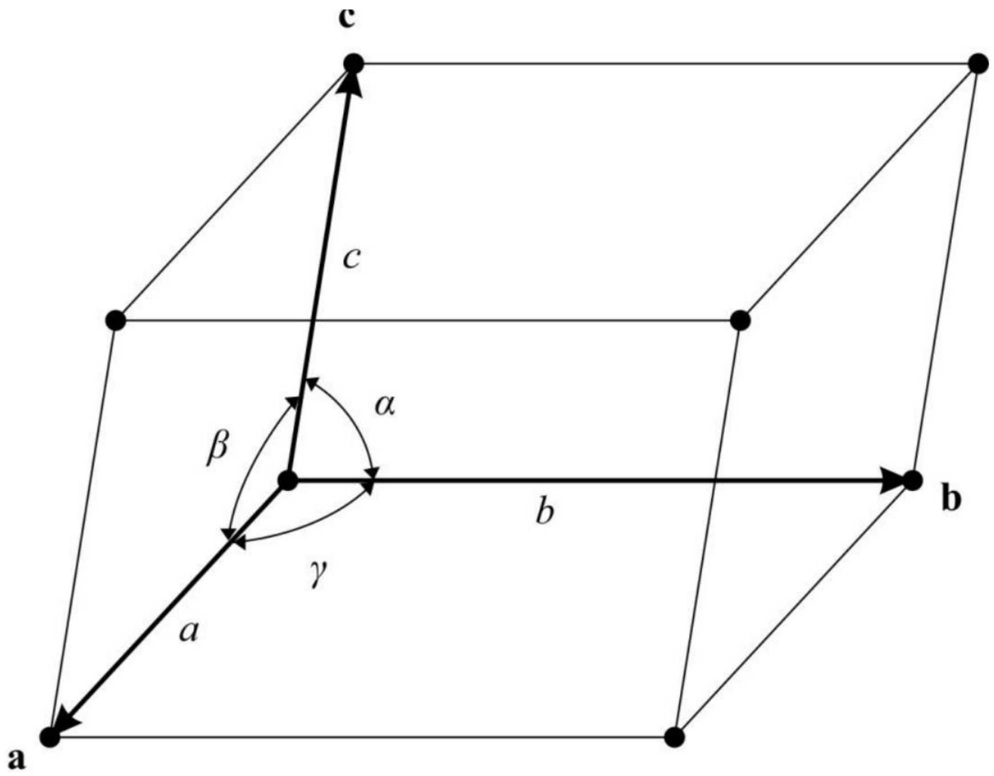

Figure 2.1 Illustration of the scalar lattice vectors and angles within a unit cell [4].

2.2 Miller Indices

Miller indices are used in crystallography to specify the position of a plane in a lattice relative to the crystallographic axis, as reciprocals of the fractional intercepts [5]. In any given lattice there are many parallel planes which is why the miller indices correspond to the nearest plane to the lattice point. Miller indices are denoted by (*hkl*). (*hkl*) means that the plane intercepts the edges of the unit cell at X=*a/h,* Y=*b/k* and Z=*c/l,* where *a, b* and *c* are the lengths of the edges of the unit cell respectively. The given equations can be rearranged to find the Miller indices values which are usually integers. In miller indices notation if a negative integer is used it will have a bar over the top, e.g. $\bar{3}$ or $\bar{h}$. If the plane does not intersect an axis the miller index would be 0, indicating that interception is at infinity. Several different types of brackets are used; (*hkl*) represents a plane as illustrated in **Figure 2.2**. [*hkl*] is used to describe a direction relative to the crystal. <*hkl*> represents a family of directions, or all directions that are equivalent to [*hkl*], and {*hkl*} represents a family of planes, or all planes that are equivalent to (*hkl*) because of the crystal symmetry.

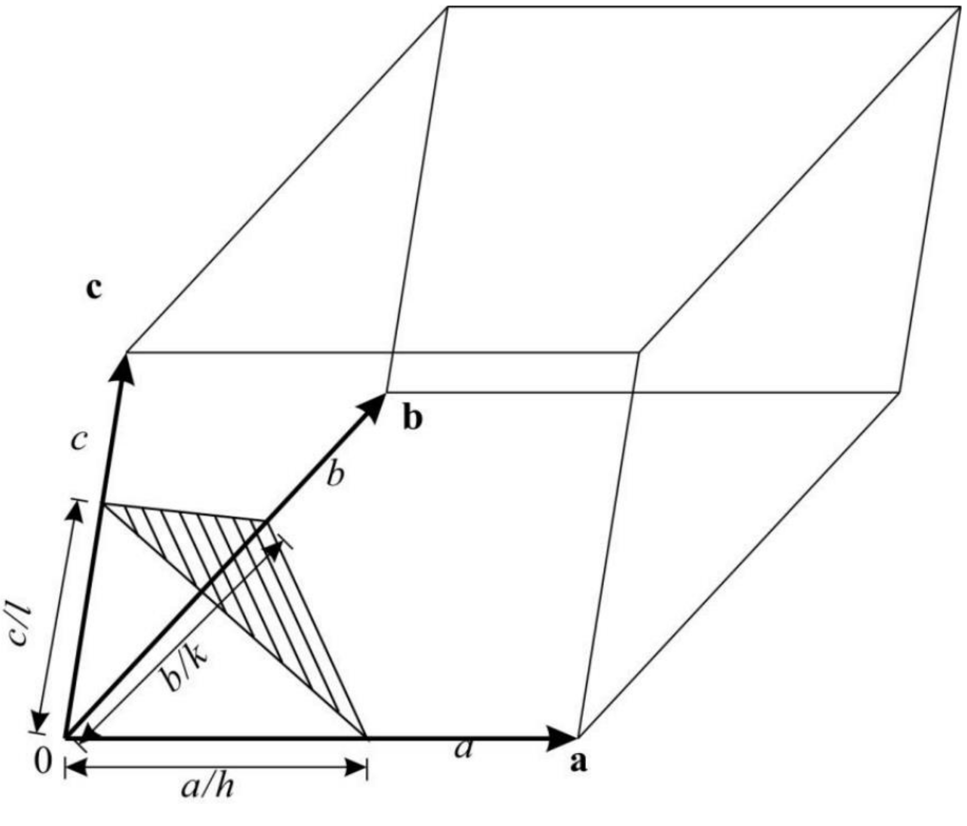

Figure 2.2 Designation of planes by Miller indices [5]. The plane shown is noted as (222).

2.3 Crystal Symmetry

Crystal symmetry often occurs when the crystal structure on one side of a plane intersecting the centre of the crystal is repeated as a mirror image on the opposite side. There are four ways in which crystal symmetry can occur: reflection, rotation, inversion and rotation-inversion. The classification of crystal systems is based on their internal or external ordering, but it is possible to reorder the system during phase changes. A crystal that has n-fold symmetry can rotate $360^0/n$ to bring itself into self-coincidence [3]. For a cubic system there is a 4-fold axis, 3-fold axis and a 2-fold axis which can be seen in **Figure 3.3**.

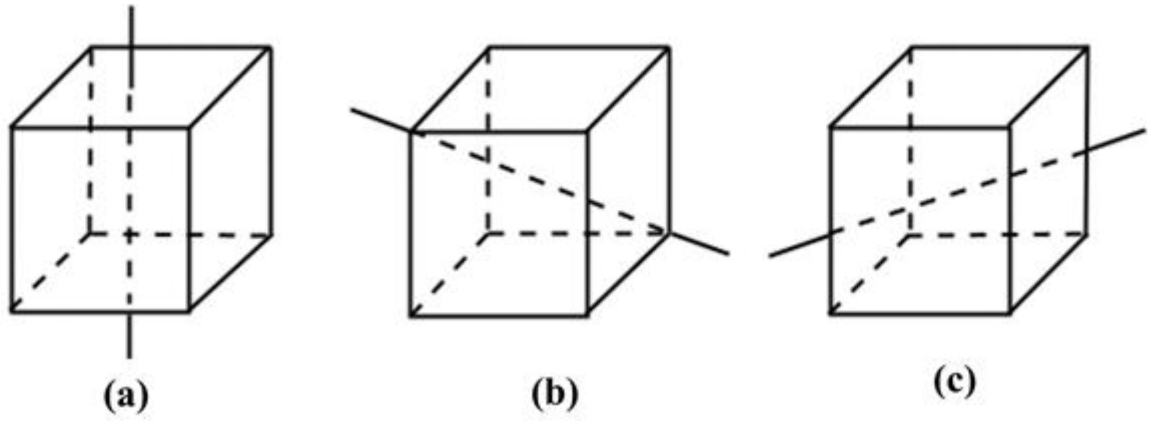

Figure 2.3 Axis symmetries for cubic system a) 4-fold axis normal to each face, b) 3-fold axis along each body diagonal and c) a 2-fold axis joining the centre of the opposite edge [4].

2.4 Space Groups

A space group is the configuration of symmetries in space. All crystal structures can be categorised into 230 space groups based on their translational or rotational symmetries. A rotational symmetry will always have a fixed point about the rotation axis, classified as a point symmetry operation. Several symmetries do not leave a point fixed; translational symmetry, screw axis or glide planes, these are known as non-point symmetry operations. A rotation about an axis is known as screw axis while a glide plane is a reflection in a plane followed by parallel translation. Space groups can be classified into the seven main crystal systems: cubic, triclinic, hexagonal, monoclinic, orthorhombic, trigonal and tetragonal. Space group in each crystal system can also be classed by their Laue class, with each Laue class having separate crystal classes, and each crystal class having one or more possible lattice centring. There are a few conventional notation methods with the simplest numbering 1-230 space groups. The Hermann-Mauguin notation describes each space group with a capital letter in relation to the Bravais lattice type, followed by the classification of the possible reflection plane (m) and/or glide plane (a, b, c, d, e or n). The screw axis may also be denoted by a number, x, which represents the angle of rotation as $\frac{360}{x}$, followed by the degree of translation along the axis in the form of a subscript. An example of a space group expressed in the Hermann-Mauguin notation would be *Pnma*, which is the orthorhombic space group for Al_3Ni. This specifies the initial lattice type (*P*), followed by the symmetry in regards to the *x*, *y*, and *z* axis: *n*-glide plane perpendicular to the *x*-axis (designated by *n*), a mirror plane perpendicular to the *y*-axis (designated by *m*), and an *a*-glide plane perpendicular to the *z*-axis (designated by *a*).

2.5 Fundamentals of Ordering Structure

The two categories of intermetallic compounds based on chemical ordering are stoichiometric and non-stoichiometric. Intermetallic compounds that display a fixed ratio of composition are stoichiometric while those that contain a range of chemical composition are known to be non-stoichiometric [6]. An example of a stoichiometric intermetallic compound would be Al_3Ni where there is a precise composition.

If we consider a hypothetical X_3Y compound with a $L1_2$ structure (ordered fcc with X on the cube faces and Y at the cube corners), then a stoichiometric compound would have X atoms on the appropriate lattice sites and Y on the Y sites. With a non-stoichiometric compound, the X and Y designated sites may not always contain X and Y atoms, in which case the X_3Y designation would be used to describe the atoms that are usually expected on those sites. For a non-stoichiometric the correct chemical formula might therefore be: $(X,Y)_3(Y,Va)$, which describes that on average there are three lattice sites that should contain X atoms but a Y atom may be found there, this would make the compound rich in Y. The second half of the chemical formula describes the Y site (1/8th of a Y atom expected on each corner) that may be vacant therefore allowing the compound to be rich in X. An example of a non-stoichiometric compound would be Al_3Ni_2, which should be correctly designated as $(Al)_3(Ni,Al)_2(Va,Ni)$. This chemical formula shows that the Al_3Ni_2 contains a total of six lattice planes, three of which are always expected to contain Al, two lattice planes that should contain Ni but may also contain Al (allowing the compound to be Al rich), and 1 plane which is usually expected to contain a vacancy but may contain Ni (allowing the compound to be Ni rich). In the case where a particular sub-lattice does contain a different atom to the one expected, for example in the $(Ni,Al)_2$ sub-lattice, the occupancy fraction is expressed as: $y''_{Ni} + y''_{Al} = 1$.

2.6 Enthalpy

The enthalpy of a system can be calculated using the following equation;

$$\mathrm{H = E + PV} \qquad 2.1$$

The enthalpy of a system tells us the heat content of a system, with E, P and V being internal energy, pressure and volume respectively. During many systems the material is cooled from a liquid to a solid state and so the pressure and volume vary only very slightly compared to the internal energy and so the approximation is usually made that H≈E [7].

The change in enthalpy during solidification is given by;

$$\Delta \mathrm{H} = \Delta \mathrm{H_f} - \int_{\mathrm{T}}^{\mathrm{Tm}} \Delta \mathrm{C_p}\, \mathrm{dT} \qquad 2.2$$

Where $\Delta \mathrm{H_f}$ is the enthalpy of fusion and $\Delta \mathrm{C_p}$ is the difference in specific heat capacity between the liquid and solid state.

2.7 Entropy

The entropy of a system shows the randomness of that system, it is known that the arrangement of atoms in a crystal structure is more ordered than the arrangement of atoms in a liquid. Using this information, it can be determined that the entropy of a crystal structure will be less than that of a liquid structure due to the atoms being more randomly arranged in the liquid phase. The entropy of a system undergoing solidification can be determined using the following equation;

$$\Delta \mathrm{S} = \Delta \mathrm{S_f} - \int_{\mathrm{T}}^{\mathrm{Tm}} \frac{\Delta \mathrm{C_p}}{\mathrm{T}}\, \mathrm{dT} \qquad 2.3$$

Where ΔS_{f} is the entropy of fusion and $\Delta \mathrm{C_p}$ is the difference in specific heat capacity between the liquid and solid state.

2.8 Gibbs Free Energy

The Gibbs free energy will determine whether a phase change is thermodynamically viable, the phase with the lower Gibbs free energy is the one that is thermodynamically more stable. This is due to the difference in Gibbs free energy between the liquid state (G_l) and the Gibbs free energy of the solid state (Gs), and it is that difference (G_l-Gs) that will be the driving force for solidification [8]. During undercooling G_l is larger than Gs, and since the system is always trying to minimize the free energy the solid state is favoured. The higher the undercooling the larger the difference in Gibbs free energy. The difference in Gibbs free energy can be calculated using the following equation;

$$\Delta G = \Delta H - T\Delta S \tag{2.4}$$

From the above equation it is possible to determine the difference in Gibbs free energy using the entropy and enthalpy the system.

2.9 Melt Subdivision

During the process of undercooling via techniques such as drop tube or gas atomization the melt is scattered into many small droplets, some of which would contain active nuclei, and some would not. It is therefore possible that some of the droplets achieve a higher undercooling than others within the same size fraction. The smaller droplets mean that most of the droplet population shall not contain an active nuclei and therefore higher undercooling is expected to take place before solidification for most of the droplets. An example of melt subdivision can be found in **Figure 2.4**, where the black dots represent active nuclei, and each square represents the division of droplets.

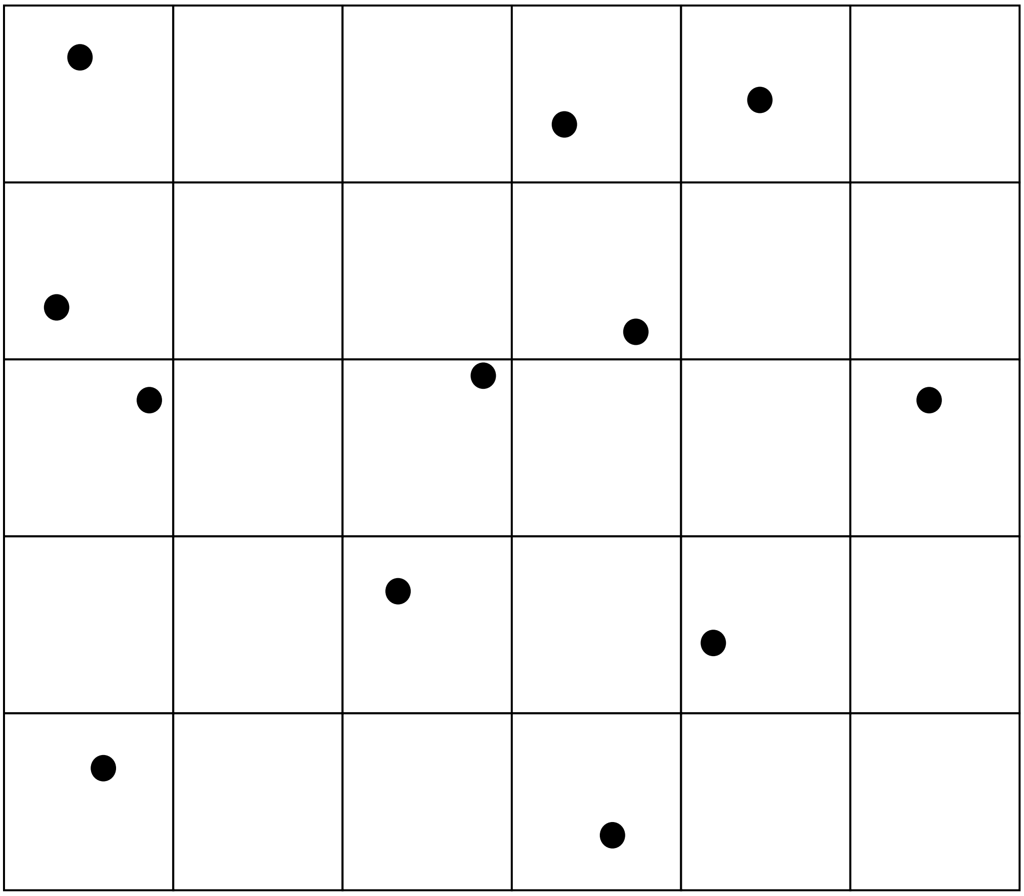

Figure 2.4 Example of how melt subdivision works. Squares represent the division of droplets and dots represent active nuclei.

Chapter 3 Literature Review

3.1 Solidification

When a material undergoes a phase change from a liquid state to a solid state as a result of a temperature decrease it is said to have experienced a phenomenon known as solidification. A shift in equilibrium stability may be caused by several factors such as composition, pressure and as mentioned above, temperature.

3.1.1 Nucleation

The first stage of solidification that a melt goes through is nucleation which is followed by growth. Nucleation is expected to occur when the temperature (T) of a metal drops below the melting temperature (T_m) using the driving force given by the Gibbs free energy. During undercooling the driving force given by the Gibbs free energy is large enough to surpass the energy barrier and therefore initiate nucleation. In some cases, a metal can remain in liquid form even when it is below the melting temperature (T_m) and this known as undercooling (T_m-T), but if the driving force exceeds the energy barrier due to increased undercooling then a solid-like cluster can transform into a solid nucleus. It has been established that a higher undercooling increases the nucleation rate and subsequent growth rate [9].

3.1.1.1 Homogeneous Nucleation

When a metal begins to nucleate without the aid of a container acting as a catalyst or any foreign materials then this is described as homogeneous nucleation. During this process a small cluster of atoms will come close to each other due to fluctuation in liquid states and therefore they will form a new interface between the liquid and solid-like states, since this cluster of atoms have spacing that can be comparable to the spacing of atoms found in solid states. During this process the system requires energy in order to create an interface between the liquid and solid-like states, which is related to the size of the cluster. It is safe to assume that the newly formed cluster is that similar to a sphere and so the free energy change can be determined using the following equation;

$$\Delta g = \frac{4}{3}\pi r^3 \Delta Gv + 4\pi r^2 \gamma_{sl} \qquad 3.1$$

Where r is the radius, $\Delta\mathrm{Gv}$ is the difference in the free energy between the solid and liquid states per unit volume and γ_{sl} represents the energy at the solid/liquid interface. The maximum value that Δg can be is the size of the energy barrier that will determine the formation of a crystal nucleus. The derivative of Δg with respect to r shall give r* which is given by the equation:

$$\mathrm{r}^* = \frac{2\gamma_{\mathrm{SL}}}{\Delta\mathrm{G_v}} \qquad 3.2$$

r* is known as critical radius, at the point at which the free energy is maximum, this characterises the minimum size of the nucleus formed by atoms for stable growth If the radius of the nucleus is below r* then the system is able to lower its free energy by dissolution of the solid cluster. The Gibbs free energy barrier for nucleation is given in the following equation:

$$\Delta\mathrm{g}^* = \frac{16\pi\mathrm{G_i}\gamma_{\mathrm{SL}}^3}{3\Delta\mathrm{H_s^2}}\,\frac{1}{(\Delta\mathrm{T})^2} \qquad 3.3$$

3.1.1.2 Heterogeneous Nucleation

More often nucleation takes place due to the container wall or the presence of impurities, such as external particles [9]. Nucleation influenced in this way would mean that the volume of the critical-sized nucleus is reduced and therefore nucleation is catalysed. This is known as heterogeneous nucleation. If the nucleus encounters any external solid particles, such as the container wall it is easy to develop nucleation by reducing the interfacial energy term. For heterogeneous nucleation to be successful the solid/liquid wettability is important. Equilibrium is assumed in **Figure 3.1** when:

$$\gamma_{\mathrm{LM}} = \gamma_{\mathrm{SL}}\,\cos\theta + \gamma_{\mathrm{SM}} \qquad 3.4$$

Where γ_{SM} is the solid surface energy at the mold, γ_{LM} is the liquid surface energy at the mold, γ_{SL} is the solid/liquid interfacial energy and θ is the contact angle. When θ=180º there is no wetting and therefore no heterogeneous nucleation, nucleation in this situation is said to be homogeneous. When θ=0º the surface is completely wet by the solid.

The important part of heterogeneous nucleation is that the contact between the solid substrate and the crystal lowers the energy barrier to nucleation. So:

$$\Delta\mathrm{g}^* = \frac{16\pi\mathrm{G_i}\gamma_{\mathrm{SL}}^3}{3\Delta\mathrm{H_s^2}}\,\frac{1}{(\Delta\mathrm{T})^2} \qquad 3.5$$

becomes:

$$\Delta g^{*} = \frac{16\pi\Delta G_{i}T_{m}^{2}}{3H_{f}^{2}}\frac{1}{(\Delta T)^{2}}S(\theta) \qquad 3.6$$

Where S(θ) is the shape factor defined by:

$$S(\theta) = \frac{1}{4}(2+\cos\theta)(1-\cos\theta)^{2} \qquad 3.7$$

Where S(θ) < 1, so reducing the energy barrier. The contact angle is the basis for S(θ) so as the contact angle θ increases so does S(θ). When the wetting angle improves, approaching zero, the nucleation barrier decreases.

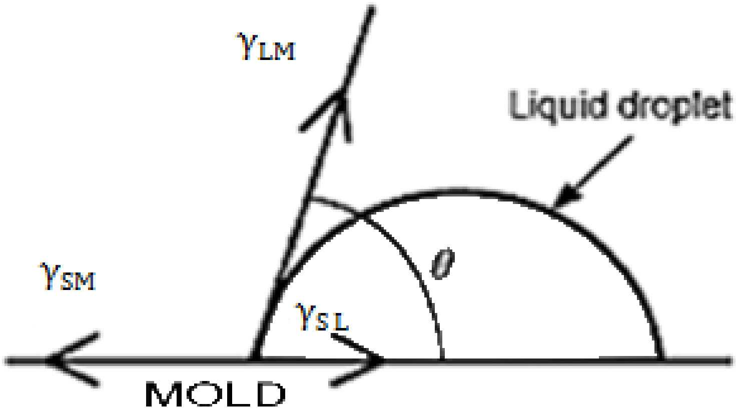

Figure 3.1 Wetting angle between a liquid droplet and a solid interface, with energy.

3.1.2 Rapid Cooling

Rapid cooling is the process in which molten materials change from a liquid to a solid state, thereby releasing latent heat very quickly. This could be achieved by means of undercooling or by simply increasing the cooling rate using an appropriate cooling medium.

The interest of rapid cooling has increased [10] due to the discovery of a range of unique features that are found during this process; the grain size and/or the spacing between dendrites have been proven to be reduced (finer grain structure), whilst also increasing the solute solubility. There is a huge variation between the microstructures that are found in rapidly solidified materials and those that are solidified in equilibrium, using rapid cooling it is possible to retain metastable phases at a fully cooled temperature that would otherwise have gone to completion if cooled at equilibrium. There exists an established hierarchy of effects related to rapid cooling as the departure from equilibrium increases:

Scale refinement → Increased solid solubility → Metastable phase formation → Formation of amorphous structures

There are a few things to consider when trying to achieve desirable microstructures using rapid cooling via undercooling; one of which is the amount of undercooling that takes place (ΔT). It is possible to achieve high levels of undercooling by avoiding heterogeneous nucleation from the wall of a container to modify the evolution of microstructures, this is because the rate of cooling can contribute to the motion of the solid-liquid interface [11].

Quenching and splat quenching are examples of rapid cooling, they usually involve cooling the material using an external medium such as contact with a liquid or solid. It should be noted that rapid cooling may only be achieved if one or more dimensions of the material is sufficiently small; sheets and/or ribbons (one small dimension), wires (two small dimensions) and particles (three small dimensions). Using these types of rapid cooling would cause the microstructure of the material to not be uniform throughout since the contact is made with the external source of cooling at the surface of the material. When cooling using splat quenching the metallic liquid is poured into two plates of copper, so when the metal solidifies it does not have enough time to rearrange its atoms and so remains with a near-amorphous structure.

During cooling, in order to allow nucleation to initiate subsequent growth it is necessary to overcome the energy barrier, this is possible due to undercooling. In order to rapidly solidify a material a high cooling rate and/or undercooling is required, which will in turn affect the growth rate. As the growth rate increases, a level of departure from metastability, or diffusional equilibrium, shall occur. This hierarchy of departure can be seen in **Table 3.1**.

Table 3.1 Hierarchy of departure from metastability as growth velocity is increased [9].

I	***Full Diffusional Equilibrium***
	No chemical potential gradients (phase compositions are uniform)
	No temperature gradients
	Lever rule applies
II	***Local Interface Equilibrium***
	Phase diagram gives compositions and temperatures only at liquid/solid interface
	Corrections made for interface curvature (Gibbs – Thomson effect)
III	***Metastable Local Interfacial Equilibrium***
	Stable phase cannot nucleate or grow sufficiently fast
	Metastable phase diagram gives the interface conditions
IV	***Interfacial Non-Equilibrium***
	Phase diagram fails at the interface
	Chemical potentials are not equal at the interface
	Free energy functions of phases still lead to criteria which predict impossible reactions

3.1.3 Undercooling

By increasing the undercooling of a material during solidification it is possible to change certain attributes of that material; features such as corrosion can be significantly improved through the manipulation of metastable and refined microstructures. Undercooling can be achieved, but not restricted to, using containerless solidification, where a material can remain in liquid form whilst existing in temperatures that are below the melting point. This is possible since there is no container for the material to nucleate with, therefore avoiding heterogeneous nucleation [12]. During undercooling the likelihood of heterogeneous nucleation is larger due to the relationship between undercooling and ΔG^*;

$$\Delta g^* = \frac{16\pi G_i \gamma_{SL}^3}{3\Delta H_s^2}\frac{1}{(\Delta T)^2} \tag{3.8}$$

From **Equation 3.8** it is apparent that as undercooling increases the energy barrier for heterogeneous nucleation is reduced, permitting smaller nuclei to become viable. This would allow any impurities and/or oxides that may be present to initiate nucleation.

During rapid solidification the level of undercooling shall determine the fraction of solid that grows during recalescence. If the fraction of solid is more than 1 then solidification will proceed without diffusion of heat at a rate limited only by interface kinetics. Recalescence is the rapid warming during which solid is formed at, or very close to, the melting temperature. When the solid fraction is above 1 then recalescence shall occur up to, or before, the melting point. The solid fraction during recalescence is expressed in the following equation:

$$f_s = \frac{\Delta T}{{}^{L}/_{C_p}} \tag{3.9}$$

Where ΔT is the amount of undercooling expressed in Kelvin, L is the latent heat expressed in $\mathrm{Jkg^{-1}}$ and C_p is the specific heat expressed in $\mathrm{Jkg^{-1}K^{-1}}$. L/C_p is defined as the hypercooling limit.

During Recalescence the undercooled liquid acts as a heat sink for the latent heat released from the growing solid [11]. The remaining liquid, (1-f_S) will solidify post recalescence at the rate determined by the heat extraction rate.

Once a material is undercooled it would experience nucleation and the recalescence process shall begin. During recalescence latent heat shall be released and the material shall begin to return to the solidus temperature. This could affect the microstructure whereby the evolved microstructure shall be disturbed and possibly lost. Rapid solidification techniques, such as magnetic levitation or drop tube, are used to minimise the possibility of heterogeneous nucleation and therefore achieve a high level of undercooling; hypercooling. Hypercooling is an advanced level of undercooling where the amount of undercooling is larger than critical undercooling. Critical undercooling is the term given when undercooling is equal to the temperature change during recalescence, $T_S = T_R$, resulting in the material returning to precisely the solidus temperature. In order to retain the evolved microstructure achieved during undercooling the cooling rate after recalescence has taken place must be sufficiently quick. It is possible to achieve metastable or anomalous phases using the non-equilibrium undercooling process [13].

3.2 Solute Partitioning

During solidification the composition of the growing solid and the composition of the liquid would be different. When the temperature of an alloy falls below the liquidus line of the phase diagram the solid begins to grow. By looking at the phase diagram the composition of that solid, W_s, can be estimated by drawing a horizontal tie-line until it reaches the solidus line. Similarly, the composition of the remaining liquid, W_l, can be calculated in a similar fashion by drawing the tie-line to the liquidus. In the case of Si-Ge the phase diagram would illustrate that the early solid to be formed would be Si rich as Si has a higher melting temperature than Ge. As solidification proceeds the Ge concentration increases and the Si concentration decreases in the solid fraction accordingly, this is because the remaining liquid is becoming more and more Ge rich. The final solid to form would be Ge rich as the concentration of the remaining liquid would be indicated by the liquidus line on the Ge-rich side of the phase diagram. At any point during the solidification when the temperature is between the solidus and liquidus the partition coefficient, k_E, can be calculated using the following formula:

$$\mathrm{k_E} = \frac{\mathrm{W_s}}{\mathrm{W_l}} \tag{3.10}$$

The free energy curves are a function of temperature, with the common tangent giving the equilibrium concentrations of the solid and liquid. As the liquid becomes rich in component B the free energy curve for W_l would be lower than W_s and the common tangent would appear to be in favour of the liquid composition. The partitioning is illustrated in **Figure 3.2** with the free energy curves and common tangent in **Figure 3.3**.

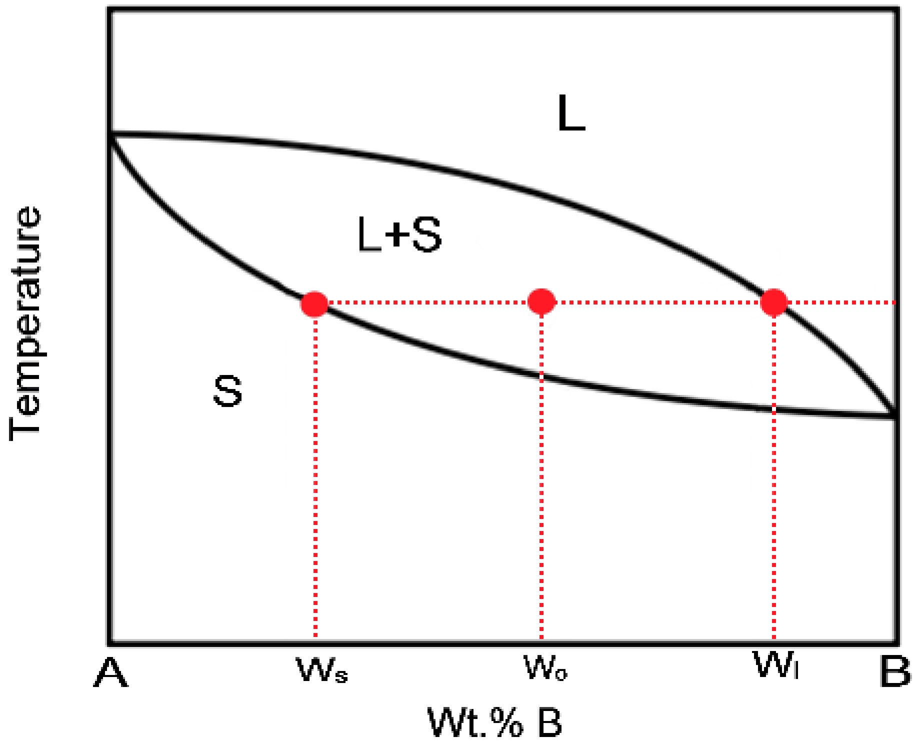

Figure 3.2 Simple phase diagram illustrating the composition of the solid being formed, W_s, and the remaining liquid composition, W_l. W_o is the original composition of the material.

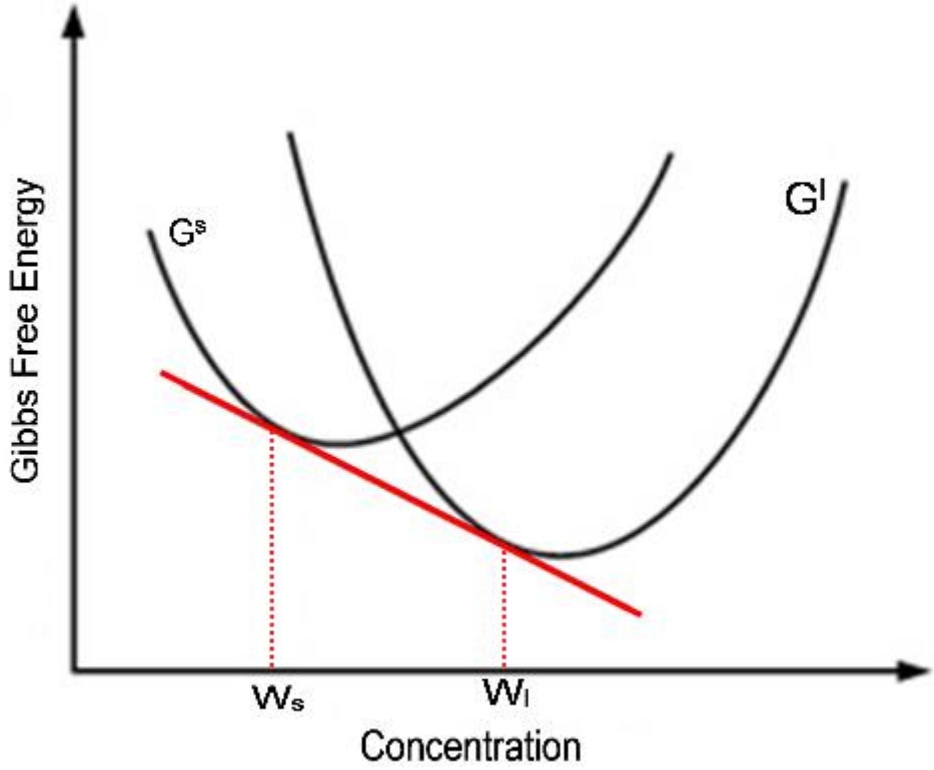

Figure 3.3 Free energy curves for the composition of liquid and growing solid with common tangent.

3.3 Scheil Calculation

It is advantageous to be able to quantitatively predict the concentration of solute in the solid, during solidification, since it would help to understand the properties of an alloy. The Scheil equation goes some way to predict the composition of solid and liquid during solidification. To allow the Scheil equation to predict the phases present within an alloy the following assumptions must be made:

- Once solid phases are formed diffusion does not occur in the solid
- At all temperatures diffusion occurs infinitely fast in the liquid
- Equilibrium takes place at the solid/liquid interface therefore compositions from the phase diagram are valid

The Scheil equation for composition of the liquid during solidification is:

$$\mathrm{C_L = C_O(f_L)^{k-1}} \qquad 3.11$$

and for the solid composition:

$$\mathrm{C_S = kC_O(1 - f_S)^{k-1}} \qquad 3.12$$

Where $\mathrm{C_S}$ and $\mathrm{C_L}$ are the concentrations of solute in the solid and liquid respectively, $\mathrm{f_L}$ and $\mathrm{f_S}$ are the fraction of liquid and solid respectively, $\mathrm{C_O}$ is the initial concentration of the liquid and k is the partition coefficient.

Partitioning at any temperature is often determined using the phase diagram, where a tie line is drawn horizontally from one phase to another and through the temperature and weight % of the alloy. Where the tie line intersects the 2 phases the weight % is compared to the weight % of the composition to determine how much of each phase is present. This is expressed in the form of a percentage or a fraction.

3.4 Reactions

The eutectic reaction is defined as:

$$Liquid \ \rightarrow Solid\ Solution\ \alpha + Solid\ Solution\ \beta$$

The eutectic reaction appears on a phase diagram as a 'V' shape as seen in **Figure 3.4**.

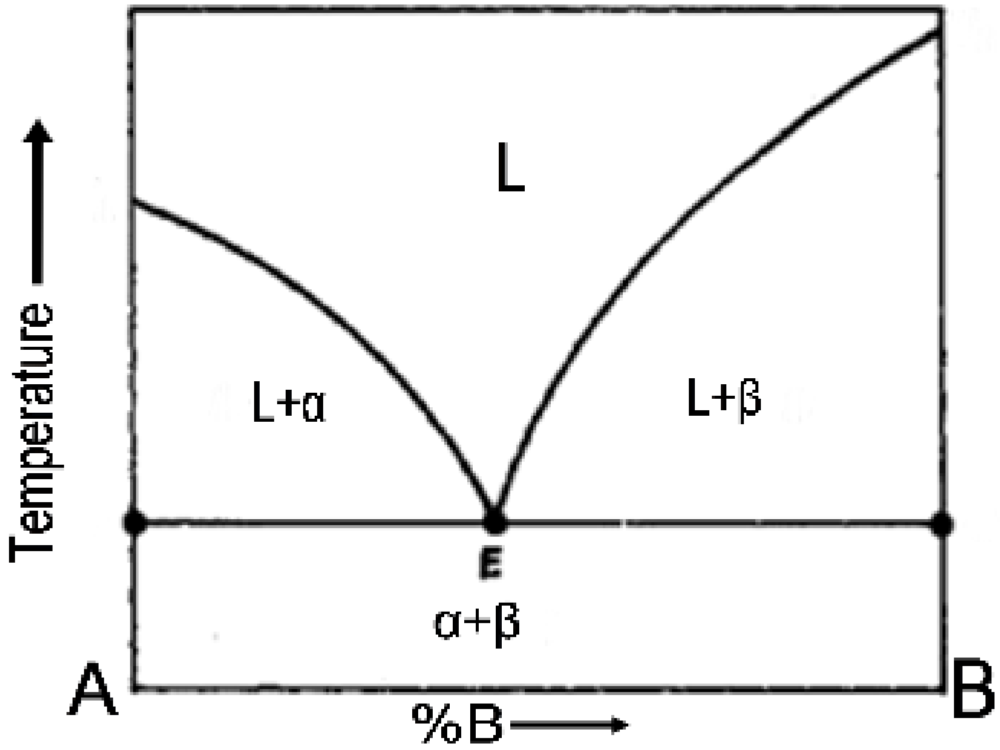

Figure 3.4 Example eutectic point shown on a phase diagram.

With L representing liquid, α and β are assumed to be 2 individual solid phases and E is the eutectic point.

During the solidification of a two element alloy the liquid solidification at the eutectic point shall result in two solid phases. To predict what type of eutectic morphology is expected the following must be considered: are the phase fractions equal and are the phases continuous. The variation in possible eutectic morphologies means that four different types of morphologies can be formed. If the phase fractions are similar and the phases are continuous then a lamellar morphology can be expected. This is shown in **Figure 3.5**.

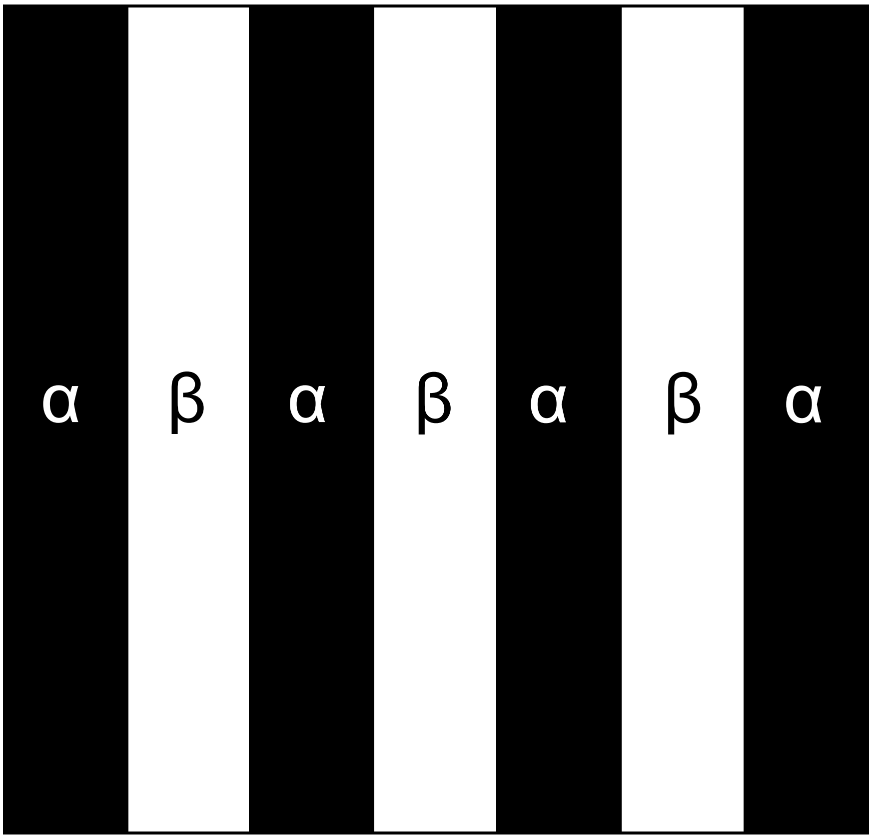

Figure 3.5 Lamellar structure showing solid phases α and β arranged in layers.

The lamellar morphology is found to be the most common but other morphologies are possible. If the two phases are continuous but not of equal phase fractions, then a rod-like morphology is expected. This is illustrated in **Figure 3.6**.

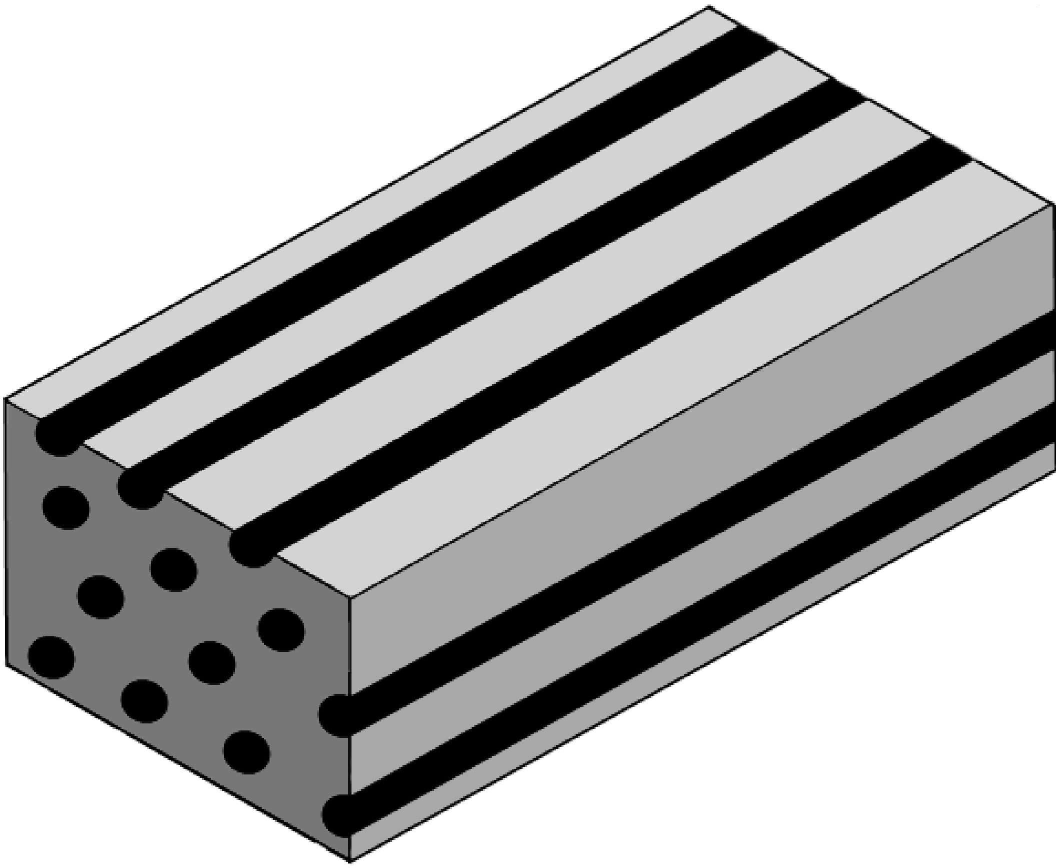

Figure 3.6 Example of a rod-like morphology.

Other eutectic morphologies are formed when one or more phase displays faceting.

The peritectic reaction is defined as:

$$Liquid + Solid\ Solution\ \alpha \rightarrow Solid\ Solution\ \beta$$

The peritectic reaction appears on a phase diagram as seen in **Figure 3.7**.

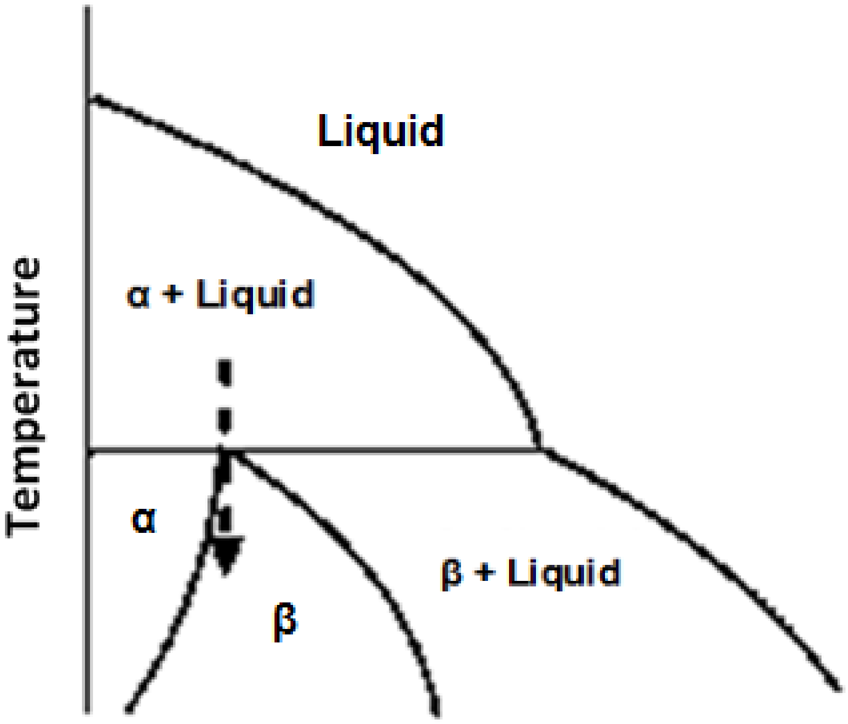

Figure 3.7 Example peritectic point shown on a phase diagram.

Where α and β represent 2 individual solid phases and the peritectic point is the point where the dotted arrow intersects the α + Liquid phase and the β solid phase.

During a peritectic reaction the β phase begins to form a thin shell around the α phase until it is completely encased. There is a triple junction present where all 3 phases, including the liquid phase, and that is where growth occurs. When the α phase is completely encased the growth of the β phase requires diffusion between the 2 phases at the boundary and therefore solid-solid peritectic reactions are relatively slow. This is backed by work carried out by Mullis *et al.* in 2015 [14]. With the Al-Ni the Al_3Ni phase is β and Al_3Ni_2 is α therefore Ni must diffuse from the Al_3Ni_2, through the growing layer of Al_3Ni and into the liquid, with Al diffusing in the opposite direction. As Al_3Ni cannot support a concentration gradient, diffusion is slow. The difficulty in a peritectic transformation of a stoichiometric intermetallic lie with their ability to support a concentration gradient. The small compositional range of a stoichiometric means that less thickening of the peritectic phase is formed due to the small range of solubility. **Figure 3.8** shows type B and type C peritectic classification by St John and Hogan [15] and described by Kerr and Kurz [16]. In type C classification the range of solubility, $C_\beta^\alpha - C_\beta^L$, in the peritectic phase is much smaller than in type B.

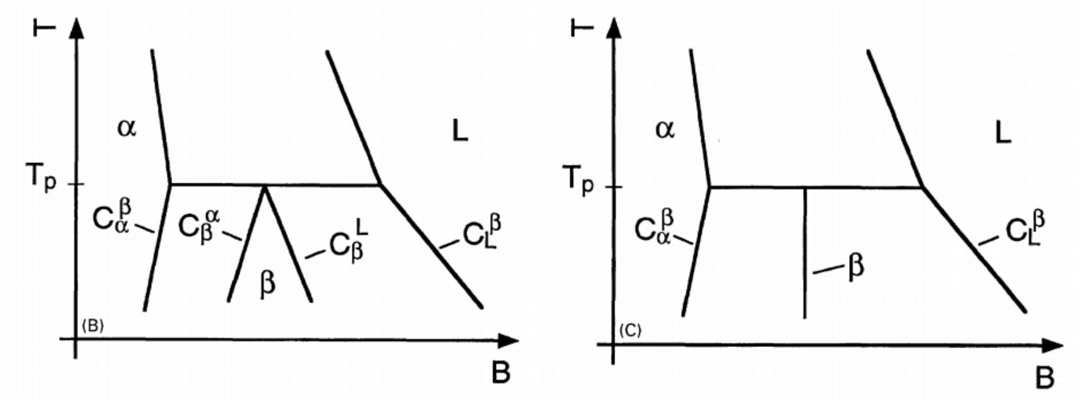

Figure 3.8 Type B (left) and type C (right) classification of peritectic reactions according to compositional range of the peritectic phase [16].

The peritectic reaction results in a core-shell morphology where the resulting phase is formed around the edges of the α phase. **Figure 3.9** shows the core-shell structure that is described.

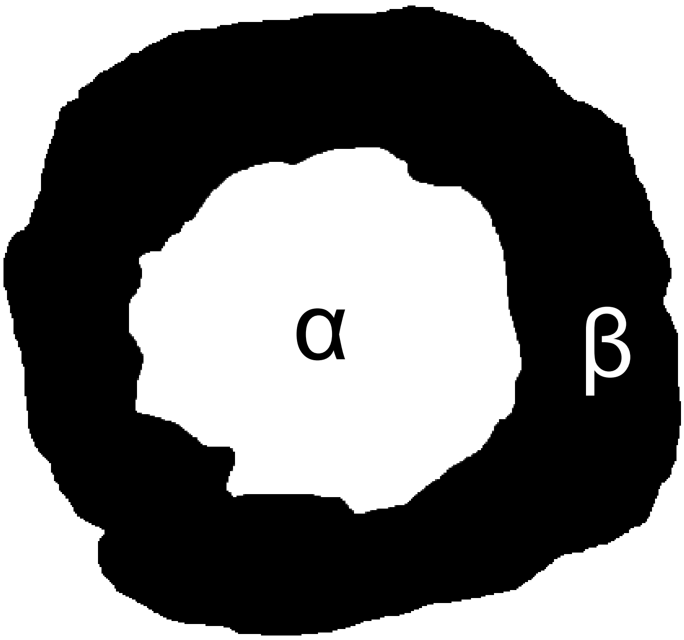

Figure 3.9 Core-shell morphology showing α and the solid phase β, typical of a peritectic reaction.

3.5 Interface Structure

During crystal growth the interface between the solid and liquid will have great impact on the crystal morphology. With most metallic systems the solid/liquid interface is thought to be non-faceted and atomically rough.

During the solidification process the solid/liquid interface requires the addition of atoms. The faceted, or atomically smooth, interface does not contain many sites favourable for atoms to attach during diffusion, and available sites are frequently occupied to create the smooth interface. Faceted growth often occurs at re-entrant corners or with twinning. Atoms are regularly attached to create lateral growth. A faceted interface often requires nucleation and/or undercooling. A non-faceted, or atomically rough, interface will contain many favourable sites available for atoms to be attached. Because this interface is rough it shall create a continuous non-faceted crystal. Unlike the faceted interface the non-faceted interface allows the atoms to be attached from any direction, as the interface itself is not smooth, therefore allowing solidification to occur in any direction [8] [9].

3.6 Dendritic Growth

In metal and alloy solidification quite often, the primary crystal is formed into a tree-like structure called dendrites. The structure is formed when the molten metal solidifies rapidly in favourable directions. The dendrites formed in alloy solidification are as a result of a solute-diffusion-controlled process, and a heat-flow-controlled process in pure metals. During solid growth the interface stability is important in the formation of dendrites, particularly whether a perturbation is favoured or not. Constitutional undercooling and a negative temperature gradient (explained in **Section 3.7**) both destabilise a plane interface and hence lead to dendritic growth. During near-equilibrium stages the morphology of metal crystallization exhibit strong directionality, which affects the materials characteristics due to the atomic structure. Typically metals with a cubic symmetry will result in dendrite that display established side branches alongside a distinct centre trunk. During a higher departure from equilibrium these dendrites may become less distinct or cease to form in the favourable directions [17]. The level of unfavourable growth directions can be attributed to the level of undercooling as a range of growth directions can be found in the microstructure before a seaweed formation has occurred.

3.7 Rapid Solidification

Departure from equilibrium can occur during high speed solidification. If the growth velocity is sufficiently high the it can exceed the atomic diffusivity, the liquidus and solidus lines overlap, and the solid/liquid interface can pass through the melt. This would result in the solid and liquid having the same composition and because of partitionless solidification solute trapping will have occurred. The solute trapping model proposed by Aziz [18] characterises the velocity-dependant partition coefficient:

$$k(V) = \frac{k_E + {}^{V}\!/_{V_D}}{1 + {}^{V}\!/_{V_D}} \tag{3.13}$$

Where V is the growth velocity and V_D is the diffusive velocity of atoms at the solid-liquid interface. Since k is dependant of V there is often a continuous change in the partition coefficient and therefore a continuous change in the level of solute trapping. For partitionless solidification to occur the following conditions need to be satisfied:

- At high cooling rate the solid and liquid composition can converge.
- The T_0 temperature, where the liquid and solid phases have the same molar-free energy, of the corresponding composition must be larger than the interface temperature.

During rapid solidification the time available for diffusion to take place is reduced which would result in the solidification of a non-equilibrium phase structure. A supersaturated solid solution is formed when there is more solute in the phase than if it were to form during equilibrium, this is the principle behind solute trapping. In order for solute trapping to occur the solidification velocity must be sufficiently high in order to overcome the diffusivity and trap the solute solution into a solid phase. It is also necessary for the free energy of the solid and liquid to be equal (k_E=1) in order to avoid the driving force for chemical segregation, this is achieved when the temperature of the melt is below the T_0 temperature. Partial solute trapping can also occur above the T_0 temperature due to the variation of k_E during solidification. If undercooling is achieved to that higher than the hypercooling temperature, then the entire melt would crystallise into a supersaturated solid solution under non-equilibrium conditions as the heat of fusion that is released during recalescence is not adequate to heat the sample up to the T_0 temperature. This can also be achieved at modest cooling rates for specific materials [19].

Rapid solidification can be achieved primarily in two ways: rapid cooling and undercooling. Rapid cooling is conducted when the heat within the material is transferred rapidly, this can occur through contact of a cool surface or medium. It is important to note that for rapid cooling to occur at least one dimension of the material must be small in order for the latent heat to transfer. An example where one dimension is small would be a sheet, two small dimensions result in a wire and all three dimensions being small would result in a particle or droplet. The latent heat is released in the opposite direction to solid growth through the solid and towards a possible cool surface. Since the temperature of the liquid is higher than the solid the solidification is said to have a positive temperature gradient. Rapid solidification by way of undercooling varies due to the absence of a nucleation site, since there is no cool surface or container wall in contact. When the energy barrier is surpassed homogeneous nucleation will take place and solid growth will begin. The temperature in the solid is higher than the liquid and therefore the latent heat is being extracted from the solid out of the liquid, this solidification is characterised as having a negative temperature gradient. **Figures 3.10** and **3.11** illustrate rapid cooling and undercooling, the red colour indicates the highest temperature and pink illustrates the lower temperature, this, and consequently the temperature gradient, is different in the two rapid solidification methods. For both **Figures 3.10** and **3.11** a graph is presented which illustrates the temperature gradient across the cross section of the material. Since latent heat is being extracted out of the growing solid in undercooling, any perturbations that are created out of the growing solid are encouraged to develop, this is not the case in rapid cooling as the latent heat is extracted out of the liquid through the solid.

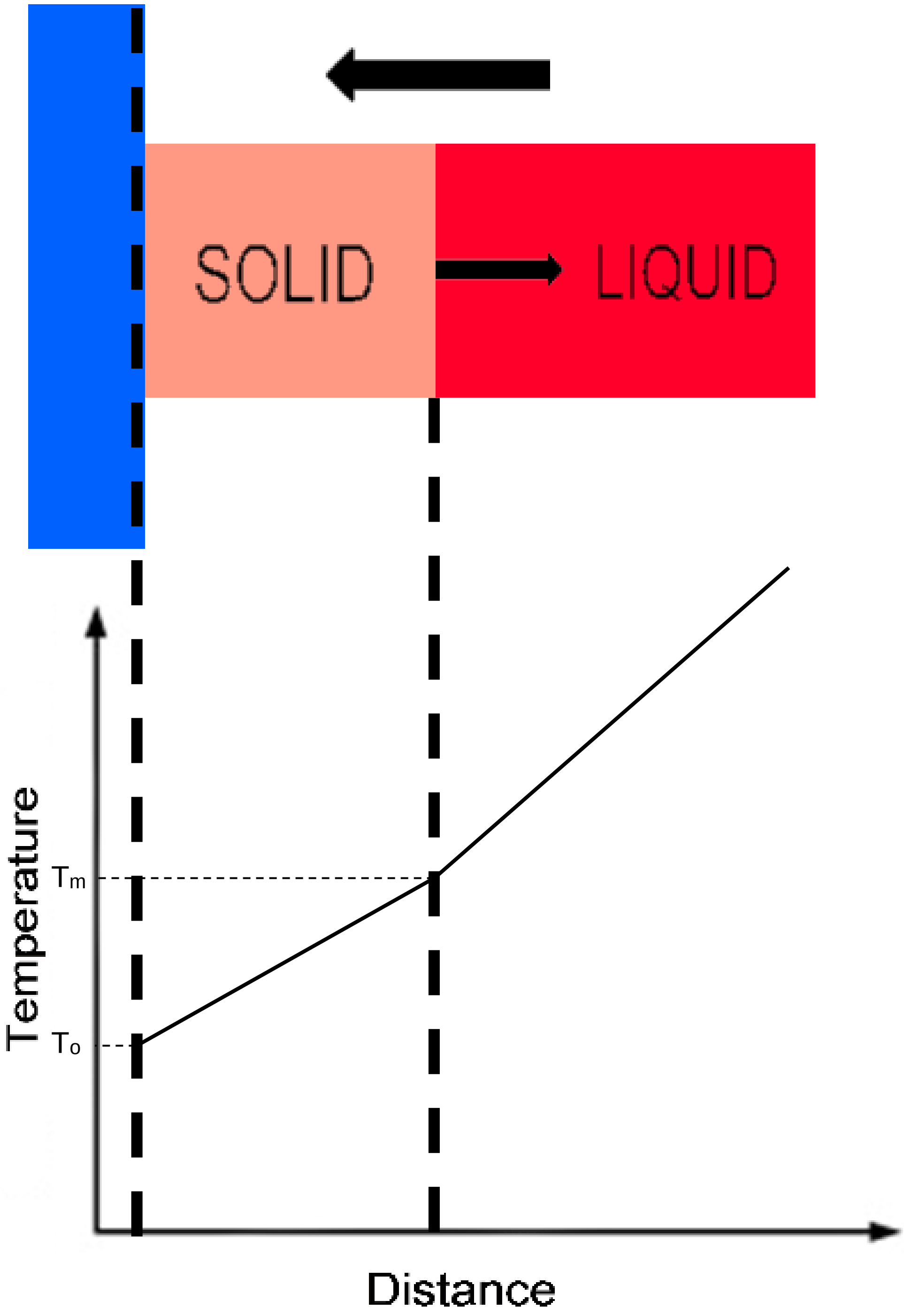

Figure 3.10 Rapid solidification achieved by rapid cooling with the use of a chill plate (blue) to initiate nucleation. The small arrow illustrates the direction of growth and the large arrow illustrates the direction of latent heat being extracted. The dotted lines intersect the graph at the temperature of the chill plate, T_o, and the melting temperature, T_m, (left and right respectively).

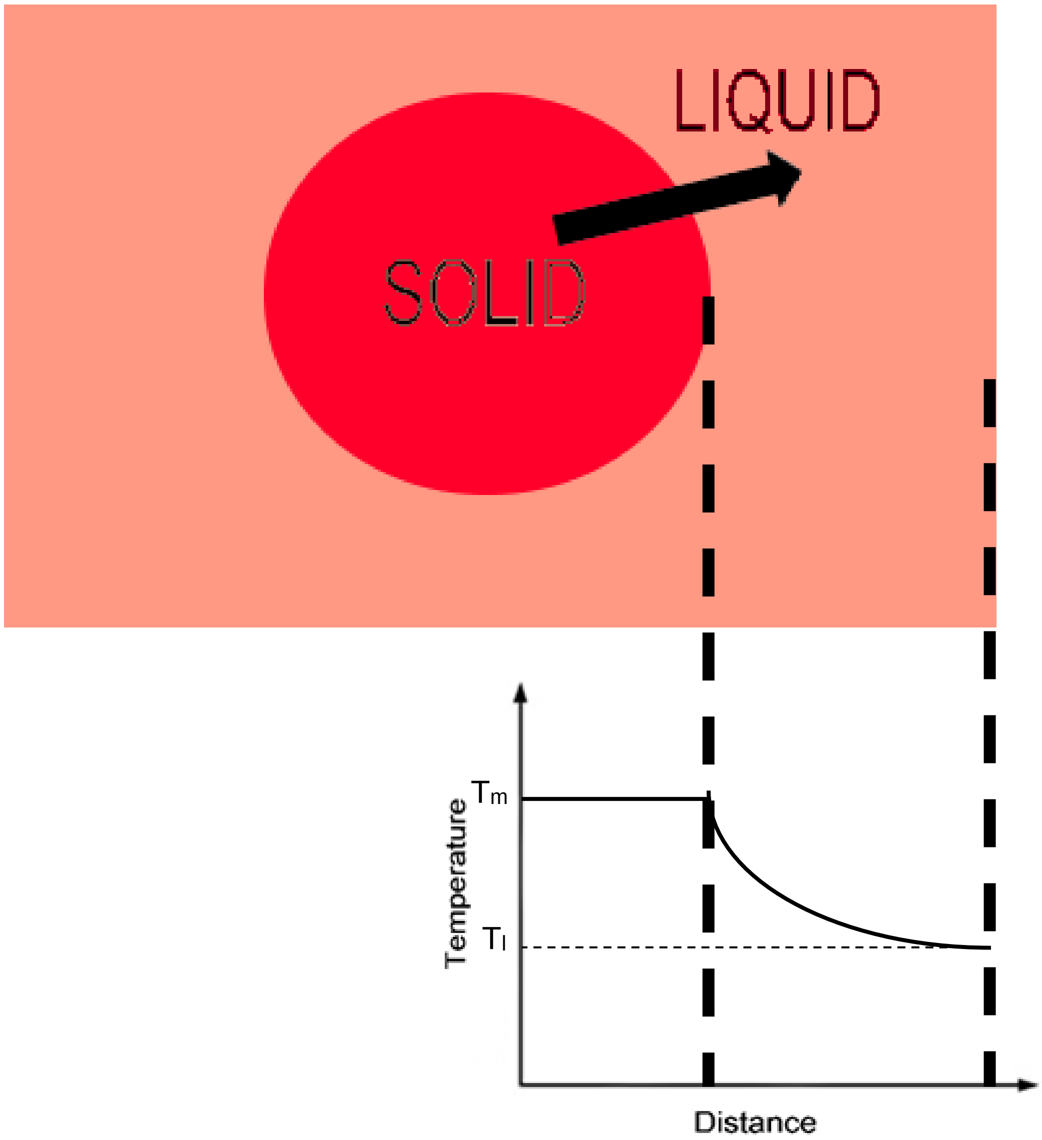

Figure 3.11 Rapid solidification achieved by undercooling. The arrow illustrates both the direction of growth the direction of latent heat being extracted. The dotted lines intersect the graph at the melting temperature, T_m, and the temperature of the liquid, T_l, (left and right respectively).

3.8 Grain Refinement

Grain refinement has been a valued aspect in the solidification of materials. It is advantageous in achieving desirable properties such as strength, toughness and ductility, which would allow superplasticity in some materials. Generally, as the undercooling (or cooling rate) is increased the grain size will decrease for most systems. Spontaneous grain refinement takes place when critical undercooling, ΔT^*, has been exceeded and the grain size abruptly changes [20].

Spontaneous Grain refinement was first observed in 1959 when the grain sizes in Ni melts abruptly changed sizes as ΔT^* was exceeded. The change was a decrease is 1-2 orders of magnitude. One of the proposed mechanisms for the abrupt change in grain size was copious nucleation, or dynamic nucleation, which is caused by the vibration and collapse of voids [21]. Copious homogeneous nucleation can occur when the equilibrium-freezing temperature is affected by the pressure difference due to cavitations, which are induced at the solid-liquid interface due to a volume change during solidification.

In 1966, Jackson *et al.* proposed that grain refinement may occur due to dendrite fragmentation during or post-recalescence due to remelting [22]. This was proposed due to the observation of secondary dendrite arms that detached from primary dendrite arms during remelting and attached at the primary dendrite stem. Fragmentation was also studied by Schwarz *et al.* and Karma *et al.* who concluded that the equiaxed microstructure (as observed by Jackson *et al.*) is due to fragmentation that takes place at post-recalescence [23] [24].

Mullis and Cochrane demonstrated that at low undercooling and high undercooling alloys with a concentration above a critical value are unstable for dendritic growth [25]. In 2001 they proposed a model for spontaneous grain refinement (SGR) by repeated multiple tip splitting of a pure undercooled melt [26].

3.9 Metastable Crystalline Phases

Materials that have been cooled under equilibrium would exhibit the most stable state, but during rapid solidification metastable crystalline phases that differ from stable phases due to crystallographic structure or composition may be favoured. The Fe-Ni system was studied, and it was found that the metastable bcc phase could be crystallized during increased undercooling in the concentration regime where the fcc phase is stable. This was achieved by a technique called ‘phase seeding’, whereby a trigger needle was used, made of Fe-Mo with a bcc structure, to induce nucleation and begin bcc growth [27].

It is possible to detect metastable phases by investigating the phase morphology. Liu *et al.* conducted drop tube experiments on Co-Ge and found that an increase in cooling rate affected the final microstructure as lamellar eutectic was transitioned to an anomalous eutectic. A similar observation was made for the hypereutectic Co-Ge alloy as dendrites were no longer columnar but instead equiaxed [28]. An anomalous eutectic is usually formed as a result of the nucleation and growth of two eutectic phases that are not allowed to form into a lamellar or rod like morphology. Anomalous eutectic regions are often found as a result of rapid solidification during which there is less time for the formation of a lamellar or rod like morphology. An example of an anomalous eutectic microstructure can be seen in **Figure 3.12c**. Anomalous eutectics have been found to demonstrate a greater thermodynamic stability than lamellar eutectics [29].

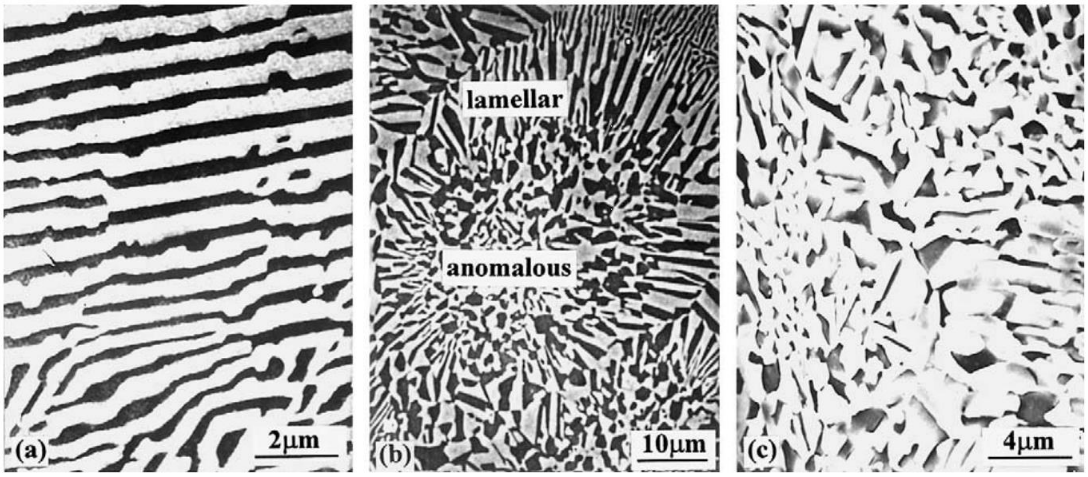

Figure 3.12 An example of (a) lamellar eutectic, (b) mixed lamellar and anomalous eutectic, and (c) anomalous eutectic [28].

3.9.1 Quasicrystalline Alloys

Quasicrystalline phases have been studied due to their non-periodic ordering within the crystal structure. As a result, the local symmetry is somewhat rare for a normal crystal. The two types of quasicrystalline phases are known to be icosahedral, I phase, and decagonal, T phase, though the more common of the two is short range icosahedral in liquid metals. The difference between the two quasicrystalline phases lie in the crystal orientation since the icosahedral phase is quasiperiodic in three dimensions [30] while the decagonal phase in only quasiperiodic in two dimensions with the third dimension being periodic. The formation of quasicrystalline phases is permitted when the required critical cooling rate is achieved, which is lower than the required cooling rate of metallic glass but high enough to avoid crystallization [31]. Most quasicrystalline phases have been discovered to form from peritectic reactions and have been metastable though some quasicrystalline phases have been found to be stable [32]. Systems such as Al-Cu-Fe [33], Al-Pd-Re and Al-Pd-Mn [34] have been studied and stable quasicrystalline phases were found.

The earliest detection of quasicrystalline phases was reported in 1984 on the rapidly quenched Al-Mn system [31]. A long range icosahedral group symmetry was found in in the metallic solid which was stable at 400°C and 350°C for 6 hours and 1 hour respectively. The phase then transformed at 400°C to the stable phase Al_6Mn.

3.9.2 Metallic Glasses

Metallic glass is formed when the cooling rate is high enough to exceed the critical value and therefore avoid the formation of nuclei and crystallization, once the temperature falls below the glass transition temperature, T_g, the material will form into an amorphous solid with a lack of long range crystallographic order [35]. During high temperature the mobility of the atoms is high enough for them to form into structures, but as the temperature decreases the viscosity of the melt becomes seemingly higher and therefore limiting the mobility, this in turn results in the atoms lacking the ability to form into an ordered structure as easily [36]. **Figure 3.13A** shows the solidification of a eutectic phase that solidifies to below the T_o temperature and is allowed to crystallise. The eutectic phase solidification shown in **Figure 3.13B** does not fall below the T_o temperature at the current composition and therefore avoids crystallisation, this results in limited mobility of atoms and therefore metallic glass.

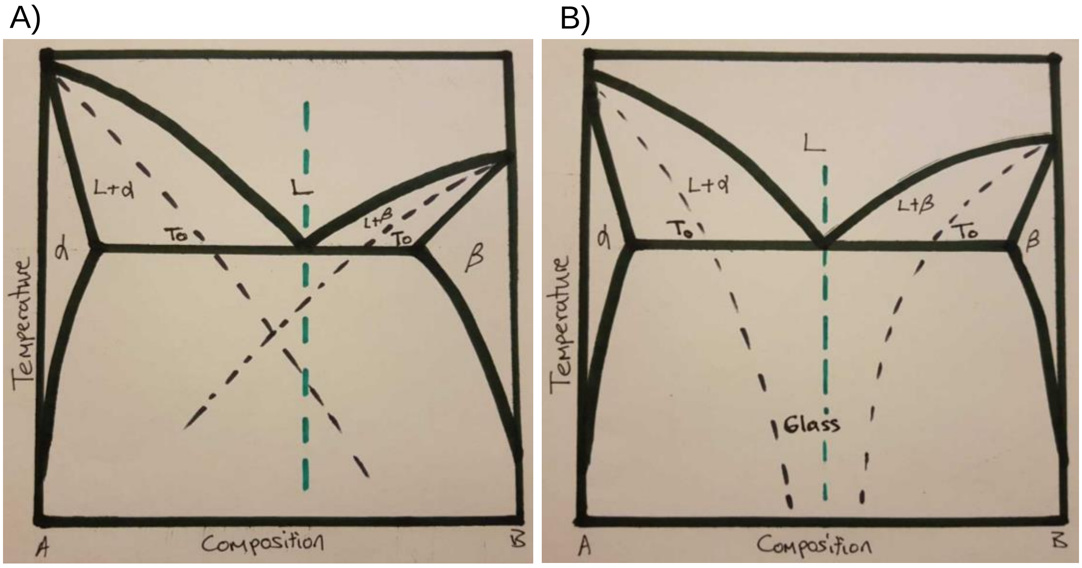

Figure 3.13 Phase diagrams illustrating black dotted T_0 lines for solidification of eutectic reaction A) allowed to crystallise, and B) not allowed to crystallise and therefore form into a metallic glass. The green dashed lines represent the composition of solidification.

The non-crystalline materials show several desirable properties; the lack of crystal structure would mean the absence of grain boundaries which offer greater resistance to corrosion and wear, and amorphous metals are also more suited for some applications than ceramics since they are tougher and more ductile. Due to their nature metallic glasses are also suitable for applications such as sports equipment and biomaterials due to their workability, as they can be softened upon heating [37].

Metallic glass was first formed in 1960 with the Au-Si system at near eutectic composition [38]. The best alloys to produce the amorphous metallic glass were found to be Pd-Cu-Ni-P alloys due to their low critical cooling rate of 0.067 K s^{-1} [39].

3.10 Intermetallic Compound

Solid phases that contain two or more metallic elements are known as intermetallic compounds. They can often include one or more non-metallic element. The solid phases formed into an intermetallic compound possess a different crystal structure to any of the initial elements [40]. A key characteristic of intermetallic compounds is their strong internal ordering along with their bonding which is mixed covalent/ionic and metallic. Intermetallic compounds are an important part of the phase diagram where the composition range is narrow due to the bonding and strong internal order between diverse atoms. Intermetallic compounds often have stoichiometric, or similar, composition. For the Al-Ni system the Al_3Ni_2 phase has a composition range of 35.9 - 40.7 at.% Ni, whereas the Al_3Ni phase is a line compound so it has a precise stoichiometry at 25 at.% Ni. These two intermetallic phases are labelled in **Figure 3.16**.

The properties of intermetallics, apart from increased strength, mean that they have a high melting point but low conductivity and poor ductility. An example of an intermetallic compound that has desirable properties is Ni_3Si which has the high melting temperature and hardness but poor ductility at room temperature means it has poor workability [41] [42]. Non-equilibrium rapid solidification is thought to be a route to achieving refined grains and therefore limit the brittleness of intermetallic compounds [43] [44].

3.11 Containerless Solidification

There are a few containerless solidification methods that can be employed to achieve a high level of undercooling in droplets, these include: drop tube, electromagnetic levitation, acoustic levitation, electrostatic levitation, aerodynamic levitation, melt fluxing, and gas atomization. Using containerless solidification it is possible to avoid heterogeneous nucleation on the potential container walls, in addition to this a clean environment can help to severely reduce the chance for heterogeneous nucleation to take place on free surfaces. The levitation techniques can also be used with a high-speed video camera in order to analyse the nature of the droplet solidification. The melt fluxing and electromagnetic levitation methods are advantageous to record and analyse the growth velocities and crystallization of the material whilst it is being cooled, so it is possible to determine the microstructure at different times during the cooling process. It is possible to develop materials using a drop tube in order to study their microstructures and also being able to determine the formation of each phase.

3.11.1 Drop Tube Techniques

The theory behind drop tubes is very simple; a droplet in liquid form can cool during freefall whilst in the controlled environment of the drop tube. The methods employed by a drop tube date back to the 1600s when shot towers were used to produce lead shot. Drop tubes can be separated into two types; long and short, each one being appropriate to the type of experiment it can perform. A drop tube with length greater than 50 meters, though the length is debatable, is generally classified as a long drop tube in which a body of molten metal is able to free fall, therefore long drop tubes are used to study the effects of microgravity on solidification without the burden of high costs associated with experimentation in space. The two most notable long drop tubes in existence are located at the NASA Marshall Space Flight Centre and at the Nuclear Research Centre in Grenoble, which measure 105 meters and 47 meters respectively. A schematic diagram of the 105m drop tube facility at NASA Marshall Space Flight Centre can be seen in **Figure 3.14**. Two drop tubes exist in Pasadena, CA, at the Jet Propulsion Laboratory in which air is accelerated downwards at the same rate as the free-falling droplet and therefore drastically reducing drag forces but using this technique would limit the level of undercooling that can be achieved due to surface heterogeneous nucleation. Accelerated drop tube, like the one in Pasadena, are useful in achieving higher-than-usual cooling rates typically found in drop tubes, this is due to the absence of conduction/convection which is the main cause for heat loss in the droplet. The experiments in drop tubes in such facilities tend to begin with evacuation of the tube which is then followed by the melting of a single droplet, usually a large droplet of between 1 and 5 millimetres in diameter, using an electron beam and/or electromagnetic levitation. When the droplet is released it is free to fall through the tube and is monitored along the length of the tube using photo-diodes to allow the detection of recalescence. Heterogeneous nucleation is eliminated at low undercooling temperatures by using a vacuum, though the low undercooling that the long drop tubes are limited to can be reproduced with great accuracy.

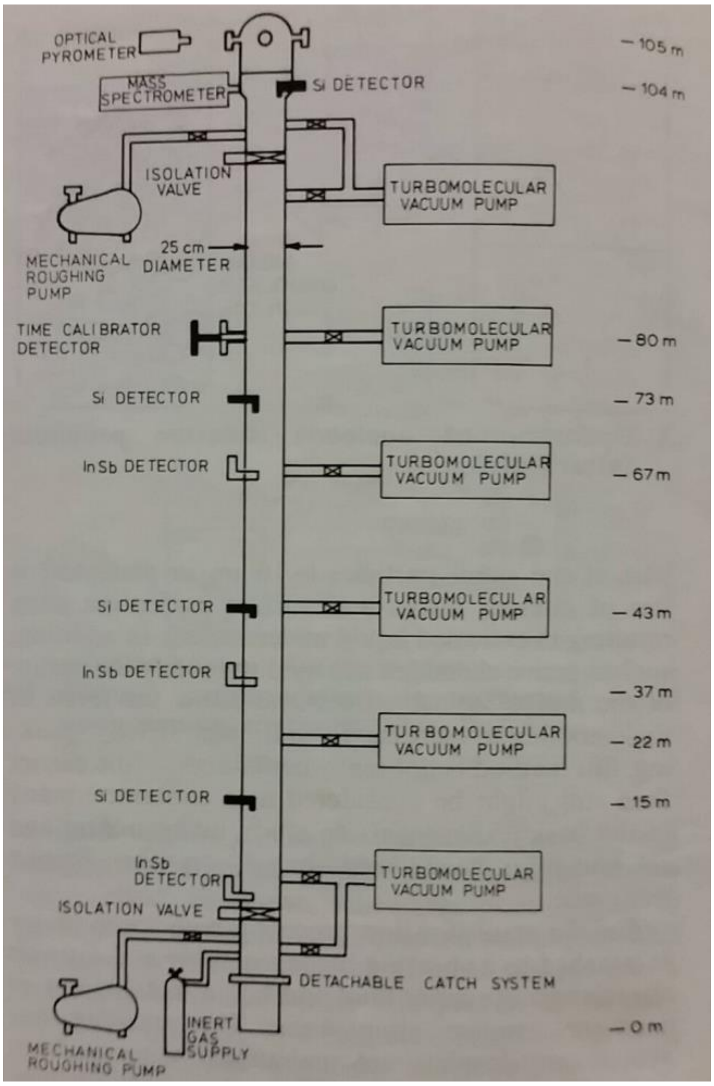

Figure 3.14 105m drop tube facility at NASA Marshall Space Flight Centre [45].

Short drop tubes are used to study the effects of containerless processing and high cooling rate on solidification. Shorter drop tubes generally employ a different technique to produce the droplet(s); they tend to spray several droplets [45]. The melt is forced through a small nozzle to disperse many small droplets. The inert gas used in small drop tubes in addition to the smaller droplet sizes will allow a higher rate of undercooling, but this will remove the ability to detect recalescence and the temperature of nucleation. Using an inert gas, it is also worth noting that the element of free-fall is lost as the gas would contribute to aerodynamic breaking of the droplets. Small drop tubes have previously been used to study the grain refinement and crystalline phases achieved by undercooling. It is common for the interchanging use of the terms 'drop tube' and 'drop tower' but they are both in fact different; where in a drop tube the droplet is allowed to drop freely without being contained in a controlled atmosphere, such as a vacuum, in order to observe the solidification. In a drop tower there is an experiment package that is dropped, this includes the furnace, instrumentation and the droplet. Since the package is enclosed within a canister there is little need for a protective atmosphere in the drop tower, but a vacuum, amongst other techniques, can be employed to reduce drag forces [45].

3.11.2 Gas Atomization Techniques

Gas atomization is the most used technique in industrial mass production, though other techniques are also used such as thermal spraying [46]. The purpose of gas atomization is to efficiently create fine particles that make up a metal powder. During the process a jet of gas is used to disintegrate molten metal into fine particles which are subsequently cooled during flight. The gas atomization process allows for particles that are advantageous because they flow well, which is important in applications such as 3-D printing or for catalysts in fluidized bed reactors. Undercooling can also be achieved using gas atomization due to the absence of impurities and the use of an inert gas in order to limit heterogeneous nucleation thus allowing metal powders with diverse microstructures. It is possible to use gas atomization techniques to produce metal particles of different sizes, and a more efficient jet stream disruption to the molten metal would prove to be superior in creating smaller particle sizes.

The gas atomization process is carried out when molten metal is uniformly fed through a nozzle into an atomization chamber at a controlled rate with the assistance of a tundish. Once the molten metal is deposited into the chamber it is then introduced to a stream of gas which interrupts the normal flow of the molten metal to disintegrate the molten metal into spherical particles which are then cooled during flight. The inert stream of gas is typically Nitrogen or Argon [14] and is often introduced into the atomization chamber using a set of Convergent-divergent jets arranged around the nozzle and positioned at a 45^{O} apex angle to allow for an efficient and effective gas stream. This is also known as de Laval, it allows controlled expansion, so the gas achieves supersonic velocity. It is very difficult to understand the relationship between the molten metal and the stream of gas at the point of contact due to the flow of gas being turbulent. The melt is then blown away from the tip of the nozzle using the stream of gas and can be broken and cooled in many small particle sizes during flight. A schematic diagram of the gas atomization arrangement is illustrated in **Figure 3.15**. There are 2 types of gas atomization techniques: free fall and close coupled.

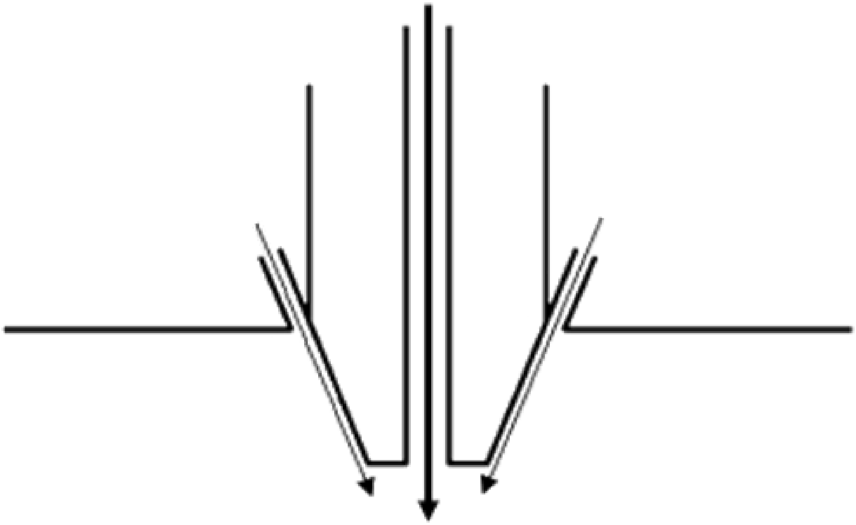

Figure 3.15 Atomizer nozzle configuration. The large centre arrow represents the inside of the nozzle where the melt is fed through. The smaller arrows represent the flow of inert gas as it is directed towards the melt.

The free fall and close coupled techniques of gas atomization differ when it comes to the melt delivery through the nozzle and into the atomization chamber. The free fall technique allows the molten metal to fall a short distance into the atomization chamber before the stream of gas interrupts the flow to form metal particles. The close couple technique does not allow the molten metal to fall into the chamber but instead due to the positioning of the jets allows for an area of low pressure with gas continuing to circle drawing the melt out of the nozzle. Due to the directional velocity of the gas the melt is forced over the face of the nozzle towards the jets, this is known as pre-filming. Once the melt reaches the edge of the jets it is blown away into particles. The former technique allows a greater control over the impact of the gas with the molten metal whereas the close coupled technique has advantages in the variable size of particles that it is possible to achieve, and finer particles are possible with close coupled gas atomization. In the free-fall technique the energy in the gas jet that is lost before it initiates contact with the molten metal means that there is little control over the resulting particle size. The melt break-up mode observed in free-fall technique is column break-up, where a column of melt is blown away by the jets, with the close coupled technique the break-up mode is sheet break-up as pre-filming allows the melt to be delivered to the jets in the form of a thin sheet, this allows for smaller particles to be formed.

Close coupled gas atomization can take place with the atomizer facing in any direction due to aspiration, where the flow of gas jets produces a region of low pressure on the melt nozzle tip to draw the molten metal. When the gas atomizer nozzle is facing upwards it allows the particles to achieve flight for longer, unless a large facility is used during a downwards atomization process. Gas atomization creates many particles of different sizes which can then be sieved into respective size fractions.

The different sized particles can affect the cooling rate of the particle itself as the larger particles require longer to release all latent heat thus allowing the variation in microstructures. The high cooling rates of gas atomization techniques allow for fine microstructures, where particular reactions may not complete during solidification. It is important to note that the larger particles remain in a part-liquid state for longer which allows the solid and liquid phases to mix due to the shear force from the gas jets acting upon the particle therefore creating microstructures which wouldn't ordinarily have formed. In contrast the smaller particles are likely to be carried away from the jet stream and are not subject to the large shear force experienced by the larger particles. In a study conducted by Bao *et al.* it was found that the cooling rates experienced in gas atomization of AlNi were high enough to limit the formation of $NiAl_3$ at the 854 ^{o}C peritectic reaction [47]. Further details on the cooling rates experienced in gas atomization and drop tube techniques is discussed in **Section 4.4**.

During the gas atomization process, it is important to maintain certain parameters which can directly affect the size of the resulting particles, which can usually range between 10 and 300μm. Typical gas flow rate for gas atomization is between 1 and 50m^3/min at pressures ranging between 350kPa and 4MPa. Due to the de Laval gas jets the gas velocity is usually more than Mach 1. Superheat of molten metal is usually between 75-150 ^{O}C, and a melt flow rate of anywhere between 1-90kg/min is normal [48].

3.12 Al-Ni

Raney Nickel was pioneered by Murray Raney who patented the catalyst in the mid-1920s which would be used for hydrogenation of cottonseed oil [49]. The Raney nickel catalyst can be used for a range of applications including; pharmaceuticals, plastics, petroleum and even food [50]. The traditional Raney Ni alloy, discovered by Murray Raney, comprises of 68.5 at.% Al but this composition is the equivalent of 50 wt.% Al and 50 wt.% Ni due to Ni having a higher atomic mass than Al. The catalyst is often produced by casting which results in ingots of the material ready to be crushed before leaching.

3.12.1 Al-Ni Solidification Sequence

Despite the initial composition, the following phases are known to exist in the precursor alloy: Al_3Ni_2 (Space group: *P*$\overline{3}$*m1* [51]), Al_3Ni (Space Group: *Pnma* [51]) and an Al-Al_3Ni eutectic [52]. Upon examining the phase diagram (**Figure 3.16**), considering the 68.5 at.% Al alloy, the first phase is expected to appear is AlNi at 1623 K. The first reaction to take place is in the form of a peritectic reaction at 1406 K; the remaining liquid reacts with the AlNi phase in the following reaction:

$$L + AlNi \leftrightarrow Al_3Ni_2$$

This reaction will result in the formation of Al_3Ni_2. It has been determined that regardless of the cooling rate, whether that be for slow cooling to produce ingots or during gas atomization, the final microstructure for this composition rarely contains AlNi. The absence of AlNi in the final microstructure has raised questions as to whether the Al_3Ni_2 phase is formed directly from the melt as the primary solidification phase, and the AlNi phase is bypassed, or whether the initial peritectic reaction at 1406 K is adequately rapid enough to go to completion [52]. Shuleshova *et al.* conducted *in-situ* time-resolved XRD experiments at the ESRF synchrotron radiation facility where levitated droplets of AlNi were solidified, resulting in the diffraction pattern of AlNi to be detected during the initial stages of solidification. The experiments conclude that, for Ni-68.5 at. % Al, the peritectic reaction at 1406 K is the reason for formation of Al_3Ni_2 and it is not formed directly from the melt [53] [54].

The second peritectic reaction occurs at 1127 K where the remaining liquid reacts with Al_3Ni_2 to form Al_3Ni:

$$L + Al_3Ni_2 \leftrightarrow Al_3Ni$$

As a result of this peritectic reaction the morphology of the final microstructure often reveals the remaining unreacted primary phase (Al_3Ni_2) to be surrounded by the secondary phase (Al_3Ni) in the form of a shell. The reason for the presence of the remaining unreacted Al_3Ni_2 lies with the fact that the second peritectic reaction at 1127 K is slow in contrast to the first peritectic reaction at 1406 K. The first peritectic reaction at 1406 K goes to completion due to the similarities in the structures of AlNi and Al_3Ni_2 as Al_3Ni_2 is a trigonal extension of the cubic B2 AlNi phase in which every third plane of Ni atoms perpendicular to the trigonal axis is missing [55]. In the second peritectic the rate of solid-state diffusion through the growing shell of Al_3Ni will be sluggish since it is a stoichiometric intermetallic, as it is difficult for the line compound to support a concentration gradient to drive diffusion. In the classification described by Kerr & Kurz [16] this peritectic, $Al_3Ni_2 \rightarrow Al_3Ni$, would be placed in Type C classification. This classification is characterised by slow transformation rates during the solid-solid peritectic transformation (SSPT) stage of the reaction.

The final stage of solidification is as a result of a eutectic reaction which takes place at 913 K, this results in the residual liquid solidifying to form an Al-Al_3Ni eutectic [50]:

$$L \leftrightarrow Al_3Ni + Al$$

It can be determined that during cooling of Al-Ni with 50-50 wt % 3 phases should be present, these 3 phases can be visible in a backscatter image (As shown in **Figure 3.17**) using a Scanning Electron Microscope (SEM) as different colours, with phases containing more Nickel appearing lighter, such as Al_3Ni_2 as it is more Nickel rich, and those with more Aluminium appearing darker. This is due to the contrasting atomic number of the two elements. Seaweed formation can also occur as an undercooling of around 250 K in AlNi has been found to display a seaweed formation. This is thought to have been caused by disorder trapping [56].

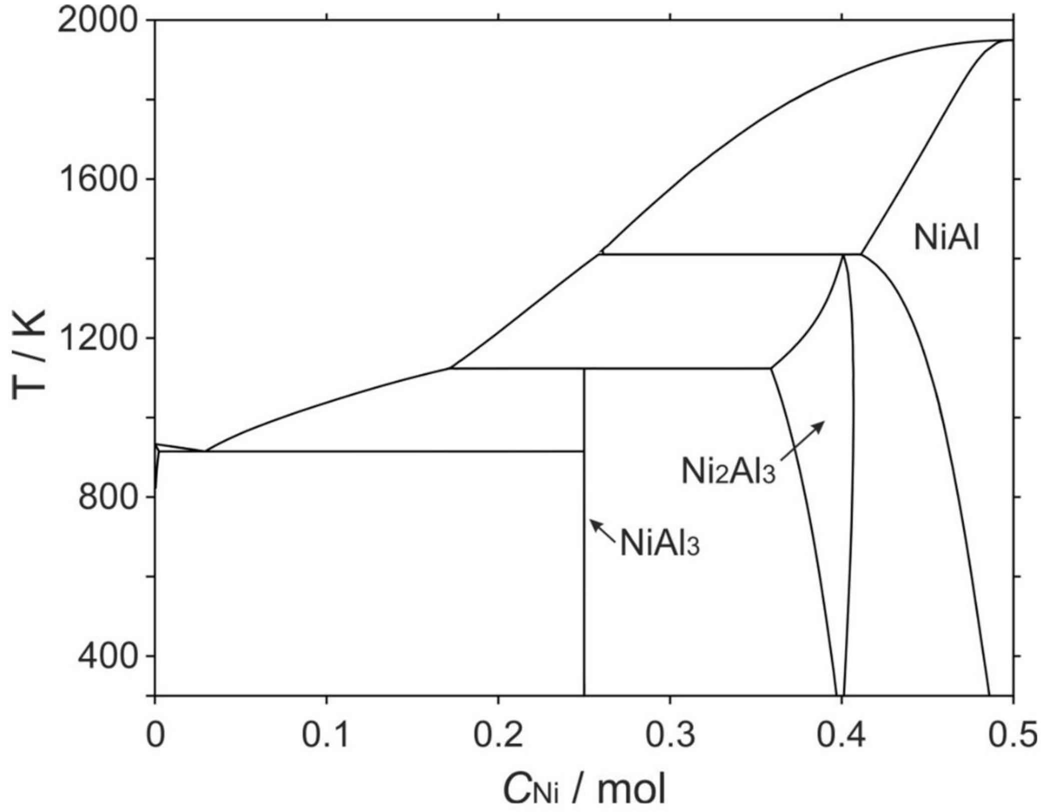

Figure 3.16 Al-Ni phase diagram.

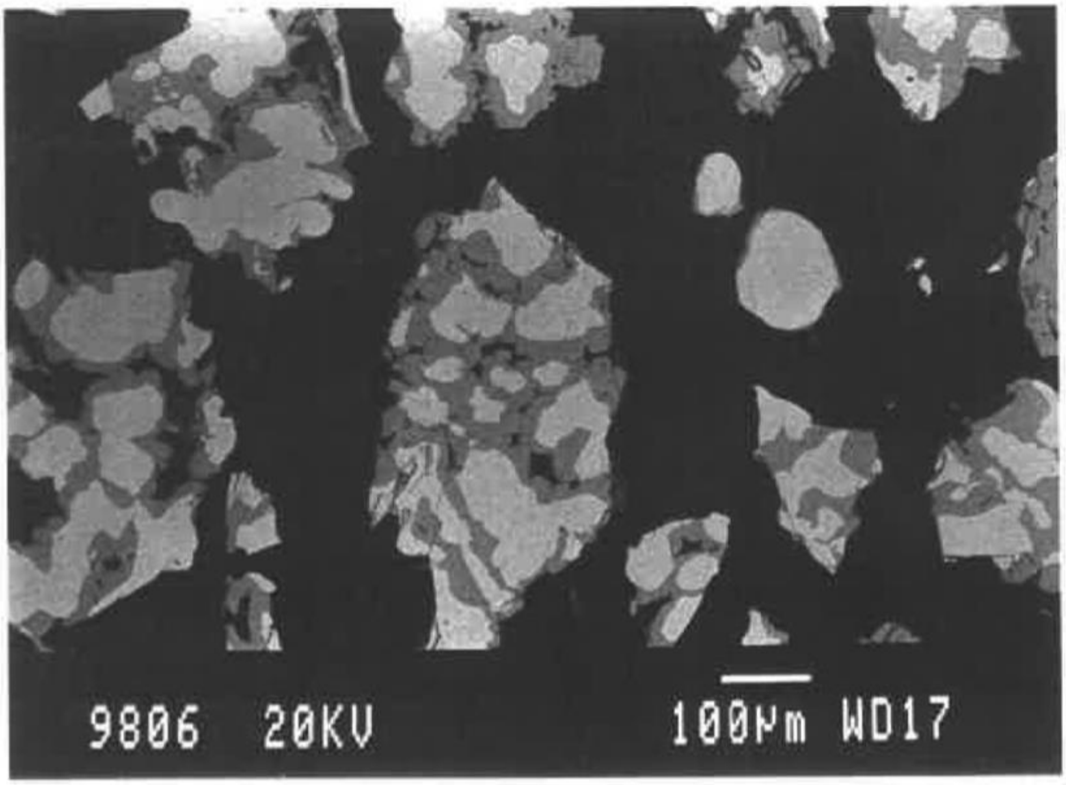

Figure 3.17 Backscatter image of Al-Ni precursor alloy at 50-50 wt% (Sample from Metal Catalyst Technology) [57].

3.12.2 Leaching

During the preparation of the catalyst, the Al is removed from the intermetallic phases and indeed the eutectic due to leaching in a concentrated sodium hydroxide solution. This process leaves nano-crystalline Ni and creates a suitable atmosphere to allow the activation of the Nickel catalyst. After leaching the dissolved aluminate and the excess alkali is removed by aqueous washing [58] and the highly pyrophoric remaining catalyst may then be stored in alcohol or water [50].

The leaching reaction is:

$$2(NiAl)_{(s)} + 2NaOH_{(aq)} + 2H_sO_{(i)} \rightarrow 2Ni_{(s)} + 2NaAlO_{2\,(aq)} + 3H_{2\,(g)}$$

In the case where the aluminate tends to hydrolyse the excess of alkali is important in limiting the decrease in pH. If the aluminate is allowed to hydrolyse then it would precipitate in the form of Bayerite which lowers the catalytic activity as the nano-crystalline pores of the catalyst may be blocked [58].

The properties of the catalysts after leaching have been found to differ in catalysts prepared with sodium hydroxide at temperatures above 100^{O}C and those prepared with sodium hydroxide at temperatures below 50^{O}C, therefore it is important to consider the temperature during leaching. For leaching at temperatures below 50^{O}C it has been found that 40 wt% sodium hydroxide solution is ideal in order to decompose the Al_3Ni_2 [50].

3.12.3 Phase Composition

The amount of each phase present in the final microstructure is heavily dependent on the preparation of the precursor alloy, this is important despite the initial composition. Phase composition can be particularly affected by the cooling rate during preparation; as higher cooling rates would allow less time for the $Al_3Ni_2 \rightarrow Al_3Ni$ peritectic to go to completion, consequently retaining greater amounts of Al_3Ni_2 and less Al_3Ni. The importance of cooling rate and the retention of certain phases is understood when they influence the properties of the activated catalyst. The least resistant phase to leach has been found to be Al_3Ni which results in a highly active catalyst but also with poor mechanical strength [52]. Consequently, catalysts based on precursor alloys with high Al_3Ni concentrations are not suitable for applications such as slurry and tubular bed reactors [14]. Al_3Ni_2 has been found to be more resistant to leaching that Al_3Ni but upon successful leaching is maintains a greater structural integrity, this is due to incomplete leaching. More Al_3Ni_2 is found in the microstructure of the cast-crush processed commercial catalyst than Al_3Ni; at regular cooling rate the slowly cooled ingots are expected to retain around 58 wt.% of Al_3Ni_2 [59], as Al_3Ni is expected to make up the majority of the remaining 42 wt.% and <1 wt.% Al eutectic is often found [59].

The advantages of rapid solidification of Raney type catalysts lie not only with the high cooling rates that modify phase distribution, but also due to it being a route to the utilisation of more Al-rich compositions [59] [60]. 38-212 μm sized Raney powders were studied as part of the IMPRESS project where they were experienced cooling rates of 200 – 5000 K s^{-1} by gas atomisation [61]. The catalytic performance was matched against the cast-crush produced 50-50 wt% alloy which exhibited an activity of 3.5 mol kg^{-1} min^{-1} for hydrogenation of nitrobenzene, while the 106-150 μm size fraction powder produced by gas atomization showed an activity of only 1.4 mol kg^{-1} min^{-1}. Catalytic performance was found to increase to 4.8 mol kg^{-1} min^{-1} when 75 at.% Al alloy, of the same size fraction produced by gas atomization, was investigated [62].

Theoretical studies have also proven to find similar results. Tourret *et al.* performed simulations using the public binary database PBIN within the ThermoCalc software[1] [63]. A previous solidification model was used to determine the thermo-physical properties, where electromagnetically levitated Al-25 at.% Ni droplets were solidified [64]. Solidification times of the three modelled particle sizes; 10 μm, 60 μm and 120 μm diameter, were between 1.3×10^{-3} s (10 μm) to 0.2 s (120 μm). When studying the Ni-80 at.% Al alloy, Tourret *et al.* found that a decrease in particle size resulted in an increase in Al_3Ni_2 phase fraction and consequently a decrease in Al_3Ni. Only the larger particles experienced this change in phase fraction when the initial alloy is melted with more Al content.

The initial elemental composition of the alloy was studied by Devred *et al.* who found that as the Al content is increased, above Ni-65 at.% Al, the amount of the Al eutectic and Al_3Ni phase increases, consequently the amount of Al_3Ni_2 decreases until there is no Al_3Ni_2 left in the final microstructure for alloys with higher than 82.6 at.% Al in the starting alloy, this is in agreement with the phase diagram [65]. The results for the Devred

---

[1] http://www.thermocalc.se.

et al. study can be seen in **Figure 3.18**. Hu *et al.* also found similar findings where Ni_2Al_3 was found to nucleate early during cooling, but it was competing with the $NiAl_3$ phase which was found to be appearing earlier. $NiAl_3$ is the favoured phase to form from the remaining liquid as Ni_2Al_3 is being formed due to the composition of the remaining liquid being more suitable for $NiAl_3$ formation [66].

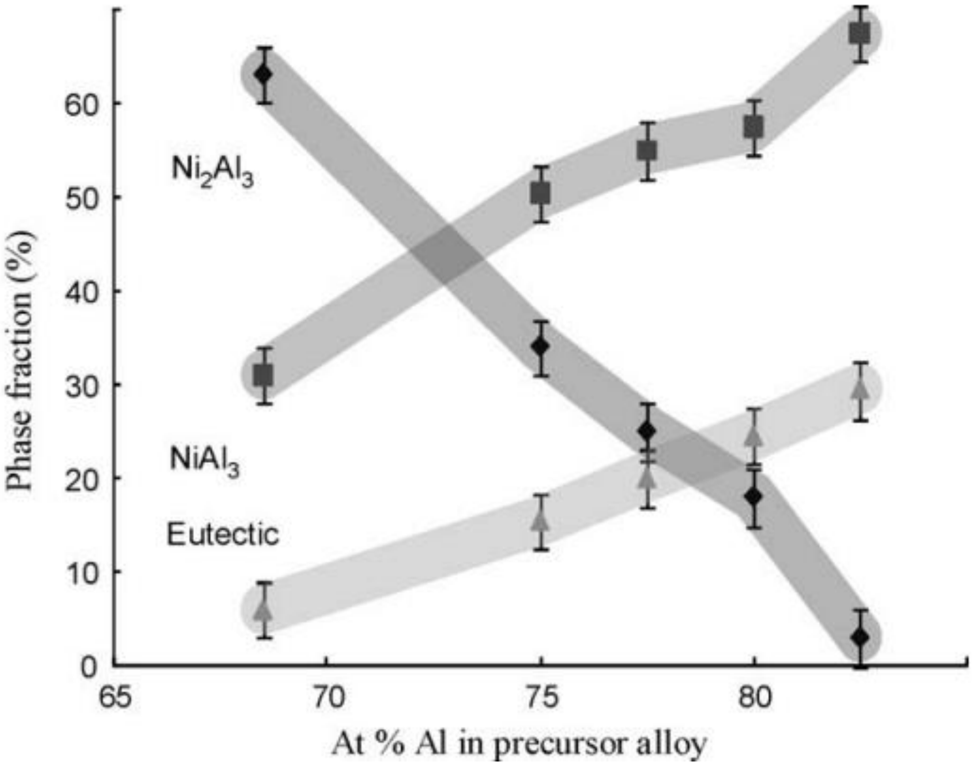

Figure 3.18 Quantitative analysis: phase fraction as a function of aluminium content in the atomized precursor alloy [65].

3.12.4 Dopants

Dopants, or promoters, are often advantageous in improving the activity of the Raney Nickel catalyst. A dopant is a third metal added to the initial alloy usually between 1-3 at.%. Even though the most common dopants are known to be Cr, Mo and Fe, there has been research conducted on Cu, Co, La and Ti as dopants to Raney Ni [50]. A study has found that all the dopants positively affect the catalytic activity of Raney Ni but the most effective was found to be Molybdenum for the hydrogenation of butyronitrile and acetone [67].

The viability of Cr as a dopant for Raney Ni has been the subject of previous research. It was found that 1.5 wt.% of Cr was the optimum level of Cr dopant in the initial alloy for the hydrogenation of butyronitrile, acetone and sodium p-nitrophenolate [50]. A study was also conducted by mechanically mixing Al-Ni and Cr-Al alloys and observing the catalytic activity; Bonnier *et al.* found that for the hydrogenation of acetophenone an increase in activity was found due to the strong segregation of Cr at the surface in an oxidised state. It was also found that more of the residual aluminium was retained in a metallic state due to the presence of Chromium oxide than in the undoped Raney Ni alloy [68]. Metallic aluminium seems to inhibit reactions such as the hydrogenation of carbonyl groups [69] which are promoted by the chromium oxide [50]. Further study on Cr as a dopant was carried out by Pisarek *et al.* who found that for the for the hydrogenation of isophorone to dihydroisophorone the Cr promoted catalytic activity but for the reaction of dihydroisophorone hydrogenation it did not [70]. Due to the chemical similarity of Ni and Cr it was assumed in previous research that Ni is randomly substituted by Cr [68].

It was found that 1.2% of Molybdenum gave the Raney Nickel alloy enhanced catalytic activity for the hydrogenation of a range of functional groups, including alkenes. When adding Mo to undoped AlNi it was found that 2% of Mo was the optimum amount in order to increase the catalytic activity of Raney Nickel, this was further investigated and showed that Raney Nickel alloys with less than 2% of Mo had more Nickel atoms at the surface than undoped AlNi. This was the case as Mo was increased until it reached a maximum at 2% Mo and then amounts of Nickel atoms on the surface declined. As Mo is increased to 2% the Al atoms at the surface increase but after Mo is increased beyond 2% the Al atoms remain constant, the decrease in Ni atoms after 2% of Mo at the surface is due to the Mo atoms at the surface in a metallic state [50].

Raney Nickel doped with Iron was previously studied by Zeifert *et al.* during which the doped alloy was subject to leaching and then a passivation step, this is due to the AlNi having pyrophoric properties. It was found that the concentration of Fe as well as the reduction temperature, during reductive treatment, influenced the composition of the catalyst as well as its activity. Zeifert *et al.* found that low levels of Fe in the Raney Nickel alloy meant that the reduction temperature did not have much effect on the hydrogenation activity, due to the formation of compounds such as $FeNi_3$ and $NiFe_2O_4$ with some Ni remaining allowing catalytic activity [71]. Catalytic activity is favoured at 10 at.% Fe at low temperatures (448 K) during which Ni and $NiFe_3O_4$ is formed allowing increased activity. When the reduction temperature is increased to 773 K the Ni is completely transformed into $FeNi_3$, meaning that there is no longer any Ni available to allow catalytic activity [50].

The catalytic activity of Titanium doped Raney Nickel has not been researched as much as the other dopants, but it has been recognized that Ti doped Raney Ni increases catalytic activity [72]. It was also reported by Mund *et al.* that the addition of Ti replaced Ni atoms in the Ni_2Al_3 and the $NiAl_3$ phases though an extra $TiAl_3$ phase was observed, this was contradicted by work by Mullis *et al.* in which the tetragonal $TiAl_3$ phase was found but no Ti was found to be dissolved in the Ni_2Al_3 and $NiAl_3$ phases [73].

It is very difficult to determine which promoter is the most efficient but that is dependent on the hydrogenation reaction. In a study conducted by Kiros *et al.* in 2003 found that the electrolytic activity of doped AlNi alloys increased with different dopants in the following order: Fe,Cu,Ti,La,Cr, with Cr having the highest electrolytic activity. The increase of Cr using electrodes found an increase of activity due to the surface enrichment of Cr particles. The hexagonal chromia were exposed to the active surface. A similar phenomenon was observed for Ti electrodes [74]. Chromium has received attention due to its efficiency and also the selectivity of some reactions. Of all the promoters studied by Bonnier *et al.* it was determined that the promoter that consistently increased the catalytic activity whilst only requiring the lowest wt.% was Cr at 1.5 wt.% with Mo, Cu and Fe all requiring 2.2 wt.%, 4 wt.% and 6.5 wt.% respectively. Chromium can be compared to Molybdenum as a promoter by observing the acetophenone hydrogenation, the difference between the 2 promoters is due to the fact that Cr segregates at the surface in an oxidized state, whereas Mo does not, its particles remain in a metallic state at the surface [50]. Hamar-Thibault and Masson found that using Al-40 at.% Ni and small amounts of Cr (up to 2.2 at.% Cr) some of the Al content is dissolved in the Ni, and a secondary phase is created; $Al_8(CrNi)_5$ or $Al_9(CrNi)_4$ depending on the amount of Cr (1.5 and 2.2 at.% respectively) [75], the study then investigated the effects of NiCr catalysts from leaching.

Research has been carried out to determine the efficiency of promoting elements using a variety of hydrogenation reaction. Work carried out in 2015 on Ti doped Raney Nickel powers proved to be of great interest as XRD analysis showed that an extra phase was present in the rapidly solidified undercooled alloy; this was $TiAl_3$. In the work carried out SEM micrographs, using backscatter detection, were obtained of both AlNi and AlNiTi (with 1.5 at.% Ti), the micrographs were then subject to EDX detection in order to determine the localisation of Ti and it was found that the $TiAl_3$ phase was segregated in a needle-like formation, and since no Ti was found anywhere else in the microstructure it is possible to conclude that Ti did not substitute for Ni, if it did it was very little. It is also worth noting that there was insufficient amount of Ti in the material to account for the volume of Al_3Ti observed, so some Ni must have been incorporated into the $TiAl_3$ structure. Due to the different crystallography of $NiAl_3$ and $TiAl_3$ it is safe to say that Ti substituting for Ni in $NiAl_3$ is not the same as Ni substituting for Ti in $TiAl_3$ [73].

The previously mentioned IMPRESS project also investigated the effect of dopants on the catalytic activity of Raney Ni. For the 75 at.% Al alloy, at 106-150 μm size fraction (gas atomized), it was found that an addition of 1.5 at.% Cr increased the catalytic activity for the hydrogenation of nitrobenzene from 4.8 mol kg^{-1} min^{-1} to 11.6 mol kg^{-1} min^{-1}. The greatest increase of catalytic activity was observed for < 38 μm size fraction gas atomized powder, when adding 1.5 at.% Cr the catalytic activity increased from 1.7 mol kg^{-1} min^{-1} to 9.8 mol kg^{-1} min^{-1}. This represents a 570% increase in catalytic activity for the hydrogenation of nitrobenzene when adding 1.5 at.% Cr [62].

It has been established that the cooling rate of gas atomized Al-Ni affects the phase fractions and consequentely the microstructure morphology. This research has been carried out with the understanding that particular phases are advantageous for certain hydrogenation reactions. The utilisation of Al-rich phases is of particular importance in this study and therefore the rapid solidification is an ideal pathway to investigate. Cr has proven to increase the catalytic activity and so the research aims to understand the mechanism(s) involved in the increase of activity. The characterisation techniques mentioned in **Section 4.5.2** are ideal in not only observing the microstructural changes, but also vital in understanding the solidification pathway of Cr-doped and undoped Al-Ni powders of varying cooling rates.

3.13 Si-Ge

The interest in Si-Ge alloys has risen recently due to applications in the photovoltaic industry. Si-Ge is commonly used for thermoelectric generation whilst Si and Si anodes are used for photovoltaic solar cells and Li-ion batteries respectively. Due to the limited research conducted on Si-Ge, the research conducted on Si shall be presented first, followed by Ge research, and finally, Si-Ge research. The research conducted on both Si and Ge has also been in the same interests as with Si-Ge. It is also worth noting that Si and Ge have similar crystallographic coordinates.

3.13.1 Thermoelectric Performance

A temperature gradient is the method of electric power generation from heat within the thermoelectric material. The dimensionless figure of merit is used to determine the performance of electricity generation from heat:

$$ZT = \sigma S^2\, T / \kappa \tag{3.14}$$

where σ is the electrical conductivity, S is the Seebeck coefficient, and κ is the thermal conductivity. The power factor is determined by the electrical conductivity and Seebeck coefficient:

$$Power\ Factor = \sigma S^2 \tag{3.15}$$

The power factor is used to determine the usefulness of a thermoelectric material in a thermoelectric generator. A material with a high power factor should generate more electrical energy from heat. The figure of merit ZT can be used to determine the maximum efficiency from the following equation:

$$\eta_{max} = \frac{T_h - T_c}{T_h}\left[\frac{\sqrt{1 - ZT_{ave}} - 1}{\sqrt{1 - ZT_{ave}} + T_c/T_h}\right] \tag{3.16}$$

where T_h and T_c are the hot-side and cold-side temperatures, respectively, and T_{ave} is the average $(T_h + T_c)$/2. $(T_h - T_c)/T_h$ Is known as the Carnot efficiency, and the rest of **Equation 3.16** is the reduction factor which together give the maximum efficiency.

3.13.2 Si

Si wafers have long been used as the preferred choice in the photovoltaic industry, but spherical solar cells have been considered as a suitable alternative due to the amount of Si feedstock available. The proposed spherical cells also address the issue of loss of material in the preparation process. The process in which the spherical Si cells are produced involves undercooling the droplets in a tube of inert gas while being dropped [76]. The spherical Si cells have been found to reduce the overall efficiency compared to a single crystal of Si as they allow for an increased surface area to absorb light. The spherical Si droplets are also cheaper to produce than Si wafers [77].

An interesting consequence of the production of Si droplets is the irregular shape, due to the faceted growth of twinned dendrites during solidification. It has been found that this growth can be affected as a result of an increased cooling rate. It has been reported that a higher undercooling would result in the growth of smoother and more spherical droplet [78] [79]. The reason for the change in growth mechanism is due to the transition from faceted to non-faceted growth. Liu *et al.* found that by electromagnetically levitating Si they were able to achieve an undercooling as high as 300 K. Furthermore, they were able to correlate the surface morphology of the droplets with the level of undercooling. They found that at low undercoolings the surface appeared jagged with pronounced edges and faces. They determined that the transition from lateral growth to continuous growth occurred at around an undercooling of 300 K as no faceted dendrites were found in the highly undercooled droplets, in addition to this no edges or special faces were found resulting in a smooth non-faceted morphology [80]. **Figure 3.19** shows the resulting surface morphologies illustrating the faceted and non-faceted morphology found by Liu *et al.*. This agreed with work carried out by Li and Herlach in 1996 [81]. Similar findings of different morphologies were also reported in 2006 when Si droplets were quenched using a chill plate, the areas of the droplets that had good contact with the chill plate showed a relatively smoother morphology than the areas with poor contact [82]. A high-speed camera was used to observe the recalescence interface of undercooled Si, the growth behaviour was classified into three categories; lateral growth at low undercoolings, isolated dendrite growth at intermediate undercoolings, and closer dendrite growth at high undercoolings. The critical undercoolings for the growth behaviour were determined as 100 K for lateral to isolated dendrite, and 210 K for isolated to closer dendrite growth [83]. In 2004 Jian *et al.* determined the critical nucleation undercoolings to be 91.9 K and 191.5 K for the growth transition [84]. It may be noted that the critical undercoolings determined from previous experiments vary slightly which may be attributed to the method of observation as some observations were performed after the solidification, only Aoyama *et al.* used a high-speed camera and observed the recalescence interface.

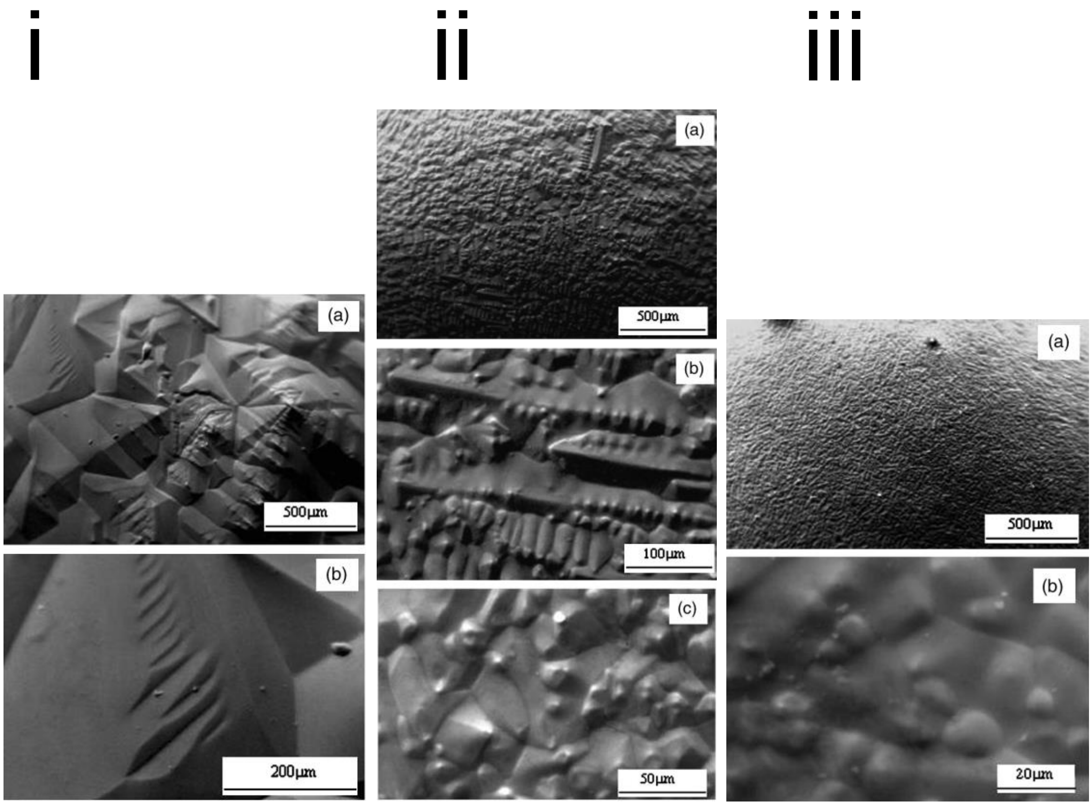

Figure 3.19 Surface morphologies of Si at different magnifications undercooled at i) 86 K, ii) 200 K, and iii) 330 K [80].

Several production techniques have been employed to successfully achieve supercooling for Si. This is since the liquid B_2O_3 flux used to purify Ge is not successful in Si. Undercooling attempts have not proved to be successful for Si when using the same flux [85]. Devaud and Turnbull were the first to successfully undercooling uncoated Si using quartz tubes, they achieved an undercooling of 275 K [86]. In 1996 it was reported that an undercooling of 350 K was achieved for Si when coated in 1mm of a new flux; SiO_2.BaO.CaO [87], though there were some precipitation at the grain boundaries of the flux-embedded Si indicating the presence of contamination. To avoid contamination or chemical reaction of Si alternative techniques have been developed; electrohydrodynamic atomization, pulsed-laser melting, electromagnetic levitation and drop tube processing. These former two techniques are rapid quenching while the latter two represent containerless solidification.

3.13.3 Ge

Ge is an ideal material to utilise in understanding the effects of non-equilibrium solidification, this is due to the covalent bonds within its structure that limit the amount of grain growth in the solid state following solidification. At solidification relatively close to equilibrium, around 10 K undercooling, a faceted growth morphology is found which is ideal for atomic attachment [88].

In 1987 Devaud and Turnbull used a fluxing technique on samples of approx. 0.3-0.5 mm using B_2O_3 flux cooled in a silica hemisphere, they reported an undercooling of 415 K which is considerably more than that achieved for Si [89]. The same flux was used in another study by Lau and Kui who melted and cooled both the 7-11 mm Ge droplets and the flux within evacuated glass tubes, they found an undercooling of only 342 K [90]. Both studies found that growth begins to proceed faceted but as higher undercooling is achieved the growth changes to non-faceted, this was established through investigation of the microstructures. They both found a critical undercooling for the transition from faceted to non-faceted growth. Battersby *et al.* found, using the microstructure, the critical undercooling to be at > 170 K for transition from stepwise to continuous growth, with spontaneous grain refinement occurring at > 270 K [20]. This finding was similar to the finding by Devaud and Turnbull that grain refinement occurred at > 300 K undercooling, they determined the cause of grain refinement to be because of dendritic break-up during solidification [89]. The theory that grain refinement is caused by dendritic break-up was confirmed by Lau and Kui in 1991 as they detected sound at undercooling of approx. 258 K from specimen break up as a result of grain multiplication [90]. The grain refinement found by Devaud and Turnbull was supported by Evans *et al.* in 1990 [91]. An SEM micrograph of the droplet found by Evans *et al.* can be seen in **Figure 3.20**. The understanding that growth experiences a transition from lateral to continuous growth with higher undercooling is well established but the transition undercooling is disputed; Aoyama *et al.* previously found the transitional undercooling to be 30 K [92], this is contrasting to the findings of Battersby *et al.* who determined it to be 170 K [20], and finally, Li and Herlach found it to be 300 K [93]. The reason for such conflicting results has previously thought to have been as a result of differing levels of impurities, but this still does not establish the scattered results. It seems, as the growth changes from lateral to continuous there is a shift in the microstructure that is found after solidification, there is also a second shift when grain refinement takes place. Aoyama and Kuribayashi found these changes to occur at 85 K and 270 K, this is where the lateral growth changes to isolated dendrites, and then to a close dendritic network [83].

These were similar to reported figures by Jian *et al.*; 87.6 K and 164.1 K [84]. Lau and Kui found these values to be 232 K and 258 K [90].

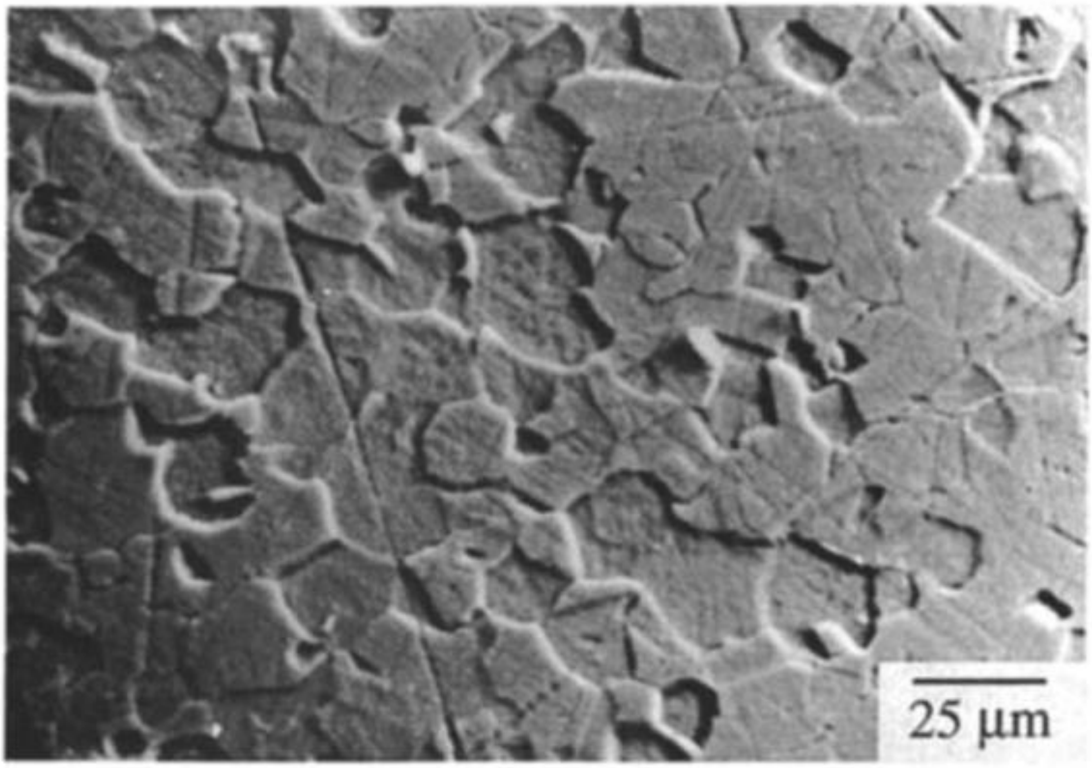

Figure 3.20 SEM micrograph of a polished and etched Ge droplet that experienced > 400 K undercooling [91].

In the interest of microstructural development of Ge, it has been stated that for the application of spherical solar cells the particles should contain few grains [94]. It is with this understanding that attempts to not only understand how undercooling affects the grain distribution, but also attempts to achieve desirable coarse grains have been made. In 2006 Nagashio *et al.* utilised a technique known as semi-solid ejection process combined with drop-tube technique to achieve this desirable microstructure in Si with some success [95]. Similar to this Masuda *et al.* used a pulsated orifice-ejection method to form 200-500 µm Ge particles and found that coarse grains are formed through lateral growth and the finer grains formed through the growth of twin-free dendrites [96]. This was achieved by varying the ejection temperature. They understood that the shift from lateral to continuous growth comes as a result of undercooling, so they believed that the ejection temperature relates to the level of undercooling, but their calculations were not able to demonstrate this. Li *et al.* also found coarse equiaxed grains above a threshold undercooling [97]. **Figures 3.20** and **3.21** show the grain distribution of undercooled Ge and illustrate the transition to finer grains with higher undercooling (**Figure 3.21**).

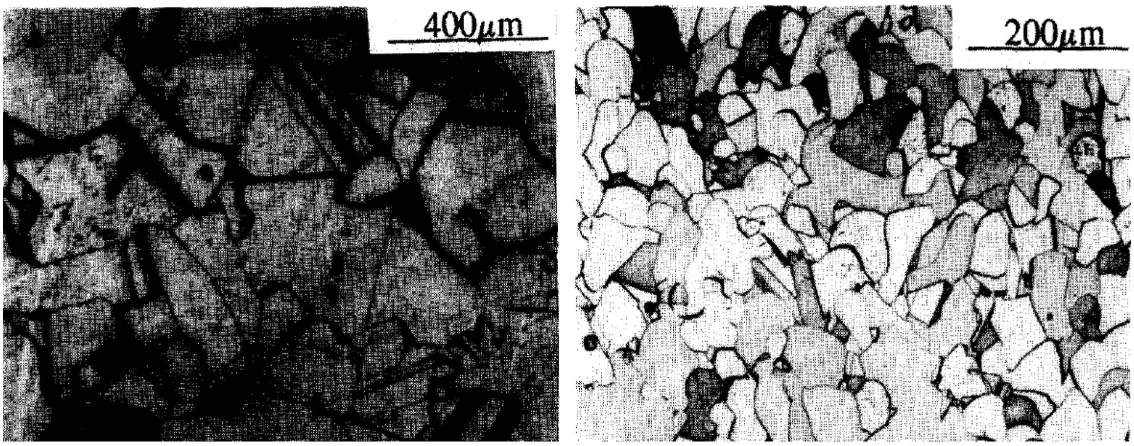

Figure 3.21 Optical micrographs of Ge showing grain distribution for undercooling of a) 316 K, and b) 426 K [97].

3.13.4 SiGe

The $Si_{1-x}Ge_x$ alloy has been one of many semiconductor materials that has been studied due to its application in microelectronics. The composition of the alloy has a desirable tunability of the band gap making it preferred over the less flexible pure silicon techniques [98]. At low temperatures, such as 900 to 1200 K SiGe alloys have been attributed to great mechanical strength. A high melting point and low thermal conductivity are also properties found in SiGe alloys [99], which allows the use of Si-Ge for the generation of thermoelectrical power.

The thermoelectrical properties of Si-Ge may be enhanced due to a composition that is homogeneous during crystal growth. Si and Ge have significantly different melting points [100]. By observing the Si-Ge phase diagram in **Figure 3.22** a relatively large difference in the solidus and liquidus line can be seen. Molten Ge and Si also have a relatively large difference in density [101].

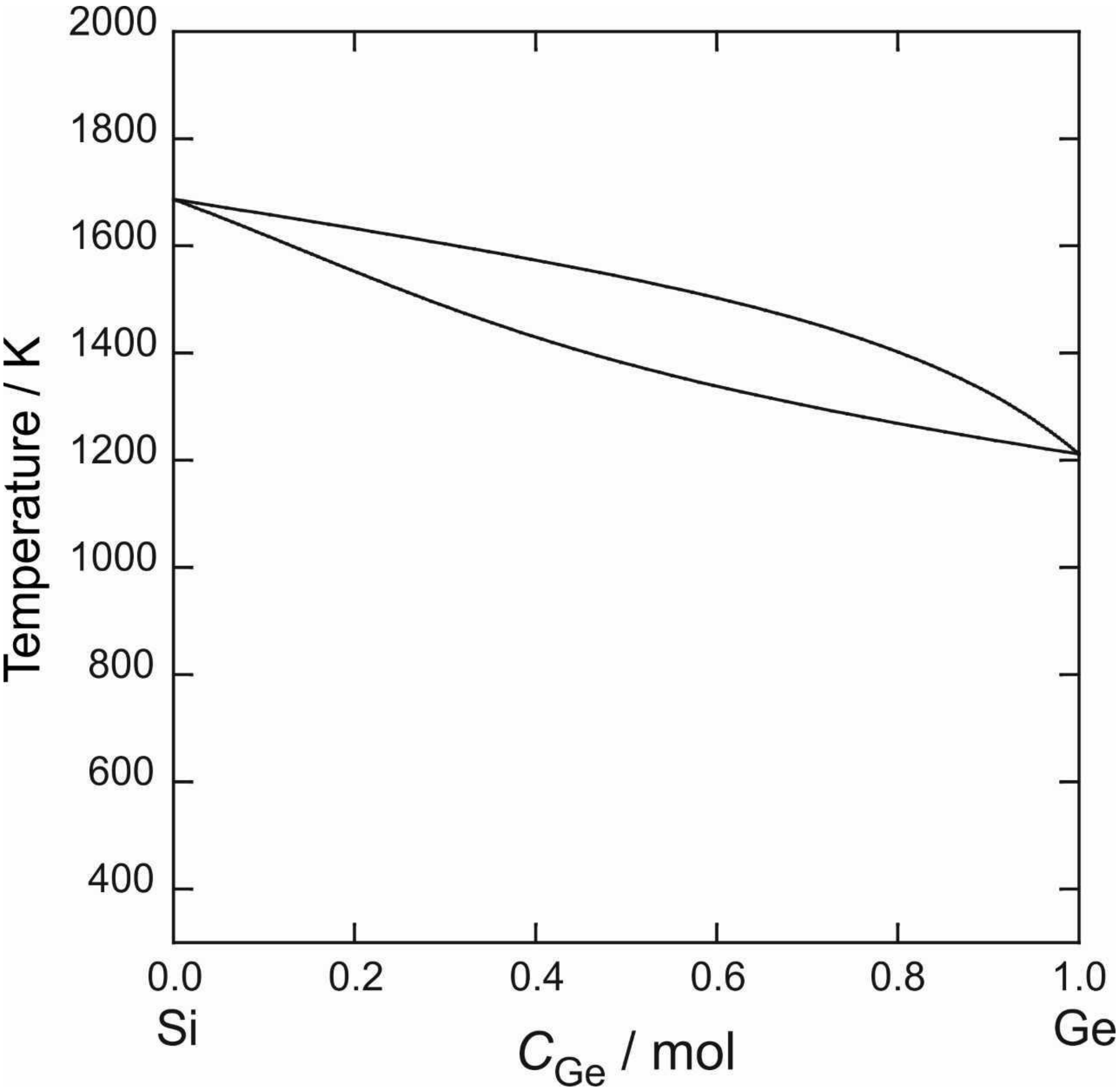

Figure 3.22 Si-Ge phase diagram.

The interest of Si-Ge is particularly due to its application in steel manufacturing; in processes such as the steel billet/strip the waste heat could be recovered as it comes off the mill. The use of Si-Ge would potentially prove to enhance cost-efficiency in commercial use due to its ability to covert waste heat into useful energy. Since Ge is more expensive than Si it is at the best interest of the industry to attempt to increase the cost efficiency of Si-Ge use by lowering the Ge content, but this must be done while maintaining the valuable thermoelectric characteristics. A nanostructuring approach has previously been employed to develop $Si_{92}Ge_8$ [102] [103] and $Si_{95}Ge_5$ [104], notably compositions of Si-Ge with a lower Ge content than commercially available.

It has been found, during electromagnetic levitation studies, that the solidification conditions affect the development of the microstructure, therefore allowing lower Ge content to decrease in thermal conductivity by departure from thermodynamic equilibrium, or undercooling [105] [80] [106]. Previously, melt spinning has been used by Zhang *et al.* to compare n-type Si-Ge samples of the same composition solidified during slow cooling. At slow cooling the SEM micrographs appear to illustrate a microstructure that appeared inhomogeneous, this was supported by EDS point measurements. It was also found that heterogeneity was not entirely suppressed in the rapidly solidified samples. The amount of segregation that was found in the samples solidified by melt spinning was less than that thought to be attributed to solute trapping. The higher cooling rate found that homogeneity was improved while grain sizes appeared to decrease [107]. The microstructures found in this study can be seen in **Figures 3.23** and **3.24**. In 2002 the Japan Microgravity Center’s (JAMIC’s) drop shaft and a 10m drop tube were used to compare Si-Ge samples to experiments conducted in microgravity. The ground-based samples experienced a higher level of segregation though the samples solidified in microgravity did not fully suppress segregation. Segregation was thought to have occurred during solidification by diffusion [108]. **Figures 3.25** and **3.26** show the microstructures found in arc-melting, ground based and microgravity solidification. For both studies the distinct Si-rich grains can be seen, found to solidify first, followed by the Ge-rich regions seen at the Si-rich grain boundaries.

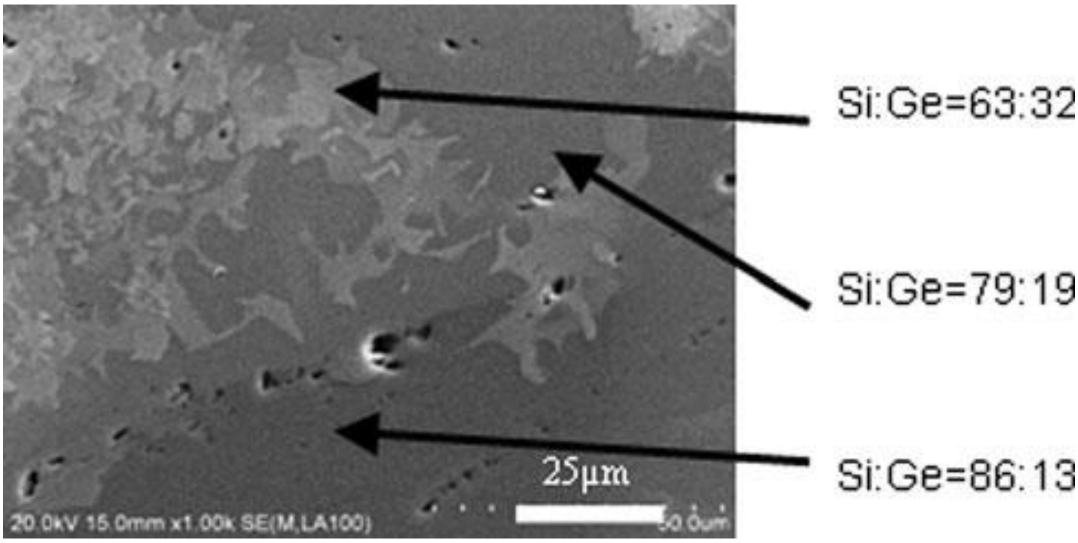

Figure 3.23 SEM micrograph of slow cooled Si-Ge sample with EDS point measurements [107].

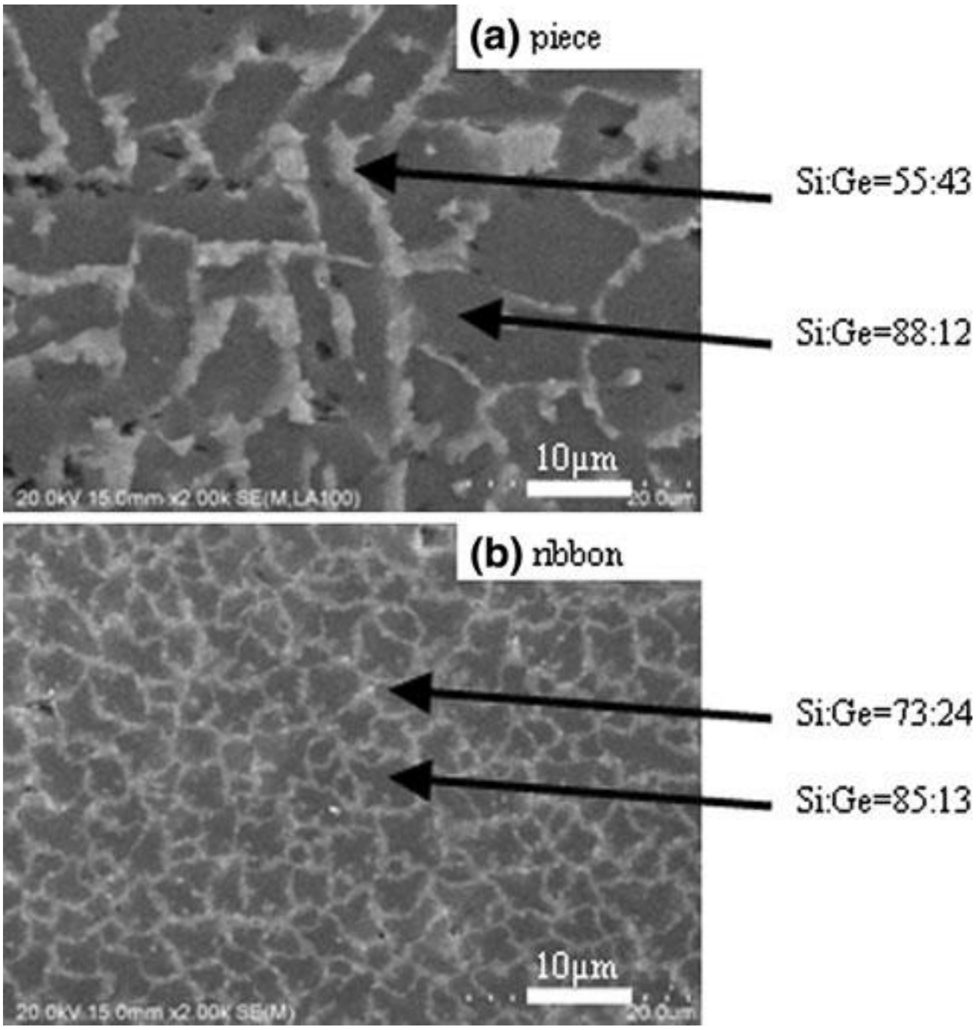

Figure 3.24 SEM micrographs of rapidly solidified Si-Ge samples by melt spinning, with EDS point measurements [107].

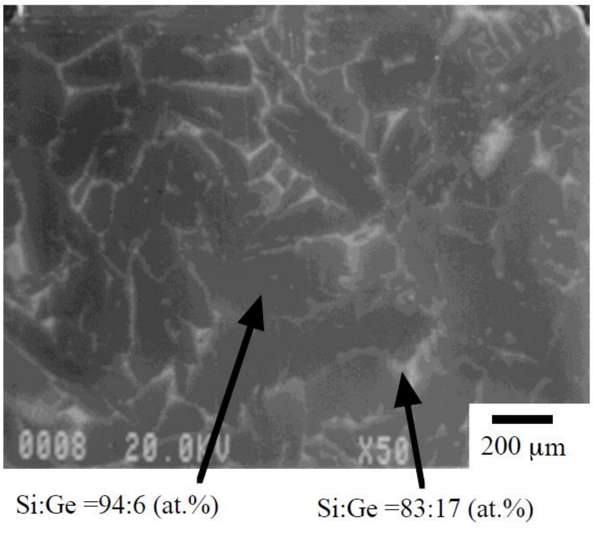

Figure 3.25 SEM micrograph of Arc-melted Si-Ge sample with EDS point measurements [108].

(a)Unidirectional solidification on the ground

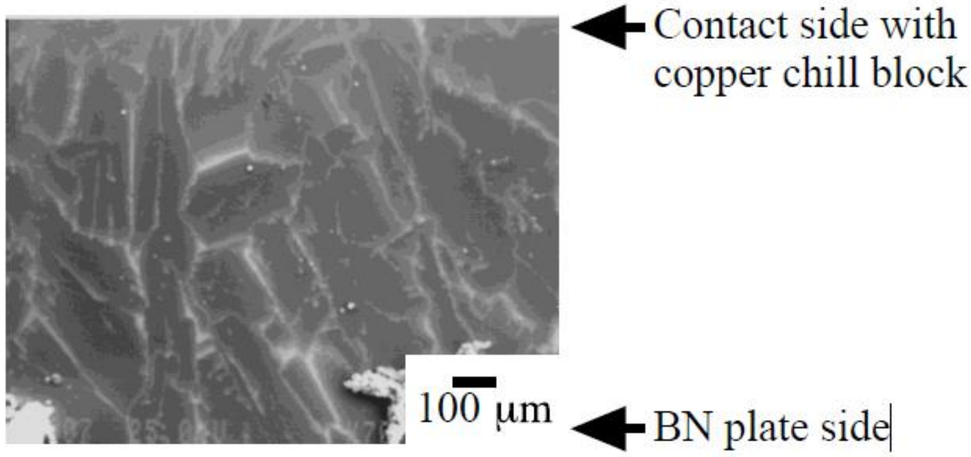

(b)Unidirectional solidification in microgravity

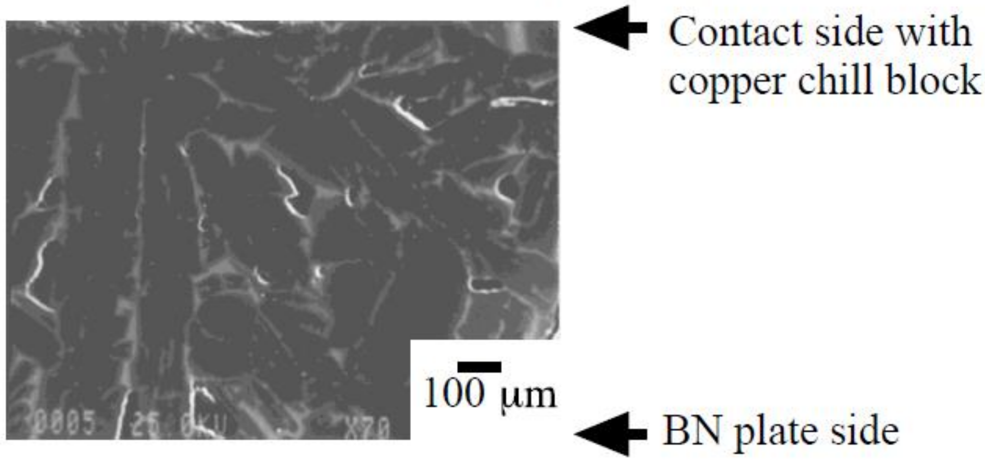

Figure 3.26 SEM micrograph of unidirectionally Si-Ge samples [108].

In relation to the growth characteristics of Si-Ge Panofen and Herlach used electromagnetic levitation and reported the results for Si-2.5 at.% Ge alloys. They determined that two regions of planar growth exist: planar faceted growth and the growth of faceted dendrites, at low and high undercooling respectively. The microstructure of the alloy at different undercoolings can be seen in **Figure 3.27**, and it was concluded that the samples solidified from the surface to the centre with Ge concentration being more in the centre, this is due to solute partitioning [109].

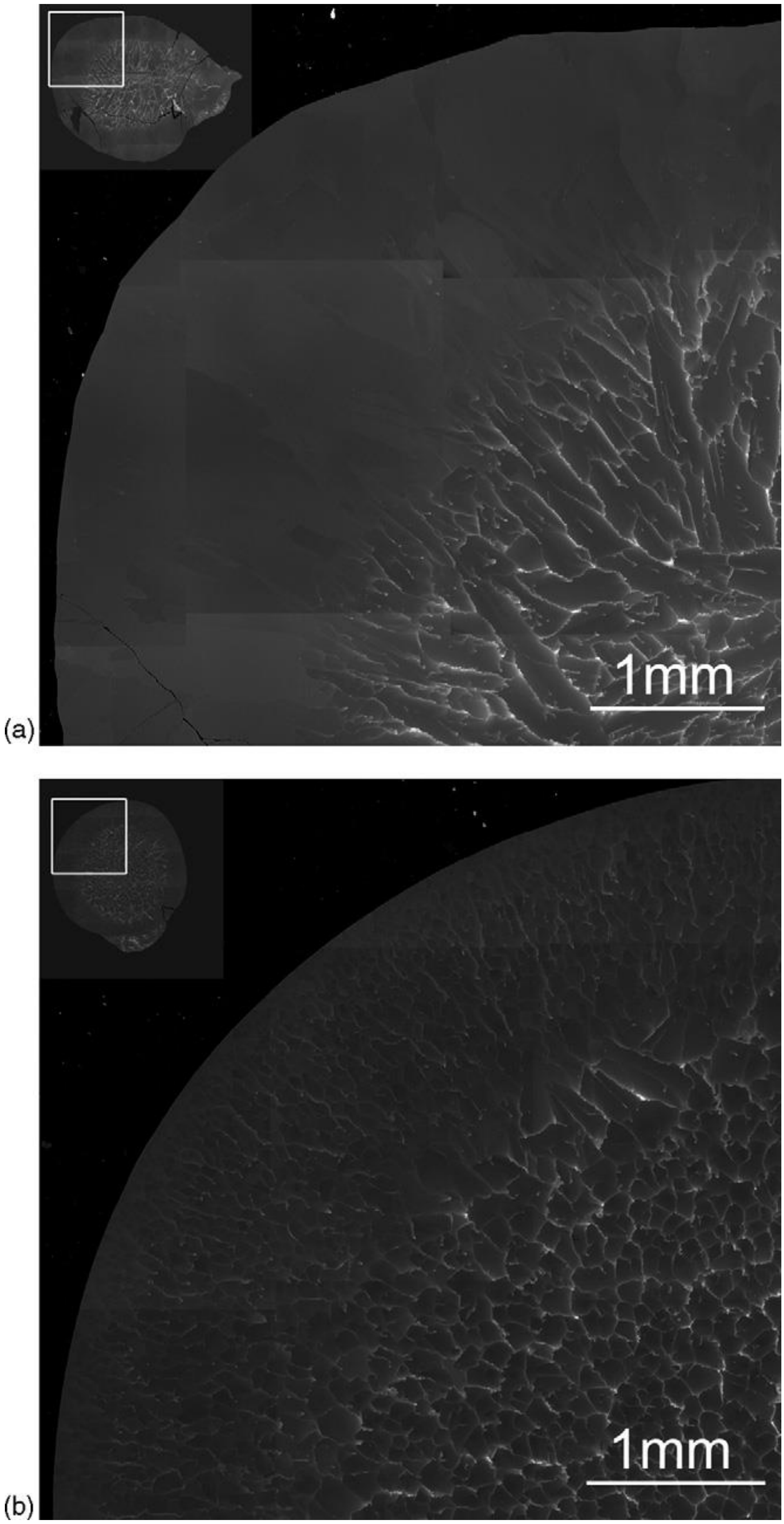

Figure 3.27 SEM micrograph of Si-2.5 at.% Ge samples solidified at undercooling of (a) 52 K, and (b) 290 K [109].

With little research conducted on Si-Ge semiconductor alloys the opportunity to greatly understand the solidification sequence is presented. Si-Ge is ideal in recovering waste heat in manufacturing processes but it comes with the understanding that a homogenous microstructure is favoured. Rapid solidification is investigated as a potential route to achieving the favoured homogenous microstructure. The experimental results following characterisation techniques presented in **Section 4.5.2** are intended to not only lead to a greater understanding of the solidification sequence but also a potential route to achieving refined microstructures.

Chapter 4 Equipment and Methodology

All experimental techniques and details of equipment that have been employed within this project are mentioned in this section. To begin with the compounds were produced using non-equilibrium experiments such as Gas Atomisation for the Al-Ni samples, while the Si-Ge samples were subject to Drop Tube processing. These processes for production ensured rapid solidification of the compounds. Material characterisation techniques were then used to analyse the microstructure and phase composition of the Al-Ni and Si-Ge samples; Optical Microscopy (OM), Scanning Electron Microscopy (SEM), Energy-Dispersive X-ray (EDX), X-ray Diffraction (XRD), Transmission Electron Microscopy (TEM), Focused Ion Beam (FIB), and Electron Backscattered Diffraction (EBSD).

4.1 High Vacuum Production and Measurement for Drop Tube Processing

The vacuum system is started with the *rotary vane pump* which employs a circular rotating rotor that sweeps gas into the vane chamber. When the pressure in the vane pump is large enough a discharge port is opened, and the gas is expelled from the pump into the atmosphere.

The *turbomolecular pump* is used when the pressure within the drop tube reaches 10^{-2} Pa and gas molecules are pushed by repeated collision to the moving solid surface of the rotary vanes.

The *Capacitance manometer* is used to measure the pressure of the gas that is backfilled. A change in the pressure results in a deflection of the plates which is measured as a change in the capacitance between the plates. The diaphragm pulls further away from the fixed capacitance plates with a higher vacuum and the distance can be measured electronically. The accuracy of this type of gauge is typically 0.25-0.5%.

The *Pirani gauge* has a range between 10 to 10^{-4} Pa and is used during the rough (rotary) pumping process. A fine-wire filament, typically Tungsten, is heated by the passing of an electrical current. The *Pirani gauge* is based on the idea that gas can conduct heat, and the gauge will adjust the voltage to allow a constant current to the filament. At high pressure the heat from the filament is taken away by molecules and transferred to the walls of the gauge head. The temperature within the filament will settle if the pressure remains constant. The change in resistance due to high temperature in the filament affects the current and this is measured to determine the pressure of the gas.

The *Penning gauge* can measure pressures between 10^{-1} and 10^{-7} Pa. The *Penning gauge* is used when the *Capacitance manometer* and the *Pirani gauge* is no longer able to measure the low pressure within the drop tube due to their respective ranges, typically the *Penning gauge* is turned on when the pressure is below 10^{-1} Pa. Once the gauge is turned on, the anode rod, which is positioned through a cylindrical cathode, is subject to several kilovolts of electricity. A magnetic field is also positioned parallel to the anode to make sure that the electric field and magnetic field are perpendicular. When an ionizing particle ionizes a gas particle the cathode and anode attract the ions and electrons respectively. Other molecules may ionize through collision. When the ions reach the cathode more electrons are produced and the resulting ions and electrons create more ions, this continues to occur until the rate at which ions are lost are also replaced. The electrons that are attracted to the anode are influenced by the magnetic field which deviates their path into tight spirals, which ultimately increases their path length. The ion current is displayed which is proportional to the pressure in the gauge head.

4.2 Drop Tube Process

A solid Si-30 wt.% Ge ingot was obtained from Goodfellow in lump form and used as the raw material to be processed via drop tube. A 6.5 m drop tube was used to induce rapid solidification and a schematic diagram of the equipment used can be seen in **Figure 4.1**. The crushed sample that weighed 4.04 g was loaded into the alumina crucible which contains three 300 μm laser drilled holes in the base. An induction furnace was used at the top of the drop tube to heat the metal and produce fine droplets extruding in the form of a spray. To achieve undercooling any potent heterogeneous nucleation sites must be avoided, this was the reason that oxygen and impurities, such as moisture, were removed from the drop tube via a vacuum system. The vacuum system used included a mechanical *rotary pump*, connected at the base of the drop tube, and a *turbomolecular pump*, based at the middle section of the drop tube, to achieve the desired pressure within the drop tube. A Nitrogen gas line was connected at the bottom of the drop tube to pressurise the drop tube itself, when required, and the gas line alongside the drop tube to force the material out of the alumina crucible at the top.

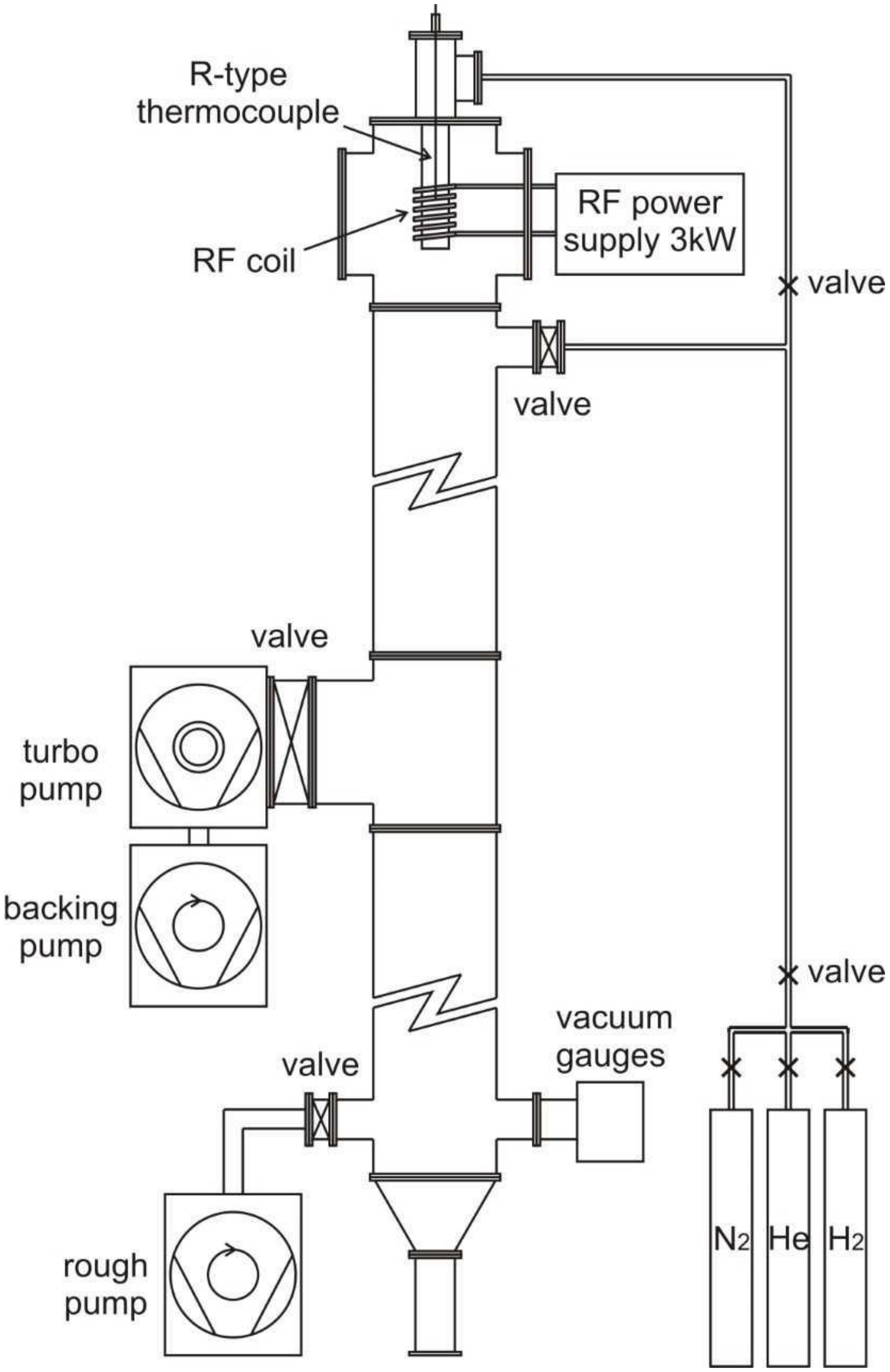

Figure 4.1 Schematic diagram of drop-tube equipment used in this project.

Three types of pressure gauges were used to determine the pressure within the drop tube; *Capacitance manometer*, *Pirani gauge*, and an *Penning gauge.*

To begin with the drop tube was evacuated using the *rotary pump* to 10^{-2} Pa before N_2 gas was used to flush the tube. This cycle was repeated three times before the *turbomolecular pump* was used to evacuate the drop tube to 10^{-4} Pa. The tube was then pressurised to 50 kPa using dried, oxygen free N_2 gas.

A graphite susceptor was subject to induction heating to heat the metal. Two alumina heat shields were used as the susceptor remaining within the heat shields. An R-type thermocouple within the crucible was used to determine the temperature of the loaded sample. The thermocouple is placed just above the level of the sample. When the desired temperature was achieved, approx. 1600 K, the crucible was pressurised using 400 kPa of N_2 gas via the gas line and the melt was ejected through the three laser drilled holes in the crucible. The melt, in the form of a spray, is then solidified whilst in flight as it falls through the drop tube and is collected at the bottom catch-pot. The 1600 K temperature was chosen as it represented a 50 K superheat based on the assumption that the initial material composition contained Si-30 at.% Ge.

When the equipment has been gradually cooled in a controlled manner the rapidly solidified samples can be removed and analysed. Once room temperature and atmospheric pressure have been achieved the removable ConFlat flange at the bottom can be opened and the samples can be removed. Before the drop tube experiment the ConFlat flange at the bottom is tightened. When the flange is opened the sample is removed, resembling almost spherical particles and needle-like ribbons because of the spray during rapid solidification. The resulting samples were then sieved into the following particle size fractions; > 850 µm, 850 - 500 µm, 500 - 300 µm, 300 - 212 µm and 212 - 150 µm.

4.3 Gas Atomization

During this project the Al-Ni samples were synthesised using the close coupled gas atomization technique. Two 6kg batches of Raney Nickel were used with the first batch containing 25% Ni and 75% Al with the other containing 23.5% Ni, 75% Al and 1.5% Cr. Before the process the batches of Al-Ni were superheated to 1813^{O}C. The molten metal batches were each fed through the nozzle into an atomization chamber at 40,000 Pa where the stream of gas was applied at 3.5 MPa using a set of 18 jets that were positioned at a 45^{O} angle to interrupt the molten metal at the nozzle tip (See **Figure 4.2**). The inert gas used was Argon. The molten metal disintegrated from the tip of the nozzle into many small particles which solidified during flight. The nozzle faced downwards so the entire process used gravity to allow the particles to fall freely through the atomization chamber. The gas and melt flow rates were $48.65 \times 10^{-3}\ \mathrm{kg\,s^{-1}}$ and $15.75 \times 10^{-3}\ \mathrm{kg\,s^{-1}}$ respectively. The solidified particle samples were then sieved into the following size fractions: $75\mu\mathrm{m} > 53\mu\mathrm{m}$, $106\mu\mathrm{m} > 75\mu\mathrm{m}$ and $212\mu\mathrm{m} > 150\mu\mathrm{m}$.

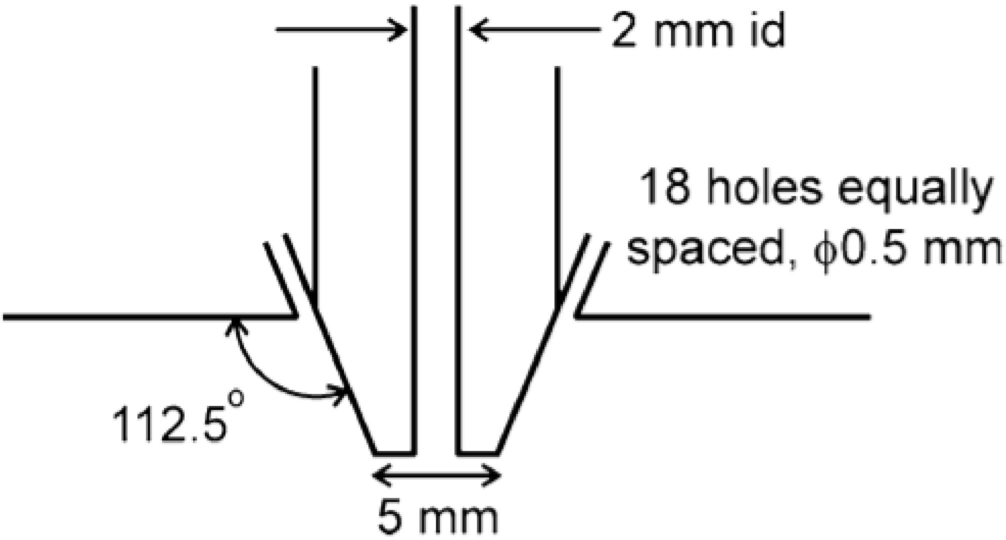

Figure 4.2 Schematic diagram of the atomizer nozzle configuration [61].

4.4 Droplet Cooling Models

It is not possible to determine the cooling rate or the amount of undercooling that is achieved during drop tube processing and gas atomisation as droplets are cooled during flight. The cooling rate, as a function of droplet size, can be estimated using the following equation:

$$\frac{dT_d}{dt}\left[c_l(1-f)+c_s f - L\frac{df}{dt}\right] = \frac{6h}{\rho d}\left(T_d - T_g\right) + \frac{6\varepsilon\sigma_b}{\rho d}\left(T_d^4 - T_g^4\right) \qquad 4.1$$

Where the instantaneous temperature of the particle is T_d. Specific heat of the metal in the liquid and solid states are c_l and c_s, f is the solid fraction, the density of the metal is ρ, d is the diameter of the droplet; ε is the emissivity of the droplet surface; σ_b is the Stefan-Boltzman constant and $\mathrm{T_g}$ the gas temperature. The heat transfer coefficient is estimated using:

$$h = \frac{K_g}{d}\left(2 + 0.6\sqrt{Re}\sqrt[3]{Pr}\right) \tag{4.2}$$

Where the thermal conductivity of the gas is K_g and *Re* and *Pr* are the Reynolds and Prandtl numbers for the flow:

$$Pr = \frac{c_{pg}\mu}{K_g}, Re = \frac{\rho_g d}{\mu}\left|v_d - v_g\right| \tag{4.3}$$

Where the specific heat capacity of the gas is c_{pg}, μ is its kinematic viscosity and $\left|v_d - v_g\right|$ is the differential velocity between the droplet and the gas. The terminal velo*city,* v_T*, for the* particle of diameter, d, can be assumed to be equal to $\left|v_d - v_g\right|$ under the drop tube conditions.

The estimated cooling rates appropriate for each sieved particle sizes of Al-Ni synthesised using gas atomization are as follows: 212 - 150 μm (320 K s^{-1}), 106 - 75 μm (1000 K s^{-1}) and 75 - 53 μm (1800 K s^{-1}) [61].

For spherical droplets the terminal velocity during the drop tube process is:

$$v_T = \left|v_d - v_g\right| = \sqrt{\frac{4gd}{3C_d}\left(\frac{\rho - \rho_g}{\rho_g}\right)} \tag{4.4}$$

Where *g* is the acceleration because of gravity and the density of gas is given by ρ_g. This is only relevant in the drop tube process as in atomisation the gas is moving so the droplets are swept along with it and do not achieve terminal velocity. The drag coefficient, C_d, is estimated using:

$$C_d Re^2 = \frac{4mg\rho_g}{\pi\mu^2} \tag{4.5}$$

Where m is the mass of the sample.

The estimated cooling rates appropriate for each sieved particle sizes of Si-Ge synthesised using the drop tube are as follows: > 850 μm (1800 K s^{-1}), 850 - 500 μm (3600 K s^{-1}), 500 - 300 μm (7200 K s^{-1}), 300 - 212 μm (12000 K s^{-1}) and 212 - 150 μm (20000 K s^{-1}).

Generally, it understood that the cooling rates experienced in gas atomization are lower than those of drop tube droplets, this is thought to be due to:

- The velocity difference between the droplet and the gas is low in gas atomization

- The high thermal load means that the gas temperature is close to that of the melt

4.5 Sample Analysis and Microstructural Characterisation

After rapid solidification the sieved particles were prepared in order to access the microstructure of the particles and analyse using several techniques. To determine the relationship between the different amounts of rapid solidification and the resulting microstructure several methods were used, these methods would allow quantitative examination of the microstructure. Techniques used to analyse the Al-Ni and Si-Ge compounds are described in this section.

4.5.1 Metallography: Specimen Preparation

For microstructural characterisation based on the cooling rate the varied particle sizes must be sieved into standard size fractions. Five wire mesh stacking sieves with decreasing apertures were used for the Si-Ge samples: > 850 µm, 850 - 500 µm, 500 - 300 µm, 300 - 212 µm and 212 - 150 µm for the Si-Ge compound and 212 - 150 µm, 106 - 75 µm and 75 - 53 µm were used for the Al-Ni compound. During the sieving process the sieve stack was vibrated until smaller particles had been sieved into their respective size fraction. Samples were then mounted, using an automatic mounting press, in their respective size fractions using Trans Optic™ resin before grinding and polishing. After the mounting process the samples were then ground using P600 and P1200 silicon carbide papers to expose the internal microstructure. 6 µm, 3 µm and 1 µm of diamond compound were then used on cloths to polish the samples with the assistance of an automatic machine. Between each diamond compound the samples were cleaned using detergent and water before methanol was used to clean the sample. The samples were dried using an electric drier. The reason for cleaning in between each diamond compound was to remove any excess sample that has been scratched away as part of the polishing process, this could further damage the sample and create artefacts within the microstructure. During the grinding and polishing process an optical microscope was used to ensure a satisfactory level of polishing with each diamond compound. The mounted samples were then sputter coated in conductive carbon and attached to an aluminium stub to allow for analysis using SEM.

It is important to take care when preparing samples for EBSD characterisation to achieve reasonable results since it is common for diffracted electrons to escape from less than a few tens of nanometres of the sample surface. Consequently, if the surface of the sample contains any deformation, oxide or the presence of a contaminant then this could affect the formation of EBSD patterns. A single size fraction, 850 - 500 μm, of Si-Ge was used for EBSD, which was ground and polished in the same method as described above. Because EBSD requires a surface finish which is advanced to that of SEM the sample was subject to polishing using 0.1 μm colloidal silica suspension which was applied for 10 minutes using the Buehler Automet 250 grinder-polisher machine. The following settings were used: Force = 25 N, speed of base = 130 rpm and speed of head = 50 rpm.

4.5.2 Characterisation Techniques

After rapid solidification experiments the Al-Ni and Si-Ge samples were analysed using characterisation techniques. The techniques used to characterise both compounds include: X-Ray Diffraction (XRD), Scanning Electron Microscopy (SEM), Energy Dispersive X-Ray Spectrometry (EDX), Focused Ion Beam (FIB) and Transmission Electron Microscopy (TEM). Electron Backscatter Diffraction (EBSD) was only used for the Si-Ge samples. The processes and methods used for these characterisation techniques shall be described in this section.

4.5.2.1 X-Ray Diffraction (XRD)

X-Ray Diffraction (XRD) is a characterisation technique used to for analysis both in industry and research. Information regarding phase identification and phase composition, preferred orientation and crystallite size can be obtained from XRD. The principle of XRD is based on the electromagnetic radiation in X-Rays with a wavelength between 0.05-0.25 nm.

In XRD a filament is heated in the X-Ray tube which acts as the radiation source. The electrons are accelerated at a high voltage (typically 40 kV) to produce X-rays, which then enter the sample that is placed in a holder at the sample stage. Core electrons within the sample are then emitted resulting in vacancies that are filled by electrons from the outer shell. This process results in X-rays being emitted with a characteristic wavelength that is diffracted by the crystalline plane and incident on the material. Bragg’s angle (ϴ) is known to be the angle between the incident beam and the crystalline plane, and it can be seen in **Figure 4.3**, where, the distance bc = dsinϴ and cb’ = dsinϴ so the following equation can be used to calculate the total path difference:

$$bc + cb' = 2dsin\Theta \tag{4.6}$$

During an XRD scan the rays that are diffracted from the different crystalline planes overlay and result in interference. When the waves are in phase there is constructive interference which results in the peaks that can be seen in a diffraction pattern. Constructive and destructive interference with the wave phases is how the diffraction pattern takes shape over a range of angles. Bragg’s Law is the principle that governs this phenomenon and a diffraction pattern can only be obtained when the following equation is satisfied:

$$n\lambda = 2dsin2\theta \qquad 4.7$$

Where θ is the angle of the reflective beam, d is the distance between the plane of atoms, λ is the wavelength of the incident waves and n is a positive integer. Bragg's Law dictates that the path difference between 2 incident waves is given by $2dsin\theta$ and is therefore a multiple of the wavelength, if this is satisfied then the 2 waves remain in phase and therefore interfere constructively.

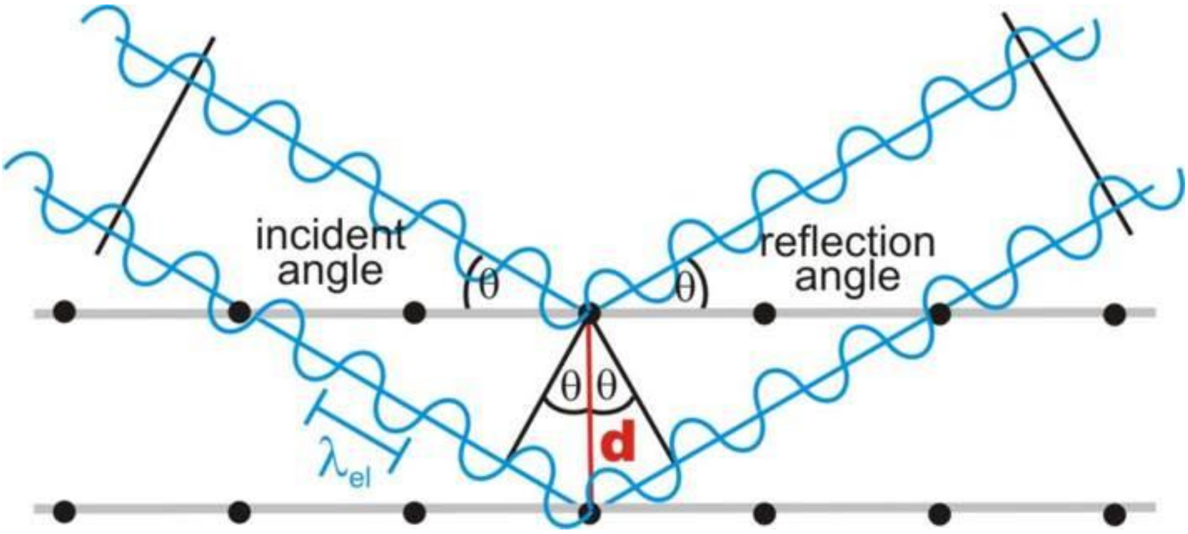

Figure 4.3 Diffraction X-rays on parallel crystalline planes illustrating Bragg’s law.

During the scan it is important to allow adequate time for scanning at each angle as a quicker scan would show unwanted noise in the result. **Figure 4.4** shows diffraction peaks obtained in a) a 13-minute scan, and the same diffraction peaks obtained from b) a 16-hour scan. The extended time in a scan reduces the noise by a square root factor of the scan time, therefore to reduce noise by a factor of 2 (to half the amount of noise) the scan time must be 4 times as long. In **Figure 4.4** the scan time was increased from 13 minutes to 16 hours therefore the amount of noise was a sixteenth of the noise in the original 13-minute scan. The absence of noise proves to be advantageous in identifying smaller peaks, especially at higher angles.

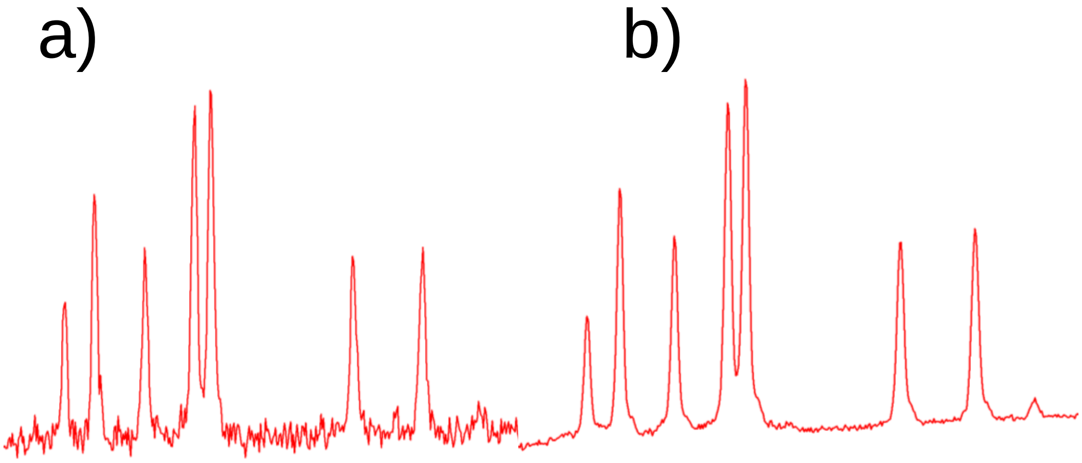

Figure 4.4 Noise present in XRD traces of a) 13-minute scan and b) 16-hour scan.

The Bruker D8 diffractometer was used to analyse the Si-Ge samples before rapid solidification and both Si-Ge and Al-Ni samples after their respective rapid solidification experiments had been completed. Cu-Kα radiation, with λ=0.15418 nm, was used between 20 - 100° in 2Θ. Both Si-Ge and Al-Ni samples were subject to XRD analysis before mounting, grinding and polishing, so the powder droplet form ensured randomly orientated crystalline planes. The strength of the diffraction pattern at any given position was recorded using the detector and this information was plotted as a diffraction pattern. The diffraction pattern is useful in characterisation as the position and intensity of the peaks can be compared against a database of known crystalline materials, meaning information regarding the identification of phases and their composition can be determined. X'pert High score plus was able to assist in phase identification against the International centre for diffraction data (ICDD) library.

4.5.2.2 Scanning Electron Microscope (SEM)

SEM is an important instrument in research due to its ability to examine and characterise both organic and non-organic materials. It is commonly used in intermetallic, ceramic material and semiconductors due to the length scale it is able to resolve (typically between micrometre and nanometre). SEM allows the user to investigate information such as topology, chemical composition and crystallography. An example of an electron column can be seen in **Figure 4.5**.

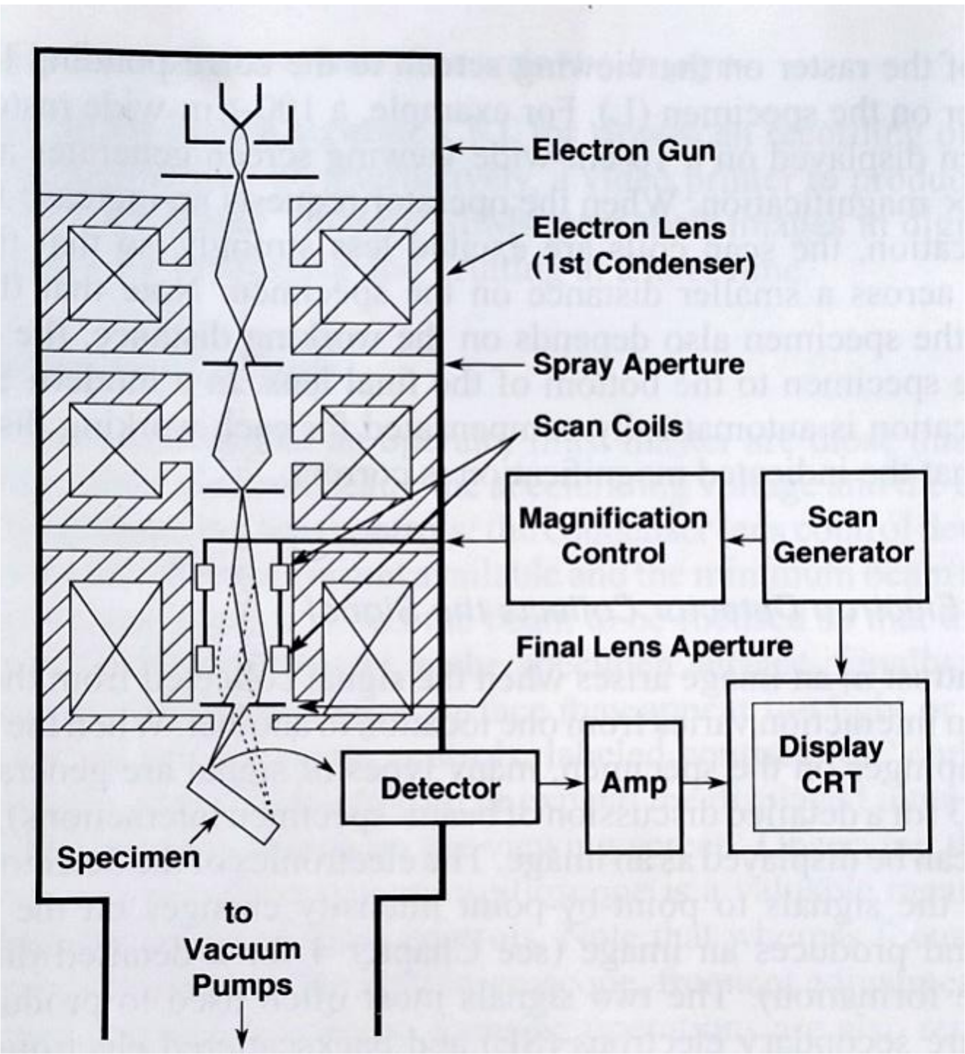

Figure 4.5 Schematic diagram of the electron column showing the electron gun, lenses, the deflection system, and the electron detector [110].

During SEM a sharp focus electron beam with a diameter of ≥ 20 nm is used to scan the surface of the sample. The two ways in which SEM is then able to obtain images is by Secondary Electron (SE) mode where the secondary electrons are capured, and by back-scatter electron mode (BSE) where the back-scattered electrons are detected and captured. Each detection mode allows the user to obtain different information about the sample: SE mode allows the user to analyse the three-dimentional features of the samples surface while BSE mode identifies the areas that contain a varied mean atomic number in the interaction volume.

During backscatter detection there is an interaction volume present; this is when some of the electrons from the beam intercept the surface of the sample and are able to then escape and be detected. Whilst the electrons are within the sample, or within the entrace surface, they undergo enough elastic scattering events in order to alter their trajectory and discharge from the surface of the sample. The volume in which the elastic scattering events take place within the surface of the sample is known as the interaction volume, and it is within this volume that the electrons must deviate at an acute angle that is less than 90 degrees before they can escape, unless the electrons undergo more than one event then it is possible that with the accumulation of many events the electron is allowed to escape. Backscattering is quantified using the below equation to find the backscatter coefficient η:

$$\eta = \frac{\eta_{BSE}}{\eta_B} \qquad 4.8$$

Where η_B is the number of beam electrons incidents on the sample and η_{BSE} is the number of backscattered electrons [110].

A technique known as the Monte Carlo electron trajectory simulation has previously been used [110] to determine the interaction volume of many materials and it has been found that the interaction volume, and subsequently the backscattering, increases with the atomic number of the material. With an larger interaction volume it would mean that the electron takes longer to resurface and would also possibly undergo more elastic scattering events therefore a stronger signal is detected. Because of the size of the interaction volume the backscatter detection mode has a lower resolution of anywhere between 10 and 1000 nanometres.

For this project the Hitachi SU8230 SEM was used with Oxford Instruments Aztec Energy EDX system. A photodiode-backscattered electron (PDBSE) detector was also used to acquire backscattered micrographs. The high-resolution settings were 5 kV accelerating voltage (V_{acc}) and 30 μA probe current (I_{e}). Appropriate magnification was selected for each sample particle size.

4.5.2.3 Electron Microscope Resolution

The advantages of electron microscopy over optical microscopy lie with the maximum achievable resolution, in the case of optical microscopy this is limited by the wavelength of the light that is used to illuminate the sample. In a perfect system during optical microscopy, two adjacent sources are resolved, the best achievable resolution is ~200nm. This is calculated from Abbe's equation:

$$d = \frac{\lambda}{2NA} \qquad 4.9$$

Where the illuminating source's wavelength is λ, NA is the objective numerical aperture (NA = nsinθ, n is the refractive index of the medium and θ the aperture angle) and d is the limit of resolution. A beam with a smaller wavelength can achieve a greater resolution:

$$\lambda = \frac{h}{2moeV\left(1 + \frac{eV}{2moc^2}\right)} \qquad 4.10$$

Where h is Planck's constant, m0 is the electron's mass, e is the electron's charge, c is the speed of light, and V is the accelerating voltage of the electron beam.

An SEM operating at (say) 20 keV, will have a higher spatial resolution than an optical microscope. This is because the de Broglie wavelength of a 20 keV electron is 0.0173 nm, whereas the typical wavelength of light is 550 nm. The advantages of SEM over optical microscopy lie in higher magnification and greater analytical capabilities while images are more easily processed.

4.5.2.4 FIB

To conduct selected area diffraction analysis using transmission electron microscopy (TEM) the samples were required to be prepared using the FEI Helios G4 FEGSEM focused ion beam (FIB). Since transmission electron microscopy (TEM) requires thin specimens to allow analysis the focused ion beam (FIB) is often used to prepare samples but is also used in the production of electronic chips amongst other applications that require relatively thin specimens.

The FIB system consists of three components; the ion column, like that in SEM except the source beam in the FIB uses the gallium ion (Ga+) as opposed to an electron beam. Alongside the ion column the chamber and the vacuum (and gas) transfer system makes up the FIB. The characteristics of Ga mean that an ion beam can be produced from a liquid metal ion source as Ga has a melting temperature of 29.76^{O}C. The electric field that is produced means that positively charged ions are discharged from the liquid Ga. The liquid Ga is located at the tip of a tungsten needle. As the Ga beam strikes the sample it is followed by the sputtering of ions and secondary electrons which are used to form an image. Platinum organometallic gas is ejected from a gun which is struck by the ion beam and subsequently breaks up, this deposits Pt onto the sample. The Pt would ensure no damage is caused to the area of interest within the sample. During FIB imagining a low primary beam current is used so relatively small amounts of the sample is sputtered, but upon application of a high primary beam current much of the sample material can be lost resulting in the ability to conduct precision milling. Once the area of interest has been isolated and removed it is then welded to the tungsten needle and transported to the TEM specimen grid (made of copper). Once the sample has been welded onto the grid it is then sliced using the ion beam to ensure a thickness of less than 100nm.

4.5.2.5 Transmission Electron Microscopy (TEM)

The Transmission Electron Microscopy (TEM) technique is often used to observe the structure and phase composition of a sample, it is a powerful technique in crystallographic characterisation.

A commonly used technique to analyse patterns of diffraction in small regions of the specimen is Selected-area diffraction (SAD). Like XRD, Selected-area diffraction is often used to determine crystal structure, but unlike XRD, Selected-area diffraction can examine areas as small as several hundred nm^2. Since the accelerating voltage found in TEM is typically 100-400 KeV the electron wavelength is very small in relation to the sample (a few thousandths of a nm) and therefore can pass through the spaces between the atoms of the sample. While optical microscopy uses the transmission of light through samples the TEM can replicate this with electrons, therefore being able to achieve a theoretical resolution lesser than atoms. During this process some electrons are diffracted at appropriate angles and others are allowed through without being deflected. The resulting image (diffraction pattern) is collected by the selected area diffraction aperture and is found to be a series of spots in relation to the crystal structure. If during this procedure the sample is tilted the appropriate spots will appear or disappear as they diffract off the atoms within the crystal structure, this is ideal in achieving a good image.

The two methods in which TEM is performed are Bright Field mode (BF) and Dark Field mode (BF). The BF mode utilises the aperture so that it only allows the unscattered beam to pass. If the beam is diffracted at the Bragg orientation or at amorphous regions, then this shall result in a darker crystalline and show as contrast in the final image. In DF mode, the sample is titled until one or more chosen diffracted rays can pass through the aperture in the back focal plane, but undeflected rays are blocked by the aperture and are not allowed to be part of the final image. It is then possible to use the chosen diffracted plane(s) to map the diffracted intensity across the entire sample to determine the crystallographic phase and study defects.

For this project the FEI Titan Themis was operated at 300kV. It was fitted with Super-X EDX system with a windowless 4 detector design. The camera used to view images was a Gatan OneView 16-megapixel CMOS digital camera. EDX was carried out using Velox 2.4 software.

4.5.2.6 Energy Dispersive X-Ray Spectrometry

Energy Dispersive X-Ray (EDX), or Energy Dispersive Spectroscopy (EDS), is a method used to analyse chemical composition and characteristics of a sample, it is often used to identify elements within a sample. The concept behind EDS is that every element has a different atomic structure and therefore a unique X-Ray emission spectrum. An electron from the incident beam excites an inner shell electron such that it leaves the atom in an excited state, the energetic atom is left as an ion. The atom then relaxes to its ground state whereby an electron from the outer shell fills the vacancy in the innner shell. The electron energies in the shells are unique to each element, known as the atomic energy levels, and therefore elements can be identified through the unique energy relased during the relaxing process. It is also possible to achieve an EDS map of the elemental distribution throughout a given area, or site, of a sample by repeating the EDS process over the area, it is a vital method of microstructure analysis as it shows the localisation of elements in particular area of a microstructure.

EDS was conducted using the SEM and TEM instruments described in **section 4.5.2.2** and **4.5.2.5**.

4.5.2.7 Electron Backscatter Diffraction

Electron Backscatter Diffraction (EBSD) is a powerful characterisation technique which gives information regarding grains within the microstructure, particularly grain sizes, boundaries and orientation. Through grain identification EBSD is also able to differentiate possible phases. EBSD is a technique based on SEM and so it mostly uses similar equipment: SEM stage and column, picoammeter, controller and EBSD detector alongside a camera which feeds an image to a display.

EBSD diffraction patterns are known as Kikuchi patterns and are obtained when the sample is tilted 70^0 from the horizontal SEM stage. An incident electron beam is fired into the sample within an interaction volume and is inelastically scattered. At every set of planes some electrons satisfy Bragg's

Law and therefore give a stronger beam due to elastic scattering. The Kukuchi pattern is formed when a set of cones are created by the diffracted electrons, the cones represent each diffracted plane. The Kikuchi patterns are then captured using the camera that is mounted on the EBSD detector. The patterns can then be matched with known reference patterns which allows the identification of crystal structure and consequently crystal orientation.

The machine used to carry out EBSD was the FEI Quanta 650 FEGSEM with Oxford/HKL Nordlys EBSD system, and a grain orientation map was acquired for a selected region.

4.5.3 Characterisation Using Software

Some of the resulting images and diffraction patterns from characterisation techniques described in **section 4.5.2** were required to be processed using computer software to accurately determine information regarding the features. These post-experimental software characterisation techniques allow for better understanding of crystallographic information, phase detection and fraction, atomic site occupancies and multiplicity, grain sizing and refinement. The processes and software used to conduct this research shall be described in this section.

3.5.3.1 Rietveld Refinement

After XRD the resulting crystallographic data was analysed using HighScore program and the International Centre for Diffraction Data (ICDD) database was used to match diffraction peaks to prospective phases.

It is possible to characterise the crystallography of a crystalline material using diffraction peaks achieved from XRD. Peak information, such as height, width and position, are vital in Rietveld refinement. The process of Rietveld refinements involves the use of previous knowledge regarding crystal structure and atomic parameter. The observed diffraction data, which is deemed to be reasonably close to the model, is then refined using a range of parameters to fit previous data. Variable parameters, among others, include atomic occupancies, 2Θ zero, scale factor, preferred orientation and background.

Rietveld refinement was carried out using the General Structure Analysis Software (GSAS) program [111] with the EXPGUI [112] interface in order to determine phase fractions and atomic occupancies for Al-Cr and Al-Ni-Cr samples.

For Al-Ni samples the refinement was straightforward; the observed data was refined with the background in a shifted Chebyshev model. 2ϴ zero and the preferred orientation were then refined. Finally, the scale factor was then refined to reveal the resulting phase fractions. Atomic occupancies were also refined to ensure fully occupied atomic positions.

The refinement of Al-Ni-Cr was more complex due to the lack of published literature for the additional phase, $Al_{13}Cr_2$, that was detected in HighScore. The crystallographic information that was found referred to the phase as also Al_7Cr and $Al_{45}Cr_7$ as well as $Al_{13}Cr_2$, and since the space group was the same for all three designations (space group: C2/m [113]) it was assumed the designation was interchangeable. It was also found that ICDD data is absent above 45^{O} deg (2ϴ) for $Al_{13}Cr_2$ and 60^{O} deg (2ϴ) $Al_{45}Cr_7$, and no data was found for Al_7Cr. The refinement was conducted using a model of a constructed $Al_{13}Cr_2$ unit cell based on published atom coordinates [113]. Similar parameters were refined for Al-Ni-Cr sample to those of Al-Ni; background in a shifted Chebyshev model. 2ϴ zero, preferred orientation and scale factor. Atomic occupancies were also refined with additional constrains to test the occupancy of Ni and Cr atoms.

3.5.3.2 Image Processing

Image processing was conducted using the open-source imagining software ImageJ [114]. Processing methods included the procurement of grey level histograms from SEM backscattered micrographs to determine phase detection using colour contrast. The software was also used to overlay images to determine elemental localisation and assist in understanding the relationship with phase localisation.

ImageJ was particularly used to analyse the microstructure of Si-Ge samples; the program can be used to detect grains and grains boundaries. SEM backscattered micrographs were converted to binary images which would determine the point where the change in contrast is highest, this is assumed to be the grain boundary. Once a binary image is achieved the software can display information such as number of grains (in a given area), and upon the application of a scale it can display grain area. This information can then be analysed to achieve an average grain area for each sample.

Chapter 5 Experimental Results

All the results obtained from experimental methods described in **Chapter 4** are presented in this chapter. To begin with the results from Al-Ni samples will be presented followed by Si-Ge experimental results. CALPHAD modelling was conducted for both Al-Ni and Si-Ge will be presented first followed by SEM and TEM results. The SEM and TEM results shall include EDX mapping, where necessary, and linescans. XRD was conducted for Al-Ni so this shall be presented while Grain size distribution and EBSD was conducted uniquely for Si-Ge.

5.1 AlNi

In this section the results of characterisation techniques will be presented for the Al-Ni and Cr-doped Al-Ni samples. To begin with the CALPHAD modelling sequence was simulated and is presented in **Section 5.1.1**. XRD measurements and subsequent Rietveld refinement are presented in **Sections 5.1.2** and **5.1.3**. This is followed by SEM and TEM characterisation presented in **Sections 5.1.4** and **5.1.5**, EDX was also conducted with both SEM and TEM techniques.

5.1.1 CALPHAD Modelling

A Scheil solidification sequence was simulated and was used to assist in understanding XRD data to find suitable additional phases that may be present in the Cr-doped alloy. This understanding was furthered by the identification of the location of phases to reveal information as to which reactions were active during solidification.

The CALPHAD modelling software package MTDATA [115], with version 4.3 of the SGTE database was used to calculate a Scheil solidification sequence for Al-25 at.% Ni which is presented below, for equilibrium solidification the pathway is shown as a series of reactions:

1381 K: $L \rightarrow Al_3Ni_2$ (primary)

1123 K: $L + Al_3Ni_2 \rightarrow Al_3Ni$ (peritectic)

913 K: $L \rightarrow Al_3Ni + Al$ (eutectic)

The Scheil solidification sequence for Al-23.5 at.% Ni-1.5 at.% Cr was also calculated. The pathway is presented below with additional compounds highlighted in red:

1353 K: L → Al_3Ni_2 (primary)

1139 K: L → Al_3Ni_2 + Al_4Cr (primary)

1117 K: L + Al_3Ni_2 → Al_3Ni + Al_4Cr (peritectic)

1069 K: L + Al_4Cr → Al_3Ni + $Al_{11}Cr_2$ (peritectic)

983 K: L + $Al_{11}Cr_2$ → Al_3Ni + $Al_{13}Cr_2$ (peritectic)

915 K: L → Al_3Ni + Al (eutectic)

The Scheil solidification sequence predicts that three additional compounds are formed during equilibrium solidification. It is predicted that the first additional compound to be formed is Al_4Cr, and it formed via primary solidification direct from the melt. Due to the early formation of Al_4Cr, if found in the final microstructure it should be located towards the centre of grains. It is possible for the Al_4Cr phase to affect the primary peritectic reaction at 1117 K as the Al_3Ni_2 could be isolated from the liquid due to extensive amount of Al_4Cr. During the secondary peritectic reaction at 1069 K the second additional compound, $Al_{11}Cr_2$, is expected to form. This compound is predicted to form because of Al_4Cr reacting with the remaining liquid. Since the $Al_{11}Cr_2$ is expected to form from the Al_4Cr, and alongside Al_3Ni, it would be located interspersed with the Al_3Ni phase. The final additional compound is $Al_{13}Cr_2$ and is expected to form via another peritectic reaction. At 983 K the $Al_{11}Cr_2$ is expected to react with the remaining liquid. If $Al_{13}Cr_2$ does form via the peritectic reactions it would be located within Al_3Ni towards the early stages of formation near the Al_3Ni_2 phase.

5.1.2 XRD Measurements

For the Al-Ni alloy the XRD pattern showed that the predicted three phases were present: Al_3Ni_2, Al_3Ni and Al (as Al-Al_3Ni eutectic). The same three phases were found in the Cr-doped alloys but with some additional peaks. HighScore software[2] was used to conduct a preliminary analysis and it was suggested that the additional peaks found in the Cr-doped alloys may tentatively be associated with the $Al_{13}Cr_2$ phase. For both Al-Ni and Al-Ni-Cr the findings were consistent for all particle size fractions. The XRD patterns are given in **Figures 5.1** and **5.2** for undoped and doped samples in the 150-212 μm sieve fraction.

---

[2] http://www.panalytical.com.

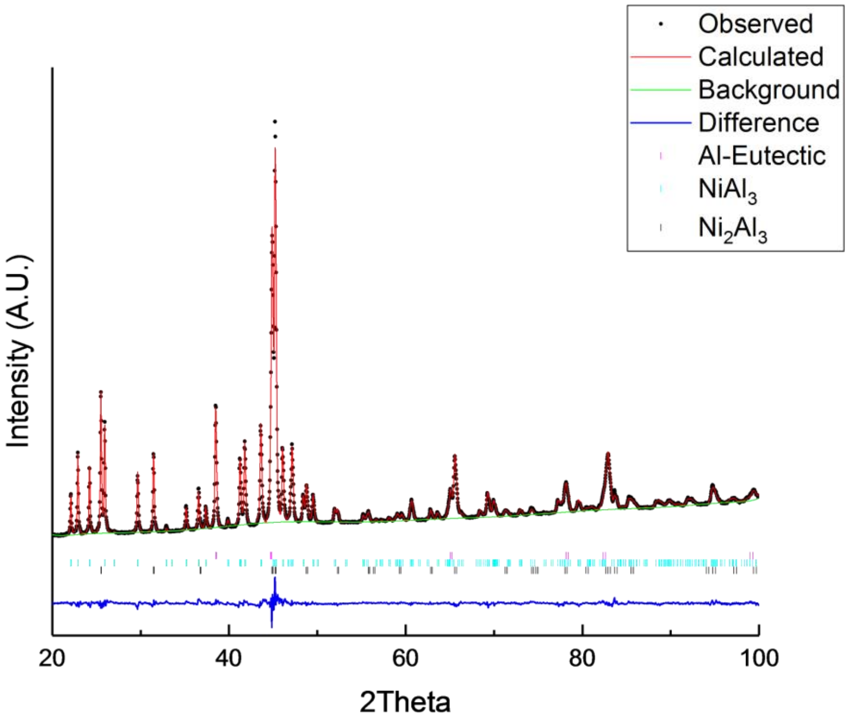

Figure 5.1 XRD pattern and Rietveld fit for 150mm - 212mm size fraction of Al-25 at.% Ni alloy powder.

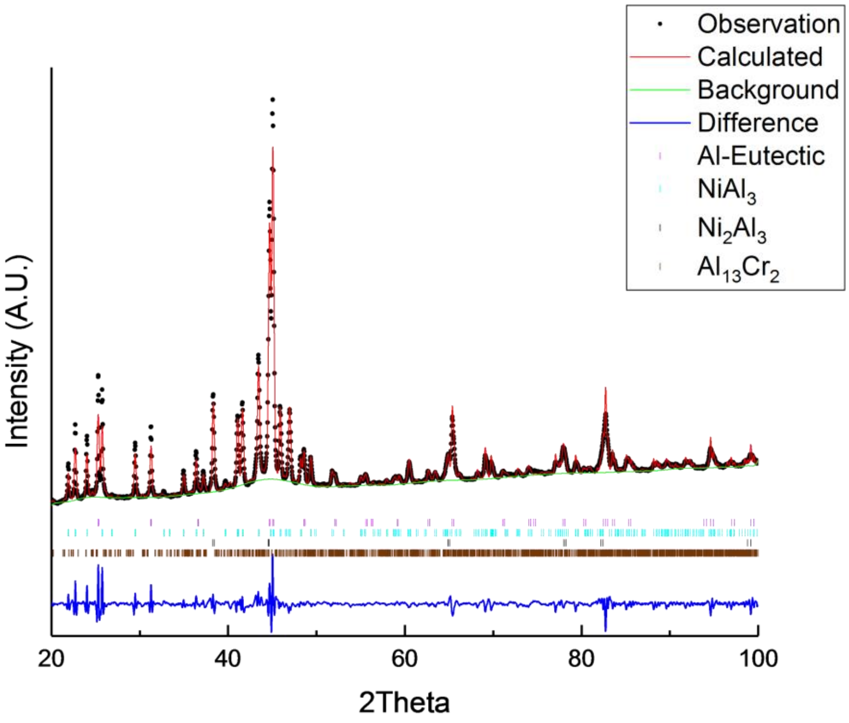

Figure 5.2 XRD pattern and Rietveld fit for 150mm - 212mm size fraction of Al-23.5 at.% Ni-1.5 at.% Cr alloy powder.

For all size fraction of the Cr-doped samples the additional peaks were identified as a single monoclinic $Al_{13}Cr_2$ phase (space group: *C*2/*m* [113]) and consistent phase fraction data was obtained. There was no evidence of Al_4Cr or $Al_{11}Cr_2$, this would mean that the Al-Cr peritectic reactions predicted in the Scheil solidification calculation would go to completion.

5.1.3 Rietveld Refinement

Using the XRD data it is possible to conduct Rietveld refinement to understand the effect of cooling rate on phase composition. **Figures 5.1** and **5.2** show example Rietveld fits to the raw XRD data for undoped and Cr-doped samples respectively.

It was difficult to conduct Rietveld refinement of the Cr-doped XRD data due to the additional phase: $Al_{13}Cr_2$. In previous literature this phase was found to be referred to as not only $Al_{13}Cr_2$, but also Al_7Cr and $Al_{45}Cr_7$. The space group for all designations of $Al_{13}Cr_2$ was the same: C2/m [113], which seems to suggest that despite the designation the crystal structure of all phases ($Al_{13}Cr_2$ is referred to) are the same. Regardless of the designation in literature there was limited crystallographic information available for this phase. No ICDD data was found above 45^{O} deg (2Ө) for $Al_{13}Cr_2$ and 60^{O} deg (2Ө) for $Al_{45}Cr_7$, with significant differences between the $Al_{13}Cr_2$ and $Al_{45}Cr_7$ reference patterns (00-029-0014 and 04-004-3588 respectively), even in the region of overlap. For Al_7Cr there was no data available at all. Due to the limited information there have been previous studies that have omitted the $Al_{13}Cr_2$ phase (e.g. [116]). Published coordinates were used to construct a model of the $Al_{13}Cr_2$ unit cell in order to obtain a fit [113].

In **Figure 5.2** there is a dense collection of hkl markers (seen in dark brown) which are generated due to the crystal structure data generating many lattice planes for the $Al_{13}Cr_2$ phase. It can also be seen that at around 45^{O} deg there is a departure of the baseline from linear, a combination of all phases present in that region and the dense number of planes generated is likely to be the reason for this. To achieve consistent and stable results the refinement had to be completed with care. Alongside the background parameter, crystal orientation and the phase fractions, the atomic occupancies were also refined to test the theory of Ni substituting for Cr in the $Al_{13}Cr_2$ phase. A constraint was set to allow for the refinement of Cr sites to be occupied by Ni atoms, this led to a more suitable fit alluding to the fact that Ni substitutes for Cr. Several refinements were run to observe the sensitivity of the results which resulted in consistent and stable results.

Once Rietveld refinement was successfully completed the resulting phase fractions were analysed. The phase fractions can be seen in **Tables 5.1** and **5.2**. As particle size decreases there is more Al_3Ni_2 and less Al_3Ni. The Al eutectic is also seen to increase with decreasing particle size. This data agrees with the assumption that the peritectic reaction L + $Al_3Ni_2 \rightarrow Al_3Ni$ does not have enough time complete in the smaller particles that experience a higher cooling rate. The remaining Al also follows the expected trend as the remaining liquid in the smaller particles is more Al-rich allowing a higher fraction of the eutectic phase.

Table 5.1 Weight fractions of Al-25 at.% Ni obtained using Rietveld refinement of XRD

Compound	Size fraction	Weight %			
		Al_3Ni_2	Al_3Ni	Al eutectic	$Al_{13}Cr_2$
Al-25 at.% Ni	$150\mu m < 212\mu m$	33.5	53.8	12.7	N/A
	$75\mu m < 106\mu m$	34.1	50.4	15.5	N/A
	$53\mu m < 75\mu m$	36.3	47.3	16.4	N/A

Table 5.2 Weight fractions of Al-23.5 at.% Ni-1.5 at.% Cr obtained using Rietveld refinement of XRD

Compound	Size fraction	Weight %			
		Al_3Ni_2	Al_3Ni	Al eutectic	$Al_{13}Cr_2$
Al-23.5 at.% Ni	$150\mu m < 212\mu m$	29.1	45.2	9	16.8
-1.5 at. %Cr	$75\mu m < 106\mu m$	30.4	38.9	13.7	16.9
	$53\mu m < 75\mu m$	32.9	37.1	13.4	16.6

In **Table 5.2** the phase fractions for the Cr-doped samples are shown. The Al_3Ni_2, Al_3Ni and Al eutectic follow the same trend as the undoped samples, so the cooling rate affects theses samples in the same way. It is noticeable that there is a larger amount of $Al_{13}Cr_2$ present than would be accounted for by the Cr composition in the original melt. If all the Cr atomic sites of $Al_{13}Cr_2$

were occupied by Cr, then the maximum amount of $Al_{13}Cr_2$ would be 9.6 wt%, based on a mass balance calculation for this phase:

$$\frac{\text{atomic weight of Cr} \times \text{Cr at.\%}}{(\text{atomic weight of Cr} \times \text{Cr at.\%}) + (\text{atomic weight of Al} \times \text{Al at.\%})} \times 100$$
$$= \text{Cr wt.\%}$$

$$\frac{51.9961 \times 13.33}{(51.9961 \times 13.33) + (26.982 \times 86.67)} \times 100 = 22.86$$

With only 2.2 wt.% of Cr in the entire alloy making up 22.86 wt.% of the $Al_{13}Cr_2$ phase a simple calculation would determine the maximum amount of the $Al_{13}Cr_2$ phase allowable in the final alloy if all Al and Cr sites were occupied by Al and Cr respectively:

$$\frac{2.2}{22.86} \times 100 = 9.62 \text{ wt.\%}$$

In **Table 5.2** it can be seen there is more $Al_{13}Cr_2$ than possible without substitution. Ni is therefore predicted to substitute into the Cr lattice within the $Al_{13}Cr_2$ phase. This would be similar to a previous study where a $(Ti,Ni)Al_3$ phase was found in a Ti-doped Raney type alloy, this additional phase had a *I4/mmm* $TiAl_3$ crystal structure [14]. If Ni does substitute onto the Cr lattice then the additional phase should be correctly designated as $Al_{13}(Cr,Ni)_2$, though it is referred to as $Al_{13}Cr_2$ within this thesis due to its crystal structure. During Rietveld refinement a deficiency of Cr was found on all three Cr sites within the $Al_{13}Cr_2$ phase. From the three sites the deficiency within the first site was the lowest at 25%, and the highest in the third site at 80% with all the atomic sites being 40% Cr deficient in total. Following the observation that more $Al_{13}Cr_2$ exists in the microstructure, and the deficiency of Cr, the refinement was also conducted with the understanding that the deficient Cr sites are substituted by Ni. All the Cr deficient sites were accounted for by Ni. If a calculation was conducted for the 40% deficiency of Cr on Cr sites, and all of the Cr was still contained within the $Al_{13}Cr_2$ phase then the maximum amount of the as $Al_{13}(Cr,Ni)_2$ phase allowable would be:

$$\frac{2.2}{13.56} \times 100 = 16.22 \text{ wt.\%}$$

This agrees with the weight fractions of $Al_{13}Cr_2$ in **Table 5.2** allowing for reasonable error. Further analysis of Ni substitution is presented in **Sections 5.1.4** and **5.1.5**.

5.1.4 SEM and EDX Microstructure Characterisation

The SEM backscattered micrographs for the undoped alloys can be seen in **Figures 5.3** and **5.4**, these correspond to the smallest and largest size fraction: 212 - 150 µm and 75 - 53 µm. The backscatter mode shows the three phases with a unique shade of grey. Al_3Ni_2 appears the lightest due to its high mean atomic number, with Al_3Ni adopting a mid-grey, and finally the Al-Al_3Ni eutectic with the lowest mean atomic number appearing the darkest. Evidence of peritectic reactions is visible with the morphology adopting a core-shell characteristic. Al_3Ni can be seen to surround the Al_3Ni_2 core, even in the case of dendrites. The larger particles seem to have a rather more globular morphology than the smaller particles which exhibit a dendritic character. The Al-Al_3Ni eutectic can be seen in further detail in **Figure 5.5** which has a higher magnification. The morphology of the eutectic appears to be rod-like due to the low volume fraction of the Al_3Ni phase within the eutectic. This characterisation is observed in all samples including the Cr-doped samples. **Figures 5.6** and **5.7** show the SEM backscattered electron images for the Cr-doped alloys of the same size fractions. The microstructure morphology appears to be very similar to the undoped alloys as Al_3Ni_2 is encased by Al_3Ni. The smaller particles also exhibit more developed dendrites than the larger particles but interestingly the for all particles sizes the dendrites are more defined in the Cr-doped samples than the undoped alloys. The particle size has the same effect on Cr-doped samples than with the undoped samples as the dendrites become more developed with a smaller particle size.

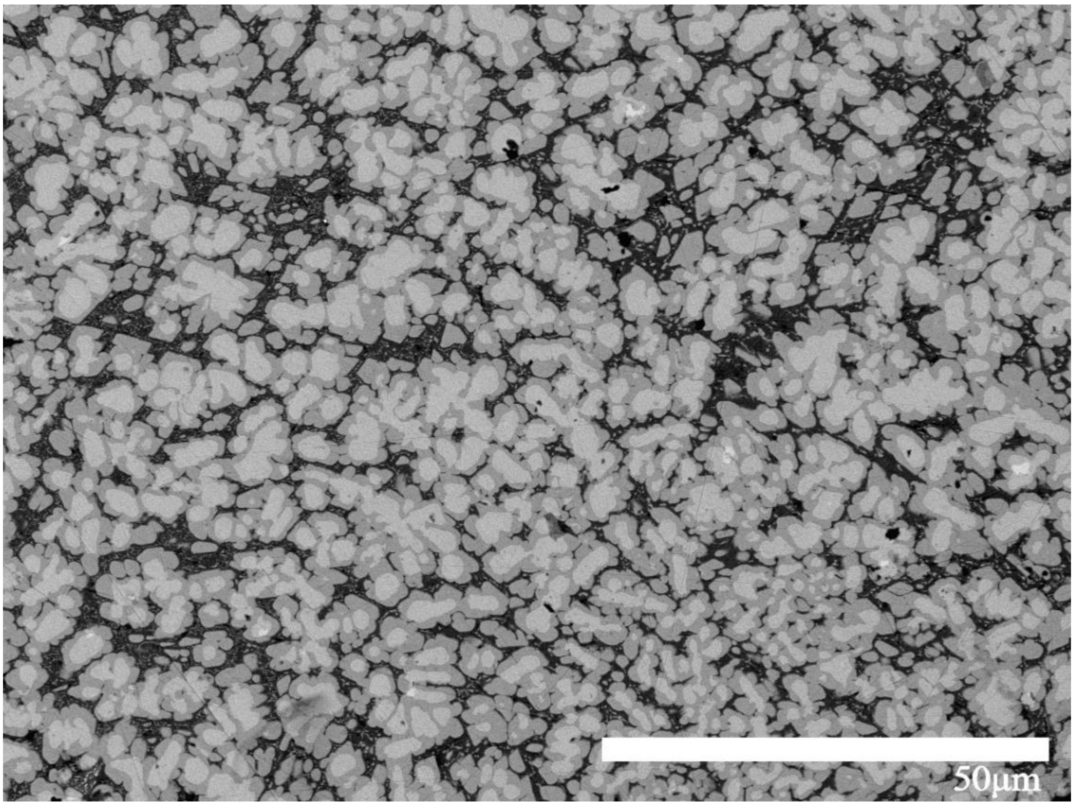

Figure 5.3 SEM backscattered micrograph of Al-25 at.% Ni alloy at 212 - 150 µm particle size fraction.

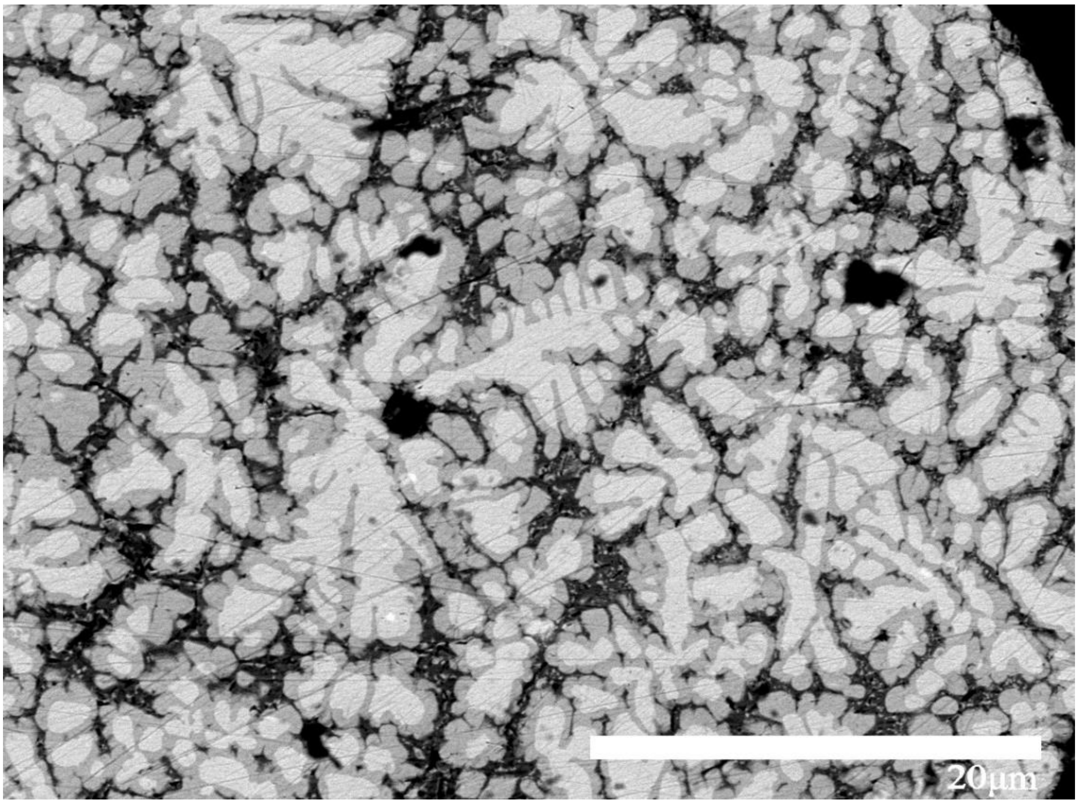

Figure 5.4 SEM backscattered micrograph of Al-25 at.% Ni alloy 75 - 53 µm particle size fraction.

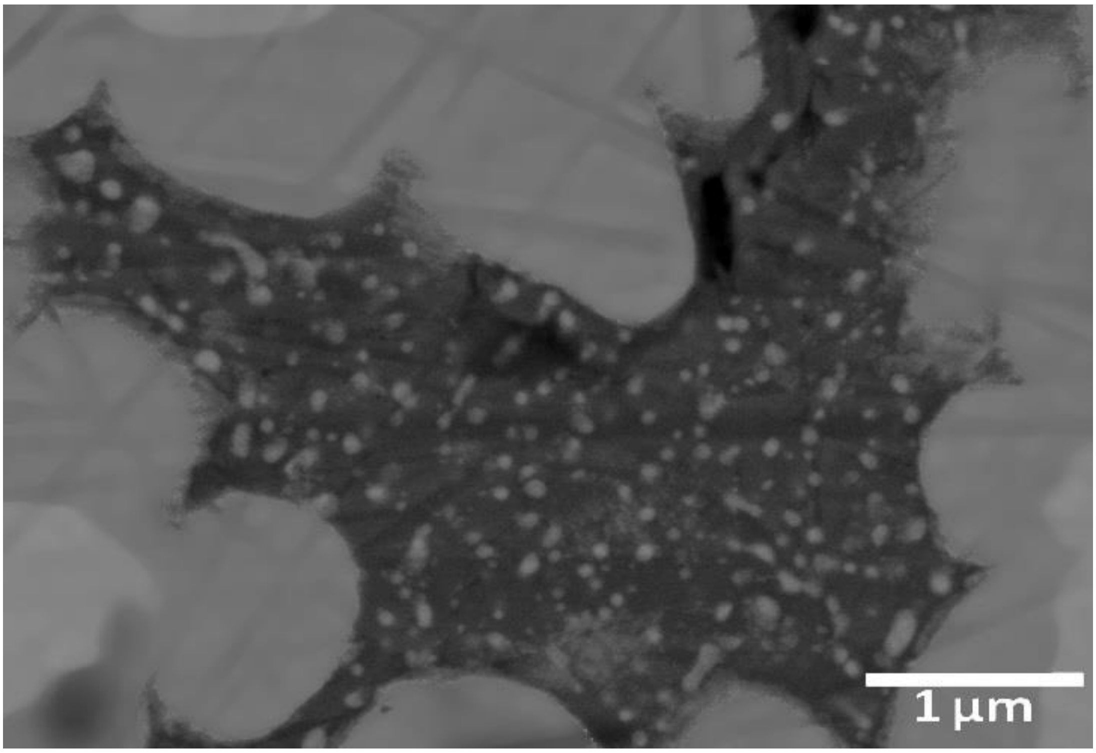

Figure 5.5 High magnification SEM backscattered image of Al-25 at.% Ni alloy at the at 212 - 150 µm size fraction showing the Al-Al_3Ni eutectic.

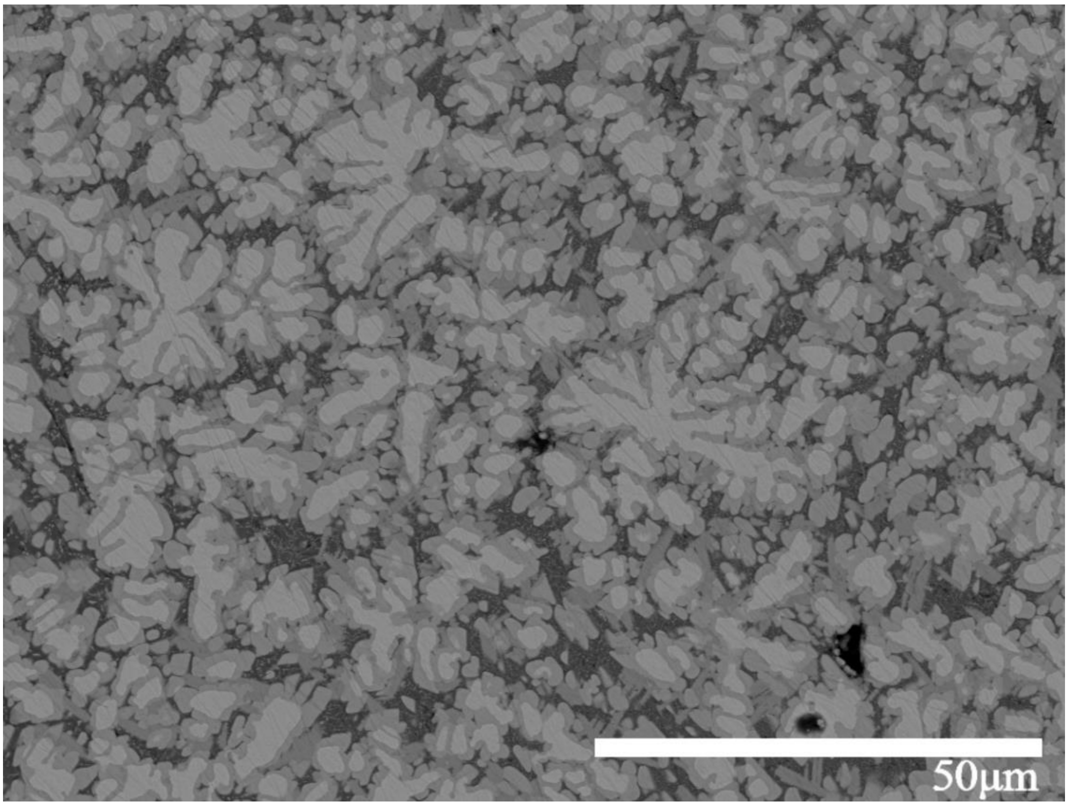

Figure 5.6 SEM backscattered micrograph of Al-23.5 at.% Ni-1.5 at.% Cr alloy at 212 - 150 µm particle size fraction.

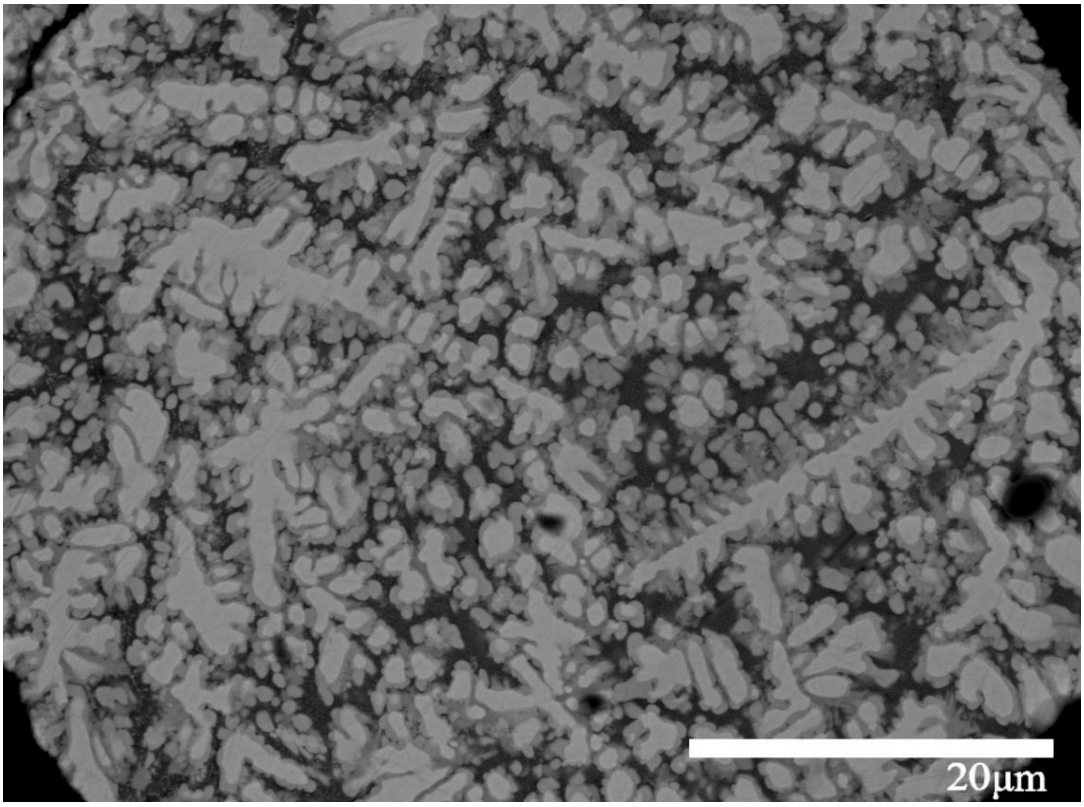

Figure 5.7 SEM backscattered micrograph of Al-23.5 at.% Ni-1.5 at.% Cr alloy at 75 - 53 µm particle size fraction.

EDX was also carried out and Cr localisation was determined. The EDX map of Cr localisation can be seen in **Figure 5.8** as it is overlaid onto the backscattered SEM micrograph from **Figure 5.6**. Almost all the Cr seems to be co-located with the Al_3Ni phase, mainly on the boundary between Al_3Ni and the Al eutectic, with a small amount in the eutectic phase. The location of Cr does not agree with the Scheil calculation, which suggests the additional $Al_{13}Cr_2$ phase is a result of a series of peritectic reactions. If the Scheil solidification sequence was correct then the $Al_{13}Cr_2$ phase would form from its precursor Al_4Cr and would be co-located within the Al_3Ni_2 phase. The findings presented in **Figure 5.8** would suggest that $Al_{13}Cr_2$ is formed as a primary solidification phase directly from the melt towards the end of Al_3Ni growth.

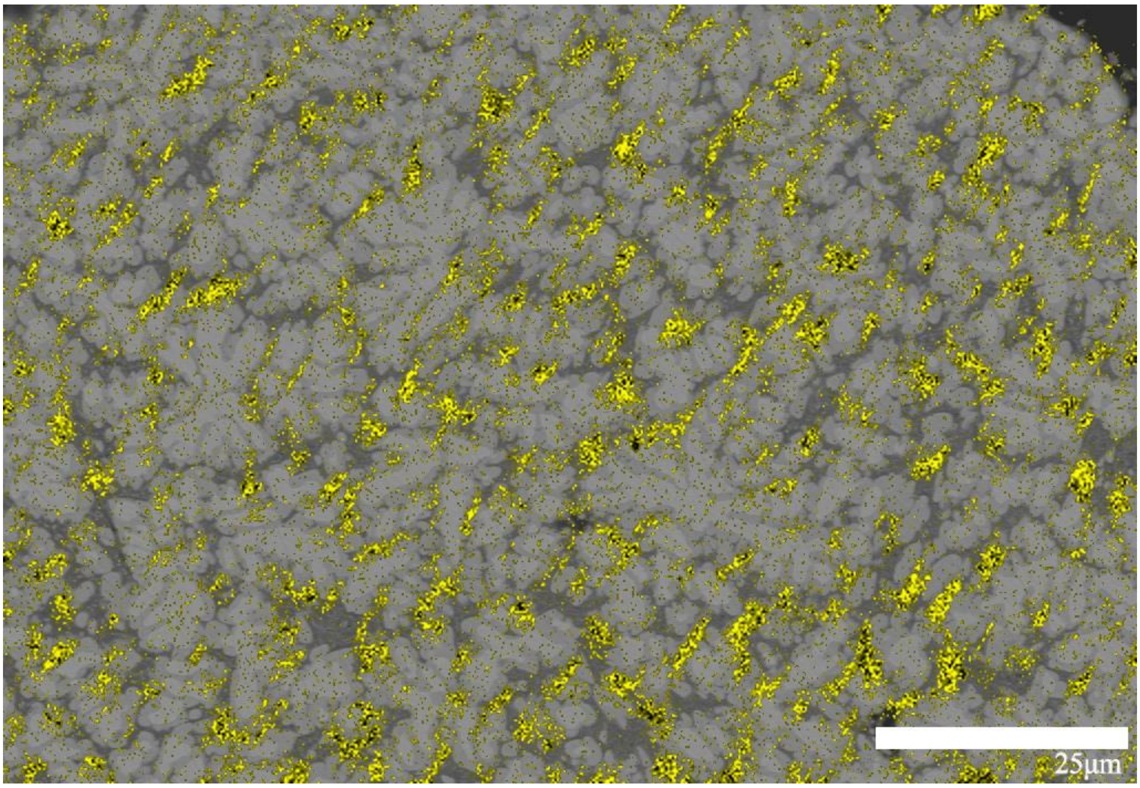

Figure 5.8 SEM backscattered micrograph of Al-23.5 at.% Ni-1.5 at.% Cr alloy at 212 - 150 µm particle size fraction overlaid with Cr EDX map illustrating Cr localisation within the microstructure.

From the Rietveld refinement in **Section 5.1.3** it is apparent that four phases are present despite the fourth phase not appearing in SEM backscattered images. Due to its mean atomic number the $Al_{13}Cr_2$ phase should appear as a mid-grey, lighter than the Al-Al_3Ni eutectic but darker than Al_3Ni.

In **Figures 5.9** and **5.10** the colour-level histograms are presented which show the grey-level intensity for **Figures 5.6** and **5.7**. There are three distinct peaks present in the histograms which each correspond to a phase (due to atomic mean number). The Al_3Ni_2 peaks appear to the far left and the Al-eutectic peaks appear towards the right with the middle distinct peak representing the Al_3Ni grey-level. Please note that the isolated small peaks on the far right of the histograms are a result of pull-out, which occurs when the Al-eutectic becomes loose from the mounted, ground and polished sample. In each histogram there can be seen a fourth peak (can be seen as a close up) which appears less developed, in **Figure 5.10** the peaks appear a shoulder to the Al_3Ni peak. This fourth peak correctly corresponds to the $Al_{13}Cr_2$ phase due to its location. Although it is not easy visible to the naked eye, the fourth phase is present in the SEM backscattered micrographs in **Figures 5.6** and **5.7**, upon a more detailed observation this can be seen.

The grey-level histograms for the undoped samples can be seen in **Figures 5.11** and **5.12** for comparison, they also feature a peak to the far right due to pull-out or account for the area outside the droplet within the micrograph. For the undoped samples only three grey-level peaks can be seen as expected.

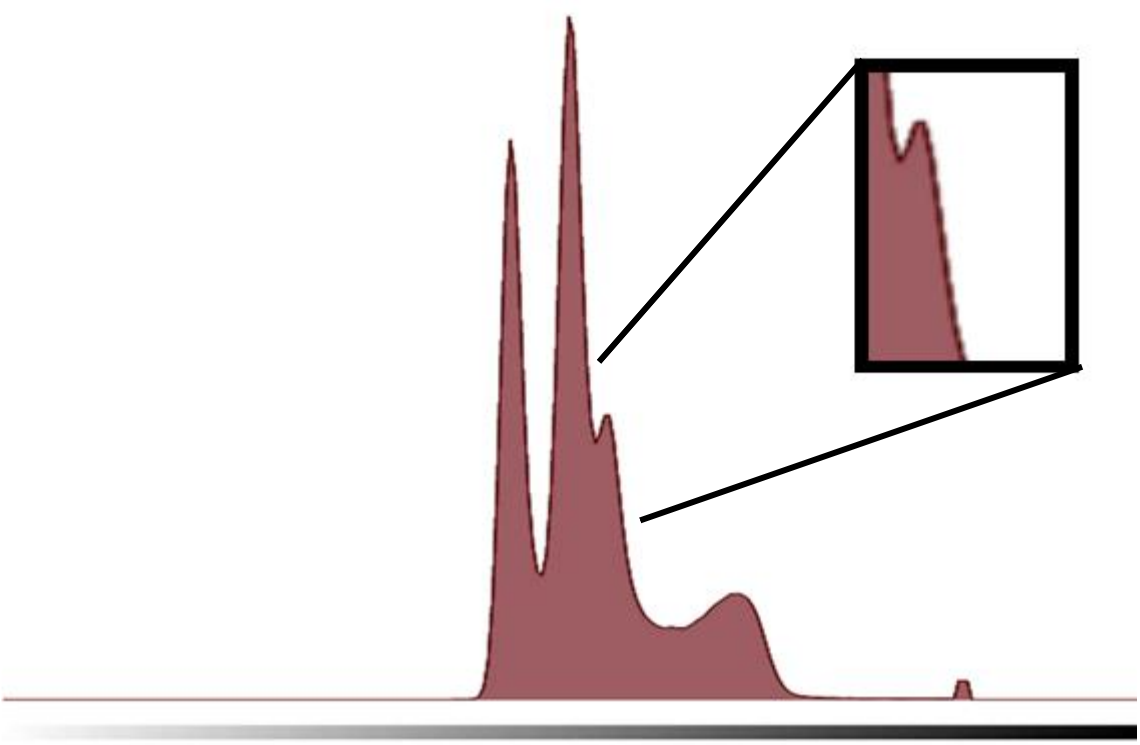

Figure 5.9 Grey-level histogram for the SEM backscattered image in **Figure 5.6**.

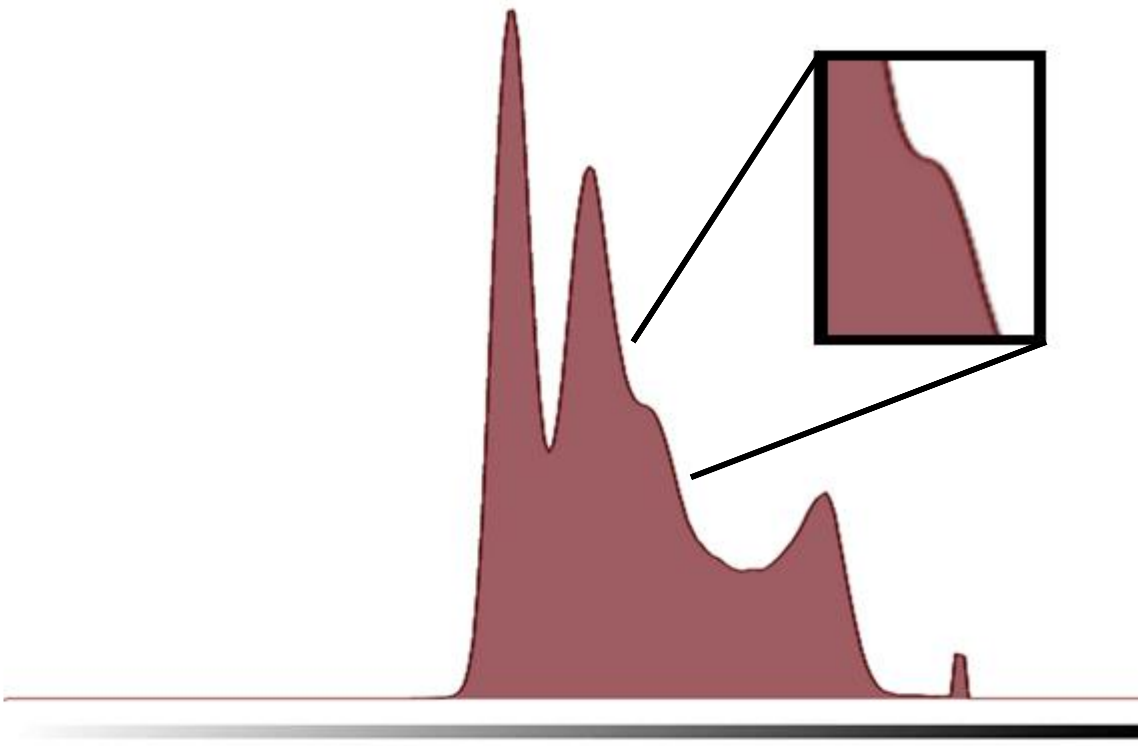

Figure 5.10 Grey-level histogram for the SEM backscattered image in **Figure 5.7**.

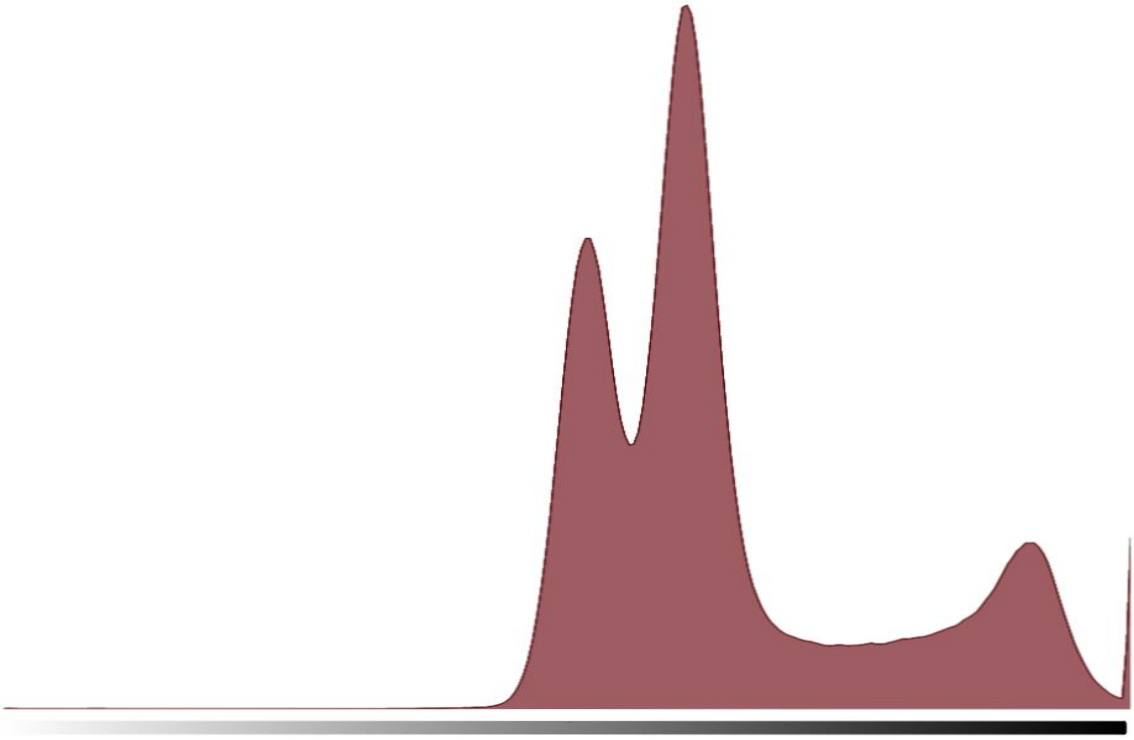

Figure 5.11 Grey-level histogram for the SEM backscattered image in **Figure 5.3**.

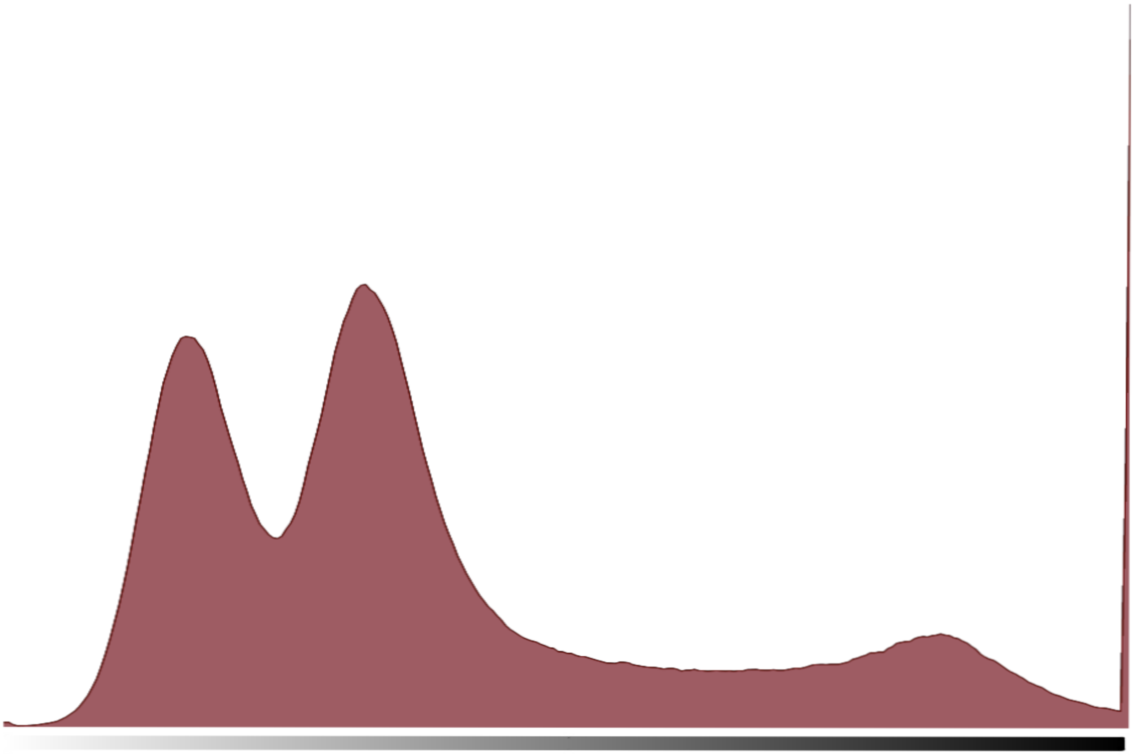

Figure 5.12 Grey-level histogram for the SEM backscattered image in **Figure 5.4**.

The maximum for the $Al_{13}Cr_2$ peak in **Figure 5.9** is at grey-level 99 and is demarcated by grey-levels 83 - 101 at the dark and light ends of the spectrum respectively. In **Figure 5.13** the grey-levels between 83 and 101 are highlighted in green, which appear to be very similar to the Cr localisation seen in **Figure 5.8**. **Figure 5.14** is the highlighted grey-levels from **Figure 5.13** overlaid onto the Cr-localisation map obtained from EDX and presented in **Figure 5.8**. This confirms that the grey-level 83 to 101 correspond almost exactly to the Cr-localisation which allows a higher level of confidence in associating this grey level range with the $Al_{13}Cr_2$ phase.

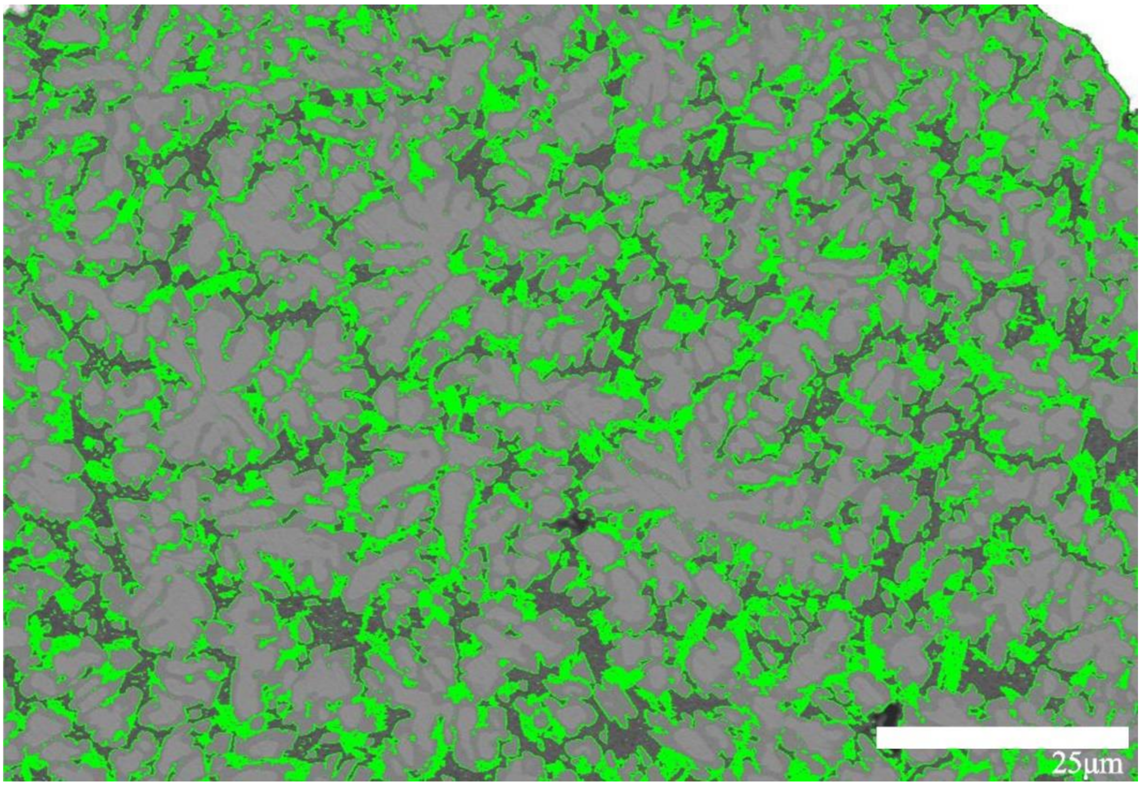

Figure 5.13 SEM backscattered micrograph from **Figure 5.6** with 83 – 101 grey-level highlighted in green.

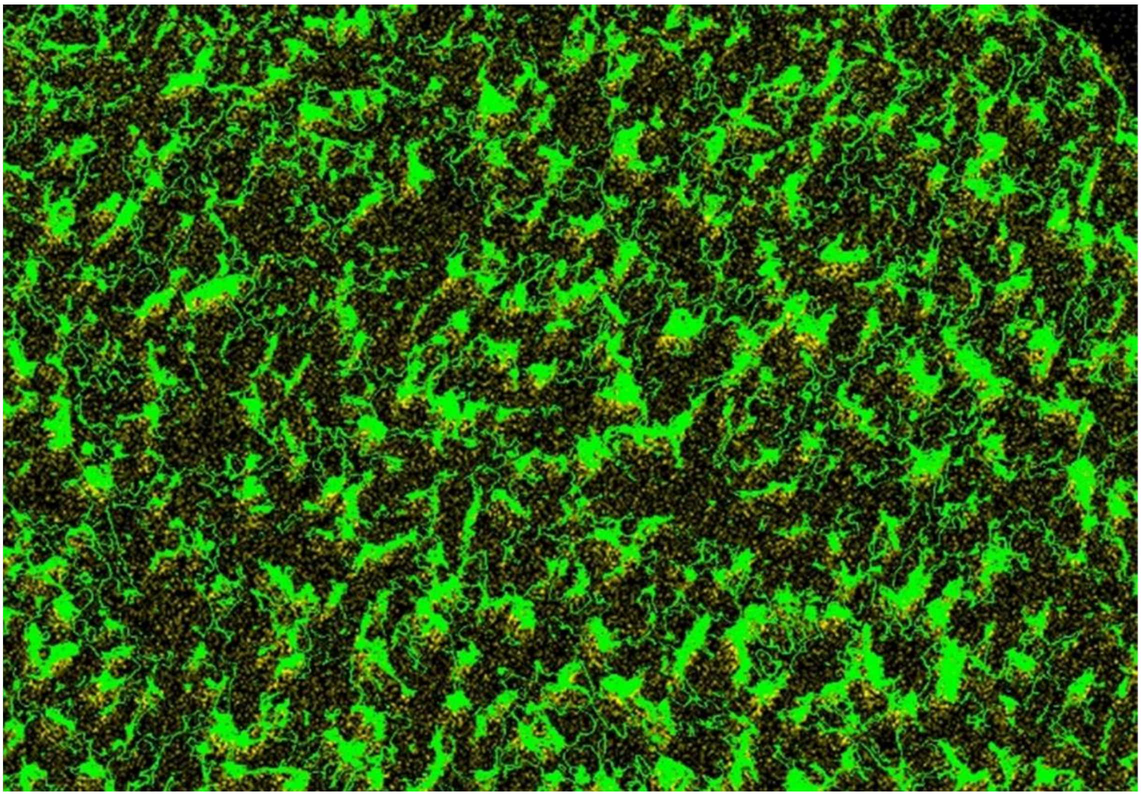

Figure 5.14 Grey-level data from **Figure 5.13** overlaid onto Cr localisation from **Figure 5.8**.

Furthermore, the grey-level that corresponds to the $Al_{13}Cr_2$ phase represents 21% of the total pixel count of **Figure 5.13**, therefore it is estimated that there is 21 vol.% of $Al_{13}Cr_2$ in the sample. When comparing this to the phase fraction data in **Table 5.2** the 16.8 wt.% of $Al_{13}Cr_2$ converts to 20.1 vol.% for the 212 - 150 μm size fraction. There were similar findings for the remaining two size fractions as the grey-level range for 106 -75 μm is 76 – 98, and for 75 – 53 μm it is 72 – 92. These represent 18.5% and 19.1% of the pixel counts respectively. If the data from **Table 5.2** is converted to volume % they would be 19.6 and 19.4 vol.% respectively. This result seems to agree well and allows greater confidence in the Rietveld refinement results.

With the higher amount of $Al_{13}Cr_2$ than could be accounted for, EDX point analysis was conducted on the $Al_{13}Cr_2$ phase to understand the composition of the phase. The findings of EDX point analysis can be found in **Table 5.3** where four spots were chosen for each size fraction of the Cr-doped samples. Standard error is presented in brackets. The Cr content found in the $Al_{13}Cr_2$ phase agrees with the amount of Cr added to the alloy, assuming all the Cr is located in the $Al_{13}Cr_2$ phase. It is noticeable that there is less Al in the $Al_{13}Cr_2$ phase than expected at stoichiometry, which would be 86.6% at.%. Consequently, the alloy is rich in Cr and Ni. The reason for the low Al content could mean that Ni is not only substituting for Cr but also Al, but it is more likely that the relatively large interaction volume during the EDX process produces this artefact. The large interaction volume could mean that a higher amount of Ni is being detected from the Al_3Ni phase that largely surrounds the $Al_{13}Cr_2$ phase. The results of further investigation on the composition of the $Al_{13}Cr_2$ phase using TEM techniques shall be presented in **Section 5.1.5**.

Table 5.3 Composition of $Al_{13}Cr_2$ for each size fraction of Al-23.5 at.% Ni-1.5 at.% Cr found via Point EDX analysis.

Spectrum	Atomic % (Standard error)		
	$150\mu m < 212\mu m$	$75\mu m < 106\mu m$	$53\mu m < 75\mu m$
Al	76.92 (3.19)	74.28 (9.17)	82.8 (7.43)
Cr	8.31 (5.83)	6.55 (2.92)	6.65 (2.39)
Ni	14.78 (5.83)	19.18 (10.65)	10.56 (5.33)

5.1.5 TEM and EDX

A TEM brightfield image can be seen in **Figure 5.15** for the Cr-doped Al-Ni alloy. At the high magnification and resolution that is available by the TEM the four phases can clearly be seen as different shades of colour. **Figure 5.15** has the 4 phases labelled: A) Al_3Ni_2, B) Al_3Ni, C) $Al_{13}Cr_2$, and D) Al-Al_3Ni eutectic. The same morphology found by SEM images is seen in the TEM image as the lightest Al_3Ni_2 phase is surrounded by the darker grey Al_3Ni phase. The black areas of the microstructure correspond to the eutectic phase and the fourth phase, $Al_{13}Cr_2$, relates to the dark grey regions. The location of the $Al_{13}Cr_2$ agrees with the hypothesis that $Al_{13}Cr_2$ is formed directly from the melt.

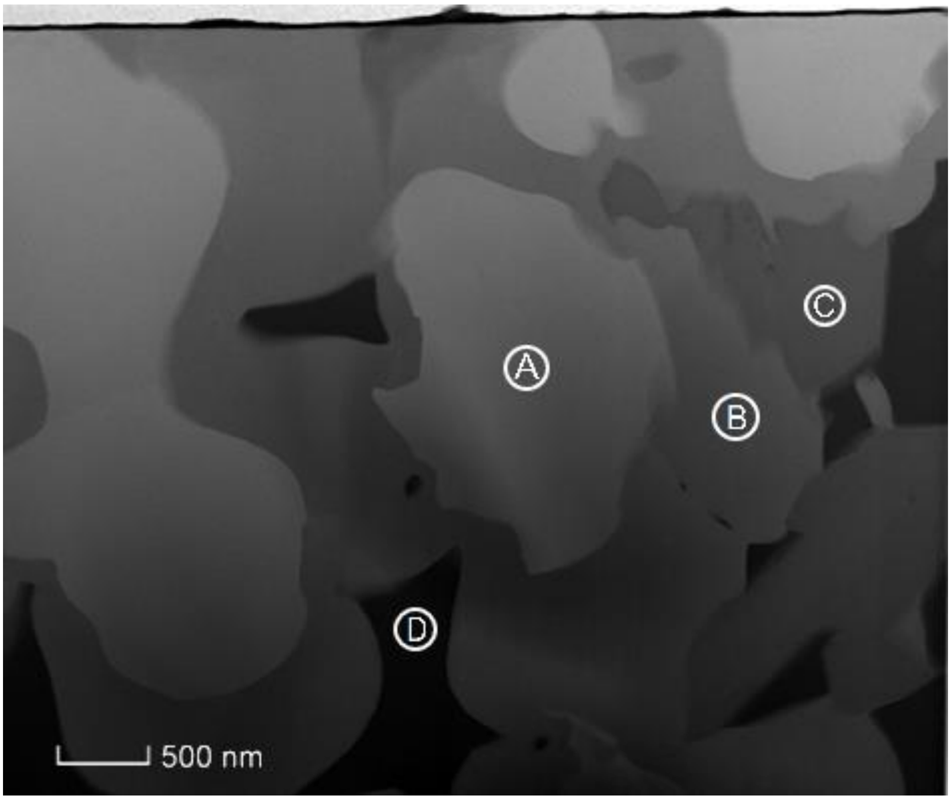

Figure 5.15 TEM brightfield image of Al-23.5 at.% Ni-1.5 at.% Cr alloy at 106 - 75 µm particle size fraction.

The high resolution of the TEM (operating at 300kV) also allowed the opportunity to study the Cr localisation within the entire microstructure. **Figure 5.16** shows the EDX Cr localisation in relation to the microstructure seen in **Figure 5.15**. Virtually all the Cr within the area of interest is found to be contained with the $Al_{13}Cr_2$ phase, with very small amounts elsewhere, this could be due to noise generated with a high accelerating voltage.

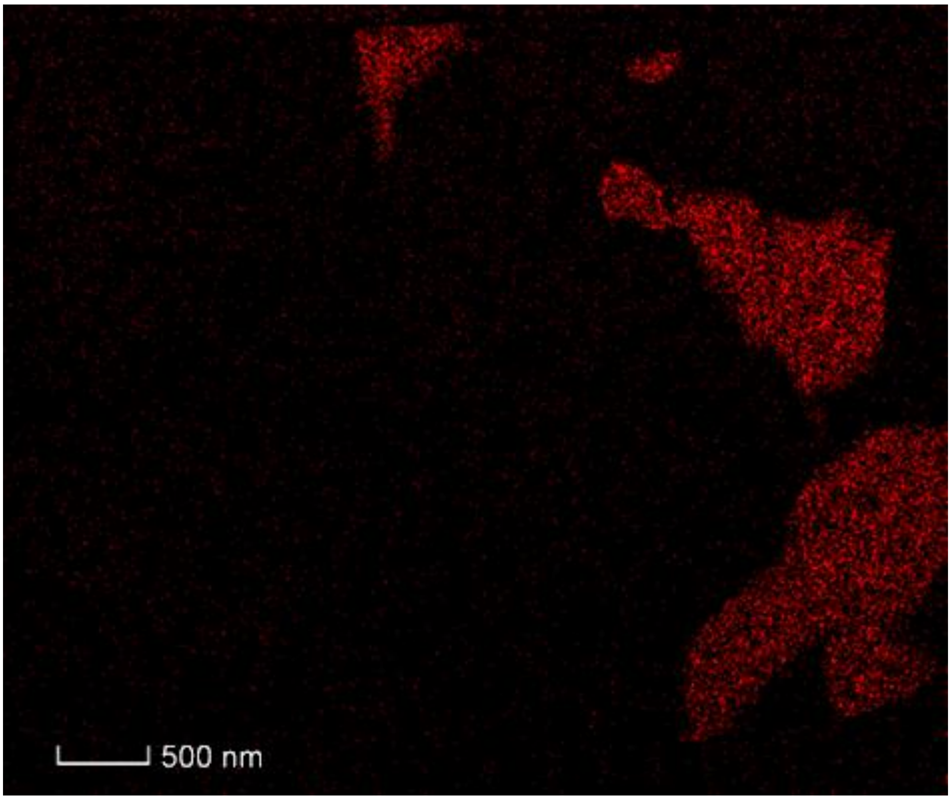

Figure 5.16 EDX Cr localisation map for **Figure 5.15**.

EDX linescans were also conducted on the sample to further understand the elemental composition of each phase. In **Figure 5.17** the area which underwent the EDX linescan is emphasised by the green rectangular box. This meant that the linescan could capture data across all 4 phases to allow for a greater understanding. **Figure 5.18** shows the results of the linescan across the selected area. The black line represents the recorded intensities of each phase. The three coloured lines represent the Al, Cr and Ni atomic composition within each phase (green, red and blue respectively). For the first phase, Al_3Ni_2, the elemental atomic composition seems to steady at close to 60% Al and 40% Ni, this is within the stoichiometric range of the compound determined from the phase diagram. Since the linescan begins from left to right it was able to record data from the earlier stages of solidification first, the inner-most part of the Al_3Ni_2 grain that was scanned shows a slightly higher Ni content and consequently lower Al content. This is considered to be due to the diffusive flux attracting Ni atoms more easily towards the beginning of Al_3Ni_2 formation. The second phase, Al_3Ni, is recorded from approx. 0.4 μm from the left and shows the typical 25/75 Al/Ni stoichiometry. The phase recorded from approx. 0.8 μm to 1.7 μm is the $Al_{13}Cr_2$ phase, it shows Al content to be slightly less than 80 at.% and Cr content to fluctuate around the 10-12 at.% range. Ni can also be seen in the linescan for this phase at around 10 at.% or slightly less. The final phase included in the linescan from **Figure 5.18** is the Al-Al_3Ni eutectic which shows a very high amount of Al and small amounts of Ni. Some Cr can also be seen in this phase which may have been leftover.

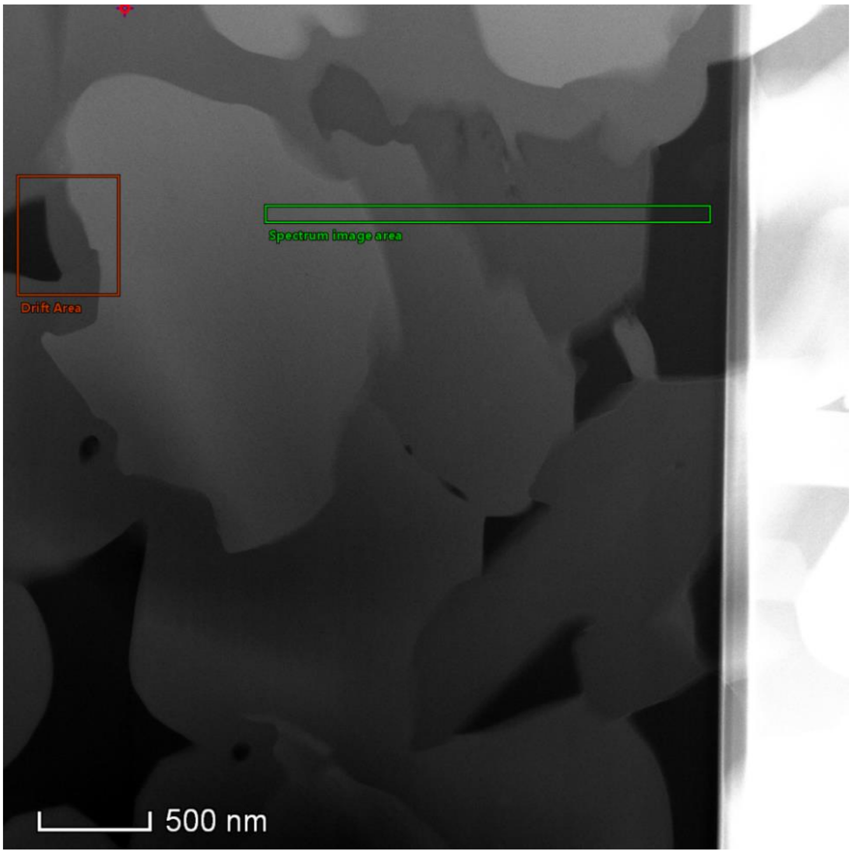

Figure 5.17 TEM brightfield image from **Figure 5.15** with green rectangular box illustrating linescan area.

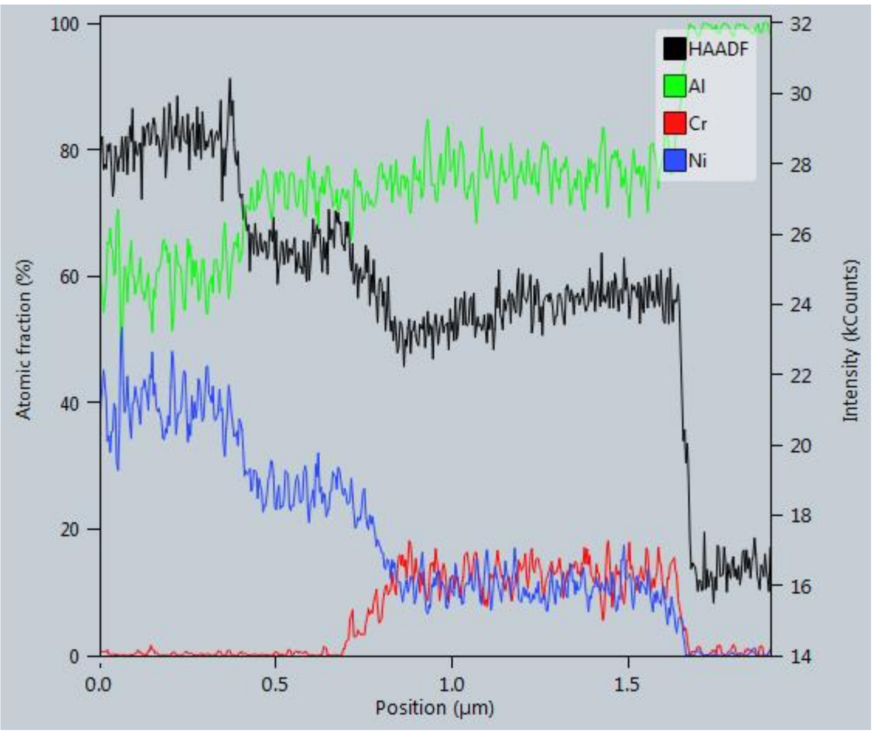

Figure 5.18 Elemental atomic fraction from linescan across entire sample morphology.

Figure 5.20 looks at the $Al_{13}Cr_2$ phase in further detail (highlighted in **Figure 5.19**) and confirms the elemental composition of Al, Cr and of course Ni. From the results Ni does appear to be present at the correct composition to allow substitution onto 40% of the Cr sites but the deficiency of Al may also be a cause for the presence of Ni. Quantitative data for the $Al_{13}Cr_2$ phase is presented in **Table 5.4**, in order to allow analysis of only the $Al_{13}Cr_2$ phase the region selected for the analysis was from 100 to 350 nm. The Cr composition appears to be stoichiometric as 13.57 at.% Cr is very close to the 13.33 at.% Cr expected to be found in the $Al_{13}Cr_2$ phase. Around 10.5 at.% deficiency of Al from stoichiometry can be seen which appears to be accounted for by Ni.

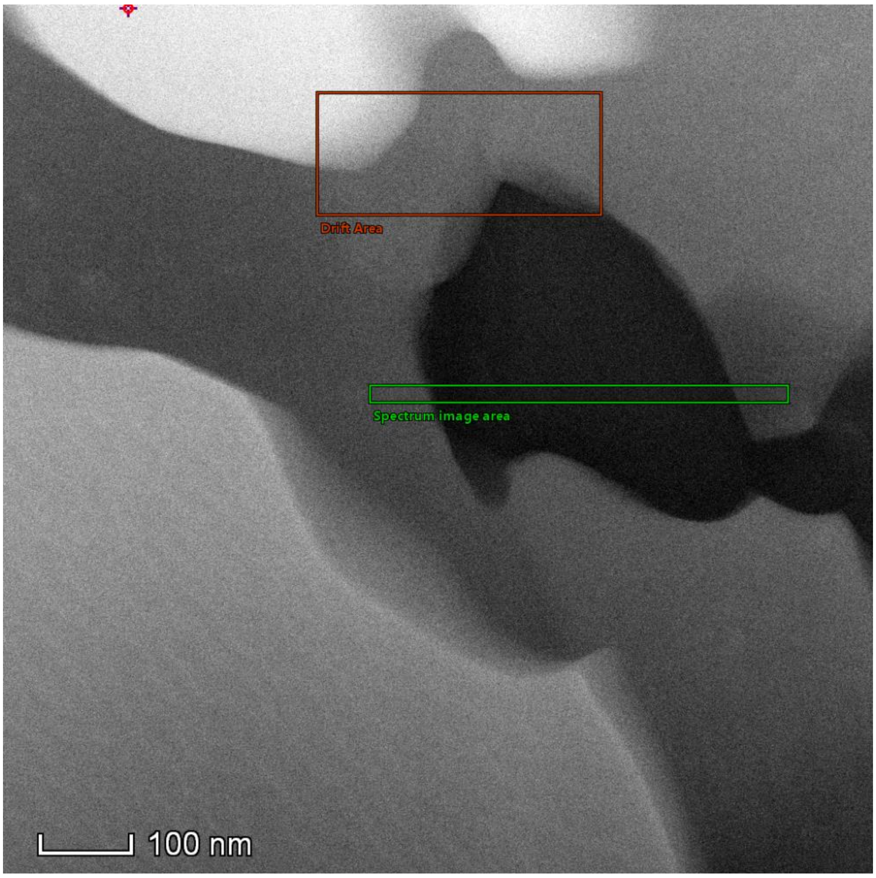

Figure 5.19 TEM brightfield image focusing on $Al_{13}Cr_2$ phase with green rectangular box illustrating linescan area.

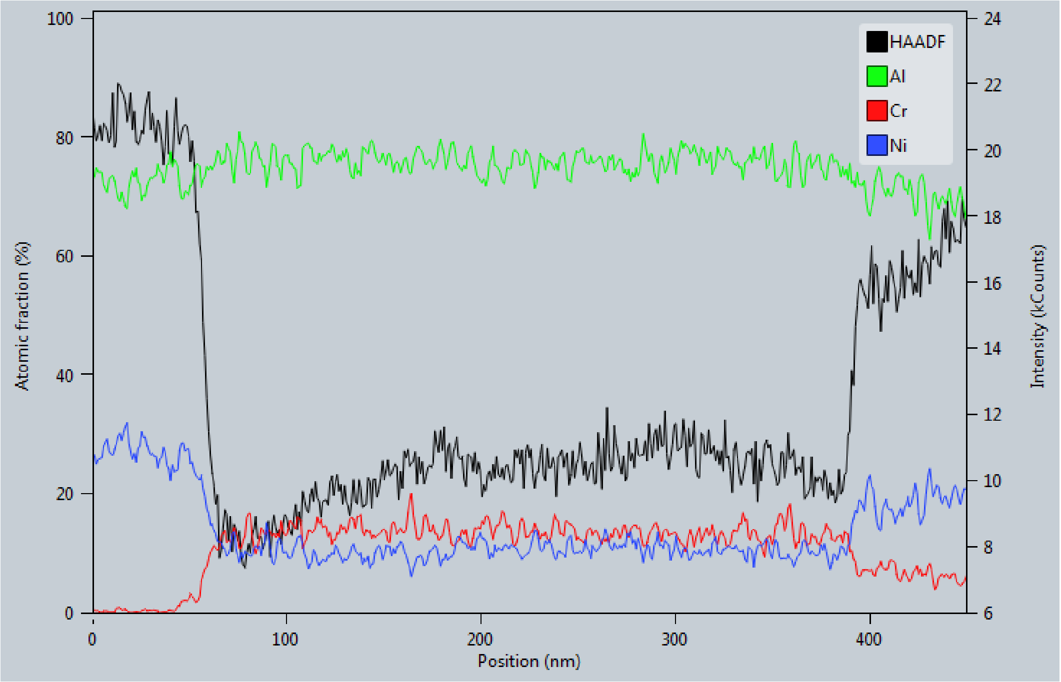

Figure 5.20 Elemental atomic fraction from linescan across the $Al_{13}Cr_2$ phase.

Table 5.4 Quantitative data for plateau section of $Al_{13}Cr_2$ phase in **Figure 5.20** from 100-350 nm.

	Atomic %		
	Average	Median	Standard Deviation
Al	75.96	76.01	1.79
Cr	13.57	13.52	1.5
Ni	10.45	10.53	1.36

Further analysis will be presented in **Chapter 6 Discussion**.

A TEM selected area diffraction (SAD) pattern was obtained for the $Al_{13}Cr_2$ phase in order to further understand the somewhat unknown phase. The SAD pattern can be seen in **Figure 5.21** which shows an abundance of superlattice spots. The superlattice spots would support the understanding that the phase is chemically ordered. The SAD patterns was indexed to the ICDD crystallographic data file with the following reference number: 00-029-0014. Interestingly the SAD pattern in **Figure 5.21** may also be indexed to the $Al_{45}Cr_7$ data list (reference number: 04-004-3588) with very similar d spacings and peak intensities, and so it is therefore inconclusive which compound designation is the correct one.

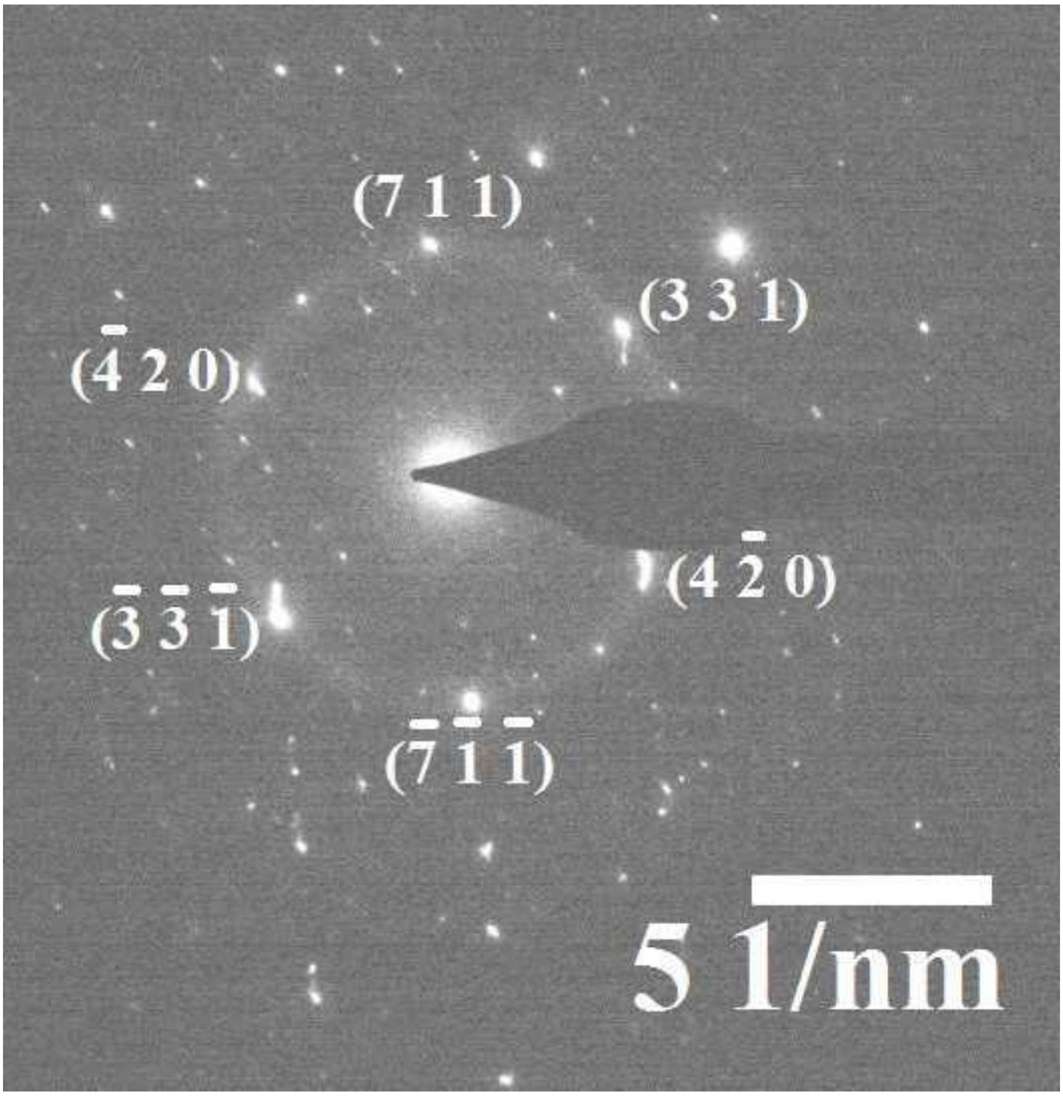

Figure 5.21 Selected Area Diffraction pattern of $Al_{13}Cr_2$ phase.

5.2 SiGe

Results from the characterisation techniques conducted on Si-Ge samples are presented in this section. CALPHAD modelling was also conducted for the Si-Ge samples and are presented in **Section 5.2.1**. SEM measurements with EDX point measurements are presented in **Section 5.2.2** followed by EBSD. The EBSD results are presented in **Section 5.2.3**. The TEM section is **Section 5.2.4**. Finally, the EDX linescans conducted using the TEM and SEM are presented in **Sections 5.2.5** and **5.2.5.1** respectively.

5.2.1 CALPHAD Modelling

A Scheil calculation was conducted for Si-Ge with a starting composition of 30 wt.% Ge. **Figure 5.22** shows the solid fraction as a function of temperature as the liquid alloy cools. The elemental concentration can also be seen in **Figure 5.23**, this is a function of solid fraction where diffusivity is assumed to be 0 in the solid fraction and infinite in the liquid. It is noticeable that the solid fraction seems to increase relatively quickly to begin with at approx. 0.0374 K^{-1}, and the increase concentration of Ge in the forming solid fraction to begin with is rather slow. This would suggest the early solidification of Si which is in line with the solidification sequence as Si has a higher melting point. The first solid fraction to be formed is expected to contain 85.3 wt.% Si and 14.7 wt.% Ge.

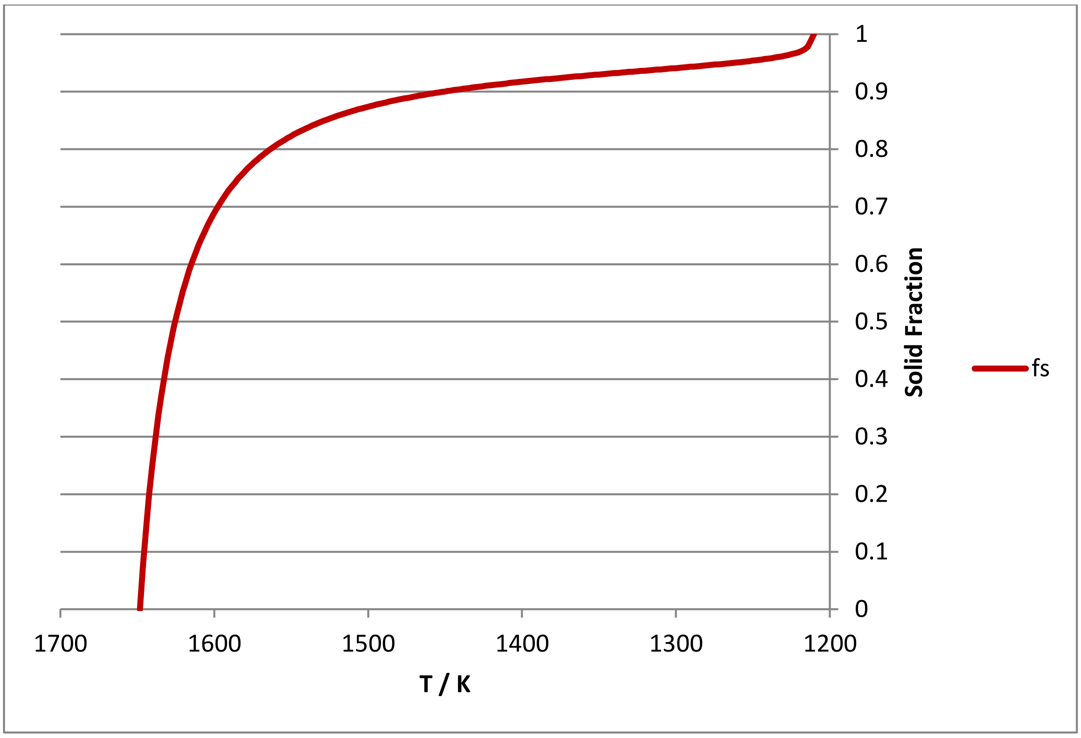

Figure 5.22 Scheil solidification sequence of the growing solid fraction as a function of temperature.

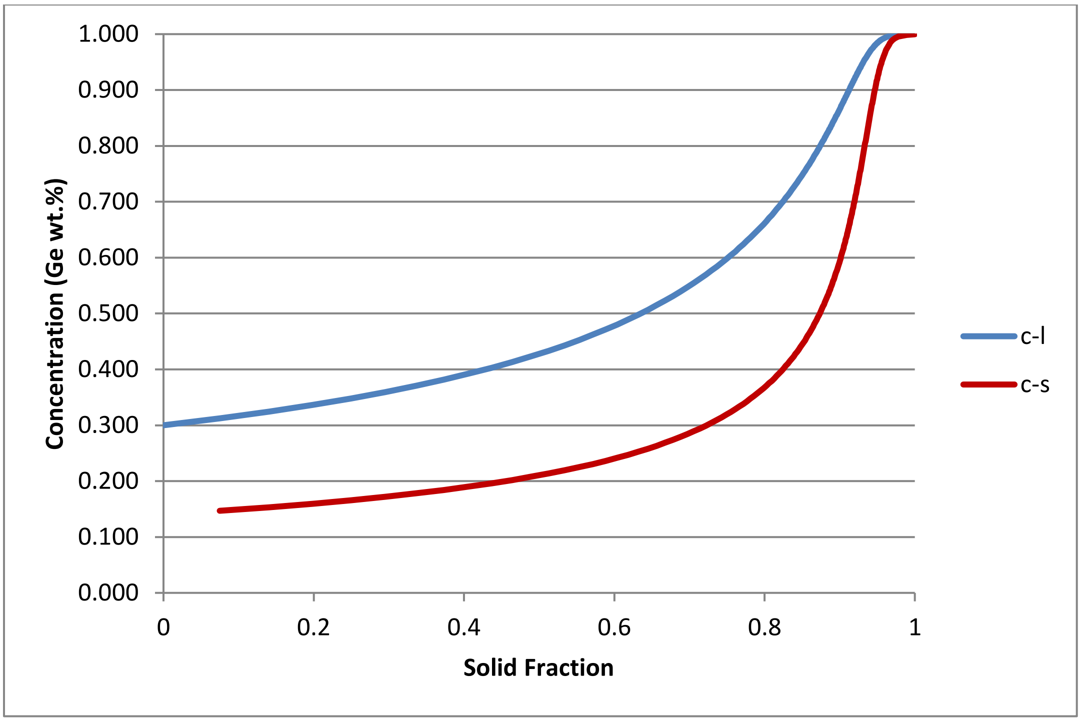

Figure 5.23 Scheil solidification calculation of Ge composition in the growing solid fraction during solidification.

As the temperature decreases the rate at which the solid fraction is formed is expected to slow down until it approached around 0.000221 K^{-1} at 0.93 solid fraction, with more Ge being solidified within the solid fraction. By this point the solid fraction being formed is expected to contain between 81-85 wt.% Ge. The increase in Ge within the solid fraction is attributed to the fact that most of the Si has already been solidified as the concentration of Ge within the liquid is over 95 wt.%. As the solid fraction approaches 1 the rate at which it is formed increases heavily as the remaining liquid is increasingly Ge-rich and so the last parts of the microstructure expected to form would contain the highest concentration of Ge (approaching almost 100% Ge concentration).

The predicted concentration of the solid and liquid fractions observed by the Scheil calculation agree with the partitioning observed using the phase diagram, this is because the partition coefficient, k, used in the Scheil calculation is obtained from the phase diagram . The partitioning tie-lines (blue dotted lines) for the first and last stage of formation are displayed in **Figure 5.24** for Si-30 wt.% Ge (red line). It is apparent that the liquid composition during the earliest stages of formation (top image), denoted as C_l, is close to the predicted 30 wt.% Ge, the tie-line has been placed slightly lower for illustration, but the immediate concentration of the liquid would be

30 wt.% Ge as this is the starting composition for the melt. In the top image the composition of the first solid to form is denoted by C_s and this is predicted to be around 14 wt.% Ge, which agrees with the Scheil calculation. The lower image illustrates the partitioning for the later stage of solidification as the liquid composition is 90 wt.% Ge the solid composition would be predicted to be around 66 wt.% Ge. This is also in good agreement with the Scheil calculation which suggests great confidence in the calculation.

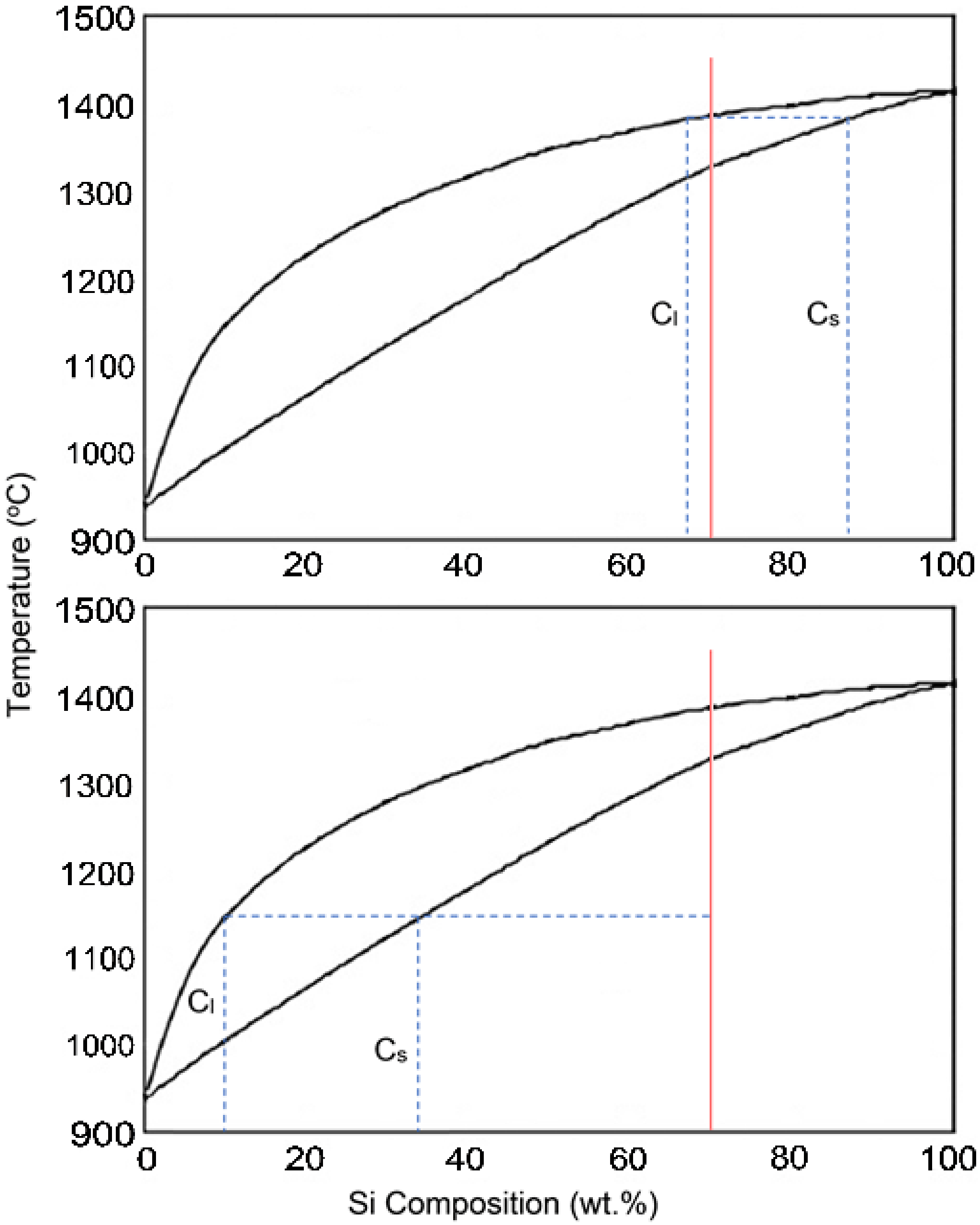

Figure 5.24 Partitioning illustrated on Ge-Si phase diagram using tie-lines.

5.2.2 SEM and EDX Point Microstructure Characterisation

Before drop tube processing was conducted on the Si-Ge samples a section of the starting ingot was removed for characterisation against the rapidly solidified samples. **Figure 5.25** shows the SEM backscattered micrograph for the starting sample. A heterogeneous microstructure can be seen with significantly varied Ge content in some regions. During the drop tube process a small amount of the melted material remained in the crucible and is referred to as the ‘residual’ material. The microstructure of the residual material is presented in **Figure 5.26**. The residual material also exhibits a heterogeneous microstructure with significantly varied Ge content in some regions.

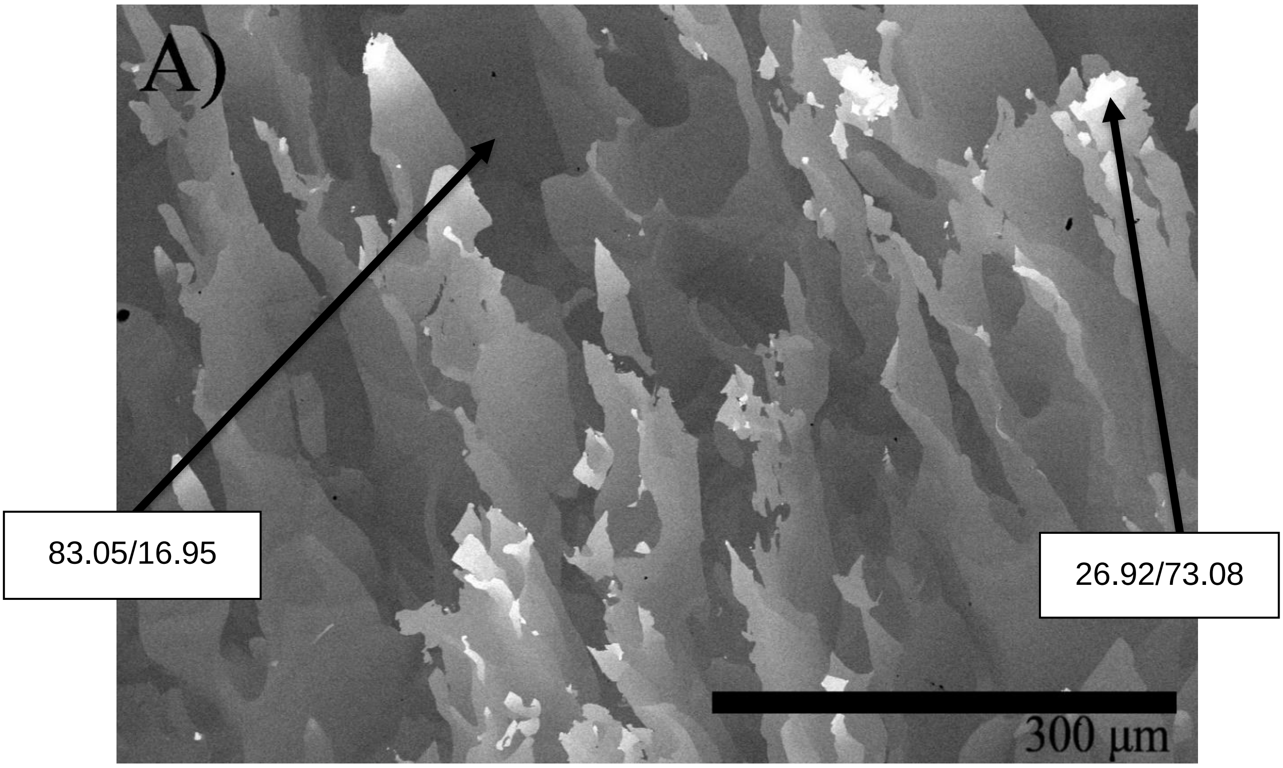

Figure 5.25 SEM backscattered micrograph with EDX point measurements of starting material.

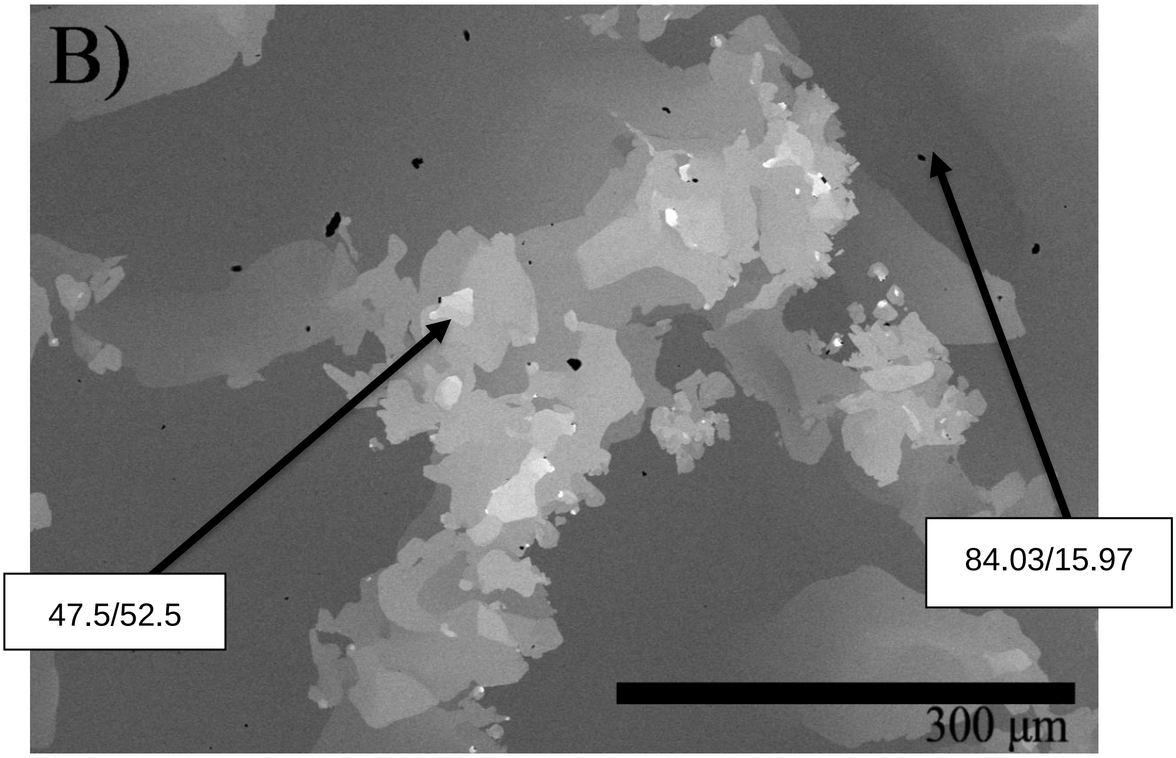

Figure 5.26 SEM backscattered micrograph with EDX point measurements of crucible residual material.

SEM backscatter micrographs are presented in **Figures 5.27**, **5.28**, **5.29**, **5.30**, and **5.31** for the > 850 μm size fraction through to the 212 - 150 μm size fraction of rapidly solidified Si-Ge samples. These figures illustrate the effect on the microstructure that the cooling rate has during drop tube processing. All of the microstructures presented for the rapidly solidified samples display the same features in a gradual manner based on their respective cooling rates. Further discussion shall be presented in **Section 6.2**. A greater inhomogeneity can be seen in the rapidly solidified samples than in the residual and starting materials, as the length scale is refined the partitioning is more pronounced. This may be due to the high cooling rate suppressing back diffusion. There appears to be many relatively large Si grains which are decorated by the Ge that is localised at the grain boundaries. Upon further examination the Ge localised on the boundaries on the Si grains appear to have formed into apparent grains as well. The Si-rich and apparent Ge-rich grains illustrate a bimodal grain size distribution. Zhang et al. [107] and Nagai et al. [108] found similar findings with partitioning occurring and Ge localising at the grain boundaries of the Si grains, but there was no reports of a bimodal distribution with Si-rich and apparent Ge-rich grains. Another interesting finding among the rapidly solidified samples is the formation of consistent grains at higher cooling rates. As the cooling rate is increased the size of grains seems to appear increasingly similar to one another (**Figure 5.30** and **5.31**), this is contrasting in the slower cooled drop tube processed samples (**Figure 5.27** and **5.28**) where grains of varied sizes are found. Several light crosses can be seen in the large Si-rich grains and are predicted to be as a result of coring indication the early stages of dendrite formation. These coring features are marked out on **Figures 5.29**, **5.30**, and **5.31** by red circles, but they are easily visible elsewhere within each micrograph. Ge-rich Regions

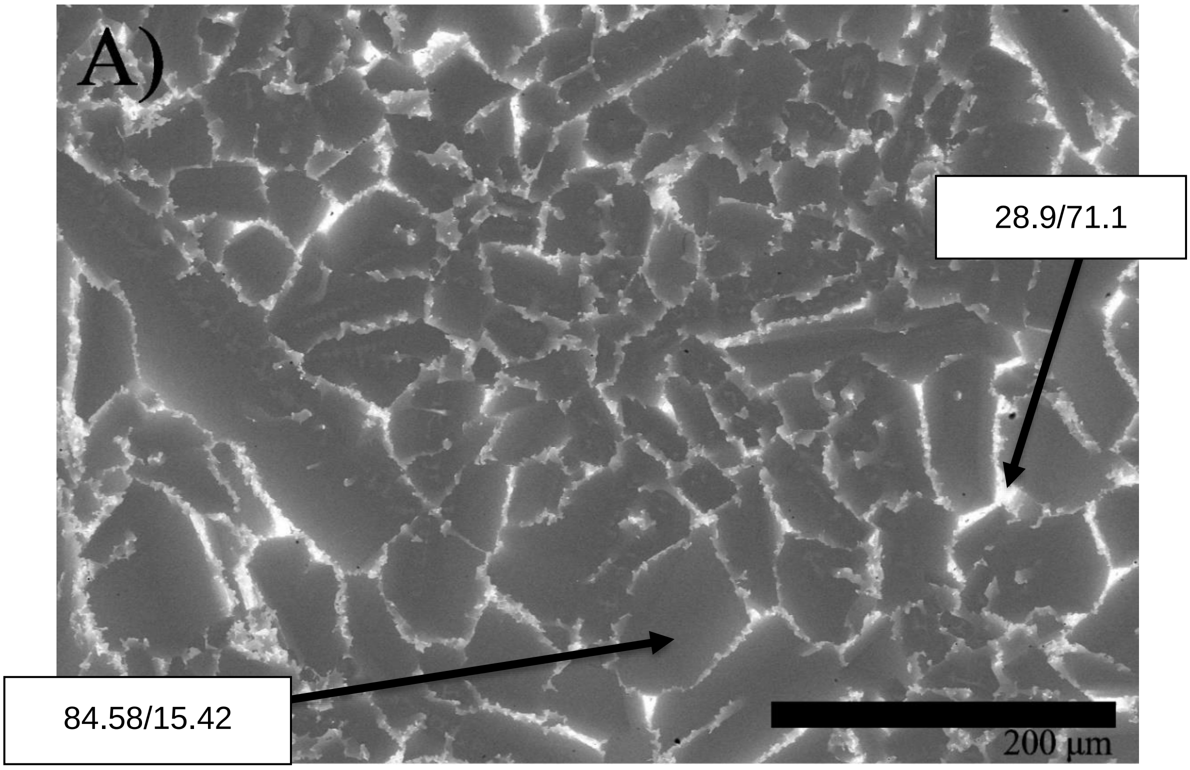

Figure 5.27 SEM backscattered micrograph with EDX point measurements of rapidly solidified samples with particle size fractions of > 850 µm.

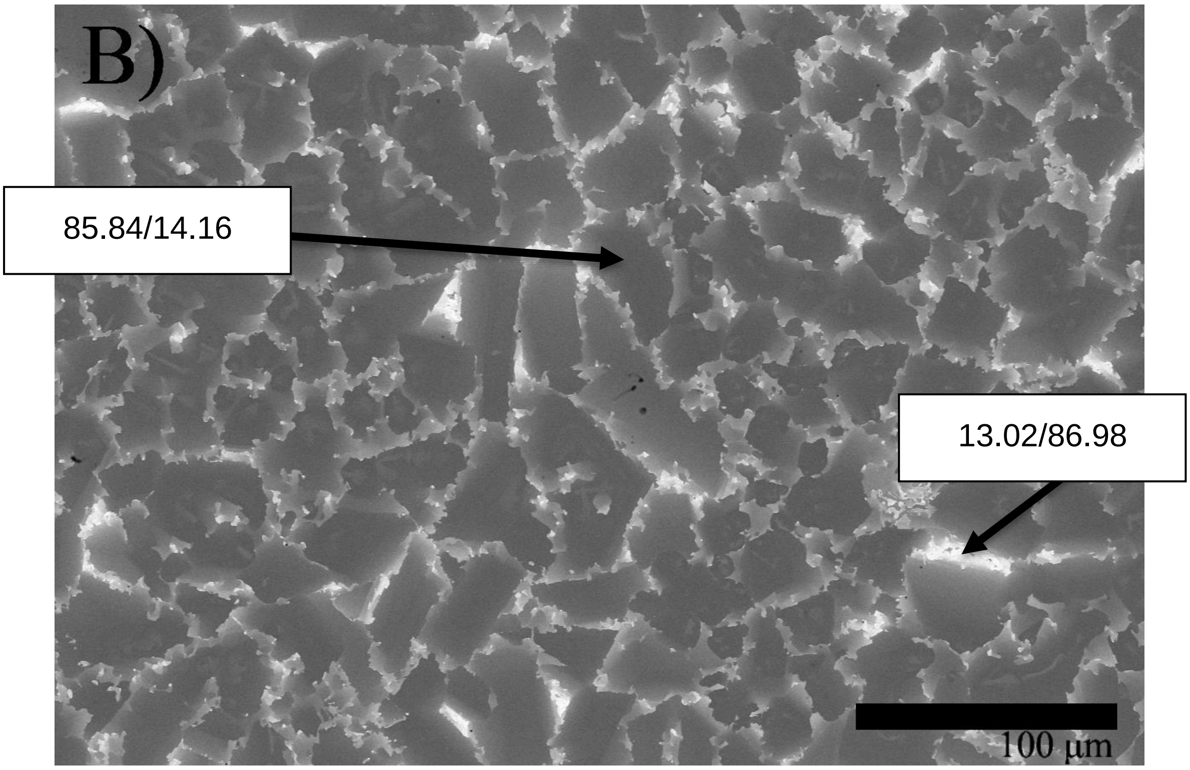

Figure 5.28 SEM backscattered micrograph with EDX point measurements of rapidly solidified samples with particle size fractions of 850 - 500 µm.

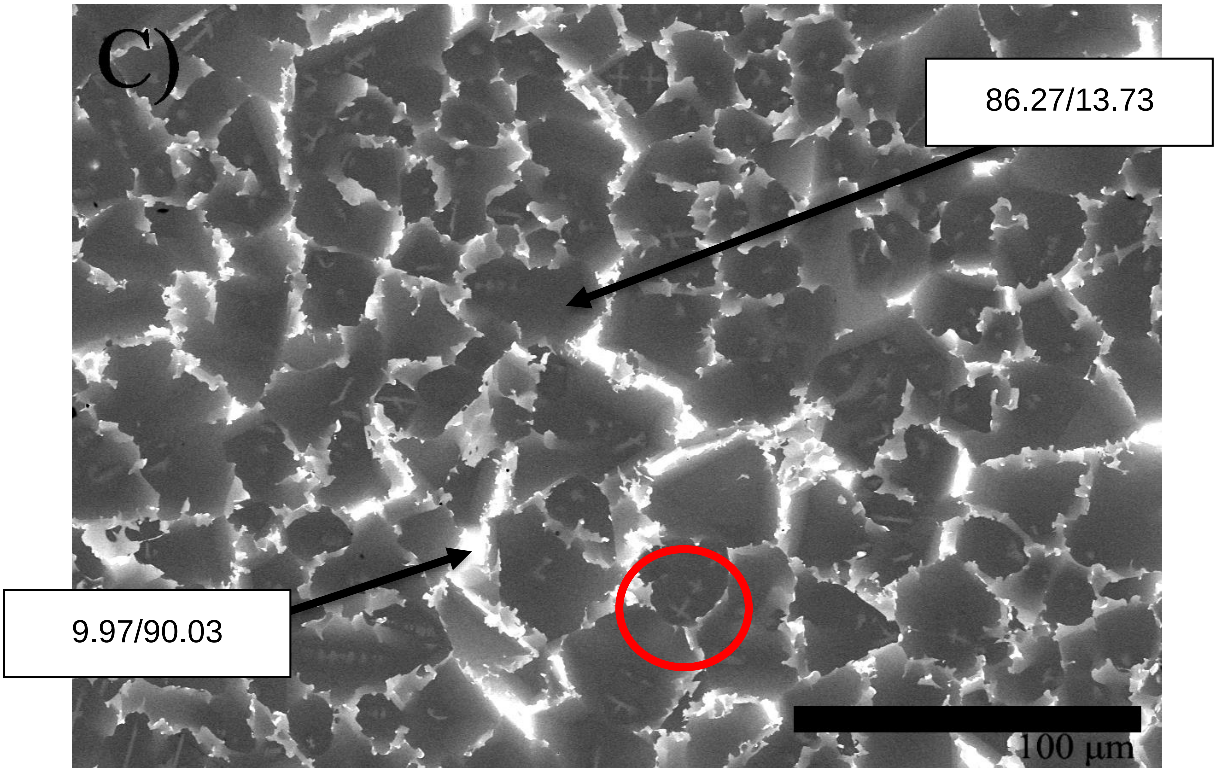

Figure 5.29 SEM backscattered micrograph with EDX point measurements of rapidly solidified samples with particle size fractions of 500 - 300 µm.

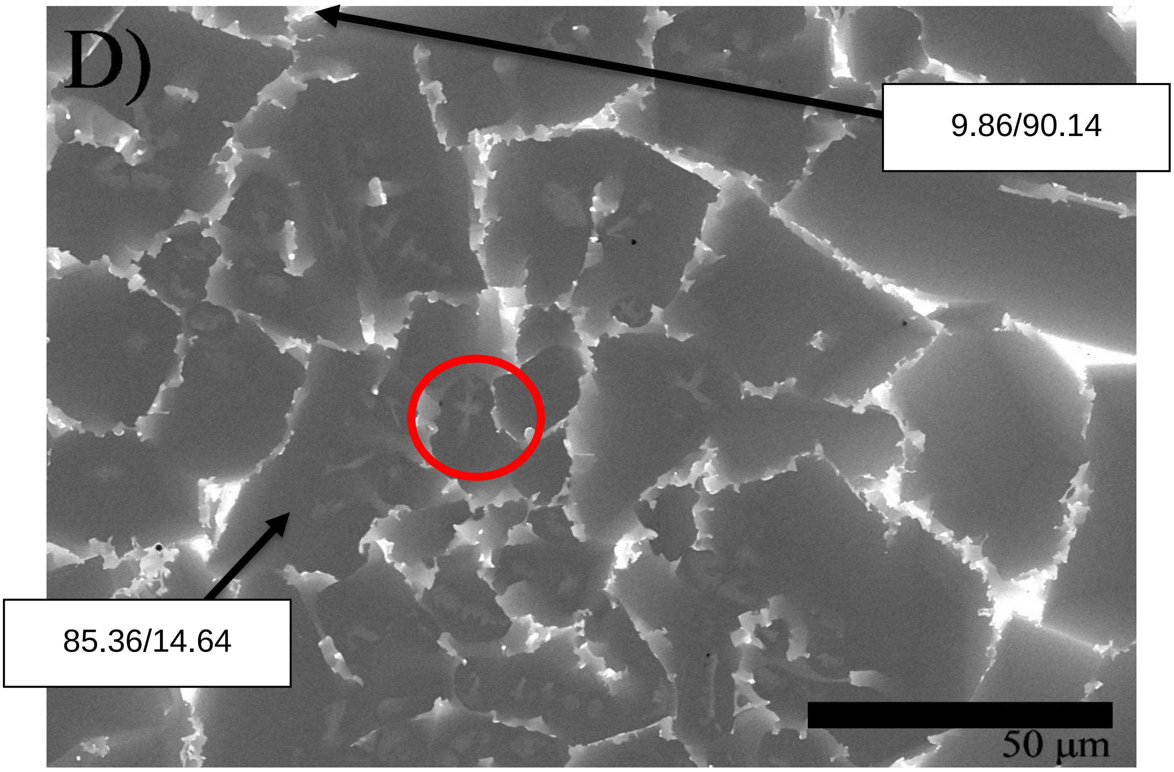

Figure 5.30 SEM backscattered micrograph with EDX point measurements of rapidly solidified samples with particle size fractions of 300 - 212 µm.

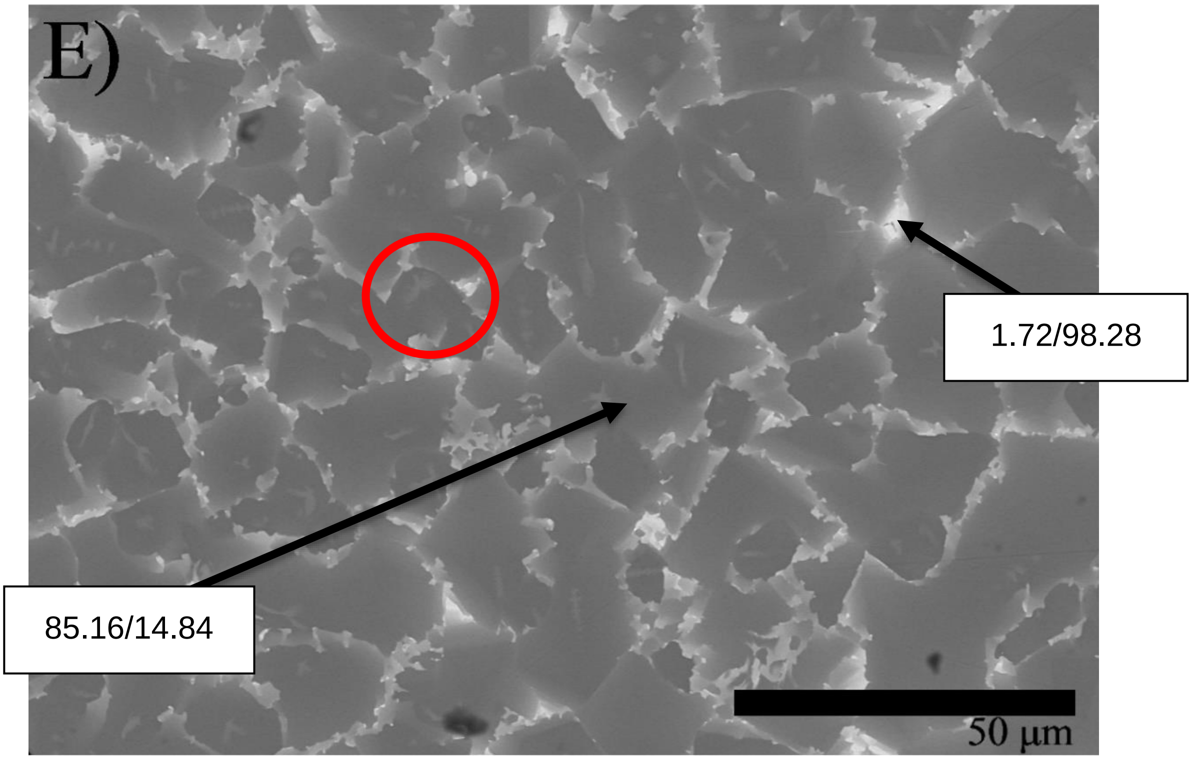

Figure 5.31 SEM backscattered micrograph with EDX point measurements of rapidly solidified samples with particle size fractions of 212 - 150 µm.

5.2.2.1 EDX Point Measurements

EDX was conducted on all samples which indicated the same bulk elemental composition (± 2 wt. %). Regions of maximum Si and Ge concentrations were detected using EDX maps and then point measurements were conducted. **Figures 5.25**, **5.26**, **5.27**, **5.28**, **5.29**, **5.30**, and **5.31** are all labelled with elemental composition in wt.% of Si/Ge. The high level of partitioning in the rapidly solidified sample is confirmed by the EDX point measurements as the Si-rich grains show a greater composition of Si at maxima than the original starting alloy. Ge composition in the apparent Ge-rich grains is consistently higher than 70% which also suggests a high level of partitioning. **Figures 5.32** and **5.33** graphically show the wt.% of Si and Ge at the Si-rich and Ge-rich regions respectively of all of the rapidly solidified samples. From **Figure 5.32** it can be seen that the wt.% of Si at maxima remains relatively consistent across all cooling rates but in **Figure 5.33** Ge-rich regions appear to be increasingly Ge-rich as the cooling rate is increased. This illustrates the increase of partitioning that is observed as a result of increased cooling rate. The partitioning would also go some way in helping to understanding the dendrite fragments visible within some grains as a high diffusive flux is expected to have taken place. The high diffusive flux would be a result of the Ge being diffused away from the Si-rich solid fraction that is formed early during solidification.

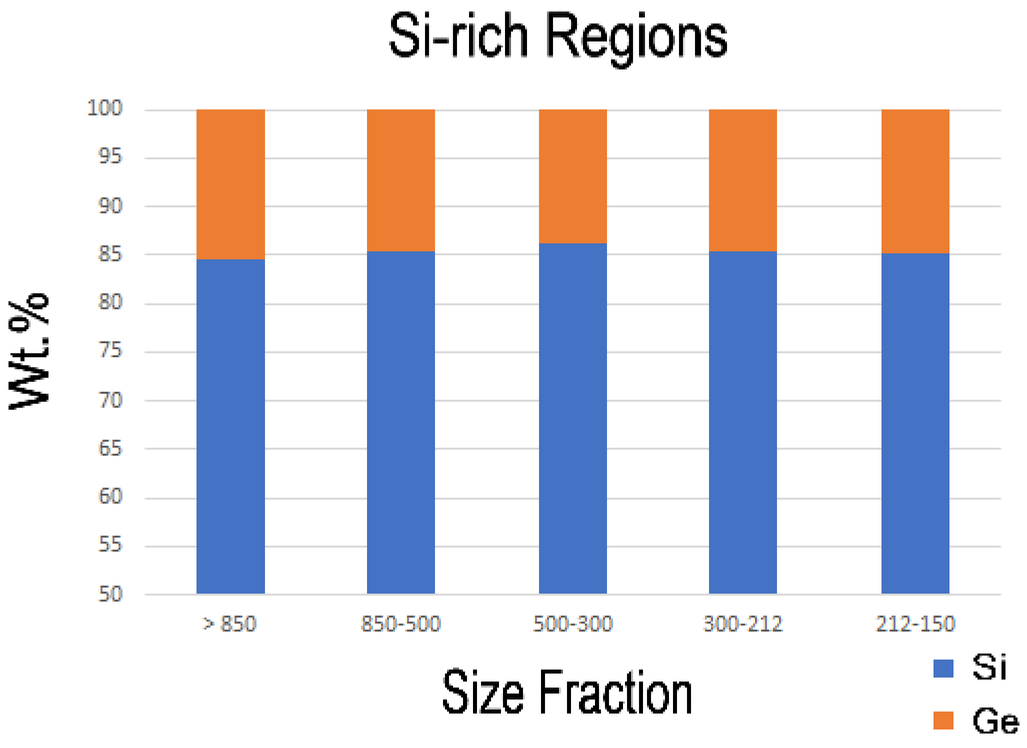

Figure 5.32 EDX point measurements presented in wt.% obtained using SEM of Si-rich regions for rapidly solidified Si-Ge samples.

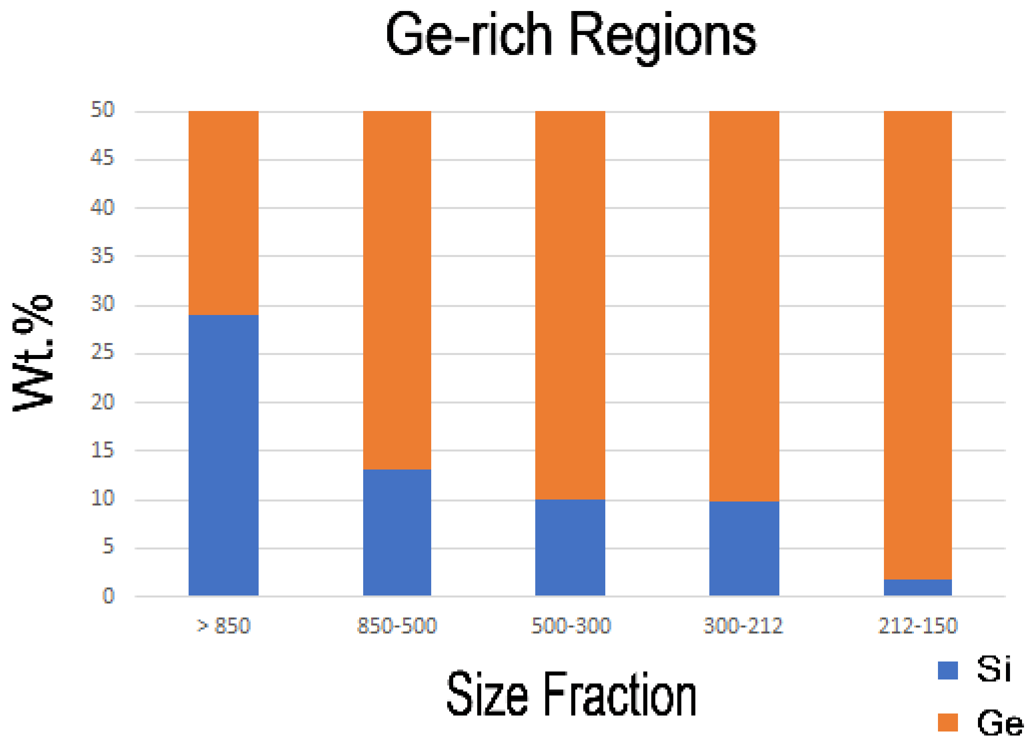

Figure 5.33 EDX point measurements presented in wt.% obtained using SEM of Ge-rich regions for rapidly solidified Si-Ge samples.

5.2.2.2 Grain Size Analysis

An area of interest with the SiGe samples was the grain size distribution because of changing cooling rates. Grains were identified, and the measurement of apparent grain areas can be found in **Table 5.5**.

Table 5.5 Average area, in μm^2, of A) Si-rich grains, B) Apparent Ge-rich grains and C) Overall average grain area observed in N number of SEM backscatter micrographs.

Grain area distribution		Average grain area in [μm^2] (and standard error)		
		Si-rich grains	Apparent Ge-rich grains	Overall average
850 μm < d	$N=3$	844.57 (93.73)	60.74 (6.95)	264.04 (13.54)
500 μm < d < 850 μm	$N=4$	812.02 (229.61)	40 (3.39)	192.26 (20.97)
300 μm < d < 500 μm	$N=3$	679.4 (10.22)	24.0 (0.72)	132.81 (4.87)
212 μm < d < 300 μm	$N=4$	467.31 (70.62)	17.51 (0.35)	102.47 (3.84)
150 μm < d < 212 μm	$N=3$	321.81 (30.79)	9.75 (0.65)	65.21 (2.44)

Si-rich and Ge-rich regions were assumed to be independent grains, so the ImageJ software was tasked to identify these separately. In order to quantitatively differentiate the Si-rich regions to the Ge-rich regions each SEM backscattered micrograph was analysed for the grey-level histograms. For each image a region of shifting contrast was observed, as this indicated a sudden change in atomic density. **Figure 5.34** illustrates an example of this region that was quantitively identified and used as a threshold. Once the threshold had been selected a margin was used to avoid any overlap from the Si-rich and Ge-rich apparent grains. For all of the micrographs used the margin was determined to be between 5 and 10 grey-level, an example of a margin selected can also be seen in **Figure 5.34** which has been marked with white lines. The larger peak to the right of the right hand side line was determined to be Si-rich apparent grains, and all of the grey-level the left of the left hand side line was determined to be Ge-rich apparent grains. When

EBSD findings (**Section 5.2.3**) suggested that Ge-rich regions are not independent grains the grain area distribution analysis was reattempted, but the ImageJ software was not able to accurately identify the grain boundaries.

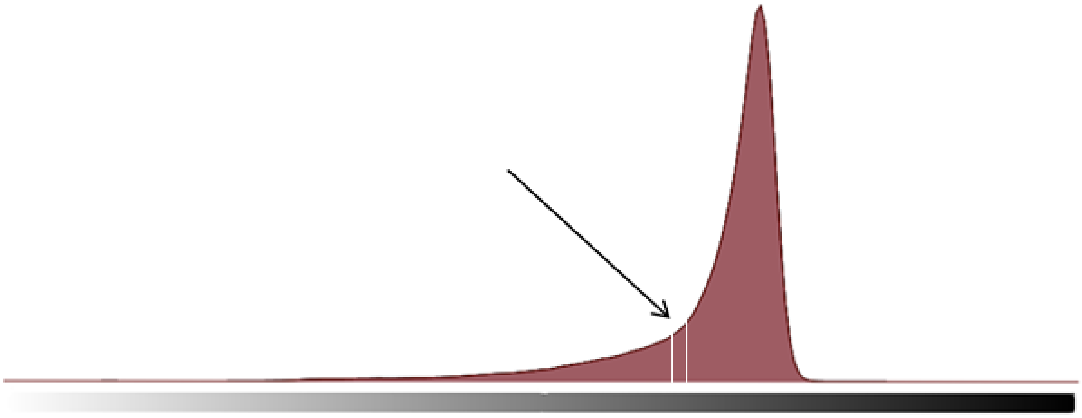

Figure 5.34 Example grey-level histogram illustrating threshold chosen to conduct grain size analysis.

Several SEM images (N) were used and the grain areas were identified, these are found in **Table 5.5** in μm^2, with the number of images used for each particle size fraction shown in column 2. Standard error can also be found in brackets beside each recording. Ultimately **Table 5.5** does not show the true grain areas, this is due to the findings presented in EBSD section: **Section 5.2.3**. Ge-rich regions are found to form as a continuation of the Si-rich regions as the same grain. The data in **Table 5.5** does give reliable insight into the grain size distribution within rapidly solidified SiGe samples at varied cooling rates. In all cases the Si-rich, Ge-rich and total grain areas decrease as the cooling rate is increased. For Si-rich grains the data is illustrated in **Figure 5.35** showing the change in grain area as a result of varying cooling rates, this includes the crucible residual sample that was cooled at approx. 0.3 Ks^{-1}.

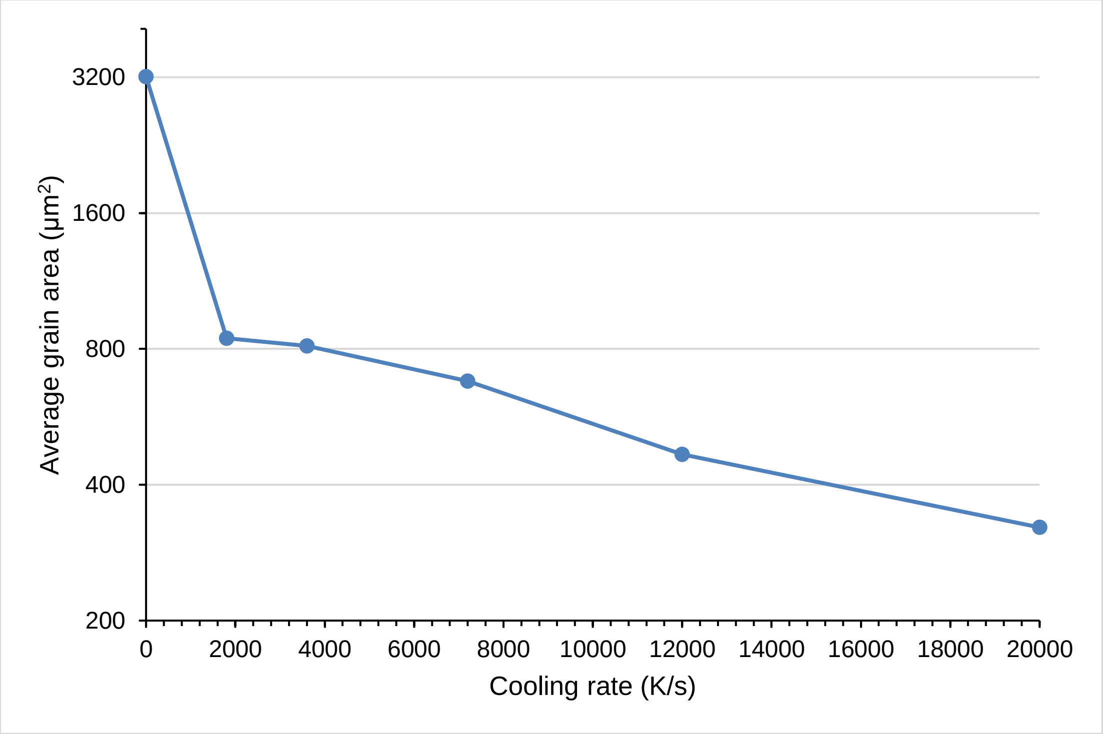

Figure 5.35 Average grain area data from **Table 5.5** of Si-rich grains as a function of cooling rate.

An example of the binary images from ImageJ after Si-rich and Ge-rich regions were detected can be found in **Figures 5.37** and **5.38**, with **Figure 5.36** being the reference image.

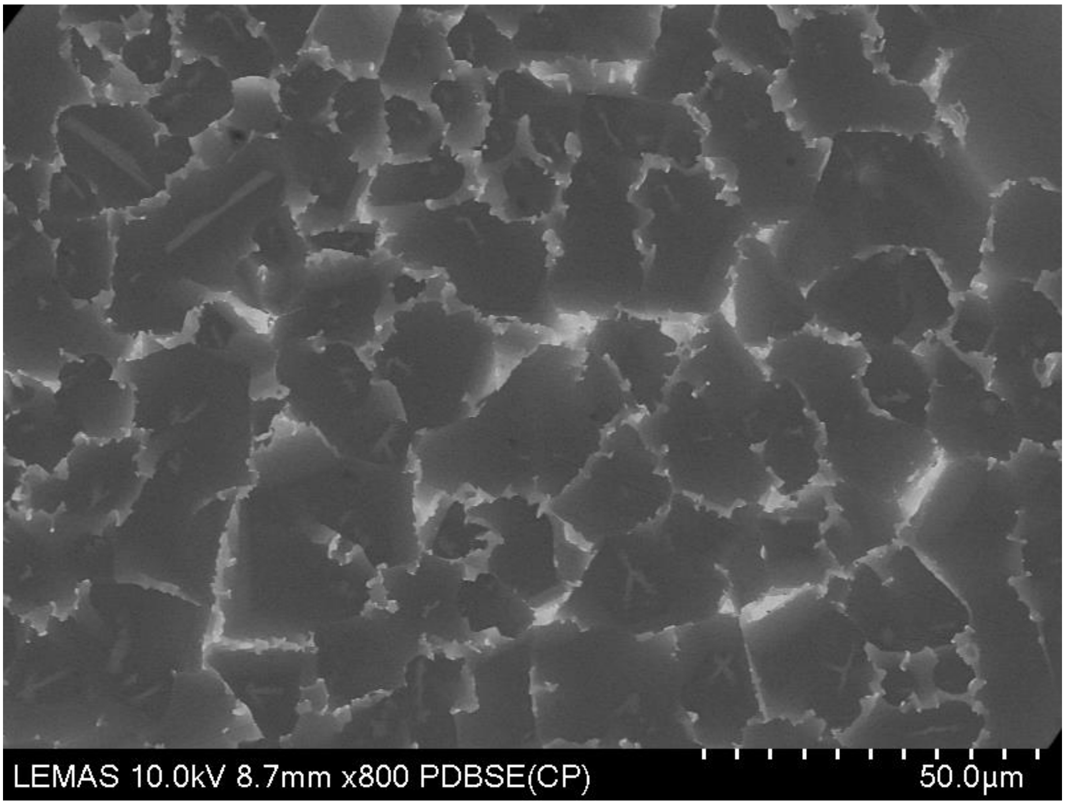

Figure 5.36 Example SEM backscattered micrograph of 212 - 150 µm Si-Ge sample to illustrate grain size analysis.

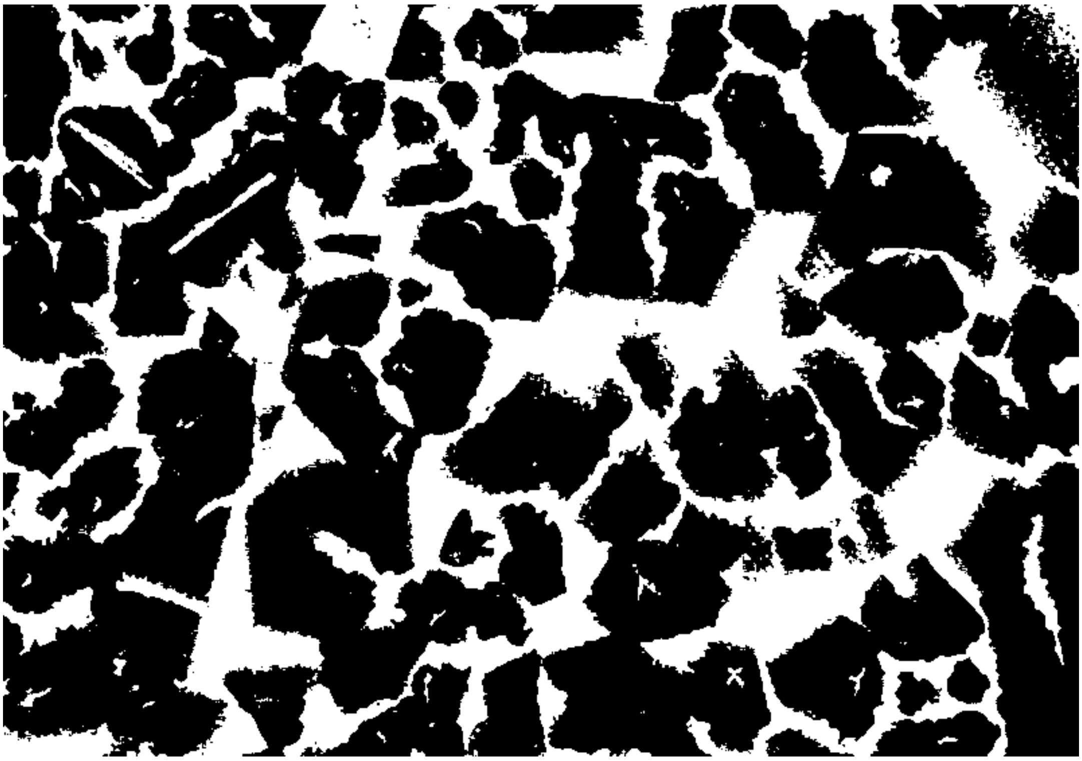

Figure 5.37 Binary image obtained using SEM micrograph from **Figure 5.36** in ImageJ highlighting the detection of Si-rich grains.

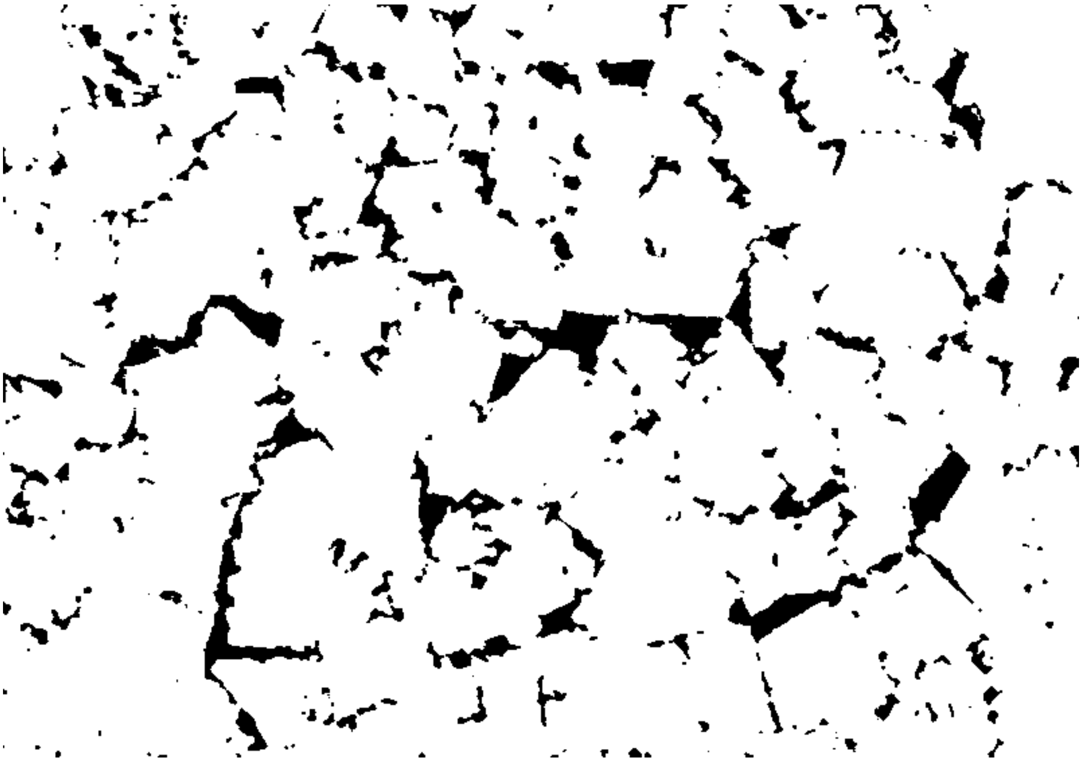

Figure 5.38 Binary image obtained using SEM micrograph from **Figure 5.36** in ImageJ highlighting the detection of Ge-rich apparent grains.

5.2.3 EBSD

The interest in crystal orientation emerged from the SEM backscattered micrographs where the Ge-rich regions appeared to be grains independent from the Si-rich regions. This revelation had not previously been characterised despite similar morphology being reported by Zhang *et al.* and Nagai *et al.* [107] [108].

Figures 5.39 and **5.41** show the crystal orientation mismatch by a series of contrasting colours and it is immediately apparent, from observing the reference image in **Figures 5.40** and **5.42**, that the Si-rich regions make up most of the grain morphology. It can also be seen that the crystal orientation boundaries ignore the Ge-rich region indicating that they are not formed as independent grains but instead by epitaxial growth from the Si-rich grains, this can be seen at, but not limited to, the regions that have been labelled by arrows. The Ge-rich regions still appear at the edges of grains, but partitioning is not influenced by growth direction which appears random in all directions.

It is also apparent in that the grain orientation map in **Figure 5.41** shows extensive twinning which may be due to that particular particle experiencing a lower growth undercooling hence being more faceted. Growth twins would then occur to help atom attachment at the faceted Si/L interface.

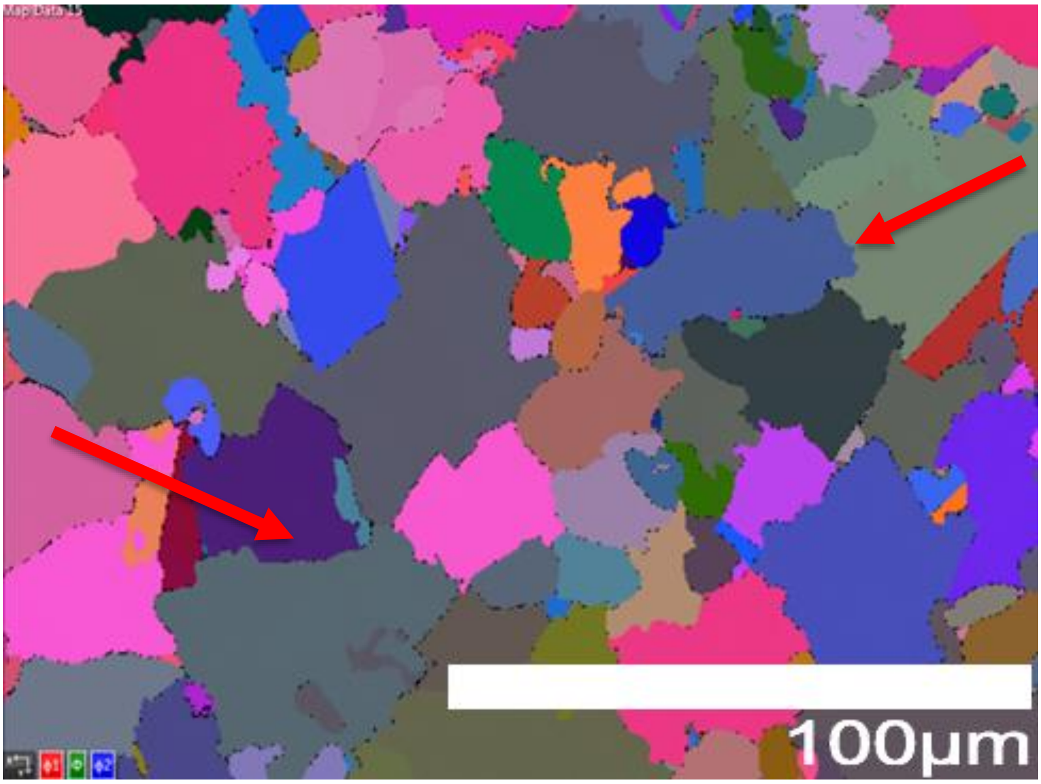

Figure 5.39 Crystal orientation mis-match (Euler) map of 850 - 500 µm Si-Ge.

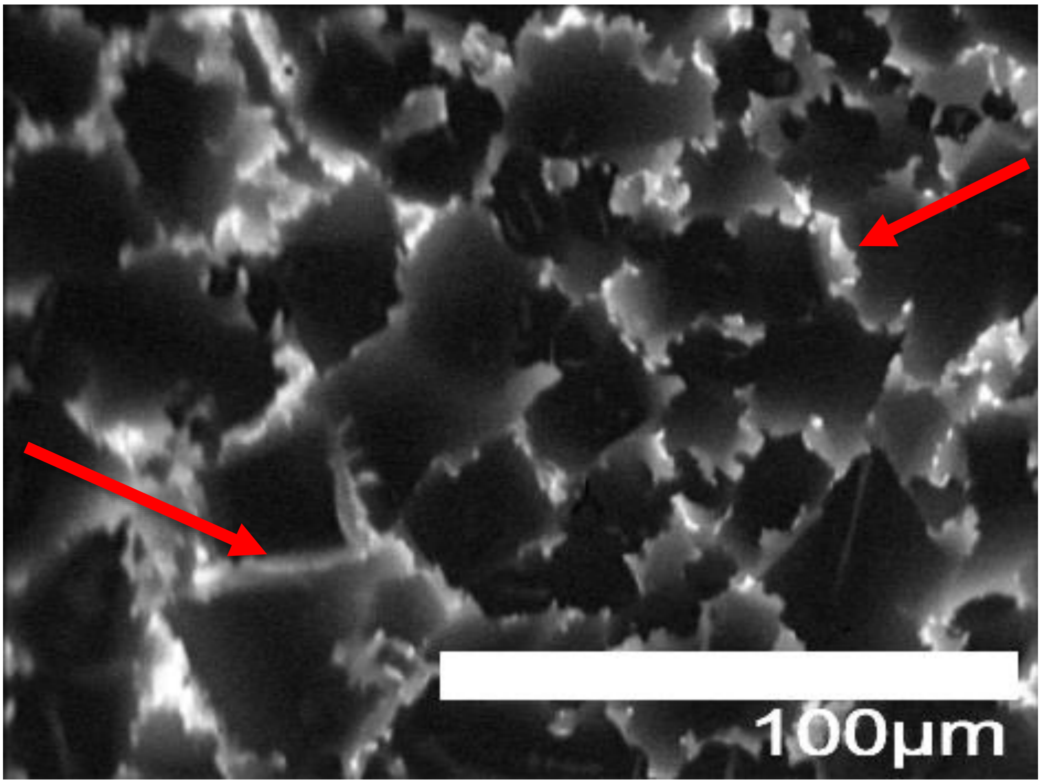

Figure 5.40 SEM backscattered image of 850 - 500 µm Si-Ge illustrating the area of interest for crystal orientation mis-match in **Figure 5.39**.

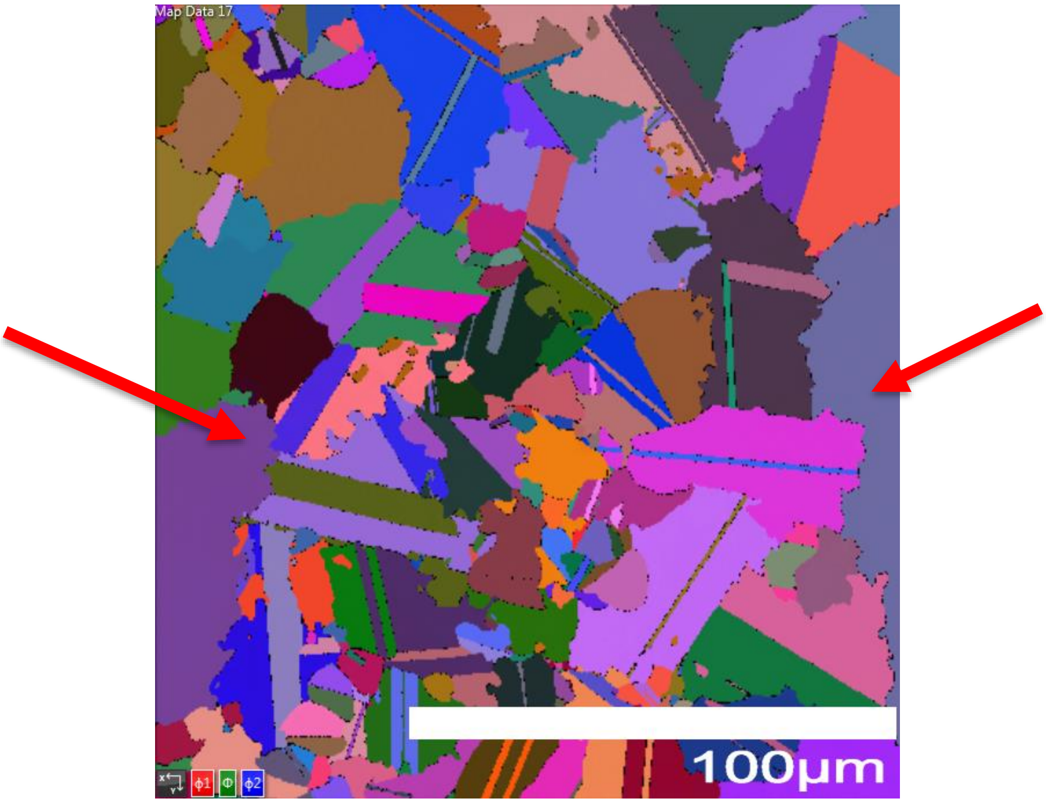

Figure 5.41 Crystal orientation mis-match (Euler) map of 850 - 500 µm Si-Ge.

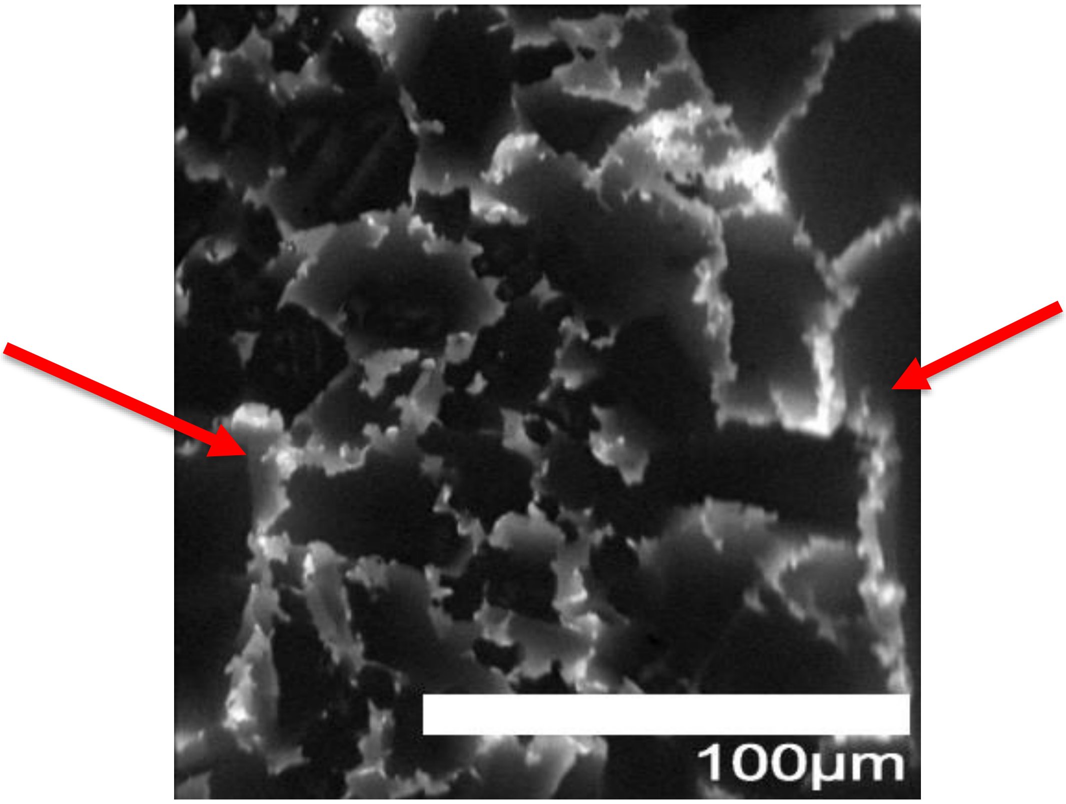

Figure 5.42 SEM backscattered image of 850 - 500 µm Si-Ge illustrating the area of interest for crystal orientation mis-match in **Figure 5.41**.

5.2.4 TEM

From the TEM brightfield image in **Figure 5.43** it is apparent that at the point where there is very little amount of Si left during solidification a compound is formed before the Ge-rich region. The Si-rich region can be seen in the top left corner as the darker compound whilst the lightest compound in the bottom right corner is the Ge-rich region. The area of interest was indeed the mid-grey region in the middle. This region is contrary to the Scheil calculation as the change is not gradual at this point despite it being so for the majority of Si-rich region solidification and growth.

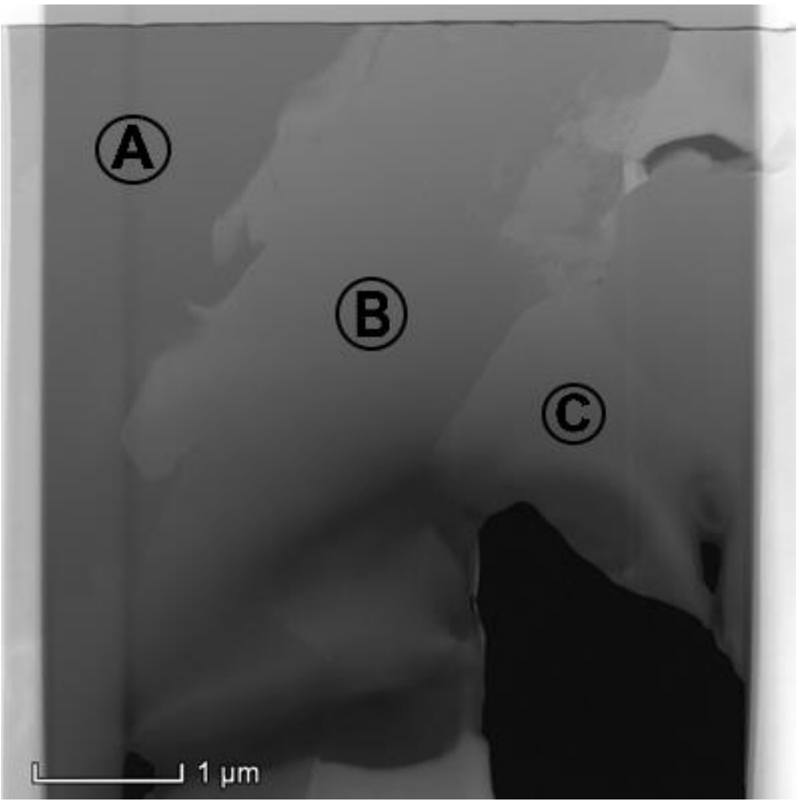

Figure 5.43 TEM brightfield image of Si-Ge alloy exposing Si-rich and apparent Ge-rich grain interface.

5.2.5 TEM EDX Linescan

A linescan was also conducted along the region highlighted in **Figure 5.44** with the findings being presented in **Figure 5.45**. Immediately apparent there are two regions with preferred composition present with different intensities, and there is a gradient in intensity for each compound. The very first region to the far left is the Si-rich solid solution despite its preferred composition in **Figure 5.45**, similar to a stoichiometric compound.

The Si and Ge content are shown as red and green lines respectively. The Si-rich region is found to contain 70 at.% Si at the interface which means that this is expected to be the lowest composition of Si within the Si-rich regions. The Ge-rich region contains over approx. 86 at.% Ge (average) which is expected, this agrees with the findings in EDX Point analysis conducted on the SEM and also with the Scheil solidification sequence. The middle compound between 0.6 and 2.2 μm is found to contain a composition of approx. Si-60 at.% Ge (average) which is not as expected, tentatively referred to as Ge_3Si_2. The 86 at.% Ge found in the Ge-rich region also appears to be stoichiometric which would not be far off from a Ge_7Si compound. With these findings and known ICDD data it is therefore predicted that the Si-rich and Ge-rich regions share a single grain (as found in **Section 5.2.3 EBSD**) with the same crystal structure, albeit with varying occupancies.

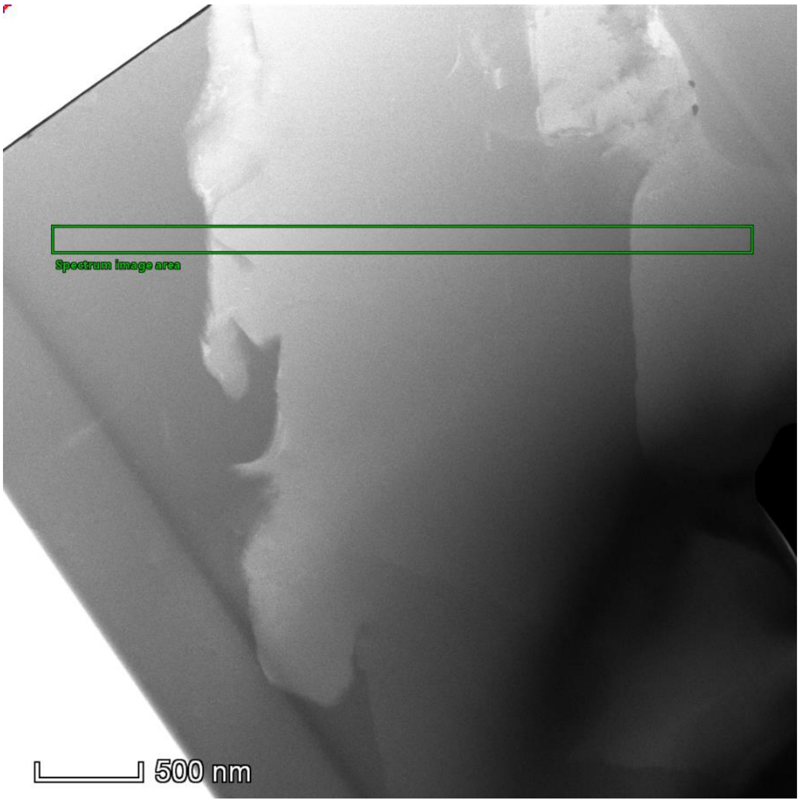

Figure 5.44 TEM brightfield image of Si-Ge alloy with green rectangular box illustrating linescan area.

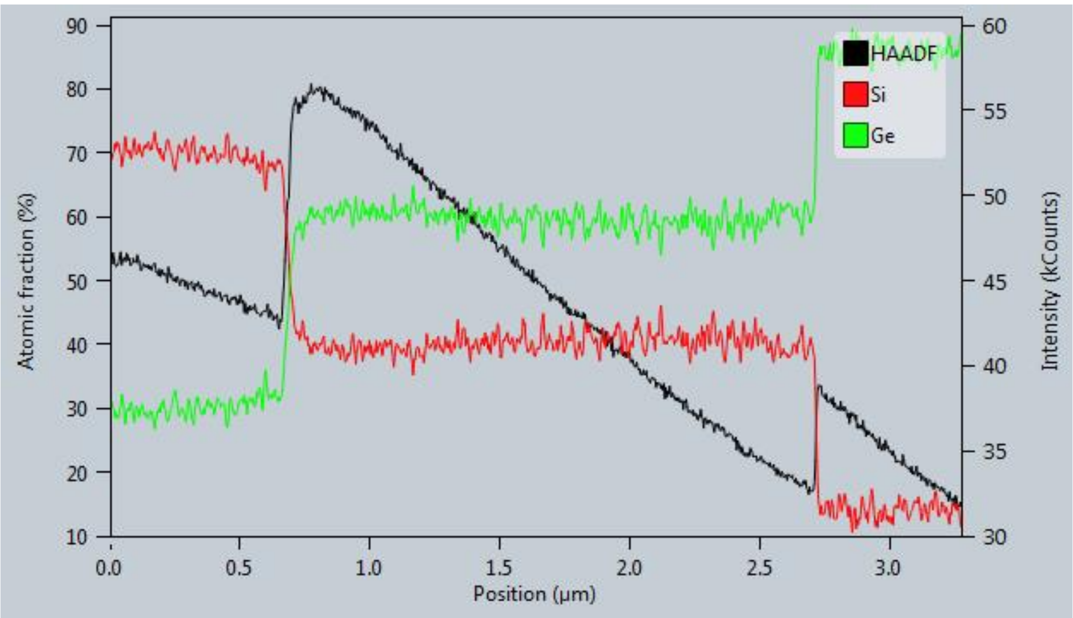

Figure 5.45 Elemental atomic fraction from linescan across the Si-rich and apparent Ge-rich grain interface.

TEM selected area diffraction (SAD) patterns are shown in **Figures 5.46**, **5.47** and **5.48**, for the Ge-rich, intermediate and Si-rich regions respectively (indexed using ICDD crystallographic data files with the following references respectively: 01-071-4636, 04-008-2206 and 04-006-2527). It is immediately apparent that all three regions have the same crystal structure, diamond cubic, and none of the regions are chemically ordered due to the absence of superlattice spots, this is as expected in a solid solution but rather interesting for the intermediate region which appears to have a 60/40 Ge/Si stoichiometry.

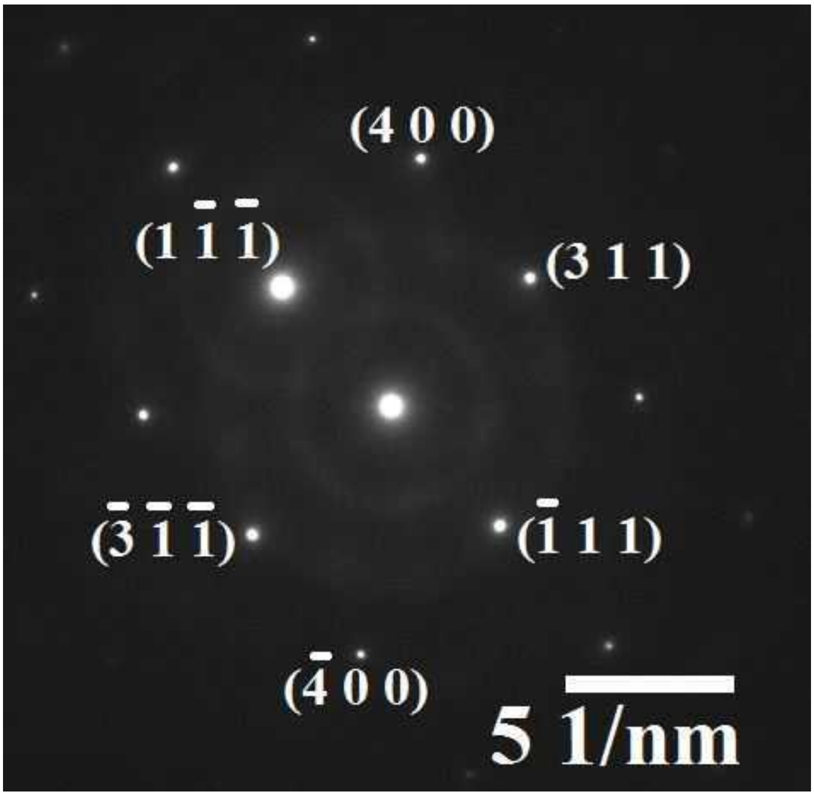

Figure 5.46 Selected Area Diffraction pattern of Ge-rich region labelled A in **Figure 5.43**.

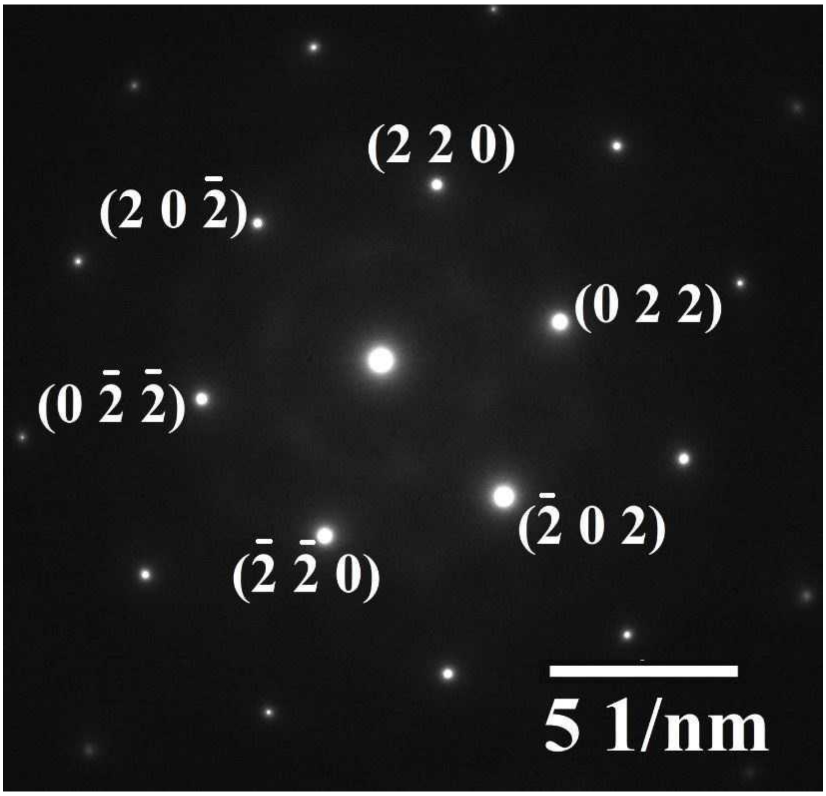

Figure 5.47 Selected Area Diffraction pattern of Ge_3Si_2 compound in the region between Si-rich and Ge-rich regions labelled B in **Figure 5.43**.

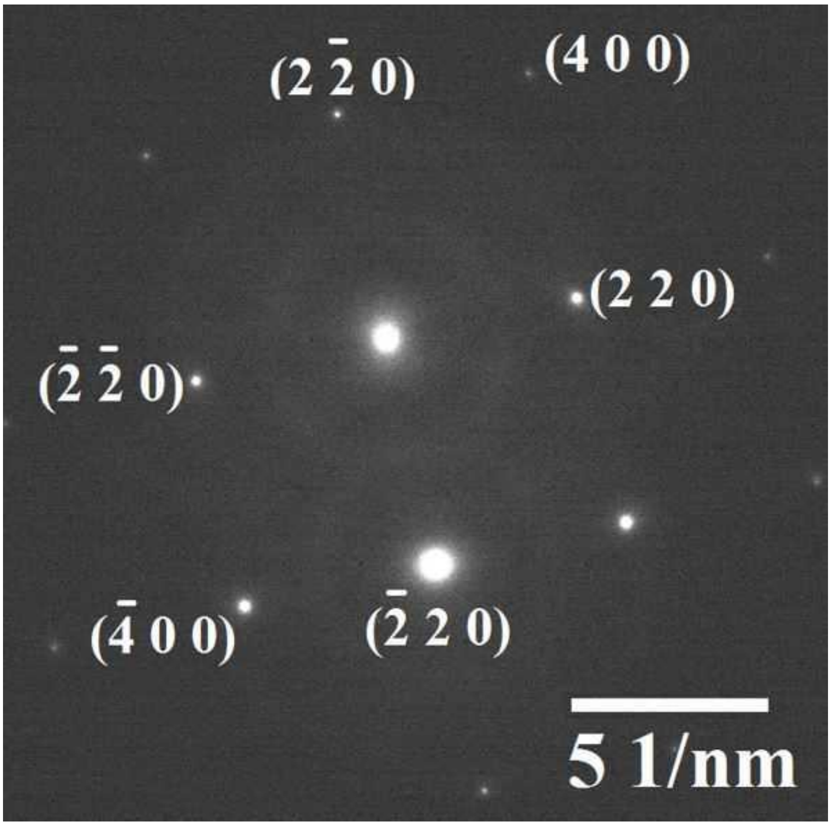

Figure 5.48 Selected Area Diffraction pattern of Si-rich region labelled C in **Figure 5.43**.

5.2.5.1 SEM EDX Linescan

Following the Scheil calculation an EDX linescan was also conducted using SEM to understand the solidification sequence from the Si-rich grains to the apparent Ge-rich grains. Due to the large Si-rich grains it was not possible to conduct the linescans using the TEM, but the SEM can allow this research. A selection of Si-rich grains were scanned and even Ge-rich features to understand the transition between them. **Figure 5.49** shows the region that was selected alongside the at.% of Si and Ge present. There is a gradual decrease in Si and a gradual increase in Ge as the scan reaches the boundaries of the Si-rich grain, which means that the solidification sequence does follow the Scheil solidification sequence. It is interesting to also notice that there is a sharp change in composition as the scan moves to the Ge content despite this not being an area of high Ge composition, such as the maxima. In **Figure 5.50** the same result can be seen but with the elemental composition of parts of the Ge-rich region to appear stochiometric at close to 60 at.% Ge, this is in line with the TEM EDX findings.

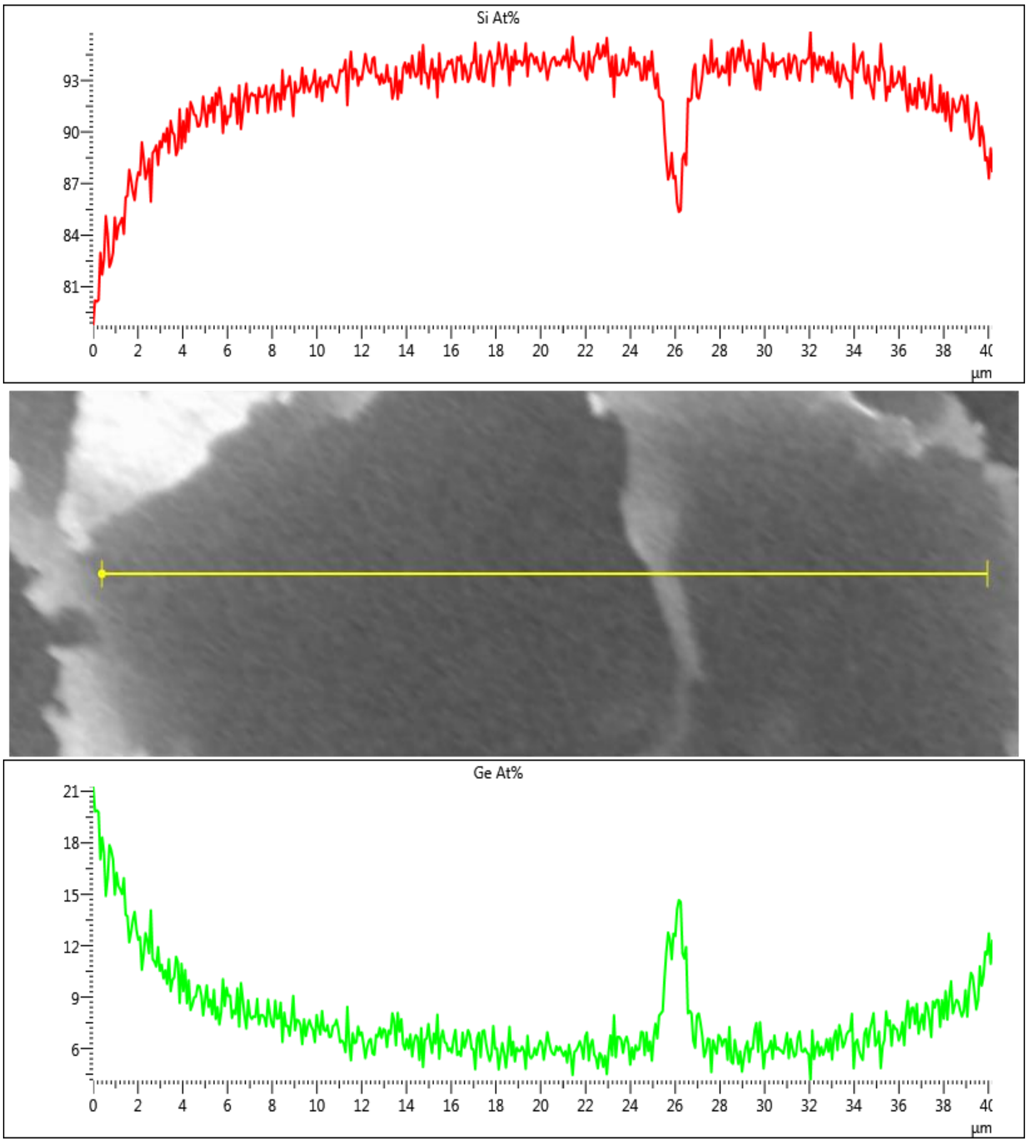

Figure 5.49 EDX linescan conducted using SEM on a rapidly solidified > 850 µm sample with elemental atomic fraction.

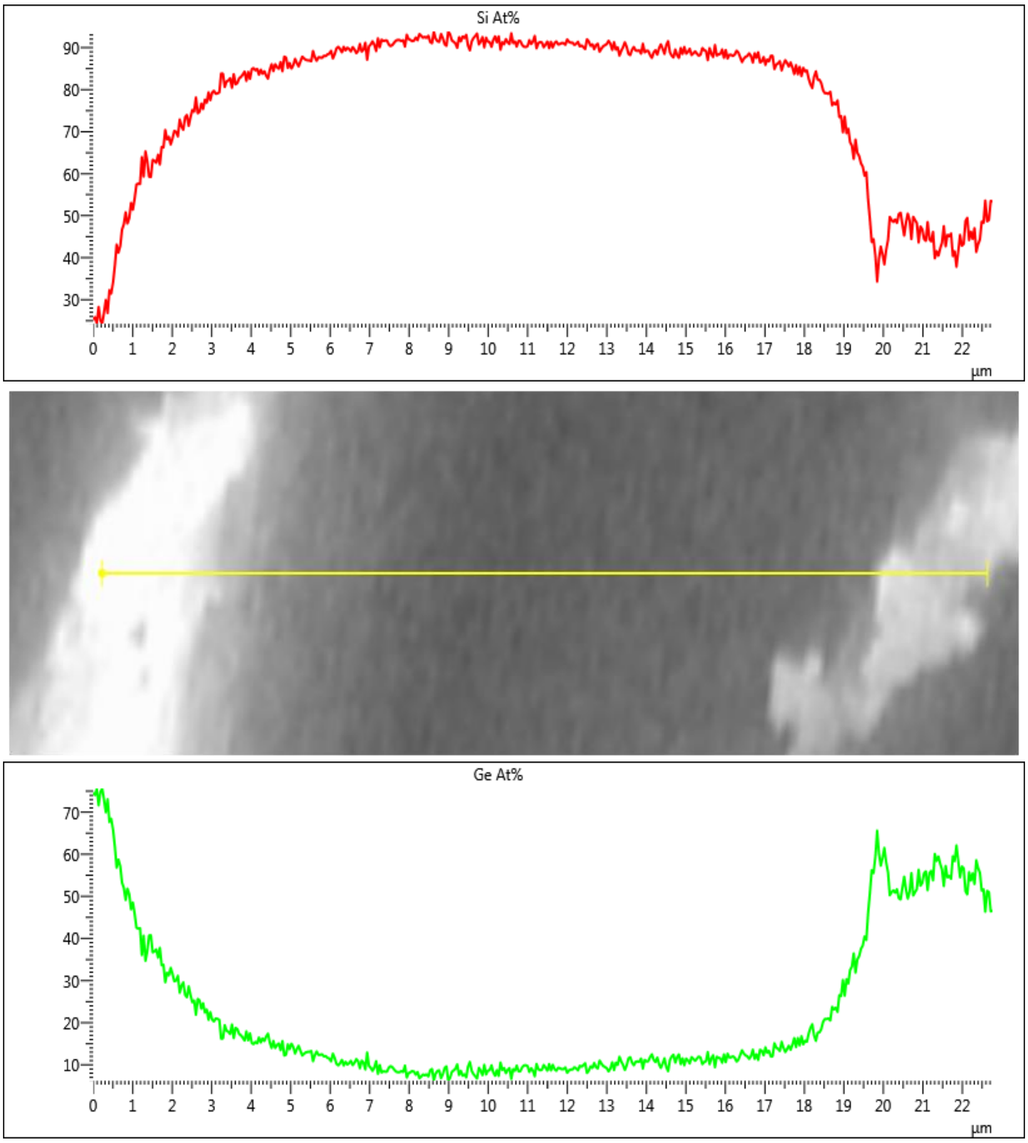

Figure 5.50 Elemental atomic fraction from linescan conducted using SEM on > 850 µm Si-Ge sample illustrating signs of apparent stoichiometric compound.

Further SEM EDX linescans were conducted on the slower-cooled starting and crucible residual samples to further understand the solidification of Si-Ge. The motivation behind this was due to the observation of potential compounds found in the rapidly solidified samples, and to determine if the formation of preferred compounds was indeed a result of rapid solidification. By looking at **Figures 5.51**, **5.52**, and **5.53** it is apparent that even in slower cooled samples there is evidence of different compounds with varying stoichiometry. In addition to Ge_3Si_2 and Ge_7Si observed in TEM linescans for the rapidly solidified samples, there is also potentially $Ge_{11}Si_9$ (Ge-45 at.% Si) in the starting sample. A major plateau in the linescan for the starting sample represents a stoichiometry similar the previously observed Ge_3Si_2, except with slightly lower Ge content. In the crucible residual sample linescans there are many plateau sections to the linescan curves which seem to possess between 70 to 80 at.% Si. The many plateau regions to the linescans illustrate the formation of varying preferred stoichiometric compounds.

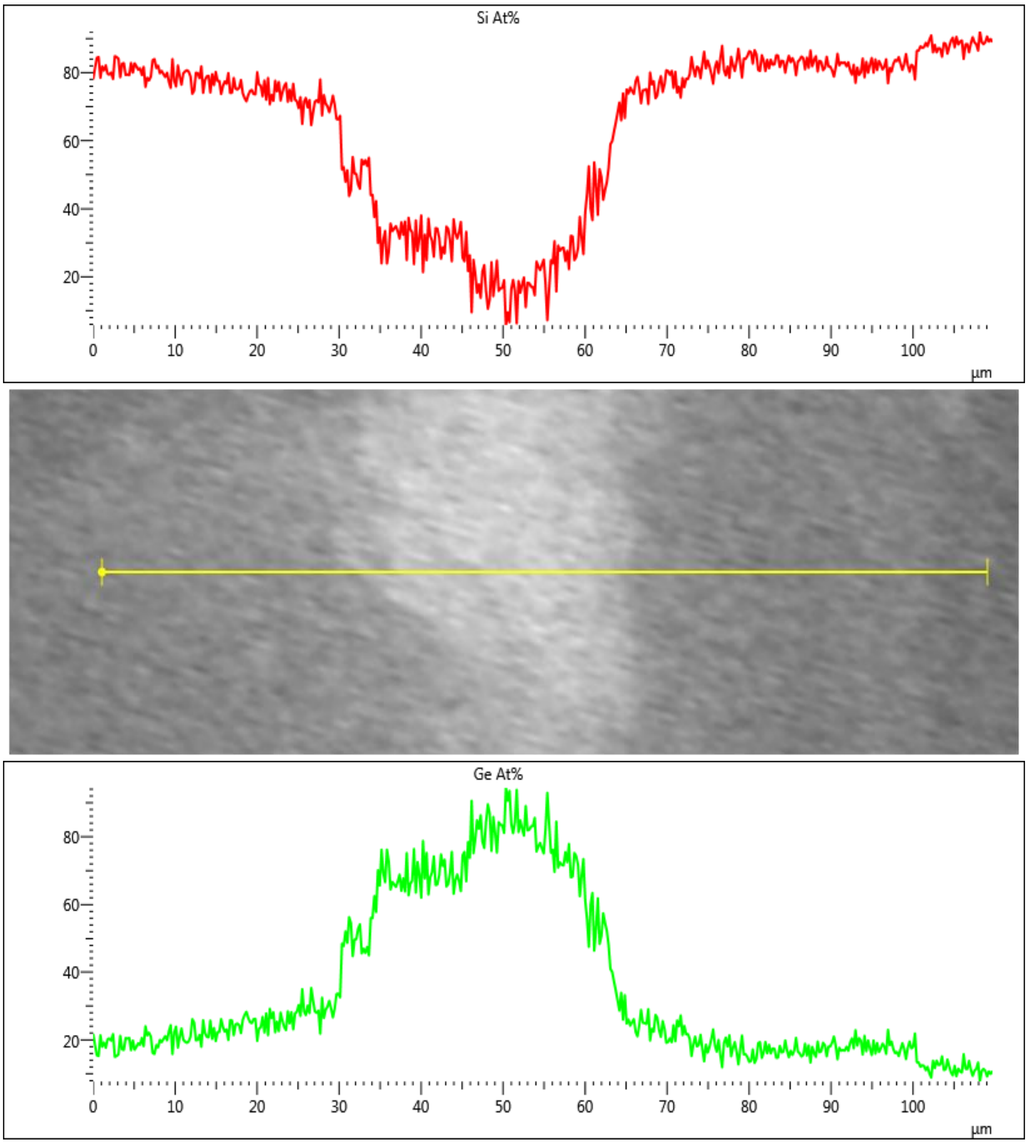

Figure 5.51 EDX linescan conducted using SEM on the slow cooled starting sample with elemental atomic fraction.

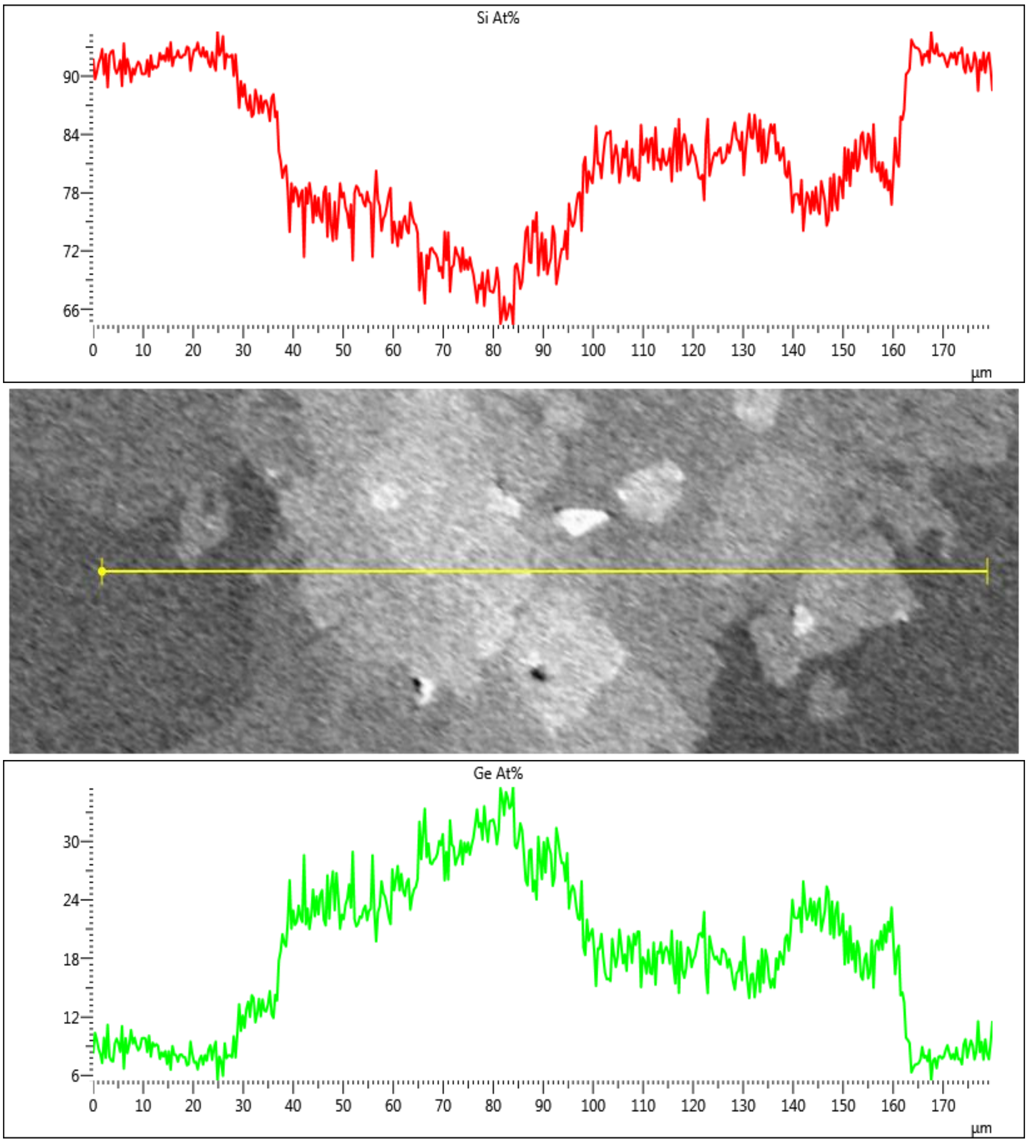

Figure 5.52 EDX linescan conducted using SEM on the crucible residual material with elemental atomic fraction.

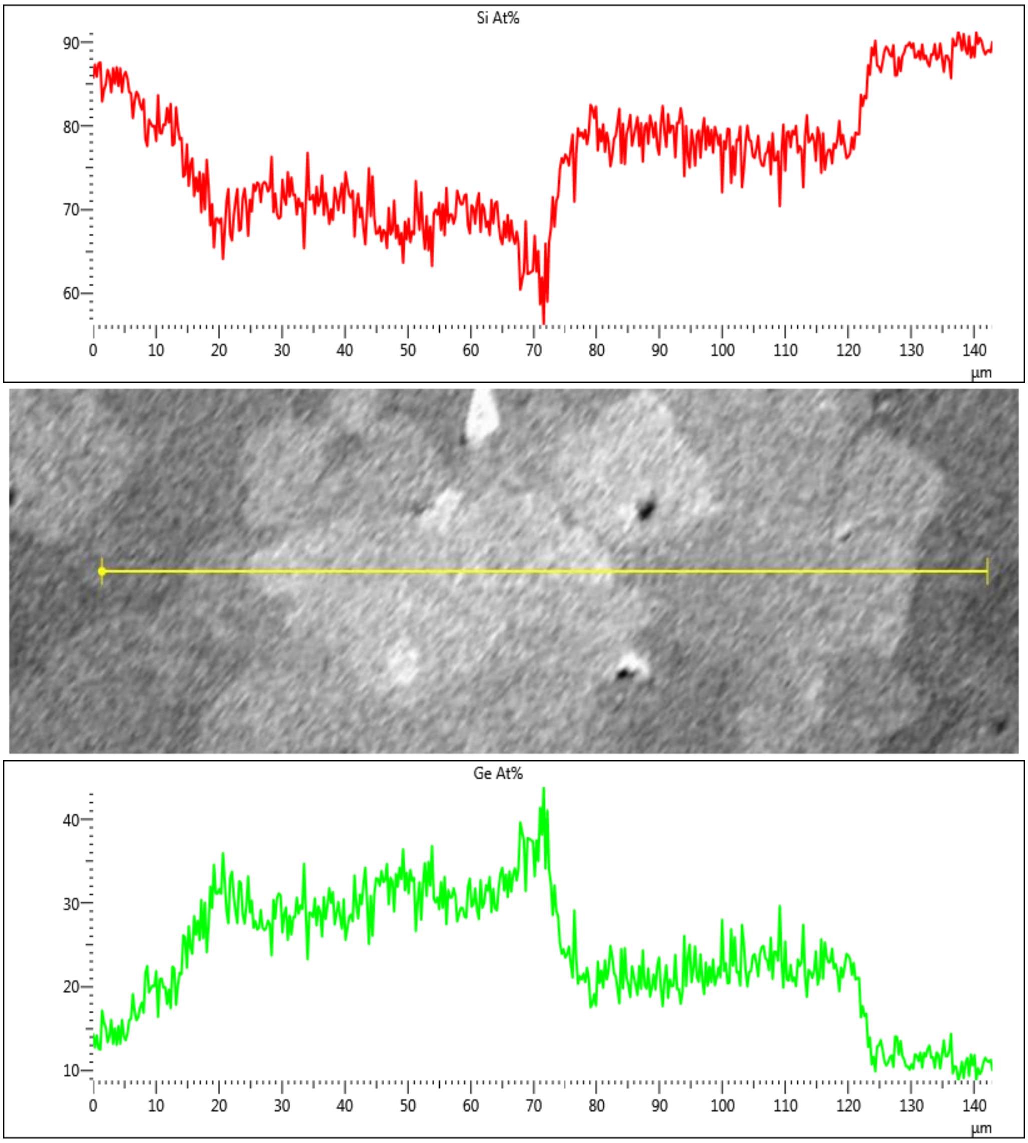

Figure 5.53 EDX linescan conducted using SEM on crucible residual material with elemental atomic fraction illustrating more potential stoichiometric compounds.

Chapter 6 Discussion

The findings observed in **Chapter 5** shall be discussed in this chapter. To begin with the effect of cooling rate on the Al-25 at.% Ni alloy shall be discussed followed by the effects of Cr doping. The microstructure and crystal structure characterization shall be discussed and compared against their effect upon catalytic activity. The additional $Al_{13}Cr_2$ phase shall be investigated. In the second section of this chapter the findings from the Si-Ge drop tube processing shall be discussed with the microstructure characterization results assisting in the understanding on undercooling effects on the microstructure. The Si-Ge microstructure morphology shall be compared against previous literature with novel findings being discussed.

6.1 AlNi

It is clear from the results that a change in cooling rate has a huge effect on both the phase composition and the microstructure morphology of the Al-25 at.% Ni. It is also noted that the addition of 1.5 at.% Cr (Al-23.5 at.% Ni-1.5 at.% Cr) also has interesting outcomes which are expected to be useful in not only catalytic activity after leaching but the further study of Raney type alloys. By observing **Table 5.1** we can immediately realise that the phase fraction is affected by the cooling rate. The larger particles that experience a lower cooling rate appear to contain less Al_3Ni_2 than the smaller particles, and consequently more Al_3Ni. The reason for this change may be attributed to the fact that the quicker cooling rate experienced by the smaller particles allows less time for the sluggish peritectic reaction which converts Al_3Ni_2 into Al_3Ni. Since there is less time for this peritectic reaction to take place there is a larger amount of Al-eutectic left over due to the lower amount of Ni atoms left available to continue the formation of Al_3Ni. The excess remaining Al solidifies within the eutectic.

The effect of varied cooling rate also shows a microstructural change in the morphology of the samples. **Figures 5.3** and **5.4** illustrate the microstructural changes in morphology due to cooling rate. The microstructure of the larger particle displays the same core-shell morphology as the smaller particles but differ due to their globular microstructure, while the smaller particle displays the formation of fully developed dendrites. The differing microstructure morphologies, because of the cooling rates, are attributed to the gas atomization process itself, with the larger particles experiencing a larger shear force than the smaller particles on their surface from the supersonic gas. Not only do the larger particles experience the larger shear force but also, they take longer to solidify allowing longer time for the shear force to act upon the semi-solid material resulting in the break-up of any dendrites that may have started to form. The smaller particles do not experience the same shear force and are also more likely to be carried away by the high velocity gas stream. Since the smaller particles have a higher cooling rate, alongside the melt subdivision effect they will experience a higher undercooling due to the absence of an active nuclei in most of the droplets, this would allow the high undercooling to develop a more dendritic character in the smaller particles.

By observing **Figures 5.6** and **5.7** to the respective undoped samples with the same size fractions, **Figures 5.3** and **5.4**, we can analyse the effect of Cr doping on the Raney type powders. Interestingly with the Cr-doped samples even the larger particles seem to exhibit a dendritic morphology with fully developed dendrites, and minimal evidence of the same globular morphology found in the undoped samples. Both sets of alloys were sieved into the same size fractions and are expected to have the same cooling rates, shear forces and solidification times are also expected to be the same with the undoped alloys. It is therefore concluded that any changes found with the Cr-doped particle morphology would be attributed to the solidification dynamics facilitated by the addition of 1.5 at.% Cr. By looking at **Figure 5.8** it is apparent that almost no Cr is co-located in the Al_3Ni_2 phase therefore during the initial phase of solidification all Cr was rejected and was required to diffuse away from the growing solid. dendrites are often formed because they are the most efficient geometry for diffusion. During the solidification of undoped Ni-75 at.% Al alloy the first phase to form is Al_3Ni_2, which is said to have roughly 60% Al, therefore diffusion is thought to have taken place with a flux of Al atoms being diffused from the Al_3Ni_2 phase into the liquid, and a flux of Ni atoms are thought to be diffused into the Al_3Ni_2 phase, to result in 40% Ni that the Al_3Ni_2 contains. In 1.5 at.% Cr doped Ni-75 at.% Al alloy a flux of Ni atoms are thought to diffuse into the Al_3Ni_2 phase, with a larger flux consisting of both Al and Cr atoms to be diffused away from the Al_3Ni_2 phase, since there is no Cr in the Al_3Ni_2 phase. The additional solute flux experienced in the Cr-doped alloys would be the reason for an increased dendritic morphology. This is also backed up by the linescan shown in **Figure 5.18**.

If particular attention is paid towards the SEM micrograph of the Cr-doped sample in **Figure 5.7**, which is comparable to the undoped sample in **Figure 5.4** it can be observed that the dendrites appear to be finer in the Cr-doped samples. In dendritic morphology the radius of the curvature at the tip of the dendrite is given by the following equation:

$$R = \left\{ \frac{\Gamma}{\sigma^*(\sum mG_C - \bar{G})} \right\}^{\frac{1}{2}} \tag{6.1}$$

Where Γ is the Gibbs-Thomson coefficient, σ^* is the constant parameter in marginal parameter theory and becomes a function of the surface energy anisotropy in microscopic solvability theory. G_C and $\bar{G}$ are the solute and thermal gradients respectively. There is a focus on the mG_C term which has units of a temperature gradient and is given by the following equation:

$$\sum mG_C = m_{Ni}G_{Ni} + m_{Cr}G_{Cr} \tag{6.2}$$

The Al-Ni liquidus gradient m_{Ni} in the Al_3Ni_2 compound is 33 K/at.%, and in the $Al_{13}Cr_2$ the Al-Cr liquidus gradient m_{Cr} at 1200 K is 115 K/at.% which can be seen in **Figure 6.1**, and since the G_{Cr} may be smaller than G_{Ni}, due to the less amount of Cr being diffused, the overall mG_C is consequently larger. This affects **Equation 6.1** since the larger denominator would mean the overall radius of the curvature at the tip of the dendrite, R, is smaller, therefore resulting in the finer dendrites observed in the Cr-doped sample.

Since both the undoped and the Cr-doped samples are likely to be growing at a similar Peclet number the following equation can be used to further understand the microstructure morphology:

$$P = \frac{VR}{2D} \tag{6.3}$$

Where *P* is the Peclet number, *V* is the dendrite growth velocity and *D* is the diffusivity. If the radius of the curvature at the tip of the dendrite, R, is reduced, as previously mentioned, then the dendrite growth velocity must increase in order to keep *P* constant. And since the effect of flow in the melt, i.e. shear forces from the gas jets, is reduced with a higher growth velocity, that would explain the reason why the dendrites Cr-doped samples are less affected by the shear force as they grow more quickly, therefore resulting in a more dendritic character than the undoped microstructure.

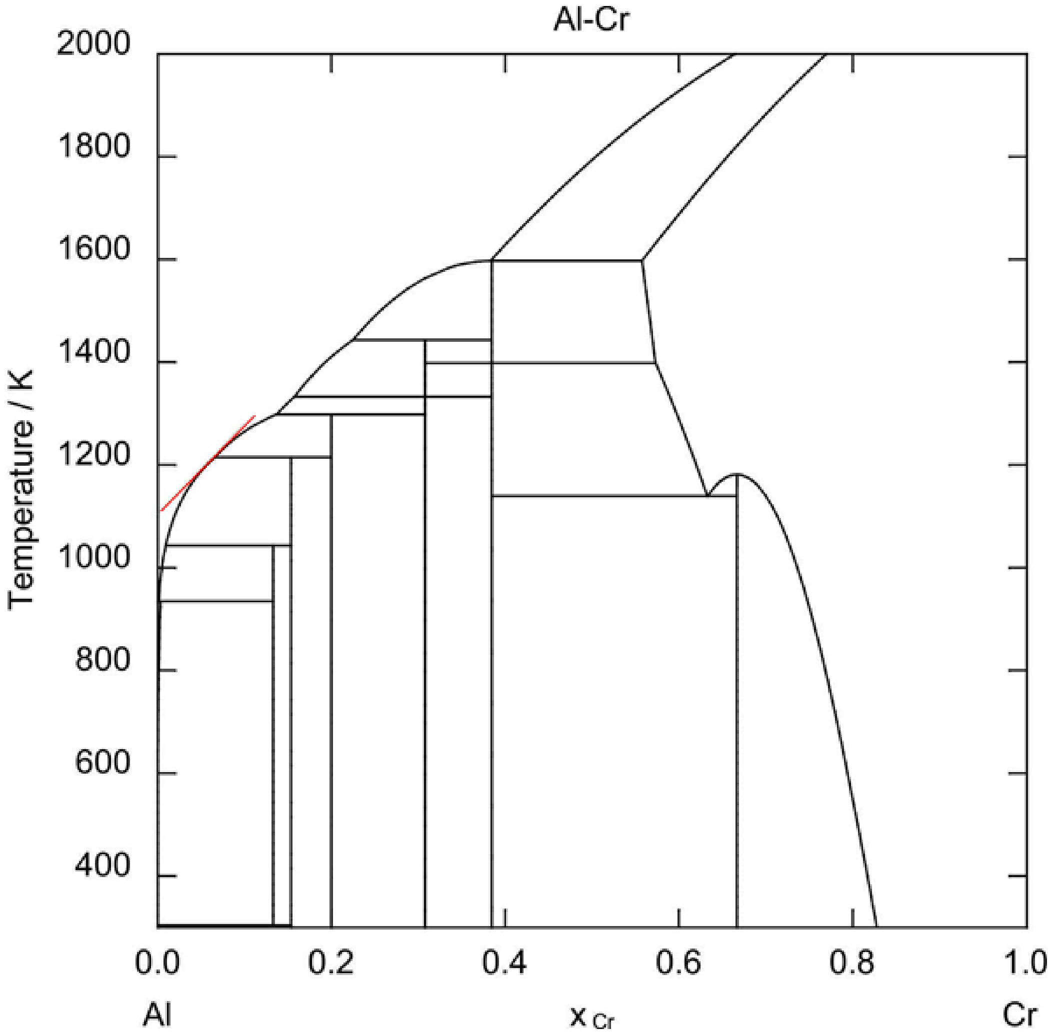

Figure 6.1 Al-Cr phase diagram.

Another interesting effect of Cr-doping the Raney type powder is the formation of the $Al_{13}Cr_2$ phase. By consulting **Figures 5.13** and **5.14**, and with the support of the linescan in **Figure 5.18** it is apparent that practically all the Cr within the sample is located within this additional phase. The localisation of Cr contests the assumption, rather conclusively, that Ni is often substituted by Cr [68]. While practically all the Cr is found in the $Al_{13}Cr_2$ phase, the phase itself is not located as expected by the Scheil solidification sequence generated by CALPHAD. As per the calculation the phase is expected to form as a result of a series of peritectic reactions, with Al_4Cr being the second phase to form after Al_3Ni_2. The $Al_{13}Cr_2$ phase is actually co-located in the Al_3Ni phase and on the boundary with the eutectic, this suggests that the Cr is retained within the liquid during the early stages of solidification and solidified almost entirely in the $Al_{13}Cr_2$.

The amount of $Al_{13}Cr_2$ present in the Cr-doped samples is considerably more than that which is expected with the addition of 1.5 at.% Cr. The Rietveld refinement phase fractions presented in **Table 5.2**, and the Image analysis presented in **Section 5.1.4** and **Figure 5.13** both support the argument that there is more $Al_{13}Cr_2$ than can be accounted for by 1.5 at.% Cr. During Rietveld refinement the excess $Al_{13}Cr_2$ phase was accounted for by a 40% deficiency in the Cr atomic sites which is substituted by Ni. EDX point measurements presented in **Table 5.3** also support the theory that the excess $Al_{13}Cr_2$ phase within the microstructure is due to the Ni substituting for Cr. From the EDX point measurement there can also be seen a deficiency in the Al composition with an excess of Ni, this was previously thought to have been an artefact of the SEM EDX process due to the interaction volume detecting some of the Al_3Ni phase. TEM linescan data presented in **Figure 5.20** and quantified in **Table 5.4** however, suggests that the Cr within the phase is very near stoichiometry and there is around 10% deficiency in the Al which is accounted for by the Ni. It seems that Ni not only substitutes for Cr, but also for the Al within the $Al_{13}Cr_2$ phase, and so the phase should be correctly designated as $(Al,Ni)_{13}(Cr,Ni)_2$. The excess amount of the $Al_{13}Cr_2$ phase within the microstructure is useful, since the Al is dissolved during leaching leaving a nanoporous structure, and the Ni substitution onto the Cr lattice would allow for larger amounts of the phase available (due to limited amount of Cr within the alloy). With the observed results however, the Al is also found to be deficient and Ni also substitutes for it, the Al has close to a 75 at.% composition which is similar to the Al composition found in the stoichiometric line compound Al_3Ni. It is therefore suggested that while the nanoporous structure found in the $Al_{13}Cr_2$ phase after leaching is advantageous for catalysis due to the larger amount of vacancies that are potential sites for catalytic activation, the addition of Cr itself may exhibit a greater catalytic activity.

The explanation that the solidification pathway does not follow the Scheil sequence may lie in the Al_4Cr phase itself which, during the gas atomization condition does not nucleate easily. ε-Al_4Cr has previously been described as a complex Cmcm orthorhombic phase [117]. It contains, within its unit cell, 55 atoms, out of which 40 have icosahederal ordering. As such ε-Al_4Cr has been extensively studied as a potential quasicrystal [118], but it is easy to suppress the nucleation of a phase as such. As the Scheil sequence predicts, the next phase to form would be the η-$Al_{11}Cr_2$ phase, which is part of the monoclinic C2/c space group with 80 atoms per unit cell and also a complex icosahedral ordering [119]. Nucleation would also be difficult to initiate in this phase. When the Scheil sequence was recalculated with the Al_4Cr and $Al_{11}Cr_2$ phases suppressed the $Al_{13}Cr_2$ phase was found to solidify directly from the melt, but at a higher temperature, 1100 K. This is comparable to the 983 K temperature that it was predicted to form at if it were to form via the series of peritectic reactions. The recalculated Scheil solidification sequence agrees with the experimental data found as the $Al_{13}Cr_2$ phase is formed coincident with Al_3Ni.

The findings in relation to the addition of 1.5 at.% Cr within this research allows an explanation to the increased catalytic activity of Cr-doped Raney type alloys, like the 140% increase in activity for the hydrogenation of nitrobenzene. With the morphology observed in the Cr-doped samples, during leaching the Al eutectic would be washed away leaving the Cr on the surface without the need for migration of Cr, this is due to the formation of $Al_{13}Cr_2$ directly from the melt. This agrees with the finding by Bonnier *et al.* that the activated catalyst would have a surface Cr coating [68]. Without the consideration of whether Cr is a more active catalytic species than Ni, the $Al_{13}Cr_2$ would alone be expected to enhance catalytic activity due to its nano-porous structure upon leaching, this is due to it being significantly more Al-rich than Al_3Ni, this however would not be the case if $(Al,Ni)_{13}(Cr,Ni)_2$ contains 75 at.% Al as observed by EDX point measurements and EDX linescans, but not supported by Rietveld refinement. The assertion that the increased catalytic activity of the Cr-doped Raney alloy is due to the Al-rich phase, $Al_{13}Cr_2$, would allow potential future developments as the resulting nano-porous structure of $Al_{13}Cr_2$ means that any Al-rich phase precipitating late in solidification is likely to result in enhanced catalytic activity.

6.2 SiGe

The backscattered SEM micrographs in **Figures 5.25, 5.26, 5.27**, **5.28**, **5.29**, **5.30**, and **5.31** illustrate the effects of undercooling to morphology. The starting compound solidified at equilibrium displays a directional morphology with heterogeneity, as the solute partitioning appears to be quite large. With the crucible residual there is also a heterogeneous microstructure but with no obvious direction. The microstructure found in the crucible residue is also like the microstructure found by Zhang *et al.* in their slow cooled sample [107]. The rapidly solidified samples are contrasting to the slow cooled samples, they exhibit distinct Si-rich grains with Ge deposited in the grain boundaries. This morphology is similar to previous studies [107] [108] [109]. The light shapes at the centre of the grains have not previously been reported, which are remnants of the initial dendritic growth. This may support the theory that at higher undercoolings equiaxed grains are formed by dendritic break-up [89]. Although similar microstructure morphologies have been reported there is no mention of a bimodal distribution in literature. Interestingly, the quicker cooled samples do display grains that appear more consistent in size with one another, and this is gradually less apparent in the slower cooled samples.

Figures 5.25, 5.26, 5.27, **5.28**, **5.29**, **5.30**, and **5.31** were also subject to EDX point measurements which aid our understanding to the overall solidification mechanism. At equilibrium the Si-rich regions seem to solidify with approx. 83-84 wt.% Si composition, and high amounts of Ge getting clustered together as the last parts of the microstructure to solidify. This suggests a level of partitioning but due to the low cooling rate the partitioning is not as severe as with the rapidly solidified samples, though it is still more severe than the partitioning observed by Zhang *et al.* [107]. In the crucible residue Ge seems to be surrounded by Si which suggests that what is being observed is possibly the boundary between a number of large Si-rich grains. There have been various studies, including this one, which suggest that grain size increases when the cooling rate is slower due to the lower nucleation and growth rates. This would be an explanation to the morphology that suggests Si surround Ge. Essentially the same solidification mechanism is allowed to take place that determines the larger grain size in the much slower cooled crucible residue. This would also explain why although there is a level of heterogeneity in the crucible residue there does not seem to be as much partitioning as the rapidly solidified samples, this is due to the relatively vast amount of time allowed for cooling to allow back diffusion to take place. Partitioning in the rapidly solidified samples appears to be much more severe as Ge-rich regions contain up to 98.28 wt.% Ge in the sample that solidified the quickest. Again, while the microstructures appear to be similar to those observed by Zhang *et al.* the partitioning is much more severe [107]. There seems to be an implicit suggestion that the higher cooling rate would allow the microstructure to exhibit more partitioning as there is less time for the Si and Ge to mix as a result of back-diffusion during solidification, this is further argued by observing the results presented in **Figure 5.33**. During rapid solidification (increasing departure from equilibrium) a common observation is solute trapping, where there is not enough time for the melt to form into a preferred microstructure, which would result is less partitioning. With the rapidly solidified Si-Ge samples however, there is more partitioning as the cooling rate is increased which contradicts solute trapping leading to the conclusion that despite the high cooling rates solute trapping did not occur. This is supported by the Scheil calculation which predicted a near-100% Ge composition in the last part of the solution to solidify, which agrees with the observed microstructures. The observations made in the rapidly solidified samples display a higher level of partitioning as the cooling rate is increased, and those that were slow cooled (starting and residual samples) display less partitioning. This is thought to be as a result of back-diffusion taking place in the solid-state allowing the Si-rich and Ge-rich regions to mix to a certain extent. As the cooling rate is increased more of the back-diffusion is being suppressed, with only very small amounts of evidence of back-diffusion in the rapidly solidified samples, due to the limited time available in the solid-state. This conclusion also has the support of the Scheil calculation as the microstructure morphology of the rapidly solidified samples appears to be as expected from the Scheil calculation, which assumed no back-diffusion.

With the rapidly solidified samples, as the cooling rate is increased the average grain size decreases, this can be seen in **Figures 5.27**, **5.28**, **5.29**, **5.30**, and **5.31** simply by the scale bar. Quantitative grain size analysis shows that this is indeed true as the average grain area for each of the particle size fractions was obtained and compared. As the cooling rate is increased finer grains are to be expected due to the competition between the increasing nucleation rate and the increasing growth rate, and eventually the increased nucleation rate is more dominant resulting in more nucleation sites, more grains, and consequently finer grains.

In order to understand the solidification sequence, the Scheil calculation was also tested for its validity against SEM linescans across Si-rich grains and into the Ge-rich regions as this seems to be the sequence that the solidification follows. The Scheil calculation suggests that the composition profile of Ge within the growing solid seems to increase smoothly. The linescan in **Figure 5.49** does illustrate this to some extent but there is a noticeable sudden increase in Ge composition as the Ge-rich regions begin to form, this suggests that the Scheil calculation isn’t entirely accurate. **Figure 5.50** goes further to illustrate what may be the formation of a stoichiometric compound. The TEM brightfield image in **Figure 5.43** also goes further to discredit the Scheil calculation as a distinct compound can be seen between the Si-rich and Ge-rich regions. The linescan in **Figure 5.45** suggests that a compound: Ge_3Si_2, is formed at the boundary between the Si-rich and Ge-rich regions. There is a break in the smooth increase of Ge composition in the growing solid. Selected area diffraction however, illustrated that the additional stoichiometric compound is not ordered, similar to the rest of the solid solution. The Ge rich region also appeared to form as a compound with 86 at.% Ge, which could suggest a Ge_7Si compound. Interestingly a number of other potential compounds were found when SEM linescans were conducted on the slower cooled samples, with around 80 at.% Si and 70 at.% Si respectively, which would be denoted as Si_4Ge and Si_7Ge_3. There was also the a plateau section observed at approx. 75 at.% Si which would suggest a Si_3Ge compound. The formation of such compounds in a diamond cubic structure is rather interesting, as there are 8 atoms in the unit cell of a diamond cubic structure. This would suggest that compounds Ge_7Si and Si_3Ge would fit well within the structure, but Ge_3Si_2, Si_4Ge and Si_7Ge_3 are rather unusual.

Conducting EBSD allowed further understanding in the formation of grains and the bimodal distribution. TEM linescans revealed the formation of at least one (possibly two) stoichiometric compound(s), and the TEM SAD patterns show that the lattice spacings are very similar. The SEM micrographs in **Figures 5.27**, **5.28**, **5.29**, **5.30**, and **5.31** seemed to suggest that Ge-rich grains are formed independently at the grain boundaries of the larger Si-rich grains. The Euler map illustrates that this is not true, while there is some minimal orientation mismatch between the Si-rich and Ge-rich regions most of the morphology shows that Si-rich and subsequence Ge-rich regions have the same crystal orientation and growth is epitaxial. The Ge-rich regions/compounds appear to grow as a continuation of the Si-rich regions in any directions. By observing the arrows in **Figures 5.39**, **5.40**, **5.41**, and **5.42** which illustrate a few examples of Ge-rich regions growing from the Si-rich solution, the Ge-rich regions can be seen to be growing from the bottom, right, right, and left margins of the Si-rich regions respectively.

One of the key findings from this research is that during rapid solidification of Si-30 wt.% Ge via drop tube processing the grain size is decreased as the cooling rate is increased, and the partitioning is also found to increase. With smaller grain there does not seem to be any evidence of increase homogeneity. The implications that this finding has on the thermoelectric performance of the material is unknown. It is also unknown what implications the additional regions of preferred composition between Si-rich and Ge-rich regions would have on the performance of the material. It has also been found that quicker cooled samples appear to exhibit consistent sized grains, the advantages of which is also unknown.

Conclusions

Conclusions for work carried out on gas atomized Al-25 at.% Ni and Al-23.5 at.% Ni-1.5 at.% Cr samples is presented below:

1. The effect of increased cooling rate upon the microstructure morphology of Al-25 at.% Ni is the formation of well-defined dendrites, with lower cooling rate particles displaying a globular structure. This is thought to be a result of larger shear force acting upon the larger particles for a longer time in the liquid state.

2. The phase fractions of Al-25 at.% Ni are affected because of cooling rate as more Al_3Ni_2, and less Al_3Ni, is found in the smaller particles. This is due to the amount of time available for the second peritectic reaction to take place, with less time for the sluggish peritectic to take place more Al_3Ni_2 is retained with less Al_3Ni being formed. This also means that remaining liquid is more Al-rich therefore allowing a greater amount of Al-Al_3Ni eutectic.

3. Doping the Al-Ni alloy with 1.5 at.% Cr (leaving 23.5 at.% Ni) results in better defined dendrites at all cooling rates, this is due to the higher diffusive flux allowing Cr atoms to flux away from the Al_3Ni_2 and the Al_3Ni phases. Dendrites appear finer in the Cr-doped samples due to higher $\sum mG_C$ as a result of a higher liquidus slope, this characterises the radius of curvature at the tip of dendrites. Since the radius of curvature is smaller in the Cr-doped samples compared to the undoped samples, and since both sets of samples are thought to grow at a similar Peclet number, the velocity of growth is higher in the Cr-doped samples allowing them to be less affected by shear forces acting via gas jets.

4. Cr doping allows a similar change in Al_3Ni_2 and Al_3Ni phase fractions as a result of cooling rate but also forms the additional phase: $Al_{13}Cr_2$. The amount of $Al_{13}Cr_2$ remains constant despite a change in cooling rate. All of the Cr is found within the $Al_{13}Cr_2$ phase.

5. The location of $Al_{13}Cr_2$ means that it forms directly from the liquid, and not as a series of peritectic reactions (as predicted by Scheil calculation). The location of $Al_{13}Cr_2$ also agrees with the findings by Bonnier *et al.* [68] that Cr is found on the surface after leaching.

6. Cr was previously thought to substitute for Ni in the Al_3Ni_2 and Al_3Ni phases, but in fact Ni substitutes for Cr, and possibly Al, in $Al_{13}Cr_2$ which accounts for the large amount of $Al_{13}Cr_2$ in the final microstructure. The phase should be correctly designated as $(Al,Ni)_{13}(Cr,Ni)_2$.

7. The reason for increased catalytic activity in Cr-doped Raney type alloys may be due to the Al-rich $Al_{13}Cr_2$ phase which when leached would leave a nano-porous Cr structure. But some evidence suggests the $Al_{13}Cr_2$ phase contains 75 at.% Al which is no more Al-rich than Al_3Ni, this may suggest that Cr itself is more effective in producing a higher catalytic activity.

Conclusions for work carried out on drop tube processed Si-30 wt.% Ge samples is presented below:

1. Microstructures of slow-cooled Si-Ge display a heterogeneous morphology, with relatively low levels of visible partitioning, while rapidly solidified microstructures exhibit grains that illustrate higher partitioning.

2. EDX point measurements show that partitioning is higher in the rapidly solidified samples, and higher than previously observed by Zhang *et al.* [107]. It was also found that with increased cooling rate the amount of partitioning is also increased, this means that although solute trapping is suppressed even in the quickest cooled samples back-diffusion in the solid state does take place and is limited by cooling time as the cooling rate is increased.

3. Quantitative grain area distribution shows that average grain size decrease in the SEM micrographs as cooling rate is increased. This is as expected in most metallic rapid solidification systems.

4. EBSD of Si-Ge samples shows illustrates that Ge-rich regions do not form into grains but grow epitaxially as part of the larger Si-rich grains.

5. Linescan data suggests that the Scheil calculation is not entirely accurate as the smooth composition profile in the solid solution is interrupted by the presence of a stoichiometric compound. A previously unknown stoichiometric compound, Ge_3Si_2, is found between the Si-rich and Ge-rich regions using high magnification microscopy.

6. The potential presence of other stoichiometric compounds was also discovered using SEM linescans.

Recommendations for Future Work

The work carried out in this project has found some interesting results, yet there is more work to be done to understand the undercooling mechanisms that exist for both the Al-Ni alloy and the Si-Ge compound.

Suggestions for future work that can potentially help to understand Cr doped and undoped Al-Ni alloys are:

1. The lack of knowledge and data regarding the additional phase found in the Cr-doped samples: $Al_{13}Cr_2$ would create an interesting opportunity to further study, particularly for any crystallographic data above 45^0 (2ϴ). It may be possible to isolate the $Al_{13}Cr_2$ phase in order to conduct further XRD experiments, with the potential use of a synchrotron beam.

2. In a previous study it was found that undercooled Al-Ni alloys follow a reverse velocity trend; where the cooling rate of the alloy decreases as the amount of undercooling, ΔT, increases [2]. This characteristic has been observed as unique to the Raney nickel alloy. The experiments conducted by Lengsdorf *et al.* made use of the electromagnetic levitation technique which has been known to suffer from overwhelming effects of stirring at low growth velocities (<0.3m/s). This is thought to be because of the magnetic field on the sample therefore not allowing natural crystal growth. An interesting direction to take the Lengsdorf *et al.* study would be to conduct experiments using a technique that does not have similar stirring effects as found in electromagnetic levitation therefore a more accurate determination of low growth velocities is possible. An ideal solidification technique that minimises stirring effect would be melt fluxing, as the droplet of given sample would be encased in a flux. Another study also determined that the reverse velocity trend may be caused by the release of heat and rejection of solute from the solid/liquid interface [120]. The increased nucleation sites seem to slow down the solidification front from propagating. Also, the above mentioned experiments may also be conducted using Cr-doped samples in order to understand whether the reverse-velocity trend is

also followed, and whether the solidification front also experiences the same effect of an increase nucleation probability.

3. An interesting direction for this study would be to conduct drop tube solidification techniques as such processes would give powders similar to those obtained by gas atomization. The drop tube technique differs from the gas atomization technique as higher cooling rates can be experienced by particles of a given size than cooling rates experienced in gas atomization. Another advantage of the drop tube techniques over the gas atomization techniques relate to stirring effects; the drop tube technique is not as violent as gas atomization due to the absence of gas jets; therefore, fragmentation of dendrites should be minimised. This would help to further the understanding of the role that Cr plays in the formation of finer dendrites with the absence of a large shear force acting on the droplets.

4. A rather important recommendation for the study of Al-Ni alloys that are doped with Cr is to test the catalytic activity of the samples produced in this study (or similar samples). In order to entirely understand the cause of a higher catalytic activity when doped with Cr it is necessary to focus on the $Al_{13}Cr_2$ phase; Since this phase is Al-rich, and with that being one of the potential reasons for relatively high catalytic activity it may be useful to create an $Al_{13}Ni_2$ (or similar) compound to assess the effect on catalytic activity of an Al-rich compound that is leached leaving nanoporous Ni. Similarly the cause for a higher catalytic activity may simply be due to the addition of 1.5 at.% Cr and so Cr itself (or possibly $Al_{13}Cr_2$) may be tested for catalytic activity.

Suggestions for future work that can potentially aid the understanding of Si-Ge semiconductors are:

1. Due to the higher cost of Ge, rapid solidification experiments can be conducted to understand the solidification sequence for low Ge-content Si-Ge compounds in order to save money whilst maintaining the same thermoelectric efficiency.

2. Several unexpected compounds found between the Si-rich and Ge-rich regions present an opportunity to study the undercooling and solidification of Si-Ge. The compound, Ge_3Si_2 among others, has not previously been reported and no crystallographic data can be found for it. Solidification of Ge-rich Si-Ge samples may help to understand the reason for the presence of such compounds, particularly samples with a starting composition similar to the stoichiometry of the compounds that were found.

3. A key recommendation for future work would be to study the thermal conductivity of the samples from this work. It would be interesting to see how the grain size affects the thermal conductivity. Current samples can be pressed together to form larger pellets to conduct appropriate experiments on.

4. Similarly, it may be useful to understand the effect on thermal conductivity of the partitioning found in the samples. Annealing is a great technique that can be used to heat the samples and initiate further back diffusion while allowing the grain size to remain the same. This technique would mean that the ideal grain size and ideal level of partitioning can be found for thermoelectric efficiency therefore benefitting the industry.

References

[1] S. Reutzel, H. Hartmann, P. Galenko, S. Schneider and D. Herlach, “Change of the kinetics of solidification and microstructure formation induced by convection in the Ni–Al system,” *Applied Physics Letters,* vol. 91, no. 4, p. 041913, 2007.

[2] R. Lengsdorf, D. Holland-Moritz and D. M. Herlach, “Anomalous dendrite growth in undercooled melts of Al-Ni alloys in relation to results obtained in reduced gravity,” *Acta Materialia Inc,* vol. 62, pp. 365-367, 2010.

[3] S. William F and J. Hashemi, Foundations of materials science and engineering, 4 ed., McGraw-Hill, 2006.

[4] W. D. Callister, Materials science and engineering : an introduction, 7 ed., Hoboken, NJ: John Wiley & Sons, 2007.

[5] C. Bernard Dennis and S. R. Stock, Elements of X-ray diffraction, 3 ed., Prentice-Hall International, 2001.

[6] D. R. Askeland, P. P. Phulé and W. Wright, The science and engineering of materials, 6 ed., Stamford, CT: Cengage Learning, 2011.

[7] D. A. Porter, K. E. Easterling and M. Y. Sherif, Phase transformations in metals and alloys., 3 ed., CRC Press, 2009.

[8] M. Flemings, “Solidification Processing,” *Metallurgical Transactions,* vol. 5, no. 10, pp. 2121-2134, 1974.

[9] W. Kurz and D. Fisher, Fundamentals of solidification, 4 ed., Uetikon-Zuerich, Switzerland: Trans Tech Publications Ltd, 1998.

[10] W. Kurz, B. Giovanola and R. Trivedi, “Theory of Microstructural Development During Rapid Solidification,” *Acta Metallurgica,* vol. 34, no. 5, pp. 823-830, 1986.

[11] A. Ilbagi, H. Henein, J. Chen, D. M. Herlach, R. Lengsdorf, C.-A. Gandin, D. Tourret and A. Garcia-Escorial, “Containerless Solidification and Characterization of Industrial Alloys (NEQUISOL),” *Journal of*

Physics: Conference Series, vol. 327, 2011.

[12] D. Turnbull, “Kinetics of Heterogeneous Nucleation,” *The Journal of Chemical Physics,* vol. 18, no. 2, pp. 198-203, 1950.

[13] C. Wang and G. Yang, “Thermodynamics of metastable phase nucleation at the nanoscale,” *Materials Science and Engineering: R: Reports,* vol. 49, no. 6, pp. 157-202, 2005.

[14] A. M. Mullis, T. D. Bigg and N. J. Adkins, “A microstructural investigation of gas atomized Raney type Al-27.5 at.% Ni catalyst precursor alloys,” *Journal of Alloys and Compounds,* vol. 648, pp. 139-148, 2015.

[15] D. St John and L. Hogan, “A simple prediction of the rate of the peritectic transformation,” *Acta Metallurgica,* vol. 35, no. 1, pp. 171-174, 1987.

[16] H. W. Kerr and W. Kurz, “Solidification of peritectic alloys,” *International Materials Reviews,* vol. 41, no. 4, pp. 129-168, 1996.

[17] E. G. Castle, A. M. Mullis and R. F. Cochrane, “Evidence for an extensive, undercooling-mediated transition in growth orientation, and novel dendritic seaweed microstructures in Cu–8.9 wt.% Ni,” *Acta Materialia,* vol. 66, pp. 378-387, 2014.

[18] M. Aziz, “Nonequilibrium Interface Kinetics During Rapid Solidification,” *Materials Science and Engineering: A,* vol. 178, no. 1-2, pp. 167-170, 1994.

[19] D. M. Herlach, “Direct measurements of crystal growth velocities in undercooled melts,” *Materials Science and Engineering, A,* Vols. 179-180, pp. 147-152, 1994.

[20] S. Battersby, R. Cochrane and A. Mullis, “Growth velocity-undercooling relationships and microstructural evolution in undercooled Ge and dilute Ge-Fe alloys,” *Journal of Materials Science,* vol. 34, no. 9, pp. 2049-2056, 1999.

[21] G. Horvay, “The tension field created by a spherical nucleus freezing into its less dense undercooled melt,” *International Journal of Heat and Mass Transfer,* vol. 8, no. 2, pp. 195-243, 1965.

[22] K. Jackson, J. Hunt, D. Uhlmann and T. Sewards, “On origin of

equiaxed zone in castings," *Transactions of the Metallurgical Society of AIME,* vol. 236, no. 2, p. 149, 1966.

[23] M. Schwarz, A. Karma, K. Eckler and D. Herlach, "Physical Mechanism of Grain Refinement in Solidification of Undercooled Melts," *Physical Review Letters,* vol. 73, no. 10, pp. 1380-1383, 1994.

[24] A. Karma, "Model of grain refinement in solidification of undercooled melts," *International Journal of Non-Equiulibrium Processing,* vol. 11, no. 2, pp. 201-233, 1998.

[25] A. Mullis and R. Cochrane, "Grain refinement and the stability of dendrites growing into undercooled pure metals and alloys," *Journal of Applied Physics,* vol. 82, pp. 3783-3790, 1997.

[26] A. Mullis and R. Cochrane, "A phase field model for spontaneous grain refinement in deeply undercooled metallic melts," *Acta Materialia,* vol. 49, no. 12, p. 2205–2214, 2001.

[27] D. Herlach, B. Feuerbacher and E. Schleip, "Phase seeding in the solidification of an undercooled melt," *Materials Science and Engineering: A,* vol. 133, pp. 795-798, 1991.

[28] X. Liu, C. Cao and B. Wei, "Microstructure evolution and solidification kinetics of undercooled Co–Ge eutectic alloys," *Scripta Materialia,* vol. 46, no. 1, pp. 13-18, 2002.

[29] B. Wei, D. M. Herlach, B. Feuerbacher and F. Sommer, "Dendritic and eutectic solidification of undercooled Co-Sb alloys," *Acta Metallurgica Et Materialia,* vol. 41, no. 6, pp. 1801-1809, 1993.

[30] S. Coriell and D. Turnbull, "Relative roles of heat transport and interface rearrangement rates in the rapid growth of crystals in undercooled melts," *Acta Metallurgica,* vol. 30, no. 12, pp. 2135-2139, 1982.

[31] D. Shechtman, I. Blech, D. Gratias and J. Cahn, "Metallic Phase with Long-Range Orientational Order and No Translational Symmetry," *Physical Review Letters,* vol. 53, no. 20, pp. 1951-1953, 1984.

[32] H. Kimura, K. Sasamori and A. Inoue, "Al–Fe-based bulk quasicrystalline alloys with high elevated temperature strength," *Journal of Materials Research,* vol. 15, no. 12, pp. 2737-2744, 2000.

[33] A. Tsai, A. Inoue and T. Masumoto, “A Stable Quasicrystal in Al-Cu-Fe System,” *Japanese Journal of Applied Physics,* vol. 26, no. 9, pp. 1505-1507, 1987.

[34] A. Tsai, A. Inoue, Y. Yokoyama and T. Masumoto, “Stable icosahedral Al-Pd-Mn and Al-Pd-Re alloys,” *Materials Transactions, JIM,* vol. 31, no. 2, pp. 98-103, 1990.

[35] F. Gillessen, D. Herlach and B. Feuerbacher, “Glass formation by containerless solidification of metallic droplets in drop tube experiments,” *Journal of the Less Common Metals,* vol. 145, pp. 145-152, 1988.

[36] M. Telford, “The case for bulk metallic glass,” *Materials Today,* vol. 7, no. 3, pp. 36-43, 2004.

[37] B. Zhang, M. Pan, D. Zhao and H. Wang, ““Soft” bulk metallic glasses based on cerium,” *Applied Physics Letters,* vol. 85, no. 1, pp. 61-63, 2004.

[38] W. Klement, R. Willens and P. Duwez, “Non-crystalline structure in solidified gold–silicon alloys,” *Nature,* vol. 187, no. 4740, p. 869–870, 1960.

[39] N. Nishiyama and A. Inoue, “Glass-forming ability of Pd42.5Cu30Ni7.5P20 alloy with a low critical cooling rate of 0.067 K/s,” *Applied Physics Letters,* vol. 80, no. 4, pp. 568-570, 2002.

[40] G. Schulze, Metallphysik, Berlin: Akademie-Verlag, 1967.

[41] R. Fleischer, “High-strength, high-temperature intermetallic compounds,” *Journal of Material Science,* vol. 22, no. 7, p. 2281–2288, 1987.

[42] N. Stoloff, C. Liu and S. Deevi, “Emerging applications of intermetallics,” *Intermetallics,* vol. 8, no. 9-11, pp. 1313-1320, 2000.

[43] D. Herlach, “Non-equilibrium solidification of undercooled metallic melts,” *Materials Science and Engineering: R: Reports,* vol. 12, no. 4-5, pp. 177-272, 1994.

[44] E. Schulson and D. Barker, “A brittle to ductile transition in NiAl of a critical grain size,” *Scripta Metallurgica,* vol. 17, no. 4, pp. 519-522, 1983.

[45] D. M. Herlach, R. F. Cochrane, I. Egry, H. J. Fecht and A. L. Greer, “Containerless processing in the study of metallic melts and their solidification,” *International Materials Review,* vol. 38, no. 6, pp. 274-347, 1993.

[46] J. Perepezko, J. Sebright, P. Hockel and G. Wilde, “Undercooling and solidification of atomized liquid droplets,” *Materials Science and Engineering A,* vol. 326, pp. 144-153, 2002.

[47] C. M. Bao, U. Dahlborg, N. Adkins and M. Calvo-Dahlborg, “Structural characterisation of Al-Ni powders produced by gas atomisation,” *Journal of Alloys and Compounds,* vol. 481, pp. 199-206, 2009.

[48] O. D. Neikov, “Chapter 5 – Atomization and Granulation,” in *Handbook of Non-Ferrous Metal Powders*, Elsevier, 2009, pp. 102-142.

[49] M. Raney, “Method of producing finely-divided nickel”. US Patent US1628190 A, 10 May 1927.

[50] F. Devred, “Raney-type nickel catalysts, the influence of promoters in hydrogenation and fuel cell reactions: a literature review,” IMPRESS project, 2004.

[51] M. Ellner, U. Kattner and B. Predel, “Constitutional and structural investigations in the aluminum-rich part of the Ni-Al and Pt-Al systems,” *Journal of the Less Common Metals,* vol. 87, no. 2, p. 305, 1982.

[52] F. Devred, A. H. Gieske, N. Adkins, U. Dahlborg, C. M. Bao, M. Calvo-Dahlborg, J. W. Bakker and B. E. Nieuwenhuys, “Influence of phase composition and particle size of atomised Ni–Al alloy samples on the catalytic performance of Raney-type nickel catalysts,” *Applied Catalysis A: General,* vol. 356, pp. 154-161, 2009.

[53] O. Shuleshova, D. Holland-Moritz, W. Löser, H.-G. Lindenkreuz and B. Büchner, “In situ observation of phase selection in undercooled Ni–Al melts,” *International Journal of Cast Metals Research,* vol. 22, no. 1-4, pp. 286-289, 2009.

[54] O. Shuleshova, D. Holland-Moritz, W. Löser, G. Reinhart, G. N. Iles and B. Büchner, “Metastable formation of decagonal quasicrystals during solidification of undercooled Al-Ni melts: In situ observations by synchrotron radiation,” *Europhysics Letters,* vol. 86, no. 3, 2009.

[55] A. Taylor and N. J. Doyle, “Further Studies on the Nickel-Aluminum

System. I. The [I-NiAl and 6-Ni2Al3 Phase Fields," *Journal of Applied Crystallography,* vol. 5, no. 3, pp. 201-209, 31 January 1972.

[56] H. Assadi, M. Oghabi and D. Herlach, "Influence of ordering kinetics on dendritic growth morphology," *Acta Materialia,* vol. 57, p. 1639–1647, 2009.

[57] U. Birkenstock, J. Scharschmidt, P. Kunert, H. Meinhardt and P. Meier, "Process for producing powdered aluminum alloys". Patent US5090997 A, 11 January 1991.

[58] N. J. E. Adkins, "Intermetallic Materials Processing in Relation to Earth and Space Solidification FP6-500635-2," Ceram Process and Materials, 2005.

[59] H. Lei, Z. Song, D. Tan, X. Bao, X. Mu, B. Zong and E. Min, "Preparation of novel Raney-Ni catalysts and characterization by XRD, SEM and XPS," *Applied Catalysis A: General,* pp. 69-76, 2001.

[60] H. Warlimont, U. Kühn and N. Mattern, "Rapidly quenched Raney catalyst precursors," *Materials Science and Engineering: A,* vol. 226–228, pp. 900-904, 1997.

[61] A. M. Mullis, L. Farrell, R. F. Cochrane and N. J. Adkins, "Estimation of Cooling Rates During Close Coupled-Coupled Gas Atomization Using Secondary Dendrite Arm Spacing Measurement," *Metallurgical and Materials Transactions B,* vol. 44B, no. 4, pp. 992-998, 2013.

[62] IMPRESS, *Intermetallic Processing in Relation to Earth and Space Solidification, EU Framework VI (Integrated) Project # NMP3-CT-2004-500635-2..*

[63] D. Tourret, G. Reinhart, C.-A. Gandin, G. N. Iles, U. Dahlborg, M. Calvo-Dahlborg and C. M. Bao, "Gas atomization of Al–Ni powders: Solidification modeling and neutron diffraction analysis," *Acta Materialia,* vol. 59, pp. 6658-6669, 2011.

[64] D. Tourret, C.-A. Gandin, T. Volkmann and D. M. Herlach, "Multiple non-equilibrium phase transformations: Modeling," *Acta Materialia,* vol. 59, no. 11, p. 4665–4677, 2011.

[65] F. Devred, G. Reinhart, G. N. Iles, B. van der Klugt, N. J. Adkins, W. J. Bakker and B. E. Nieuwenhuys, "Synchrotron X-ray microtomography of Raney-type nickel catalysts prepared by gas atomisation: Effect of

microstructure on catalytic performance,” *Catalysis Today,* vol. 163, pp. 13-19, 2011.

[66] H. Hu, M. Qiao, S. Wang, K. Fan, H. Li, B. Zong and X. Zhang, “Structural and catalytic properties of skeletal Ni catalyst prepared from the rapidly quenched Ni50Al50 alloy,” *Journal of Catalysis,* vol. 221, pp. 612-618, 2004.

[67] S. R. Montgomery, “Catalysis of organic reactions,” Dekker, New York, 1981.

[68] J. M. Bonnier, J. P. Damon and J. Masson, “New approach to skeletal nickel catalysts catalytic properties of the nickel-chromium system,” *Applied Catalysis,* vol. 42, no. 2, pp. 285-297, 1988.

[69] T. Koscielski, J. M. Bonnier, J. P. Damon and J. Masson, “Catalytic hydrogenation on raney nickel catalyst modified by chromium hydroxide deposition,” *Applied Catalysis,* vol. 49, no. 1, pp. 91-99, 1989.

[70] M. Pisarek, M. Łukaszewski, P. Winiarek, P. Kedzierzawski and M. Janik-Czachor, “Influence of Cr addition to Raney Ni catalyst on hydrogenation of isophorone,” *Catalysis Communications,* vol. 10, pp. 213-216, 2008.

[71] B. H. Zeifert, J. Salmones, J. A. Hernandez, R. Reynoso, N. Nava, J. G. Cabanas-Moreno and G. Aguilar-Rios, “Physicochemical and catalytic properties of iron-promoted Raney-nickel catalysts obtained by mechanical alloying,” *Catalysis Letters,* vol. 63, no. 3, pp. 161-165, 1999.

[72] K. Mund, G. Richter and F. Von Strum, “Titanium-containing Raney nickel catalysts for hydrogen electrodes in alkaline fuel cell systems,” *Electrochem,* 1977.

[73] A. M. Mullis, T. D. Bigg and N. J. Adkins, “Structure and phase-composition of Ti-doped gas atomized Raney-type Ni catalyst precursor alloys,” *Intermetallics,* vol. 67, pp. 63-68, 2015.

[74] Y. Kiros, M. Mijari and T. A. Nissinen, “Effect and characterization of dopants to Raney nickel for hydrogen oxidation,” *Journal of Alloys and Compounds,* vol. 360, pp. 279-285, 2003.

[75] S. Hamar-Thibault, J. Masson, P. Fouilloux and J. Court, “Selective

hydrogenation of acetophenone on chromium promoted Raney nickel catalysts. I. Characterization of the catalysts," *Applied Catalysis A,* vol. 99, pp. 131-145, 1993.

[76] Z. Liu, A. Masuda and M. Kondo, "Investigation on the crystal growth process of spherical Si single crystals by melting," *Journal of Crystal Growth,* vol. 311, pp. 4116-4122, 2009.

[77] S. Roy and T. Ando, "Solidification behavior of highly supercooled polycrystalline silicon droplets," *Materials Science in Semiconductor Processing,* vol. 15, pp. 722-730, 2012.

[78] T. Aoyama and K. Kuribayashi, "Rapid solidification processes of semiconductors from highly undercooled melts," *Materials Science and Engineering A,* Vols. 304-306, p. 231–234, 2001.

[79] Z. Jian, K. Nagashio and K. Kuribayashi, "Direct observation of the crystal-growth transition in undercooled silicon," *Metallurgical and Materials Transactions A,* vol. 33, no. 9, p. 2947–2953, 2002.

[80] R. P. Liu, T. Volkmann and D. M. Herlach, "Undercooling and solidification of Si by electromagnetic levitation," *Acta Materialia,* vol. 49, p. 439–444, 2001.

[81] D. Li and D. Herlach, "High Undercooling of bulk molten silicon by containerless processing," *Europhysics Letters,* vol. 34, no. 6, pp. 423-428, 1996.

[82] Q. Wang, R. Liu, Y. Qian, D. Lou, Z. Su, M. Ma, W. Wang, C. Panofen and D. Herlach, "Metal-like growth of silicon during rapid solidification by quenching undercooled droplets on a chill plate," *Scripta Materialia,* vol. 54, p. 37–40, 2006.

[83] T. Aoyama and K. Kuribayashi, "Influence of undercooling on solid/liquid interface morphology in semiconductors," *Acta Materialia,* vol. 48, no. 14, p. 3739–3744, 2000.

[84] Z. Jian, K. Kuribayashi and W. Jie, "Critical undercoolings for the transition from the lateral to continuous growth in undercooled silicon and germanium," *Acta Materialia,* vol. 52, pp. 3323-3333, 2004.

[85] G. Devaud, *Ph.D Thesis,* Harvard University, 1988.

[86] G. Devaud and D. Turnbull, "Undercooling of molten silicon," *Applied*

Physics Letters, vol. 46, no. 9, pp. 844-845, 1985.

[87] Y. Shao and F. Spaepen, “Undercooling of bulk liquid silicon in an oxide flux,” *Journal of Applied Physics,* vol. 79, no. 6, pp. 2981-2985, 1996.

[88] E. Billig, “Growth of Monocrystals of Germanium from an Undercooled Melt,” *Proceedings of the Royal Society of London. Series A, Mathematical and Physical Sciences,* vol. 229, no. 1178, pp. 346-363, 1955.

[89] G. Devaud and D. Turnbull, “Microstructures of undercooled Germanium droplets,” *Acta Metallurgica,* vol. 35, no. 3, pp. 765-769, 1987.

[90] C. Lau and H. Kui, “Microstructures of undercooled Germanium,” *Acta Metallurgica Et Materialia,* vol. 39, no. 3, pp. 323-327, 1991.

[91] P. Evans, S. Vitta, R. Hamerton, A. Greer and D. Turnbull, “Solidification of germanium at high undercoolings: morphological stability and the development of grain structure,” *Acta Metallurgica Et Materialia,* vol. 38, no. 2, pp. 233-242, 1990.

[92] T. Aoyama, Y. Takamura and K. Kuribayashi, “Dendrite growth processes of silicon and germanium from highly undercooled melts,” *Metallurgical and Materials Transactions A,* vol. 30, no. 5, pp. 1333-1339, 1999.

[93] D. Li and D. Herlach, “Containerless solidification of germanium by electromagnetic levitation and in a drop-tube,” *Journal of Materials Science,* vol. 32, no. 6, p. 1437–1442, 1997.

[94] S. Omae, T. Minemoto, M. Murozono, H. Takakura and Y. Hamakawa, “Crystal evaluation of spherical silicon produced by dropping method and their solar cell performance,” *Solar Energy Materials and Solar Cells,* vol. 90, no. 20, pp. 3614-3623, 2006.

[95] K. Nagashio, H. Okamoto, H. Ando, K. Kuribayashi and I. Jimbo, “Spherical Silicon Crystal Formed by Semisolid Process in Drop Tube,” *Japanese Journal of Applied Physics,* vol. 45, no. 24, p. 623, 2006.

[96] S. Masuda, K. Takagi, W. Dong, K. Yamanaka and A. Kawasaki, “Solidification behavior of falling germanium droplets produced by pulsating orifice ejection method,” *Journal of Crystal Growth,* vol. 310,

no. 11, pp. 2915-2922, 2008.

[97] D. Li, K. Eckler and D. Herlach, “Undercooling, crystal growth and grain structure of levitation melted pure Ge and Ge-Sn alloys,” *Acta Materialia,* vol. 44, no. 6, pp. 2437-2443, 1996.

[98] R. R. King, N. H. Karam and M. Haddad, “Multijunction photovoltaic cells and panels using a silicon or silicon-germanium active substrate cell for space and terrestrial applications.”. US Patent US 6340788 B1, 2002.

[99] C. B. Vining, “Thermoelectric Properties of Silicides,” in *CRC Handbook of Thermoelectrics*, 1 ed., N. Sullivan, Ed., CRC Press LLC, 1995, pp. 329-337.

[100] R. W. Olesinski and G. J. Abbaschian, “The Ge-Si (Germanium-Silicon) System,” *Bulletin of Alloy Phase Diagrams,* vol. 5, no. 2, pp. 180-183, 1984.

[101] W.-K. Rhim and T. Ishikawa, “Thermophysical Properties of Molten Germanium Measured by a High-Temperature Electrostatic Levitator,” *International Journal of Thermophysics,* vol. 21, no. 2, pp. 429-443, 2000.

[102] G. Bernard-Granger, K. Favier, M. Soulier, C. Navone, M. Boidot, B. Deniau, P. Grondin, J. Leforestier and J. Simon, “Thermoelectric properties of an N-type silicon–germanium alloy related to the presence of silica nodules dispersed in the microstructure.,” *Scripta Materialia,* vol. 93, p. 40–43, 2014.

[103] G. H. Zhu, H. Lee, Y. C. Lan, X. W. Wang, G. Joshi, Z. W. Wang, J. Yang, D. Vashaee, H. Guilbert, A. Pillitteri, M. S. Dresselhaus, G. Chen and Z. F. Ren, “Increased Phonon Scattering by Nanograins and Point Defects in Nanostructured Silicon with a Low Concentration of Germanium,” *Physical Review Letters,* vol. 102, 2009.

[104] B. Yu, M. Zebarjadi, H. Wang, K. Lukas, H. Wang, D. Wang, C. Opeil, M. Dresselhaus, G. Chen and Z. Ren, “Enhancement of Thermoelectric Properties by Modulation-Doping in Silicon Germanium Alloy Nanocomposites.,” *Nano Letters,* vol. 12, no. 4, p. 2077–2082, 2012.

[105] L. K. Eckler and D. M. Herlach, “Evidence for Transitions from Lateral to Continuous and to Rapid Growth in Ge-lat%Si Solid Solution.,”

Europhysics Letters, vol. 32, no. 3, pp. 223-227, 1995.

[106] C. Panofen and D. M. Herlach, “Rapid solidification of highly undercooled Si and Si–Co melts,” *Applied Physics Letters,* vol. 88, 2006.

[107] P. Zhang, Z. Wang, H. Chen, H. Yu, L. Zhu and X. Jian, “Effect of Cooling Rate on Microstructural Homogeneity and Grain Size of n-Type Si-Ge Thermoelectric Alloy by Melt Spinning,” *Journal of Electronic Materials,* vol. 39, no. 10, pp. 2251-2254, 2010.

[108] H. Nagai, Y. Nakata, H. Minagawa, K. Kamada, T. Tsurue, M. Sasamori and T. Okutani, “Synthesis of Si–Ge Alloy by Rapid Cooling in Short-Duration Microgravity,” *Japanese Journal of Applied Physics,* vol. 41, pp. 749-753, 2002.

[109] C. Panofen and D. Herlach, “Solidification of highly undercooled Si and Si-Ge melts,” *Materials Science and Engineering A,* Vols. 449-451, pp. 699-703, 2007.

[110] J. I. Goldstein, C. E. Lyman, D. E. Newbury, E. Lifshin, P. Echlin, L. Sawyer, D. C. Joy and J. R. Michael, Scanning Electron Microscopy and X-Ray Microanalysis, 3 ed., New York: Springer Science+Business Media, Inc., 2003.

[111] A. C. Larson and R. B. Von Dreele, General Structure Analysis System (GSAS), Los Alamos National Laboratory, 2004.

[112] B. H. Toby, “EXPGUI, a graphical user interface for GSAS,” *Journal of Applied Crystallography,* vol. 34, pp. 210-213, 2001.

[113] M. J. Cooper, “The structure of the intermetallic phase θ(Cr-Al),” *Acta Crystallographica,* vol. 13, no. 3, p. 257, 1960.

[114] J. Schindelin, I. Arganda-Carreras, E. Frise, V. Kaynig, M. Longair, T. Pietzsch, S. Preibisch, C. Rueden, S. Saalfeld, B. Schmid, J.-Y. Tinevez, D. J. White, V. Hartenstein, K. Eliceiri, P. Tomancak and A. Cardona, “Fiji: an open-source platform for biological-image analysis,” *Nature Methods,* vol. 9, p. 676–682, 2012.

[115] R. H. Davies, A. T. Dinsdale, J. A. Gisby, J. A. J. Robinson and S. M. Martin, “MTDATA - Thermodynamics and Phase Equilibrium Software from the National Physical Laboratory,” *CALPHAD,* vol. 26, no. 2, pp. 229-271, 2002.

[116] T. C. Duong, A. Talapatra, W. Son, M. Radovic and R. Arróyave, “On the stochastic phase stability of Ti2AlC-Cr2AlC,” *Nature Scientific Reports,* vol. 7, 07 2017.

[117] X. Z. Li, K. Sugiyama, K. Hiraga, A. Sata and A. Yamamoto, “Crystal structure of orthorhombic epsilon-Al4Cr,” *Zeitschrift fur Kristallographie,* vol. 212, pp. 628 - 633, 1997.

[118] X. Z. Li, K. Higara, K. Sugiyama and A. Yamamoto, “Structural relationship between the e-Al4Cr and k-Al-Cr-Ni phases, in Quasicrystals: Proceedings of the 6th International Conference on Quasicrystals, 26-30 May 1997,” in *World Scientific*, Tokyo, Japan, 1998.

[119] B. B. Cao and K. H. Kuo, “Crystal structure of the monoclinic - Al11Cr2,” *Journal of Alloys and Compounds,* vol. 458, p. 238–247, 2008.

[120] M. Reinartz, S. Burggraf, M. Kolbe, P. Paul, P. Galenko, D. M. Herlach and M. Rettenmayr, “Solidification of Al-Ni melts under terrestrial and microgravity conditions,” in *Solidification and Gravity VII*, Miskolc-Lillafüred, Hungary, 2018.